Magnetic Nanocomposites for Organic Dye Removal from Aqueous Solutions

Thesis Submitted to AcSIR for the Award of the Degree of
DOCTOR OF PHILOSOPHY
in Chemical Sciences

AcSIR

By
Harsha N
Registration No: 10CC11A39003

Under the guidance of

Dr. Satyajit Shukla

CSIR-NATIONAL INSTITUTE FOR INTERDISCIPLINARY
SCIENCE AND TECHNOLOGY (CSIR-NIIST)
THIRUVANANTHAPURAM-695 019, KERALA, INDIA

July, 2016

Dedicated to My Mother for her
Measureless Love and Support

DECLARATION

I hereby declare that the Ph.D. thesis entitled "**Magnetic Nanocomposites for Organic Dye Removal from Aqueous Solutions**" is an independent work carried out by me at the **Materials Science and Technology Division (MSTD), CSIR-National Institute for Interdisciplinary Science and Technology (CSIR-NIIST), Thiruvananthapuram** under the supervision of **Dr. Satyajit Shukla**, **Senior Scientist** and it has not been submitted anywhere else for any other degree, diploma, or title.

Harsha N

Thiruvananthapuram

July, 2016

CSIR-NATIONAL INSTITUTE FOR INTERDISCIPLINARY SCIENCE AND TECHNOLOGY (CSIR-NIIST)
Council of Scientific and Industrial Research (CSIR)
GOVERNMENT OF INDIA
Thiruvananthapuram-695019, India

AcSYR

Dr. Satyajit Shukla
Senior Scientist

Functional Materials Section
Materials Science and Technology Division

CERTIFICATE

This is to certify that the work incorporated in this Ph.D. thesis entitled *"Magnetic Nanocomposites for Organic Dye Removal from Aqueous Solutions"* submitted by *Ms. Harsha N* to the *Academy of Scientific and Innovative Research (AcSIR), New Delhi* in the partial fulfilment of the requirements for the award of the *Degree of Doctor of Philosophy* in the *Chemical Sciences* embodies original research work under my guidance. I further certify that this work has not been submitted to any other University or Institution in part or full for the award of any degree or diploma.

Harsha N

Dr. Satyajit Shukla

(Thesis Supervisor)

Thiruvananthapuram

July-2016

Telephone: +91-471-2515385; **Fax**: +91-471-2491712; **E-Mail:** satyajit_shukla@niist.res.in

ACKNOWLEDGEMENTS

Thiruvananthapuram

July   **Harsha N**

CONTENTS

Chapter 4   **Synthesis of $H_2Ti_3O_7$/γ-Fe_2O_3 Magnetic Nanocomposites via Hydrothermal and Their Dye Adsorption/ Decomposition Properties**

Chapter 5   **Synthesis of $H_2Ti_3O_7/\gamma\text{-}Fe_2O_3$ Magnetic Nanocomposite via Ion-exchange Mechanism and Its Dye Adsorption Characteristics**   **171-198**

LIST OF FIGURES

hydroxyterpthalic acid (a) and 3-aminophthalate (b) formed as a result of radical trapping (c), after the contact time of 10 min, as observed for the different catalysts at the excitation wavelengths of ~315 and ~350 nm respectively. PL intensities 1observed in (a) and (b) are proportional to the concentration of $^{\bullet}OH$ and $O2^{\bullet-}$ produced as a result of the activation of H_2O_2 using the different catalysts. 161

Chapter 5.

LIST OF TABLES

LIST OF SCHEMES

LIST OF ABBREVIATIONS

AC : Activated carbon

AOP : Advanced oxidation processes

BET : Brunauer-Emmett-Teller

CB : Conduction band

CNTs : Carbon Nanotubes

DKR : Dubinin-Kaganer-Radushkevich

EDX : Energy dispersive X-ray

GC : Gas chromatograph

HRTEM : High resolution transmission electron microscopy

HTN : Hydrogen titanate

HTNF : Hydrogen titanate-γ-Fe_2O_3

ICP-AES : Inductively coupled plasma atomic emission spectroscope

JCPDS : Joint committee on powder diffraction standards

MB : Methylene blue

NPs : Nanoparticles

PAN : Poly acrylonitrile

PL : Photoluminescence

PSA : Poly (styrene-acrylic acid)

ROS : Reactive oxygen species

SAED : Selected area electron diffraction

SEM	: Scanning electron microscope
TA	: Terepthalic acid
TEOS	: Tetraethyl orthosilicate
TNT	: Titanate nanotubes
TSF	: $\gamma\text{-}Fe_2O_3/SiO_2/TiO_2$
TEM	: Transmission electron microscopy
UV	: Ultraviolet
VB	: Valence band
XRD	: X-ray diffraction

PREFACE

The organic synthetic-dyes are extensively used in various industries such as the textile, leather tanning, paper production, food technology, agricultural research, light harvesting arrays, photo-electrochemical cells, and hair coloring. Due to their large scale production, extensive use, and subsequent discharge of colored wastewaters, the toxic and non-biodegradable organic synthetic-dyes cause considerable environmental pollution and they are health risk factors. Moreover, they also affect the sunlight penetration and oxygen solubility in the water bodies which in turn affect the underwater photosynthesis activity and life-sustainability. In addition to this, due to their strong color even at lower concentrations, the organic synthetic-dyes generate serious aesthetic issues in the wastewater disposal. Therefore, the removal of highly stable organic synthetic-dyes from the industry effluents and aqueous solutions is of prime importance. Although various physical, chemical, physico-chemical, and biological processes have been developed for this purpose, the photocatalysis, adsorption, and Fenton-like advanced oxidation processes (AOPs) are of greater interest in view of their commercial potential. The catalysts used in these three typical dye-removal processes, however, pose significant issues in the solid-liquid separation from the treated aqueous solution. The traditional methods of catalyst separation such as the filtration, centrifugation, sedimentation, flocculation are either tedious, time consuming or not applicable on the industrial scale. This has been the prime motivation in the synthesis of different magnetic nanocomposites as magnetically separable catalyst in the photocatalysis, adsorption, and Fenton-like AOPs. In the present work, the magnetic nanocomposites consisting of either magnetically responsive core with a catalytic shell or a hybrid nanostructure with a unique catalytic

activity and magnetic separatability have been processed, characterized, and their dye-removal performance has been analyzed relative to that of the respective non-magnetic counterparts.

The entire thesis has been divided into seven chapters. The first-chapter highlights the hazardous nature of industrial effluents containing organic synthetic-dyes and the urgency in the development of advanced technologies for the effective effluent treatment. Further, the recent development in magnetic nanocomposites used for the removal of organic synthetic-dyes typically via the photocatalysis, adsorption, and Fenton-like AOPs have been reviewed in this chapter. The motivation and broad objectives of the thesis are briefly outlined at the end of the chapter.

The second-chapter deals with the synthesis, characterization, and measurement of photocatalytic activity of sol-gel derived nanocrystalline titania (TiO_2)-coated maghemite (γ-Fe_2O_3) nanoparticles with and without the silica (SiO_2) interlayer. It has been systematically demonstrated that the SiO_2-coating as an interlayer between the anatase-TiO_2 shell and the γ-Fe_2O_3 magnetic ceramic core plays a crucial role in enhancing the concentration of free hydroxyl radicals ($^\bullet OH$) produced, their rate of formation, the amount of dye-adsorbed on the surface in the dark, the thermal stability against the phase transformation of magnetic ceramic core, the efficiency of magnetic separation, and the stability of magnetic ceramic core against the photo-dissolution under the UV-radiation exposure. The values of apparent first-order-reaction rate-constants (k_{app}) for the best magnetic nanocomposite sample and the commercially available non-magnetic CDH TiO_2 are measured to be 0.126 and 0.166 min^{-1} which are comparable with each other. Moreover, it is observed that the photocatalytic

activity of γ-Fe$_2$O$_3$-TiO$_2$ core-shell magnetic photocatalyst is severely affected by the photo-dissolution phenomenon in the absence of SiO$_2$ interlayer. We demonstrate, *for the first time*, that the involvement of AOPs, such as the Fenton-reaction, makes the same photo-dissolution process responsible for an enhanced photocatalytic activity.

In the third-chapter, hydrogen titanate (H$_2$Ti$_3$O$_7$) nanotubes (HTN) have been synthesized via the hydrothermal and utilized for the removal of cationic methylene blue (MB) dye from an aqueous solution via the surface-adsorption mechanism. The amount of MB dye adsorbed on the surface of HTN at equilibrium (q_e) has been examined as a function of contact time, initial dye-concentration, and initial solution-pH. A new model has been proposed to explain the observed variation in q_e as a function of above variables. Within the investigated range of initial solution-pH (2.5-11), the MB adsorption on the surface of HTN has been observed to follow the pseudo-second-order kinetics with the dye-adsorption capacity of 105 mg g^{-1} observed at the initial solution-pH of ~10. The adsorption equilibrium follows the Langmuir isotherm in a highly acidic solution (initial solution-pH~2.5) and Dubinin-Kaganer-Radushkevich (DKR) isotherm in a highly basic solution (initial solution-pH~11); while, within the intermediate range of initial solution-pH (~7.5 and 10), it exhibits a transition from the Langmuir to DKR isotherm. The obtained adsorption data serves as a reference for the similar data obtained for the HTN-based magnetic nanocomposites as processed in the chapaters-4 and 5.

The fourth-chapter illustrates the synthesis and characterization of magnetic nanocomposite (HTNF) composed of HTN and γ-Fe$_2$O$_3$ nanoparticles by subjecting the sol-gel derived magnetic photocatalyst (γ-Fe$_2$O$_3$/SiO$_2$/TiO$_2$), having the varying

amount of TiO_2 in the shell, to the hydrothermal conditions. The HTNF magnetic nanocomposite, having varying weight-fraction of γ-Fe_2O_3 nanoparticles (61-92 wt%), has been utilized for the removal cationic MB dye from the aqueous solutions via the surface-adsorption mechanism at the initial solution-pH of ~10. Very fast magnetic separation (in less than a minute) and the recyclability of HTNF magnetic nanocomposite have been demonstrated through the catalytic decomposition of previously adsorbed dye on its surface via hydrogen peroxide (H_2O_2) activation. The underlying mechanism of dye-decomposition has been revealed using the different radical trapping agents which confirms, *for the first time,* the synergy effect between the constituents of HTNF magnetic nanocomposite.

The fifth-chapter provides a facile strategy for the synthesis of HTNF magnetic nanocomposite via an ion-exchange mechanism. The interaction between HTN and γ-Fe_2O_3 in the neutral aqueous solution is demonstrated to be purely ion-exchange in nature and the bond is typically formed at highly energetic sites provided by ends of the nanotubes. The MB adsorption characteristics of HTNF magnetic nanocomposites have been investigated by varying the amount of γ-Fe_2O_3 nanoparticles (5-25 wt%), and initial MB concentration at the initial solution-pH of ~10. The recyclability of HTNF magnetic nanocomposite has been demonstrated by decomposing the previously adsorbed MB dye via the surface-cleaning treatment conducted in H_2O_2 solution.

In the sixth-chapter, the non-magnetic palladium (Pd)-flyash and magnetic Pd-magnetite (Fe_3O_4)-flyash composite particles have been processed, *for the first time,* using the combination of electroless and inverse co-precipitation techniques. The dye-

removal characteristics of the catalysts have been investigated in the dark-condition via the Fenton-like reactions involving the activation of H_2O_2 to generate the $^\bullet OH$ in the aqueous solutions containing the basic and industrial azo reactive dyes. Within the investigated test-conditions, the Pd-flyash composite particles show higher dye-removal rates than those associated with the Pd-Fe_3O_4-flyash composite particles. Conversely, the Pd-Fe_3O_4-flyash composite particles exhibit effective magnetic separation after the dye-decoloration process which is not possible without the presence of intermediate layer of Fe_3O_4. For both the catalysts, the chemical oxygen demand (COD) levels of the decolorized aqueous solutions are observed to be increased after the catalyst-treatment of the initial dye-solutions. Nevertheless, the increased COD levels are easily controlled by the post treatment with the high surface-area activated carbon (AC) which strongly adsorbs the intermediate products of the dye-decoloration and carbon leached out from the surface of flyash particles. Hence, the Fenton-like reactions backed up with the AC-based adsorption process appear to be effective combination for the fast and efficient removal of organic synthetic-dyes from the aqueous solutions.

The summary of entire thesis work has been provided in the seventh-chapter which also includes the scope for the future work.

Chapter 1

Introduction to Magnetic Nanocomposites and Their Application in Different Dye Removal Techniques

Graphical Abstract
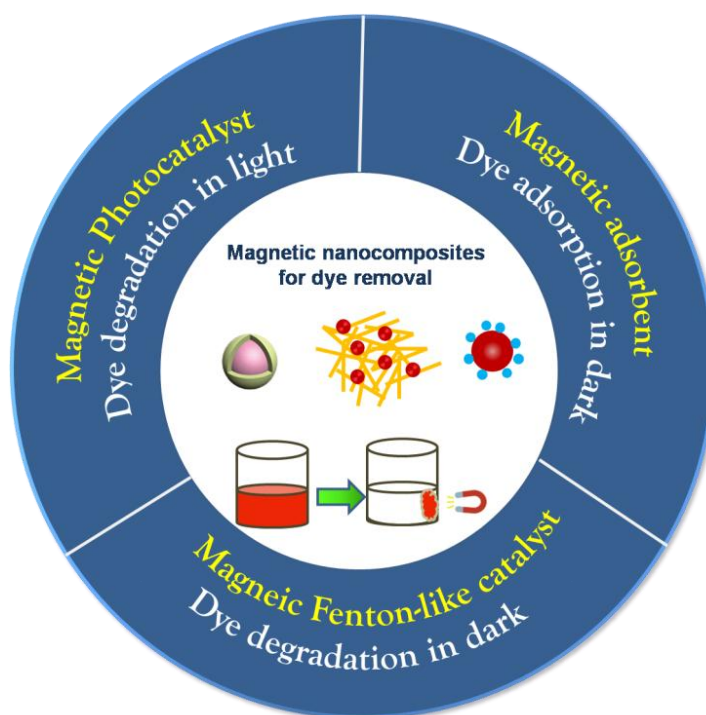
Highlights

- Different types and morphologies of magnetic nanocomposites are introduced.

- Different types of organic synthetic-dyes, their hazardous nature, and different dye-removal techniques available are discussed.

- Significance of magnetic nanocomposites in the dye-removal application is emphasized.

- Development of magnetic nanocomposites used in photocatalysis, adsorption, and Fenton-like AOPs is reviewed.

- Motivation for conducting present research work and its major objectives are described.

Abstract

Organic synthetic dyes are one of the major water pollutants and the difficulties in their removal are of great challenge to the environmental research. In addition to this, the separation of catalysts/adsorbents from the treated aqueous solution or effluent is another major challenge in this area. Much attention has been paid in the development of magnetic nanocomposites due to the ease of their separation from the treated solution using an external magnetic field. In the present chapter, the different morphologies and types of magnetic nanocomposites, in general, are reviewed first along with the classification of synthetic dyes and their hazardous nature to the human beings. Different techniques available for the removal of synthetic dyes are summarized along with their advantages and disadvantages. Considering their commercial significance, the current status of the development of magnetic nanocomposites in the area of photocatalysis, adsorption, and advanced oxidation processes (AOPs) has been reviewed in further details. The underlying mechanisms of organic dye-removal, different magnetic nanocomposites developed, and the problems and challenges associated with these technologies have been outlined. The motivation for conducting the present research work and its major objectives are described at the end of the chapter.

1.1. Magnetic nanocomposites

A nanocomposite is a multiphase solid material where one of the phases has one, two or three dimensions of less than 100 nanometers, or structures having nano-scale repeat distances between the different phases that make up the material.[1] For example, bone is a natural nanocomposite containing polymeric collagen, and calcium phosphate. The nanocomposite constitutes materials of different chemical and physical properties that are combined into a single domain. Therefore, the properties such as the mechanical, electrical, thermal, optical, electrochemical, and catalysis of the nanocomposites are different than the constituent materials.[2] In the same way, the magnetic nanocomposite is a type of nanocomposite having one magnetic component which is generally composed of the magnetic nanoparticles (NPs) embedded in a non-magnetic or magnetic matrix. Matrix-dispersed nanoparticles can be fashioned in a variety of states; for example, dispersed in a continuous amorphous matrix, grafted on larger, mesoscale particles, or well defined, three-dimensional superstructures of nanoparticles.[3]

1.1.1. Morphology

Scheme 1.1 displays various morphologies of the magnetic nanocomposite materials. Among the nanomaterials, the magnetic nanocomposites have gained significant attention due to their intrinsic magnetic properties, which makes them successful as magnetically recoverable catalysts, drug delivery agents, anticancer materials, and magnetic resonance imaging devices. Magnetic part in the magnetic nanocomposites includes metallic, bimetallic nanoparticles, metal oxides, ferrites, and superparamagnetic iron oxide nanoparticles. Generally, the stability of the magnetic nanoparticles is found to be less due to its strong tendency to aggregate. In order to

avoid the aggregation tendency of the magnetic nanoparticles, bare magnetic nanoparticles are usually coated with either organic species, including surfactants and polymers, or an inorganic layer such as silica (SiO_2) or carbon.[4] The surface-modified or functionalized magnetic nanocomposites are more effective in many functional applications.
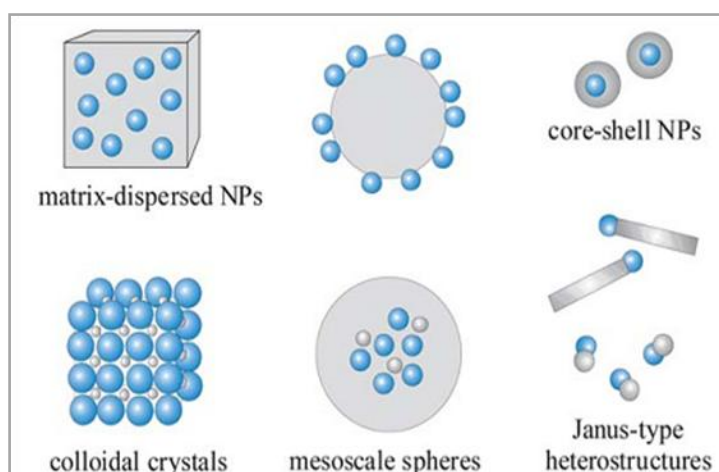
Scheme. 1.1. Typical morphologies of the magnetic hybrid nanocomposite materials. Blue spheres represent the magnetic nanoparticles and matrix materials are displayed in gray color.[5]

1.1.2. Types

Different types of magnetic nanocomposites have been synthesized which are classified depending on the morphology and nature of constituents such as the silica-based magnetic nanocomposites, self-assembled nanocomposites, core–shell inorganic nanocomposites, and organic–inorganic nanocomposites.[6] Silica is the most commonly employed coating or matrix material. The main advantages of using SiO_2 are its biocompatibility, hydrophilic nature, and stability against degradation. It can form silanol groups which may be easily derivatized with a variety of functional

groups and offers a suitable base for further functionalization.[5] Magnetic SiO_2 composite materials have been prepared via several procedures, including aerosol routes (aerosol pyrolysis, spray-drying), microemulsion polymerization, and sol–gel processes (Stober method).[3] The non-aggregated, mesoporous SiO_2 nanoparticles are of great interest for the biomedical application because their pore channel allows long blood circulation.[7] Kim et al. reported the direct encapsulation of individual magnetite (Fe_3O_4) nanoparticles into mesoporous $Fe_3O_4@SiO_2$ particles with the diameters of 45 to 105 nm.[8] In their system, the function of Cetyltrimethylammonium bromide (CTAB) was not only to stabilize the hydrophobic Fe_3O_4 NPs into the aqueous phase but also to act as a template for the formation of mesopores via sol–gel reaction. The template was removed by treating with an acidic ethanol solution. When the pH value during the extraction is very low, the leaching of Fe_3O_4 cores takes place and were fully removed if the pH decreased below 1. Lee et al. demonstrated that mesoporous SiO_2-decorated Fe_3O_4 nanoparticles have great potential in the magnetic resonance imaging, fluorescence imaging, and drug delivery.[9] In addition to this, the SiO_2-coated magnetite serves as an effective substrate for many organic reactions. Silver loaded mesoporous SiO_2/Fe_3O_4 was used an effective catalyst in the reduction of 4-Nitrophenol and styrene epoxidation reactions.[10] Supported Pd nano-catalysts onto ionic SiO_2-coated magnetic particles have been utilized for the hydrogenation of trans-stilbene and styrene in ionic liquids.[11]

The self-assembly of nanostructured materials holds a promise as a low-cost, high-yield technique with a wide range of scientific and technological applications. The self-assembly is frequently used because it permits the aggregation of nanostructures conveniently manipulated into an ordered arrays which may provide a function to the materials. In a matrix of material, both Van der Waals and dipolar interactions tend to

agglomerate the magnetic nanoparticles forming anisotropic clusters.[12] In the processing of such an anisotropic structure, the internal tuning by controlling the density is very difficult. As an alternative method, the use of an external trigger to control the anisotropy is an attractive alternative. In the frame work structure, the use of external magnetic field during the processing of polymer reinforced magnetic nanoparticles has been proposed. The poly-dimethylsiloxane encapsulated with the magnetic nanoparticles was synthesized in a simpler way in which a dispersion of magnetic nanoparticles and polymer was placed under an external magnetic field.[13] The anisotropic arrays of magnetic nanoparticles direct the final morphology and cured the polymer in the presence of magnetic field inorder to retain their microstructure.

Most of the core-shell nanostructures are developed with the idea to combine two materials - and thus incorporate two properties within one structure. The core-shell particles are typically spherical in shape, but different possible types of core-shell nanostructures based on the different core and shell shapes have been reported with the several morphologies such as the nanotubes, nanowires, nanorods, nanorings, and nanostars. The core structure can be tuned to get appropriate functions. The possible core structure may be dense, porous, or even be completely removed from the structure either via the calcination or dissolution using suitable solvents as given in Scheme 1.2a.[14] Similarly, there are different types of shells such as the continuous and dense shells, continuous and porous/particulate shells, or discontinuous/particulate shell, Scheme 1.2b. In addition, more complex nanostructures have been prepared such as core/bilayered-shell, core/composite-shell, or core/multilayered-shell nanoparticles, Scheme 1.2c. Various synthesis techniques have been developed for the

core-shell structures with the controlled composition, type, morphology, shell thickness, core size, and its distribution. The most commonly used methods are the gas phase processes, spray pyrolysis, surface oxidation, sol-gel, and hydrothermal.
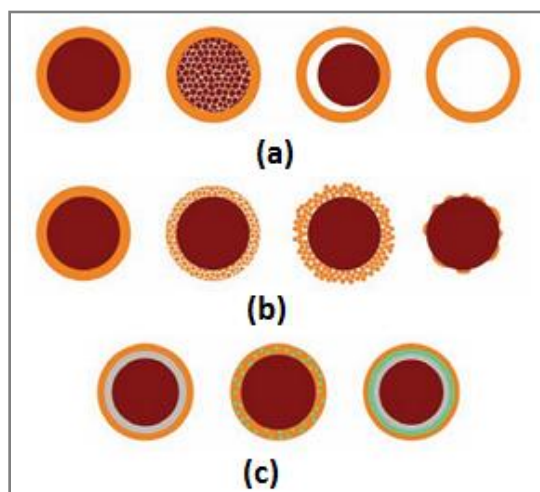
Scheme 1.2. Core-shell nanocomposites with different type of cores (a), shells (b) and complex core-shell nanostructures (c).[14]

1.2. Synthetic dye pollution in coloring industry

The history of the use of natural dyes records from 3500 BC which is mainly extracted from the natural materials like vegetables, fruits, flowers, certain insects, and fish.[15] However, they impart a dull range of colors and their numbers are limited. Besides, they show color fadedness when exposed to washing and sunlight. The discovery of synthetic dyes by Perkins in 1856 has offered a wide range of dyes that can color fast and arrive in a wider color range, and brighter shades. Today, the synthetic dyes make a substantial industry in the world which covers mostly the coloring industries such as the textile, plastic, paper, and pharmaceuticals. The improper disposal of dyes, even at lower concentrations, makes their presence highly visible and cause aesthetic issues. At higher concentration in the water sources cause

environmental damage to the living organisms by hampering the reoxygenation capacity of water and also blocking the sunlight, thereby disturbing the natural growth activity in the aquatic life. The majority of the synthetic dyes are recalcitrant, resistant to aerobic digestion, and are stable to light, heat, oxidizing agents, carcinogenic, mutagenic, and teratogenic.[16] Over 1,00,000 commercially available dyes exist and more than 7,00,000 tons per year are produced annually.[17] The textile industries are the major consumer of the synthetic dyes. During the coloration process, a large quantity of dyes is lost to the waste stream. Approximately 10-15% dyes are released as an effluent in addition to the other additives which are added at the time of coloring process.[18] Therefore, huge quantities of colored wastewaters are generated from the coloring industries. Recently, the removal of dyes from the effluent has given a great extent of attention in controlling the wastewater pollution.

1.2.1. Classification of synthetic dyes

Synthetic dyes are classified according to its use or application method.[19]

Reactive dyes. These dyes form a covalent bond with fiber usually cotton fibers, although this is used for dyeing on wool and nylon. Their chemical structures are simpler, absorption spectra show narrower absorption bands and dyeing is brighter. The principal chemical classes of reactive dyes are azo, triphendioxazine, pthalo cyanine, formazan and anthraquenone.

Disperse dyes. These are water insoluable non ionic dyes for application to hydrophobic fibres from an aqueous dispersion. They are used mainly in polyster and less extends on nylon, cellulose, cellulose acetate and acrylic fibres.

Direct dyes. These are water soluble anionic dyes. These have high affinity for the cellulosic fibers. Their principal use involves dyeing of cotton, regenerated

cellulose, paper, leather, and lesser extend to nylon. Most of the dyes in this class are poly azo compound along with stilbenes, phthalocyanines and oxazines.

Vat dyes. These water insoluble dyes are applied mainly to the cellulosic fibers as the soluble leuco salts after the reduction in an alkaline bath usually with sodium hydrogen sulphite. Leuco form is then reoxidized to insoluble keto form in exhaustion and after treatment usually by soaping to develop the crystal structure.

Sulphur dyes. These are mainly applied to the cotton from an alkaline reducing bath with sodium sulphide as the reducing agent. The low cost and good wash fastness properties of dyeing make this class important from the economic standpoint.

Basic dyes. These are water soluble cationic dyes which are applied to paper, poly-acrylonitrile, modified nylon, and modified polyesters. The principal chemical classes are diazahemicyanine, triarylmethane, cyanine, hemicyanine, thiazine, oxazine and acridine. Some basic dyes show biological activity and are used in medicine as antiseptic.

Acid dyes. These are water soluble anionic dyes which are applied to nylon, wool, silk, and modified acrylics. They are also used to some extent for paper, leather, inkjet printing, food and cosmetics.

Solvent dyes. These are water insoluble, but are solvent soluble and devoid of polar solubilizing groups such as the sulphonic and carboxylic acid. They are used for coloring plastics, gasoline, oils, and waxes. These dyes are predominantly azo and anthraquinone but phthalocyanine and triaryl methane dyes are also used.

1.2.2. Hazardous nature of dyes

The treatment of effluents containing dyes is not an easy work because most of these chemicals are not prone to aerobic digestion. Most of the dyes, used in the textile industries, are recognized only by their trade name; while, their chemical nature and biological hazards are not known. The textile dyes can cause allergies such as the contact dermatitis and respiratory diseases, allergic reaction in eyes, skin irritation, and irritation to mucous membrane and the upper respiratory tract. The reactive dyes form covalent bonds with cellulose, woollen and Nylon/Polyamid fibres. It is assumed that in the similar way the reactive dyes can bond with $-NH_2$ and $-SH$ group of proteins in the living organisms.[20] Numerous investigations of the respiratory diseases in the workers dealing with the reactive dyes have been made. Certain reactive dyes have caused respiratory sensitization of workers occupationally exposed to them. Methylene blue is an important cationic dye and is used in many textile manufacturers and it releases aromatic amines (for example, benzidine, methylene) and is a potential carcinogen.[21] Dyes like Metanil Yellow also have a tumor-producing effect and can produce enzyme disorders in the human body.[22] On oral consumption, it causes toxic methaemoglobinaemia.[23] The oral feeding or intraperitoneal and intratesticular administration of dyes in the animal produces testicular lesions due to which seminiferous tubules suffer damage and the rate of spermatogenesis is decreased.[24]

1.2.3. Methods of dye removal

The methods reported in the literature for the removal of dyes from effluents or waste waters broadly classified as chemical oxidation, physical or biological. Biological treatment is often the most economical alternative when compared with other physical and chemical processes. Methods like fungal decolourization, microbial

decolourization, adsorption by microbial biomass (living or dead) and bioremediation systems are commonly applied to the treatment of industrial effluents because many microorganisms such as bacteria, yeast, algae, and fungi can able to accumulate and degrade different dyes. Physical methods used for dye removal commonly are membrane-filtration processes (reverse osmosis, electrodialysis, nano-filtration), and various adsorption techniques. Chemical methods include coagulation or flocculation combined with floatation and filtration, precipitation, electro floatation, electro kinetic coagulation, conventional oxidation methods by oxidizing agents such as ozone, irradiation or electrochemical processes. The main advantages and disadvantages of these methods are shown in Table 1.1.[25]

Table 1.1. Advantages and disadvantages of various dye removal methods.

Methods	Advantages	Disadvantages
(i) Chemical treatment		
Oxidative process	Simplicity of application	Hydrogen peroxide (H_2O_2) agent needs to be activated by some means
H_2O_2 + Fe(II) salts (Fenton's reagent)	Fenton's reagent is a suitable chemical activator	Sludge generation
Ozonation	Ozone can be applied in its gaseous state and does not increase the volume of wastewater and sludge	Short half-life (20 min)
(ii) Biological treatments		
Decolorization by white-rot fungi	White-rot fungi are able to degrade dyes using enzymes	Enzyme production has been shown to be unreliable
Other microbial cultures (mixed bacterial)	Decolorization in 24–30 h	Under aerobic conditions azo dyes are not readily metabolized
Adsorption by living/dead microbial biomass	Certain dyes have a particular affinity for binding with the microbial Species	Not effective for all dyes
Anaerobic textile dye bioremediation systems	Allows azo and other water soluble dyes to be decolorized	Anaerobic breakdown yields methane and hydrogen sulfide

(iii) Physical treatments		
Adsorption by activated carbon	Good removal of wide variety of dyes	Very expensive
Membrane filtration	Removes all dye types	Concentrated sludge production
Ion exchange	Easy regeneration: no adsorbent loss	Not effective for all dyes
Irradiation	Effective oxidation at laboratory scale	Requires a lot of dissolved O_2
Electro-kinetic coagulation	Economically feasible	High sludge production

1.3. Magnetic nanocomposites for dye sequestration and mineralization

Introduction of magnetic nanaocomposites in the area of wastewater treatment simplifies the entire dye sequestration process. It takes very short time for the separation of dye removal material and economic compared to the conventional centrifugation, filtration, and settling process. In the dye-removal process using the magnetic nanocomposite, two strategies are commonly adopted. First one is the use of a magnetic adsorbent in which the dye is transferred from the solution to the adsorbent surface. After the adsorption, the magnetic adsorbent particles are possible to separate under the application of external magnetic field. The magnetic incorporation of carbon-based nanostructures, polymeric and metal oxides are the main candidates of this category. The second one is the degradation by different advanced oxidation processes (AOPs) or by dissolving the adsorbed dye with suitable solvents/degradation by the oxidizing agent. The adsorption process is simple, fast, no need of external energy and no side products are formed. Whereas the dye degradation process based on the AOPs involves the generation of highly potential reactive oxygen species (ROS). Most of the AOPs are based on the generation of hydroxyl radical ($^\bullet$OH) which is the second highest oxidation potential next to fluorine (Table 1.2) The AOPs assisted oxidation of the organic dyes leads to the complete removal by mineralization. However, the process is time and energy

consuming. Advanced oxidation processes involve photocatalysis, Fenton, electrolysis, ultrasound/microwave, and ozone. Most commonly, the combination of two or more processes have been applied to get a good efficiency. For example, in the Fenton reaction, in order to get a better performance the process is usually carried out in the presence of ultraviolet (UV) light where the addition of $^\bullet$OH are generated by the decomposition of H_2O_2. Recently, the magnetic nanoparticles incorporated materials are coming in the whole areas of AOPs.

Table 1.2. The oxidizing potential of some common oxidizing agents.[26]

Oxidising agent	Oxidation potential (E^0) (V)
Fluorine	3.06
Hydroxyl radical	2.80
Atomic oxygen	2.42
Ozone	2.06
Hydrogen peroxide	1.78
Hypochlorite	1.49
Chlorine	1.36
Chlorine dioxide	1.27
Molecular oxygen	1.23

1.3.1. Magnetic photocatalyst

Fujishima and Honda discovered the photocatalytic splitting of water over titania (TiO_2) as the evolution of H_2 and O_2.[27] Presently, the area of photocatalyst extends to several applications based on the generation of $^\bullet$OH. Due to its nonselective degradation nature, it is widely applied for the removal of pollutants in air and water. Several materials including the semiconductor oxides (for example, TiO_2, ZrO_2, ZnO, WO_3, MoO_3, SnO_2, and α-Fe_2O_3) and semiconductor sulfides (for example, ZnS, CdS, $CdSe$, WS_2, and MoS_2) have shown their potential in photocatalysis reaction.[28] Among these TiO_2 is considered as the best material since it is chemically stable,

inexpensive, easily available, and non-toxic. In the photocatalysis, the light having energy higher than the band-gap energy of TiO_2 is irradiated, the electrons in the valence band (VB) are excited to the conduction band (CB). Immediately after the charge separation, the electron and hole may migrate to the catalyst-surface where they undergo redox-reactions with the surface-adsorbed species. The surface-adsorbed OH^-/H_2O molecules abstract the holes and forming the $^{\bullet}OH$ in a series of reactions.[29]

$$TiO_2 + h\nu \rightarrow e_{cb}^- + h_{vb}^+ \tag{1.1}$$

$$(H_2O \Leftrightarrow H^+ + OH^-)ads + h_{vb}^+ \rightarrow {^{\bullet}OH} + H^+ \tag{1.2}$$
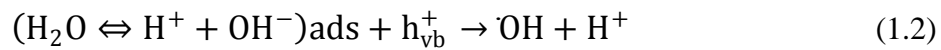
The electrons in the conduction band are also involved in the generation of $^{\bullet}OH$ through the intermediate production of superoxide radical anions ($O_2^{\bullet-}$). The mechanism of photocatalytic reaction is presented in Fig. 1.1. The superoxide radical anions continue to undergo dismutation extremely rapidly and form hydrogen peroxide.

$$O_2 + e^- \rightarrow O_2^{\bullet-} \xrightarrow{H^+} HO_2 \xrightarrow{H^+O_2^-} H_2O_2 + O_2 \tag{1.3}$$
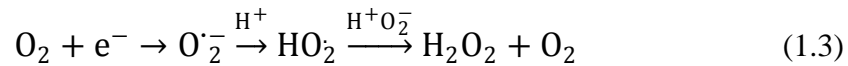
Under irradiation (≤ 250 nm), the hydrogen peroxide produces highly reactive hydroxyl radicals.

$$H_2O_2 \xrightarrow{h\nu} 2\,^{\bullet}OH \tag{1.4}$$

The suspended TiO_2 solution is reported with high photocatalytic performance typically under the UV-light. For the practical application, such suspended particles suffer the limitation of the separation properties. The TiO_2 immobilized on different substrates like zeolite, silica, and glass were studied; however, this results in a decreased activity due to lower specific surface-area and slower mass transfer

reactions.[30] Therefore, the main subject of the environmental studies is to integrate the magnetic nanoparticles with the semiconductor photocatalysts to retain the better reactive performance of the photocatalysts derived from higher specific surface-area and to enable renewable utilization by the magnetic separation.
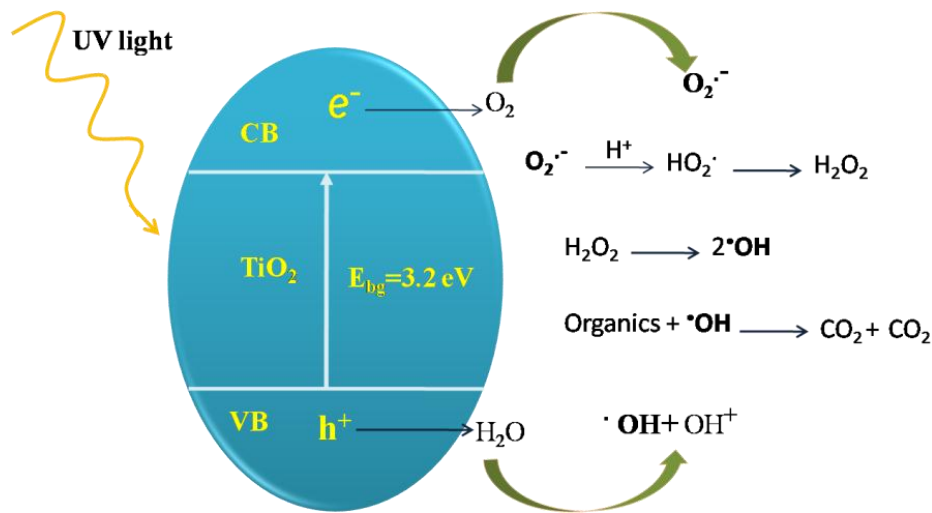
Fig. 1.1. Mechanism of photocatalysis using TiO_2.

1.3.1.1. Core-shell morphology

The first magnetic photocatalyst was designed by Hiroshi et al. and was prepared through the deposition of titanium dioxide onto a magnetite core in 1994.[31] In fact, the idea of magnetic photocatalyst was developed and patented by Atsuya and Mutsuo in 1997.[32] The structure of the magnetic nanocomposite was just a dispersion of magnetic metal particles in the matrix of photocatalytic semiconducting material. In 1998, Beydon et al. synthesized TiO_2 coated magnetite having the core-shell nanostructures.[33] These two component materials met the requirement of separation function but the activity and the stability was found to be less. This is attributed to the recombination of photo-excited electron-hole pairs in the magnetic core as well as photo-dissolution of Fe_3O_4 under the light irradiation following the heat treatment.

Therefore, an insulating layer is necessary to introduce in between the core and the shell of the magnetic composite to avoid the photo-dissolution. Silica is often used as an interlayer owing to its large band-gap energy which prevents the undesirable electronic contact. Other commonly used interlayer materials are carbon, Al_2O_3, Poly (methyl methacrylate) and poly (sodium 4-styrene sulfonate) (PPS-) polyanion coupled with poly (diallyldimethylammonium) (PDD+) cation.[34-36] The typical core-shell type structure of a magnetic photocatalyst is shown in Figure 1.2.
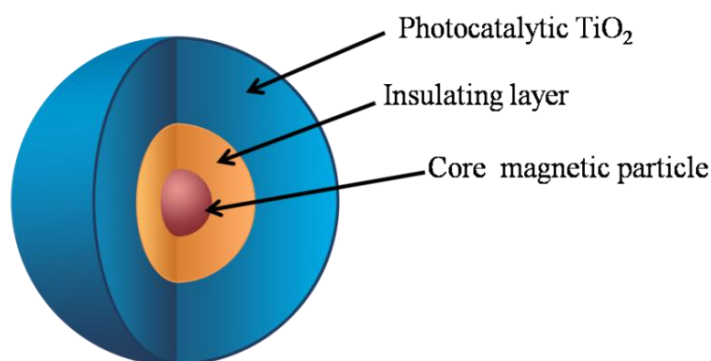
Fig. 1.2. Typical structure of core-shell magnetic photocatalyst with the core of magnetic nanoparticle, insulating middle layer, and photocatalytic outer layer.

Since SiO_2 layer can reduce the magnetic dipolar attraction, it enhances the dispersion of magnetic composite particles in the solution. Thus, it maintains the stability of magnetic composite particles and also protects them from an acidic environment. The most adopted technique for the synthesis of SiO_2 coating over the magnetic core particle has been the Stober method. The SiO_2 coating thickness can be tuned by controlling the kinetics of hydrolysis of tetraethyl orthosilicate (TEOS) in ethanol-water mixture. The formation of SiO_2 coating based on different synthetic parameters was investigated by Deng et al.[37] It is concluded that for obtaining a uniform coating requires ethanol solvent with the molar ratio of ethanol to water within the range of

2-4. Moreover, the excess TEOS and ammonia increase the irregularities on the core-shell structures.

1.3.1.2. Charge transfer mechanism

In a two component core-shell structure, the magnetic particle is enclosed within the outer TiO_2 layer. The difference in the band-gap energy of these two semiconductors direct the flow of charge carriers from higher energy levels of one semiconductor to the lower lying energy levels of second semiconductor. When the light is irradiated on TiO_2, the photo-excited electron from the CB of TiO_2 is transferred to the lower lying CB of iron oxide (Figure 1.3). Similarly, since the holes are also transferred to VB of iron oxide, the recombination of these two occurs in the iron oxide. Therefore, when an insulating layer is introduced, the transfer of charge-carriers in between the semiconductors is inhibited. Moreover, there should be an optimum thickness for the interlayer material is necessary to prevent this charge transfer. In the case of SiO_2 interlayer, Christopher's reported that the photo-generated electrons can still transfer if the thickness of the SiO_2 is less than 5 nm.[38]
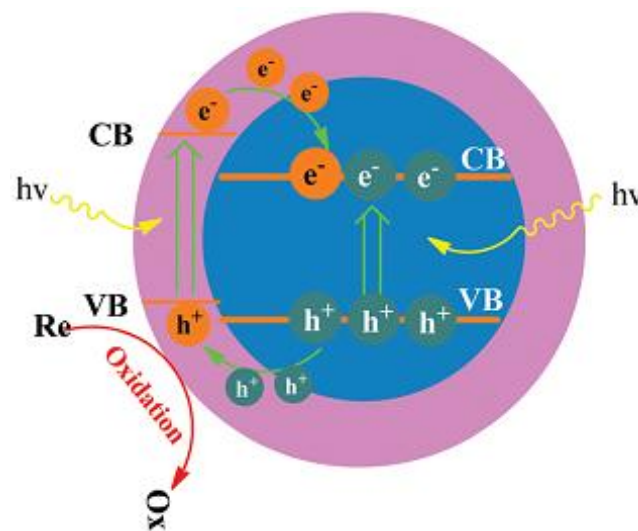
Fig. 1.3. Charge transfer mechanism in core-shell semiconducting structures.

1.3.1.3. Modifications

The outermost layer of a typical magnetic photocatalyst, ie photocatalytic titania is employed by different methods. The main coating methods include wet-chemical methods such as the sol–gel technique, dry methods such as the aerosol combustion technique, or chemical vapor deposition. Among these, the sol–gel process is advantageous since it is capable of producing photocatalysts with excellent chemical homogeneity, high purity, and more uniform phase distribution in the multi-component systems. The control of the rate of hydrolysis process is possible, and hence, the nature of TiO_2 coating can be tuned. In the most commonly reported sol-gel method, TiO_2 was coated in the amorphous form just after the hydrolysis. In order to transform it to the crystalline photoactive TiO_2, the heat treatment is required. The effect of heat treatment on TiO_2 coated iron oxide on the activity and stability of crystal phase was studied by Beydon et al.[39] The high temperature calcination reduces the photocatalytic activity and magnetic properties. The study revealed that an optimum heat treatment of $450^{o}C$ which is sufficient for the transformation of amorphous to anatase crystalline phase.[23] The high temperature decreases the numbers of surface adsorbed hydroxyl ions and make the surface become more positive.[45] Since the TiO_2 coating was porous, it allowed the oxidation of core magnetic iron oxide (magnetite) to less magnetic phase (hematite).

The heat treatment performed at the final synthesis stage of the magnetic TiO_2 photocatalyst to convert the amorphous titania formed in sol-gel process to the crystalline photoactive anatase titania cause the decrease in photocatalytic activity and magnetism. Therefore, several attempts have been made for low temperature preparation of TiO_2 coating. Makovec et al. synthesized TiO_2 nanocrystallites of

4-6 nm via the hydrolysis of $TiOSO_4$ at an elevated temperature of 90^oC.[40] Rana et al. synthesized anatase TiO_2–$NiFe_2O_4$ magnetic photocatalyst system via the reverse micelle and acid hydrolysis.[41] Heat treatment on $NiFe_2O_4$ microemulsion containing acidic titanium salt solution at a temperature of 90^oC precipitates the anatase titania. This nanocomposite was utilized for the methyl orange degradation and bacterial inactivation. The minimum temperature reported for the synthesized TiO_2 coating is 75^oC where the TiO_2 was coated over the activated carbon-Fe_3O_4 particles.[42] This composite shows higher activity than that of the commercial Degussa P25. The homogeneous and acid sol routes adopted for TiO_2 coating were also attempted and resultant activities were compared. It was found that titania-iron oxide photocatalyst prepared by acid sol method exhibited better morphology and photocatalytic activity than that of homogeneous precipitation. However, both these composites exhibited higher activity than that of pure TiO_2. Another modification strategy involves the synthesis of highly mesoporous TiO_2 shell. For this purpose, polymers like p123 is used as a template which leads to the formation of mesopores after the final calcination step.[43] Polyaniline modified TiO_2/SiO_2/Fe_3O_4 composite was reported by Huang et al. which showed a remarkable photo-degradation towards MB dye under the visible-light.[44]

Other than the introduction of semiconducting insulating interlayer and several polymer modifications, the enhanced activity of TSF is achieved by doping of nonmetal in the TiO_2 shell. Non-metals like C, S, I, and N are the potential non-metal dopants which can shift the absorbance into the visible region.[45] Aziz et al. investigated the photocatalytic activity of N-doped TiO_2 supported $SrFe_{12}O_{19}$ for the degradation of biocalcitrant and toxic pesticide 2,4 dichloro phenol.[46] The effect of

iodine doping was studied by He et al. and found that molar ratio (I/TiO_2) of 1:10 was the optimum for the efficient degradation of phenol.[47] The incorporation of carbon into the magnetic photocatalyst enhances its activity through increasing the adsorption property of the material.[48-50] Xuan et al. fabricated TiO_2/Fe_3O_4 hollow spheres in multi-step process using poly (styrene-acrylic acid) (PSA).[51] The magnetite particles were non-continuously coated over PSA and TiO_2 was encapsulated over it. At the final stage, the TiO_2/Fe_3O_4 hollow structure was obtained via the etching of PSA and solvothermal conversion of amorphous to crystalline titania. This composite showed photocatalytic activity towards Rhodamine B dye higher than that of Degussa P25.

1.3.1.4. Limitations

Although magnetic TiO_2 photocatalyst removes dyes effectively in an aqueous solution, it has certain limitations such as lengthy coating process for SiO_2 and thicker TiO_2 (typically by Stober and sol-gel processing) over the core magnetic nanoparticles. The removal of dyes takes place predominantly by degradation and therefore it will not work in dark. Prolonged light exposure time is usually required for the degradation of complex organic dye molecules having high concentrations.

1.3.2. Magnetic adsorbent

Among the various techniques suggested for the removal of toxic organic species, the adsorption method gained much popularity because of its simplicity and high efficiency compared to other techniques. This process neither uses costly equipment, external energy, nor chemicals. Thorough investigation has been conducted on the conventional low-cost adsorbent such as the clay, zeolite, orange peel, banana pith, and others.[52] However, these are inefficient for the complete removal of all types of

industrial dyes. The carbon-based materials possess large specific surface-area and they are well-known for different kinds of pollutants including dyes.[53] Magnetic nanocomposites of carbon-based materials such as the CNTs, graphene, nanocarbon have been reported recently as the strong dye adsorbent.[54-56] However, their synthetic routes are rather tedious and surface modifications are necessary for making them hydrophilic. Therefore, the environmental researchers are now looking into novel materials that can be processed using a simple route which have high adsorption capability like carbon-materials. The materials used as a magnetic dye adsorbent can be classified into pure magnetic particles, carbon or polymer or inorganic metal oxide based nanocomposite materials and others.

Magnetic nanoparticles alone having very small size and high specific surface-area have been used as good adsorbent. Nickel ferrite ($NiFe_2O_4$) magnetic nanoparticles with average size less than 50 nm in the diameter were applied for the adsorptive removal of azo dye Eriochrome black-T from an aqueous solution.[57] The maximum dye adsorption capacity was 47.0 mg g^{-1} at the pH of 6. The kinetics and adsorption isotherm studies revealed that kinetics follows pseudo-second–order and the best isotherm fit was obtained by the Langmuir model. Afkhami et al. investigated the adsorption of congo red onto γ-Fe_2O_3 nanoparticles and their desorption characteristics.[58] The maximum adsorption occurred at the pH of 5.9. The Langmuir adsorption capacity (q_{max}) was found to be 208 mg g^{-1}. Wang et al. found a novel and simple method to enhance the adsorption ability of Fe_3O_4 particles via HCl-assisted sonication.[59] The q_e value obtained for C. I. reactive blue 194 is 19 mg g^{-1}. Remarkably, with an effective desorption was carried out in H_2O_2 solution and sonication for an hour, the pretreated Fe_3O_4 exhibited good adsorption strength by

retaining the dye removal rate of about 90% after five recycles. Poedjiet al. synthesized Fe_3O_4 nanoparticles of size in the range of 5-20 nm by chemical co-precipitation method.[60] The saturation magnetism was 89.46 emu g^{-1} and adsorption capacity towards procion dye was 30.503 mg g^{-1}. Magnetically separable $MnFe_2O_4$ nanocrystals were synthesized by Zhong et al. through salt-assisted solution combustion method.[61] These particles upon dye adsorption showed that the $MnFe_2O_4$ nanocrystals prepared with KCl salt exhibited much better adsorption capacity for Congo red than those prepared without KCl since the introduction of KCl into the solution combustion synthesis process results in an obvious dispersion and increment of specific surface-area in the obtained $MnFe_2O_4$ particles. Meanwhile, the $MnFe_2O_4$ nanocrystals exhibited a clearly ferromagnetic behavior under the applied magnetic field, which allowed their high efficient magnetic separation from the wastewater.

In order to use CNTs for the dye removal application, surface modification is generally employed since the poor solubility of CNTs cause much inconvenience in their practical application. The suitable fictionalization and incorporation of magnetic nanoparticles converts into a magnetic nanocomposite which leads to efficient dispensability and reusability of adsorbent material. Acid treatment introduces oxygen containing functional groups such as OH and COOH. Depending on nature of the dyes whether cationic or anionic, proper pH adjustment is necessary to make the surface become charged. For the adsorption of cationic dyes such as Methylene blue and Neutral red, a high adsorbent surface charge is required. Madrakian et al. investigated the adsorption capabilities of CNTs on four different cationic dyes, such as crystal violet, thionine, janus green B and methylene blue.[62] Magnetic CNT nanocomposite is grafted with polymer structures have also been reported for further

enhancing the adsorption capacity. It was suggested that the mechanism of organic dye adsorption over CNTs involves hydrophobic effect, π–π interactions, hydrogen bonding, covalent bonding, and electrostatic interactions.[63] Graphene sheets are also a promising adsorbent and almost equal considerations have been given. Yao et al. reported Fe_3O_4 nanoparticles of size 30 nm that were homogeneously dispersed onto graphene sheets through a chemical deposition method.[64] Adsorption isotherm and kinetics of MB and congo red were studied in a batch system. The maximum adsorption capacities of MB and Congo red on this nanocomposite were found to be 45.27 and 33.66 mg g^{-1} respectively. As the large delocalized electron system of graphene can form strong stacking interactions with the benzene ring it might be also a good candidate as an adsorbent for the adsorption of benzenoid form of compounds. Carbon/Fe_3O_4 nanoparticles showed almost comparable adsorption capacity as that of CNTs and graphene.

Biopolymers like chitosan show better adsorption property towards organic dyes. It is a bio-polymer formed by the deacetylation of chitin. The structure consist of β-(1-4)-2-acetoemido-2-deoxy-D-glucose chains. Various chemical modification are easily possible for chitosan because it contain large number of amino and hydroxyl groups. Debrassi et al. reported N-lauryl chitosan-Fe_2O_3 having an adsorption capacity of 267 mg g^{-1} towards a reactive dye Remazol Red 198.[65] Yan et al. investigated Glutamic acid modified chitosan magnetic nanocomposite for the effective adsorption of three kinds of cationic dyes such as MB, crystal violet, cationic light yellow 7GL and their study revealed that adsorption is more efficient when the pH is higher than 5.[66]

Magnetic nanocomposites of clay mineral have been reported for their efficiency towards the adsorption of cationic dyes. Hallosite is a kind of alumino silicate clay with predominant hollow nanotube structure. Due to its negatively charged surface, it shows less adsorption in the case of anionic dyes. The adsorption capacity for cationic dyes like MB and Neutral red are 18.44 and 13.62 mg g^{-1} respectively.[67] Almost the same trend was followed by another type of clay mineral rectorite. Wu et al. synthesized rectorite/Fe_3O_4 nanocomposite of magnetization 19.14 emu/g and exhibited good adsorption for the cationic dyes MB and neutral red while adsorption was very little for methyl orange.[68] Bentonite/Fe_3O_4 nanocomposite was reported with enhanced adsorption of 1600 mg g^{-1} for MB and it was effective for the removal of cationic dyes only.[69]

Organo silane functionalized Fe_3O_4 is another class of adsorbent material and have been reported for wide range of dye classes. Wu et al. studied the dye adsorption capability of organo silane/Fe_3O_4 composite using brilliant blue FCF.[70] The mechanism of dye and the material interaction involves hydrogen bonding, electro static and hydrophobic interaction. 3-amino propyl triethoxy silane and polymers of acrylic acid and crotonic acid is presented as reusable magnetic adsorbent for the removal of cationic dyes; crystal violet, MB and alkaline blue-6B.[71] Adsorbent magnetic nanocomposite materials which are effective for both the removal of cationic and anionic dyes are very few in numbers in the literature. However, Zhang et al. modified Fe_3O_4 with 3-glycidoxy propyl trimethyl trimethoxy silane and glycine and demonstrated for the removal of anionic dyes; methyl blue, orange I and acid red 18 and cationic dyes MB and azure I.[72]

Alginate is a poly sacharide extracted from brown seaweed. It has gain significant interest in the adsorption due to its low cost, biodegradability, and non-toxicity. The adsorption mechanism of alginate based composite involves the hydrophobic interaction and ion exchange of calcium and Na ions in the structure. Therefore, it is used for the adsorptive removal of anionic dyes. The adsorption capacity estimated for methyl orange and methyl blue were 0.02 and 0.7 mmol g^{-1}.[73] An interesting magnetic adsorbent is made from an iron containing waste red mud. It is used as a catalyst for the synthesis of the carbon nanostructures from ethanol as carbon source via chemical vapor deposition method. The obtained magnetic composites showed very good results as adsorbent for methylene blue and indigo carmine compared to the pure red mud.[74]

1.3.2.1. Adsorption kinetics and isotherm models

Generally, the adsorption kinetics and isotherm models determine the adsorption performance and associated mechanism. It describes the equilibrium time required for the uptake of dyes from the solution, correlation with the capacity and other adsorption parameters. In the recent years, it has been widely used to describe the adsorption of pollutants molecules from the wastewater on different substrates; for example, the adsorption of dyes, toxic metals, pharmaceutical waste, and radioactive materials on the various substrates.

In order to investigate the mechanism and rate controlling steps such as the mass transport and chemical reaction processes, two commonly used kinetics models are pseudo-first- order and pseudo-second-order models. Lagergren presented a first-order rate equation to describe the kinetics process of liquid-solid phase adsorption of oxalic acid and malonic acid onto charcoal, which is believed to be the earliest model

pertaining to the adsorption rate based on the adsorption capacity.[75] The linear forms of the above kinetics models can be respectively expressed as,

$$\log(q_e - q_t) = \log(q_e) - \left(\frac{K_1}{2.303}\right)t \tag{1.4}$$

$$\frac{t}{q_t} = \left(\frac{1}{q_e}\right)t + \frac{1}{q_e^2 \times K_2} \tag{1.5}$$

where, k_1 (min^{-1}), and k_2 (g mg^{-1} min^{-1}) are the Lagergren pseudo-first-order rate-constant, pseudo-second-order rate-constant, and q_t the amount of dye adsorbed on the surface per unit mass (mg g^{-1}) of adsorbent after the contact of time of t. The linear plots, with the regression correlation coefficient, $<r^2>$, approximately equal to one indicate the perfect fitting to these equations.

In 1995, Ho et al. described a kinetic process of the adsorption of divalent metal ions onto peat, in which the chemical bonding among divalent metal ions and polar functional groups on peat, such as aldehydes, ketones, acids, and phenolics are responsible for the cation-exchange capacity of the peat.[76] The main assumptions for the above adsorption process may be second-order, and the rate limiting step may be the chemical adsorption involving valent forces through sharing or the exchange of electrons between the peat and divalent metal ions. If the adsorption system follows a pseudo-second order kinetics, then a plot of t/q_t versus t would be linear and k_2 and q_e can be determined from the intercept and gradient of the graph. One of the advantages of the pseudo-second-order equation for estimating q_e values is its small sensitivity to the influence of random experimental errors.

Adsorption isotherm study is very important to understand the nature of the adsorbate adsorbent interaction. Generally employed isotherm models are Langmuir,

Freundlich, and Dubinin-Kaganer-Radushkevich (DKR). The Langmuir adsorption model is based on the assumption that all adsorption sites have equal affinity for adsorbate and permit monolayer adsorption. The concept of Freundlich model involves the heterogeneity in adsorption sites and allows multilayer coverage. The type of interaction, whether ion-exchange or electrostatic attraction that exists in between the adsorbent and adsorbate, can be identified using the DKR model. The linear equation for the above three models are as given below.[77]

$$\frac{C_e}{q_e} = \left(\frac{1}{q_m}\right) C_e + \frac{1}{q_m \times K_L} \tag{1.6}$$

$$\ln q_e = \left(\frac{1}{n}\right) \ln C_e + \ln K_F \tag{1.7}$$

$$\ln q_e = \ln q_m - \beta \varepsilon^2 \tag{1.8}$$

where, K_L (l mg^{-1}) is the Langmuir constant related to the Gibb's free-energy of adsorption, K_F (mg l$^{-1/n}$ g^{-1} l$^{1/n}$) and n (g l^{-1}) are the Freundlich constants related to q_m and adsorption intensity, β a constant related to the adsorption energy, and ε the Polanyi potential which is given by,

$$\varepsilon = RT \ln(1 + \frac{1}{C_e}) \tag{1.9}$$

where, R (J mol^{-1} K^{-1}) is a gas constant and T (K) the absolute temperature. The adsorption energy, E (kJ mol^{-1}), can be calculated using the relationship of form,

$$E = \frac{1}{\sqrt{2\beta}} \times 10^{-3} \tag{1.10}$$

When the E value is in between 8-16 kJ mol^{-1}, the adsorption is due to the ion-exchange reactions; while, the E value less than 8 kJ mol^{-1} supports the electrostatic

forces of adsorption. Moreover, the degree of suitability of material towards the adsorption is estimated from the values of separation factor (R_L), which can be calculated from the following equation,

$$R_L = \frac{1}{1 + (K_L \times C_o)}$$ (1.11)

The adsorption process is unfavorable if $R_L > 1$, linear if $R_L = 1$, favorable if $0 < R_L < 1$, or irreversible if $R_L = 0$. Further, the spontaneity of adsorption can be tested from the values of change in the Gibb's free energy (ΔG^0, J mol^{-1}) which is calculated using the equation,

$$\Delta G^0 = -RT \ln K_L$$ (1.12)

1.3.2.2. Titanate Based Adsorbents

Since the discovery of CNTs by Iijima in 1991, the major focus of the research was emerging to develop nanotubular structures of inorganic materials. Various inorganic nanotubes of WS_2, MoS_2, BN, BxCyNz, VOX, $W_xMo_yC_zS_2$ and TiO_2 were reported within a decade.[78] In 1998 Kasuga first reported the processing of TiO_2 nanotubes via hydrothermal strategy.[79] The method is inexpensive and one step reaction that requires neither expensive apparatus nor special chemicals. The TiO_2 particles of various forms include anatase, rutile, amorphous TiO_2, or even Ti metal treated with highly alkaline solution at temperatures in the range 110–150°C. The reaction is normally carried out in an autoclave with chemically resistant vessels usually lined with poly(tetrafluoroethylene) (PTFE). Subsequent washing with dilute HCl, yields nanotubular structure having the composition different than the initial product. All crystalline forms can yield nanotubes but rutile requires harsher hydrothermal condition. The actual mechanism exists in the nanotubular evolution and various

nanostructures have been carried out in the later years. The hydrothermal strategy is a sensitive process, depending on the various parameters like hydrothermal temperature, duration, alkali used, and post treatment severely effects the final composition and structure. Among the various titanate structures, the titanate nanotubes (TNTs) are the most commonly reported since their application expands in various field such as the energy, dielectrics, catalysis, batteries, photocatalysis, and environmental cleaning.

Large discrepancies still exist in the evolution of titanate nanotubes and their composition. Some researchers argued that nanotubes are formed during hydrothermal reaction.[80-81] But most of the studies revealed that tubular structure is attained only after the post acid washing stages.[82-83] Based on the later studies and various HRTEM characterizations by many researchers, it can be inferred that layered structures are formed just after the hydrothermal reaction and the composition of this product is reported as sodium titanate.[84-85] The nanosheets to nanotubular morphology are formed as result of the ion-exchange reaction occurring during the acid-wash stage. The entire formation mechanism of nanotubes can be represented as a transformation from 3D (TiO_2) to 2D (Titanate nanosheets) to 1D (Titanate nanotubes) Fig.1.4. The structure of titanate is seen to be composed of corrugated ribbons of edge-sharing TiO_6 octahedrons. The ribbons are three octahedrons wide, and these octahedrons join at the corners to form a stepped layered structure. The final titanate phase is observed to be present in different crystalline forms such as the monoclinic hydrogen trititanate $H_2Ti_3O_7$,[86] monoclinic $H_2Ti_4O_9 \cdot H_2O$,[87] orthorhombic $H_2Ti_2O_5 \cdot H_2O$,[88] or lepidocrocite type structures.[89] Trititanate consist of three edge shared octahedral and non shared oxygen atom at the stepping corner is hydroxylated. Whereas hexatitanate consist of

two parallel width of three edge shared octahedral and no hydroxylated oxygen atom. In lepidocrocite type titanate, TiO_6 octahedra are completely edge shared forming lamellar layers. This structure accommodates interlayer cations and hydronium ions. The possibility of hydrogen bond in between the layers of hydrogen titanate makes it more stability than sodium titanate.
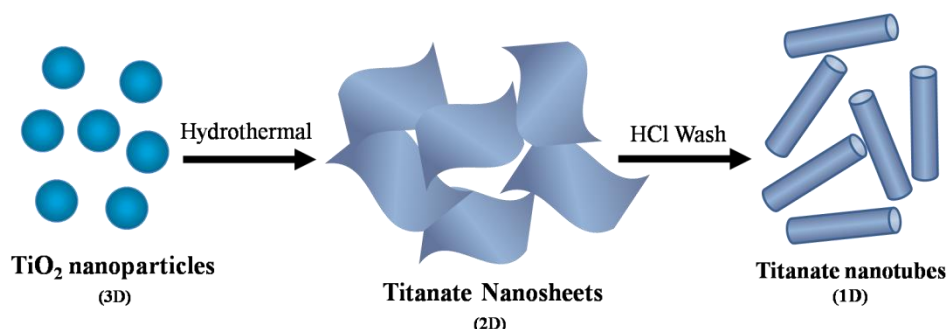
Fig. 1.4. Mechanism of titanate nanotube formation in the hydrothermal synthesis.

Zhang et al. extensively carried out structural studies using HRTEM and ab initio methods. According to zang et al., the nanotubes are evolved from the monolayered nanosheets.[90] Although an $H_2Ti_3O_7$ layer in the bulk crystals is symmetric on both the sides, the chemical environments on the two sides of a surface layer are different. The negative charge of the Ti_3O_7 layer on the side underneath the surface is neutralized by H^+ in the interlayer space. The H on the top surface, on the other hand, may undergo frequent collision by OH from the solution, Hydrogen deficiency on the surface therefore introduces surface tension that has a tendency for the surface layer to bend. First-principle calculations indicate that an asymmetric chemical environment may help to break the structural symmetry and introduce strain driving the peeling process and the formation of the nanotubes. It was found that surface tension due to an asymmetry related to H deficiency in the surface layers of the plates is the principal driving force of the cleavage and the dimension of the nanotubes is controlled by this

surface tension together with interlayer coupling energy and Coulomb force. In contrary to this, most of the reports support the nanotubular rolling occurs on multi layered nanosheets.[78]

One of the main characterization which reveals the titanate phase is XRD and corresponding 2θ values for all forms of titanate can be indexed at 10.7°, 24.7°, 28°, and 48°. The interlayer spacing is 0.83 nm from the 2θ value of 10.7°. Lu et al. proposed a model for the hydrothermal processing of titanate nanotubes which involves a rapid coalescence of nanoparticles first, followed by an exfoliation of large aggregated moieties in their peripheries into nanosheets.[91] The nanosheets were then rolled up to form short nanotubes. The nanotubes eventually transform into long tubes which assemble into nanowires. This is a stepwise evolution process common for the alkaline hydrothermal transitions. The oriented attachment model plays a vital role here, and the Oswald ripening mechanism appears to be effective.

Large specific surface-area and ion-exchanging capabilities are the two important fascinating properties of the TNTs. Sun and Li studied ion-exchanging capability and realized the potential use of the corresponding metal-substituted (Zn^{2+}, Cu^{2+}, Ni^{2+}, Co^{2+}, Ag^+ and Cd^{2+}) nanotubes with new magnetic and optical properties.[81] Liu et al. studied ion-exchange reactions that mainly focused on the sodium titanate ($Na_2Ti_3O_7$) nanotubes by substituting Na^+ through the ion-exchange process.[92] Protonated titanate nanotubes ($H_2Ti_3O_7$) prepared by the substitution of H^+ for Na^+ are revealed to exhibit a poor exchangeability. Hydrothermally-synthesized TNTs exhibited large adsorption capacities for Pb^{2+} (2.64 mmol g^{-1}), Cd^{2+} (2.13 mmol g^{-1}), Cu^{2+} (1.92 mmol g^{-1}) and Cr^{3+} (1.37 mmol g^{-1}). By means of single and competitive absorption experiments, it was demonstrated that the

adsorption of the four heavy metals on TNTs followed the sequence of $Pb^{2+} \gg Cd^{2+} >$ $Cu^{2+} \gg Cr^{3+}$ and adsorption of heavy metal was enhanced when a preferred metal co-existed in the multi-metal system. Further experiments indicated that the presence of inorganic ions had specific effects on the heavy-metal adsorption onto TNTs, with the inhibition effect observing the following sequence: Fe^{3+}, $Al^{3+} \ll Na^+ \approx K^+ \ll Mg^{2+} <$ Ca^{2+}, Na^+, K^+, Mg^{2+}, and Ca^{2+}. This inhibition effect decreases adsorption of heavy metal because they also competed for adsorption sites with heavy metal ions and promoted aggregation of titanate nanotubes which was not beneficial for the adsorption. However, Zhang et al. demonstrated high ion exchangeability under an alkaline pH (pH=10). $[Co(NH_3)_6]^{2+}$ was ion-exchanged in the whole surface as well as the interlayer of hydrogen titanate nanotubes (HTN) causes the tube walls of titanate nanotubes to get loosened up.[93] For Co ion-exchanged titanate nanotubes, the d-value of interlayer spacing is slightly larger than that of hydrogen titanate nanotubes.

Furthermore, the titanate nanotubes with abundant hydroxyl (OH) groups on the surface and lower point-of-zero charge can effectively adsorb cations via ion-exchange, and so are good adsorbents for heavy metal. Ion-exchange capacity makes titanate nanotubes an interesting material for supporting metal nanoparticles catalysts. Different metals (Pd, Au, Ru, Rh, and Pt) have been supported onto the nanotubes, with very high (up to 10 wt%) metal loadings and narrow size distribution for the metal nanoparticles have been studied in a range of catalytic reactions.[94-95]

1.3.2.3. Magnetic titanate nanotubes

Magnetic nanocomposite with titanate nanotubes were first synthesized by our group in 2009.[96] It was prepared from the core-shell $TiO_2/SiO_2/CoFe_2O_4$ composites through

hydrothermal reaction based on the conversion of TiO_2 to titanate. This work was later followed by Li et al. who studied the structural evolution during the reaction using core-shell $TiO_2/SiO_2/Fe_3O_4$.[97] Another different method involves utilization of ion exchange properties of HTN in which first it is ions is exchanged with iron ions and oxidized to magnetic oxide Fe_3O_4. Hongyun et al. synthesized the alginate-Fe_3O_4-HTN using this procedure and showed its efficiency in the removal of phthalate ester from the water samples.[98] Zou et al. also synthesized by almost same method and used for studying the adsorptive removal of radioactive ions. The adsorption experiments revealed that the Fe_3O_4@titanate nanomaterials posses saturation sorption capacity as high as 118.4 mg g^{-1} for Ba^{2+} ions.[99] Lei et al. demonstrated its efficiency in the adsorption of [109]Cd(II).[100] The removal efficiency of Lead ions on $CoFe_2O_4$/HTN was investigated.[101] The kinetics of the Pb ion adsorption follows the pseudo-second-order kinetics and attained the adsorption capacity of 442.5 mg g^{-1} at pH~5.5 according to the Langmuir isotherm model. Pb(II)-loaded magnetic adsorbent could be regenerated by EDTA-2Na solution and the adsorbent had high stability for cycling.

The magnetic titanate nanocomposite synthesized by self assembly process involving the assembly of Fe_3O_4 and HTN and that was carried in acid media. Due to the existence of an electrostatic interaction and Van der Waals forces lead to firm anchoring of Fe_3O_4 on HTN surface. The maximum adsorption capacity observed for Pb^{2+} ions is 382.3 mg g^{-1}.[102] Papa et al. synthesized an ultra small superparamagnetic iron oxide assembled HTN through one step hydrothermal method.[103] Acidic suspension of Iron oxide particles are mixed along with TiO_2 and NaOH solution before doing the hydrothermal reaction. The resulting nanocomposite showed a non uniform size distribution of iron oxide over HTN. The zeta potential measurements

and TEM observations reveal that the interaction between the nanotubes and iron oxide was not electrostatic in nature.

Other significant properties of protonated titanate nanotubes are Bronsted and Lewis acid characteristics which have been utilized in many catalytic reactions. Similar to TiO_2, the Titanate also possesses Ti^{4+} Lewis sites. Usually, BF_3 and $AlCl_3$ are the well known Lewis catalysts in many organic reactions, although they have serious drawbacks such as the production of waste, separation from the product, and corrosion of equipment.[104] The synergy between the Brønsted and Lewis acid sites has been reported to enhance the catalytic activity in isomerization, cracking, and Friedel-Crafts alkylation. It should be noted that the titanate nanosheets, such as $H_2Ti_3O_7$ which has a similar crystal structure of titanate nanotubes, do not have high catalytic activity for the Friedel-Crafts reaction, although protonated titanate nanotubes are formed from these titanate nanosheets.[101] In the case of layered $H_2Ti_3O_7$, the reactants cannot approach the Ti-OH groups in narrow interlayer spaces, resulting in no catalytic activity. Although many Ti-OH groups can be exposed to the reactants in aggregated $H_2Ti_3O_7$ nanosheets prepared by the aggregation of exfoliated $H_2Ti_3O_7$ nanosheets from layered $H_2Ti_3O_7$, this Friedel-Crafts alkylation does not proceed efficiently on the nanosheet material.

1.3.2.4. Limitations

Although the separation of a magnetic adsorbent is very easy by the application of an external magnetic field, the actual problem lies in its reusability. After the adsorption process, the organic pollutant molecules almost completely cover the adsorbent surface. The regeneration of active adsorption sites is desired for its recyclability. Several methods are suggested for the removal of dye molecules from the surface by

the desorption using a suitable solvent which may result in the secondary pollution. Most commonly used desorption method is changing the pH using NaOH or HCl solution. Ethanol is used alone or along with NaOH or HCl solutions because most of the organics are dissolved in ethanol.[72] Acetone, ethanol, acetonitrile, and ethyl acetate are also included in this category.[105]

1.3.3. Magnetic Fenton-like catalysts

Hydrogen peroxide is one of the known powerful oxidizing agents with the standard potential 1.80 and 0.87 V at pH 0 and 14 respectively and is well established in the oxidation of various organic pollutant species.[106] However, H_2O_2 alone is ineffective in the case of high pollutant concentrations due to the lower reaction rates at the ambient conditions. An enhanced oxidation rate can be achieved by using the transition metal salts (e.g. Fe, Mn, Pd, Cu etc.), ozone, or UV-light for activating H_2O_2 and forming $^{\bullet}OH$ which are the strong oxidants.

Ozone and hydrogen peroxide.

$$O_3 + H_2O_2 \rightarrow {^{\bullet}OH} + O_2 + HO_2^{\bullet} \tag{1.13}$$

 Iron salts and hydrogen peroxide

$$Fe^{2+} + H_2O_2 \rightarrow Fe^{3+} + {^{\bullet}OH} + OH^- \tag{1.14}$$

UV-light and hydrogen peroxide

$$H_2O_2 + [UV] \rightarrow 2{^{\bullet}OH} \tag{1.15}$$

Oxidation processes exploiting the activation of H_2O_2 by iron salts (ferrous iron, Fe^{2+}), classically referred to as Fenton's reagent and is known to be very effective in producing hydroxyl radicals.[107] The history of Fenton chemistry begins from 1894,

when Henry J. Fenton reported that H_2O_2 could be activated by Fe(II) salts to oxidize

tartaric acid.[108] A century later then only started its application extended to the field of

organic pollutant degradation. The reaction mechanism involves the utilization of

ferrous ions to decompose H_2O_2 as an initial step direct its reduction and form ferric

ions (Fe^{3+}). The generated ferric ions react with excess of H_2O_2 to form another

reactive oxygen radical $^{\bullet}O_2H$ (hydro peroxyl) and ferrous ions are regenerated.

However, this reaction step is relatively slower than the formation of ferric ion.

Hence, the Fenton reaction is mediated by both Fe^{2+} and Fe^{3+} as follows[109]

$$Fe^{2+} + H_2O_2 \rightarrow Fe^{3+} + OH^- + {}^{\bullet}OH \qquad (1.16)$$

$$Fe^{3+} + H_2O_2 \rightarrow Fe^{2+} + H^+ + HO_2^{\bullet} \qquad (1.17)$$

$$Fe^{3+} + HO_2^{\bullet} \rightarrow Fe^{2+} + O_2 + H^+ \qquad (1.18)$$
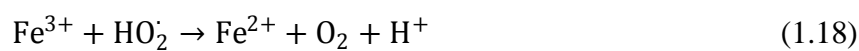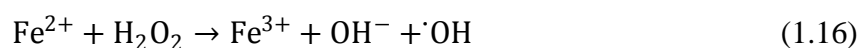
The radical-radical interactions or radical-catalyst (Fe^{2+} and H_2O_2) are also reported in

the Fenton process (Eqs. 1.19-1.23).

$$^{\bullet}OH + {}^{\bullet}OH \rightarrow H_2O_2 \qquad (1.19)$$

$$^{\bullet}OH + H_2O_2 \rightarrow {}^{\bullet}O_2H + H_2O \qquad (1.20)$$

$$^{\bullet}O_2H + {}^{\bullet}O_2H \rightarrow H_2O_2 + O_2 \qquad (1.21)$$

$$^{\bullet}OH + {}^{\bullet}O_2H \rightarrow H_2O + O_2 \qquad (1.22)$$

$$Fe^{2+} + {}^{\bullet}OH \rightarrow Fe^{3+} + OH^- \qquad (1.23)$$

1.3.3.1. Types of Fenton reactions

Conventional Fenton reaction involves the reaction of ferrous ions and H_2O_2 in order to generate $^\bullet OH$ without the aid of external energy. The external energy used in the Fenton reaction includes sono Fenton, electro Fenton, and photo Fenton processes and these are known as extended Fenton processes. The combination of extended Fenton system is also used for further enhancement is known as Hybrid Fenton reaction. The general classification for the Fenton process is shown as in Fig. 1.5.[110]
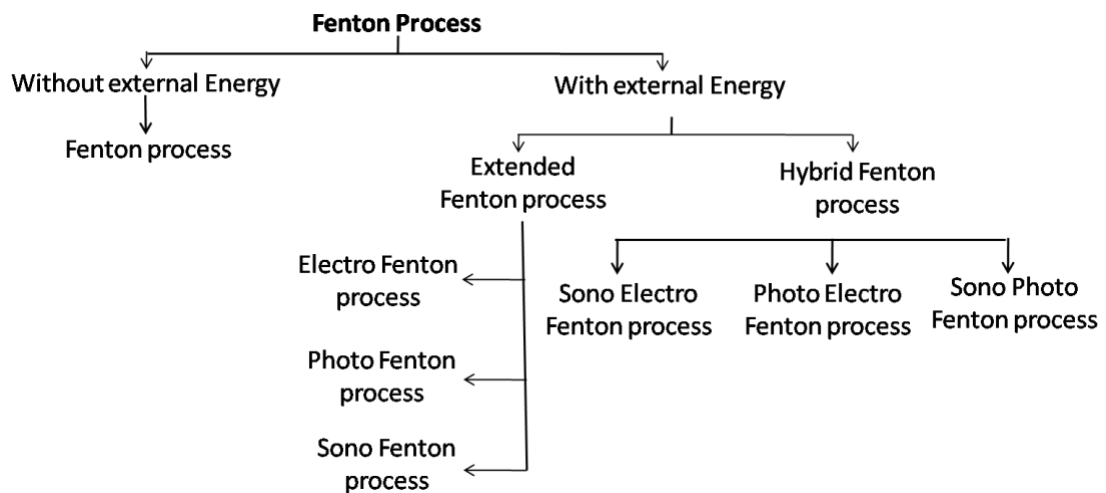
Fig. 1.5. General classification of Fenton reaction.

The combination of UV light and Fenton process, known as the photo Fenton process, enhances the generation of $^\bullet OH$ which is the consequence of H_2O_2 decomposition under the UV light. Whereas in the sono Fenton process, the presence of ultra sound irradiation generates an additional amount of $^\bullet OH$ and other radicals via the acoustic cavitation.

$$H_2O+))) \rightarrow {}^\bullet OH + H^\bullet \tag{1.24}$$

In the electro Fenton process, the ferrous ions added externally react with H_2O_2 which is produced at the cathode surface as the result of oxygen reduction in an acidic solution. The Ferric ions are immediately reduced at the cathode and ferrous ions are regenerated (Eqs. 1.25-1.26). Compared to the conventional Fenton process, number of Fenton reaction cycle is very high due to the increased rate of ferrous ion regeneration.

$$O_2 + 2H^+ + 2e^- \rightarrow H_2O_2 \qquad\qquad (1.25)$$

$$Fe^{3+} + e^- \rightarrow Fe^{2+} \qquad\qquad (1.26)$$

The degradation of dyes using the Fenton system is affected by many factors such as the initial dye concentration, solution-pH, initial catalyst concentration, H_2O_2 concentration, temperature, mixing rate and inhibitors. Generally, it is expected that the increase in H_2O_2 concentration increase the rate of Fenton reaction, whereas an optimum concentration of H_2O_2 always exists in the process. However, after a particular concentration of H_2O_2, the ability of dye removal decreases with increase in H_2O_2 concentration. At higher concentration H_2O_2 acts as a scavenger for highly potent $^\bullet OH$ and produce per hydroxyl radical thus decreases the activity. Temperature dependent study on the Fenton process reveals that the temperature beyond 30^oC decreases the degradation of dyes due to the excess H_2O_2 decomposition.[109]

1.3.3.2. Limitations of conventional Fenton system

There are several limitations associated with the conventional Fenton reaction or homogeneous Fenton process. For the practical application, large quantity of catalyst is required for the complete mineralization. The transportation of H_2O_2 in high concentrations and its handling are difficult tasks. The Fenton process is well

effective in the narrow pH range which is not applicable to the alkaline solutions. Large quantity of sludge produced as iron hydroxide ($Fe(OH)_3$) in the Fenton process generates another problem. The disposal arrangement demands an extra investment for proper design and operation of the whole system. The homogeneous nature of the catalytic system does not provide any scope for the effective separation and reuse of the catalyst.

1.3.3.3. Heterogeneous Fenton Reaction

The limitations associated with the homogeneous Fenton system are overcome by the development of heterogeneous Fenton-Like system. The main advantage is that it efficiently works in a wider range of solution-pH. Ferrous and ferric ions present inside a crystal or on the surface of the heterogeneous catalyst carry out the reaction. Various iron containing materials employed alone or along with the porous substrate have been reported very recently.[110-111] Different iron oxide phases ferrihydrite, hematite, goethite, magnetite and pyrite constitute this category. Another approach developed was immobilizing the iron in different form such as iron oxide and zero-valent iron over the porous substrates like clay, carbon, alumina, silica, and zeolite.

Magnetite is a spinel iron oxide with chemical formula of $(Fe^{3+})_{tet}[Fe^{2+}Fe^{3+}]_{oct}O_4$ where Fe^{3+} cations occupy equally both octahedral and tetrahedral sites and Fe^{2+} cations are placed only in the octahedral sites. In the Fenton process, the magnetite has gained considerable attention than other iron oxides due to its unique characteristics - (i) it is the only most abundant iron oxide with Fe^{2+} in its structure that improves hydroxyl radical production through the Fenton reaction; (ii) the presence of octahedral sites in its structure are mostly near the surface of the crystal and the catalytic activity is predominantly on account of the octahedral cations.

Higher dissolution rate of magnetite compared to other iron oxides so that higher electron mobility in its spinel structure.[112] Therefore magnetite has been used frequently in contaminant oxidation systems using Fenton process. Goethite, an iron oxyhydroxide mineral with the chemical formula of α-Fe^{III}O(OH), is another commonly used iron oxide among Fe(III) bearing minerals for the catalytic Fenton degradation / photodegradation of organic pollutants due to its (i) ability to operate in a wider range of solution-pH, (ii) positive performance under the solar radiation, (iii) higher thermodynamic stability, (iv) relatively cheaper and (v) environmentally friendly. Wang et al. compared the half-life for the photodegradation of sulfadiazine showing the performance in the order of hematite (α-Fe$_2$O$_3$) > maghemite (γ-Fe$_2$O$_3$) > lepidocrocite (g-FeOOH) > goethite (α-FeOOH) and also demonstrated better catalytic performance of goethite.[113] Under the optimal conditions, hematite has the ability to remove more than 99% of a dye from an aqueous solution after 120 min of contact time.

Flyash is a waste material produced in the coal burning power plant and its production is around 500 billion tons per year in the world.[114] The huge quantity of this waste material is a serious environmental issue. It shows a good adsorption characteristic on the metal ions and dyes. The presence of small amount of iron oxide as a constituent in the fly-ash makes it suitable for the heterogeneous Fenton-like reaction. Chen et al. used heterogeneous Fenton-like reaction on n-butyl xanthate at an optimum condition of 1.176 mmol l^{-1} H$_2$O$_2$ and 1 g l^{-1} flyash having the iron oxide mass fraction of 4.14 % at the pH of 3, which shows almost 96.9% degradation.[115] The reason for the enhanced activity at the pH of 3 is that iron leaching occurs at lower pH. A stable and separable flyash catalyst was synthesized by modifying the

flyash surface by FeOOH.[116] This catalyst shows 100% degradation of 50 mg l^{-1} methyl orange solution. Interestingly, the catalyst very effectively degraded the dye even at alkaline solution. The acid treatment improved the physicochemical properties of flyash and shown its efficiency in degradation of p-nitrophenol.[117]

Many studies on magnetic nanoparticles impregnated activated carbon (AC) suggested that activated carbon can be a good supporting material for iron. It was revealed that Fe_2MnO_4/AC showing higher Fenton catalytic activity in the degradation of methyl orange than pure Fe_3O_4/AC.[118] The possible mechanism was suggested based on the electron transfer process within the semiconductor oxide structure which leads to the efficient regeneration of Mn^{2+} ions. Yao et al. utilized ferric ions loaded activated carbon nanofibres for the degradation of Reactive Red M-3BE dye.[119] This catalyst possessed higher stability and activity at neutral as well as alkaline pH. Unlike the homogeneous Fenton reaction, the presence of hydro-peroxyl radicals are not identified in this iron loaded AC fibers assisted heterogeneous Fenton reaction. The activity of iron species supported on the alumina substrate also shows higher activity than that without the substrate.[120] Li et al. investigated the activity of hematite/alumina in aerated aqueous solution of orange II.[121] The catalytic activity shown by this catalyst was higher than that of hematite and even higher than that of silica supported hematite. Various polymer fibers are attractive candidate of this category and Polyacrylonitrile (PAN) is the most used among them.[122] PAN nanofibers were prepared using the electro-spinning technique and subsequent amidoximation leads to the coordination with iron when treating with iron chloride solution. The optimal H_2O_2 molar concentration for the best decoloration is 3.0 mmol l^{-1}. Although this complex has a relatively better catalytic activity over a wider

pH range, the optimal pH of the reaction solution is 6 for the fastest degradation of the dye. Mesoporous silica has been widely used as a support material for the various catalysis reactions. SBA-41 and SBA-15 are the important silica based substrates having highly ordered mesoporous structures. The degradation efficiency of iron-containing mesostructured silica (Fe_2O_3/SBA-15) was investigated using C.I. Acid Orange 7 (AO7) dye solution via integrated heterogeneous sono–photo-Fenton process.[123] The optimum experimental conditions for the best heterogeneous Fenton reaction performance involve the pH value fixed at 2, H_2O_2 concentration of 8 mmol l^{-1}, a catalyst loading of 0.3 g l^{-1} and an ultrasonic power of 80 W. The specific surface-area reported for the MCM-41was very high around 1400 $m^2 g^{-1}$. The study of magnetite loaded MCM-41 for the abatement of methylene blue compared with magnetite and MCM-41 revealed that the activity follows the order - magnetite-loaded MCM-41 > MCM-41 > magnetite.[124]

1.3.3.4. Limitations of heterogeneous iron-Fenton reaction

Most of the iron supported heterogeneous Fenton catalyst contains Fe^{3+} as active species. The kinetics of the Fenton reaction mediated by Fe^{3+} is 3 order magnetude slower than that mediated by Fe^{2+}.[125] Therefore, all iron impregnated catlyst containing Fe^{3+} required UV radiation for the reductive regeneration of Fe^{2+}.

1.3.3.5. Non-iron Fenton-like catalyst

The reactions involving cations other than Fe^{2+} which decompose H_2O_2 to produce the hydroxyl radicals are known as the Fenton-Like reactions.[126] The cations of elements including this category are Cr, Ce, Cu, Co, and Mn.[125] The H_2O_2 activation by Iron in +3 oxidation state is also referred as Fenton-Like reaction. A comparative study of

Fenton and Fenton-Like reactions by Shaobin Wang, reveals that the dye degradation in the Fenton oxidation was faster initially than the Fenton-like oxidation but the extent of degradation achieved was very similar after 100 min.[127] The effect of various reaction parameters like initial concentration of Fe^{2+} or $Fe^{3+,}$ initial concentration of H_2O_2, initial pH of solution and reaction temperature were also included in this study. The kinetics of Fenton oxidation is described by a combined pseudo-first-order kinetic model while the Fenton-like reaction follows comparatively simpler, pseudo-first-order kinetics.

The reaction involving Cu^{2+} ions reacting with H_2O_2 and forming copper oxide in the ultrasound assisted process follows the Fenton-like chemistry.[128] Authors proposed the mechanism for this reaction via the radical generation such as the superoxide and hydroxyl radicals. The initial rate was high as it follows the first order kinetics; however, the rate constant changes after few hours. The annealing causes the cavitation induced surface-defects which may be the reason for the decreased activity.

In the case of aluminum, the only accessible oxidation state is Al^{3+} in which no possibility for the electron transfer in between Al^{3+} and H_2O_2 as in the case of Fe^{2+} and Fe^{3+}. However, Bokare and Choi et al. first demonstrated the ability of zero valent Al to produce $^{\bullet}OH$ as a result of the electron transference through these species.[129] The use of Ce^{3+}/Ce^{4+} redox cycle was most established for the catalytic reactions owing to the presence of oxygen defects and surface Ce^{3+}. The extension of this redox-cycle found a major position in the field of removal of organic pollutants by heterogeneous Fenton-like system. Heckert et al. assessed hydroxyl and superoxide radicals in the heterogeneous Cerium Fenton-catalytic system.[130] However, the bare CeO_2 is incapable of producing $^{\bullet}OH$ and it results in a stable brown precipitate (peroxide like

species). If the CeO_2 is pretreated with sulphuric acid, it will easily generate $^\bullet OH$ since the surface anchored sulphate groups which act as the acidic sites cause the homolytic cleavage of peroxide. But its practical application is limited due to the acute cytotoxicity of Ce.

The activation of H_2O_2 via Co-based catalyst is documented in limited numbers. Like heterogeneous Fenton reaction, active elements are incorporated on the different substrates. The transition metals ions impregnated on MCM-41 and their comparative effect on the decomposition of organics was examined by Chaliha et al.[131] They synthesized Co^{2+}, Fe^{3+}, and Ni^{2+} impregnated MCM-41 which was used for the oxidation of 2,4,6-trichlorophenol in water with or without the oxidant (H_2O_2).[131] Their effectiveness on the degradation follows the order Ni(II)-MCM41 > Fe(III)-MCM41 > Co(II)-MCM41 indicating that Ni(II)-MCM41 is the best catalyst. In their studies, it was observed that the temperature has a positive effect on the reaction rate. Ling et al. investigated the homogeneous Fenton catalysis using the basic blue dye and observed the complete mineralization.[132] They performed a comparative study of two catalytic systems of Co^{2+}/H_2O_2 and Co^{2+}/peroxymonosulfate where hydroxyl radicals and sulphate radicals are respectively generated.[132] However, it was found that Co^{2+}/peroxymonosulfate system is more effective than that of Co^{2+}/H_2O_2.

1.4. Motivation and objectives

Based on the literature review presented here, it appears that in view of their commercial potential, the most effective techniques for the removal of organic synthetic-dyes from the aqueous solutions are - photocatalysis, adsorption, and AOPs. The main challenges in these processes comprise - (i) the effective separation of catalyst after the treatment process, (ii) the instabilities in the components of the

catalyst under certain environments, (iii) the formation of large quantities of sludge which causes the secondary pollution, (iv) the effective strategy for the regeneration and reuse of the adsorbent materials, (v) the utilization of cheap and industrial waste materials for the cost-reduction of the dye-removal processes, and (vi) the suitability of the latter to the wide range of organic synthetic-dyes. Although several non-magnetic and magnetic photocatalysts/adsorbents have been developed in these treatment processes, there is an urgent need for the further development of these catalysts to resolve the pending issues associated with the various dye-removal processes to make them suitable for the commercialization in the near-future. This is the prime motivation for undertaking the present thesis work.

In this perspective, the overall broad objectives of the present thesis are as follows -

(1)   To propose innovative approaches for synthesizing the novel magnetic nanocomposites as catalyst for the effective dye-removal via three different mechanisms such as the photocatalysis, adsorption, and AOPs.

(2)   To compare the efficiency of the novel magnetic nanocomposites as catalyst with that of the non-magnetic counterparts for the effective dye-removal via three different mechanisms such as the photocatalysis, adsorption, and AOPs.

(3)   To demonstrate the magnetic separation of the magnetic nanocomposites from the treated aqueous solution in the dye-removal application involving three different mechanisms such as the photocatalysis, adsorption, and AOPs.

(4)   To demonstrate the dye-removal via three different mechanisms, such as the photocatalysis, adsorption, and AOPs, without the formation of large amount of sludge using the novel magnetic nanocomposites.

(5)   To propose the cost-effective and efficient novel alternatives to the instabilities of the components of nanocomposite catalysts under the certain environments encountered during the effective dye-removal via different mechanisms such as the photocatalysis and AOPs.

(6)   To demonstrate the cost-effective and efficient novel strategies for the effective regeneration and reuse of the catalysts in the dye-removal application involving three different mechanisms such as the photocatalysis, adsorption, and AOPs.

(7)   To demonstrate the use of flyash, which is the waste byproduct of the thermal power plants, as a cheap catalyst-support in the dye-removal application typically involving the AOPs.

(8)   To demonstrate the suitability of the dye-removal processes, typically the AOPs, to the wide range of organic synthetic-dyes.

(9)   To identify a suitable dye-removal technology for the possible commercialization in the near-future based on the obtained results.

References

1.   Shivani, S.; Mrutyunjay Suar, A. S., Handbook of research on diverse applications of nanotechnology in biomedicine, chemistry, and engineering. *IGI Global, USA* **2014,** *DOI: 10.4018/978-1-4666-6363-3.ch019* (Editors: S. Soni, A. Salhotra, M. Suar), 625 - 639.

2.   Pandu, R., $CrFe_2O_4$ - $BiFeO_3$ perovskite multiferroic nanocomposites – a review. *Mat. Sci. Res. India* **2014,** *11* (2), 128-145.

3.   Wei, W.; Zhaohui, W.; Taekyung, Y.; Changzhong, J.; Woo-Sik, K., Recent progress on magnetic iron oxide nanoparticles: synthesis, surface functional

strategies and biomedical applications. *Sci. Technol. Adv. Mater.* **2015,** *16* (2), 023501.

4. Lu, A. H.; Salabas, E. L.; Schueth, F., Magnetic nanoparticles: synthesis, protection, functionalization, and application. *Angew. Chem. Int. Ed.* **2007,** *46* (8), 1222-1244.

5. Behrens, S., Preparation of functional magnetic nanocomposites and hybrid materials: recent progress and future directions. *Nanoscale* **2011,** *3* (3), 877-892.

6. Kalia, S.; Kango, S.; Kumar, A.; Haldorai, Y.; Kumari, B.; Kumar, R., Magnetic polymer nanocomposites for environmental and biomedical applications. *Colloid. Polym. Sci.* **2014,** *292* (9), 2025-2052.

7. Wu, X.; Wu, M.; Xiaojun Zhao, J., Recent development of silica nanoparticles as delivery vectors for cancer imaging and therapy. *Nanomed. Nanotechnol. Biol. Med.* **2014,** *10* (2), 297-312.

8. Kim, J.; Kim, H. S.; Lee, N.; Kim, T.; Kim, H.; Yu, T.; Song, I. C.; Moon, W. K.; Hyeon, T., Multifunctional uniform nanoparticles composed of a magnetite nanocrystal core and a mesoporous silica shell for magnetic resonance and fluorescence imaging and for drug delivery. *Angew. Chem. Int. Ed.* **2008,** *47* (44), 8438-8441.

9. Lee, J. E.; Lee, N.; Kim, H.; Kim, J.; Choi, S. H.; Kim, J. H.; Kim, T.; Song, I. C.; Park, S. P.; Moon, W. K.; Hyeon, T., Uniform mesoporous dye-doped silica nanoparticles decorated with multiple magnetite nanocrystals for simultaneous enhanced magnetic resonance imaging, fluorescence imaging, and drug delivery. *J. Am. Chem. Soc.* **2010,** *132* (2), 552-557.

10. Cheng, T.; Zhang, D.; Li, H.; Liu, G., Magnetically recoverable nanoparticles as efficient catalysts for organic transformations in aqueous medium. *Green Chem.* **2014,** *16* (7), 3401-3427.

11. Shin, J. Y.; Jung, Y.; Kim, S. J.; Lee, S. G., Supported Pd nanocatalysts onto ionic silica-coated magnetic particles for catalysis in ionic liquids. *Bull. Korean Chem. Soc.* **2011,** *32* (8), 3105-3108.

12. Ghosh, S.; Puri, I. K., Soft polymer magnetic nanocomposites: microstructure patterning by magnetophoretic transport and self-assembly. *Soft Matter* **2013,** *9* (6), 2024-2029.

13. Pisanello, F.; De Paolis, R.; Lorenzo, D.; Nitti, S.; Monti, G.; Fragouli, D.; Athanassiou, A.; Manna, L.; Tarricone, L.; De Vittorio, M.; Martiradonna, L., Radiofrequency characterization of polydimethylsiloxane – iron oxide based nanocomposites. *Microelectron. Eng.* **2013,** *111*, 46-51.

14. Srdic Srdic, V. V.; Mojic, B.; Nikolic, M.; Ognjanovic, S., Recent progress on synthesis of ceramics core/shell nanostructures. *Process. Appl. Ceram.* **2013,** 7(2), 45-62.

15. Kant, R., Textile dyeing industry an environmental hazard *Natural Science* **2012,** *4* (1), 22-26.

16. Cai, J.; Cui, L.; Wang, Y.; Liu, C., Effect of functional groups on sludge for biosorption of reactive dyes. *J. Environ. Sci.* **2009,** *21* (4), 534-538.

17. Kyzas, G. Z.; Fu, J.; Matis, K. A., The Change from Past to Future for Adsorbent Materials in Treatment of Dyeing Wastewaters. *Materials* **2013,** *6* (11), 5131-5158.

18. Ratna, P. B. S., Pollution due to synthetic dyes toxicity & carcinogenicity studies and remediation. *Int. J. Environ. Sci.* **2012,** *3* (3), 940.

19. Hunger, K., *Industrial dyes: chemistry, properties, applications*. John Wiley & Sons: **2007**, ISBN-3-527-30426-6

20. Harekrishna Jana, K. R.; Keshab C. M., Isolation and characterization of dye degrading bacteria from textile industrial waste, Panskura, West Bengal, India. *Indian J. Appl. Res.* **2015,** *5* (5), 2249-555.

21. Rauf, M. A.; Shehadeh, I.; Ahmed, A.; Al-Zamly, A., Removal of methylene blue from aqueous solution by using gypsum as a low cost adsorbent. *World Acad. Sci. Eng. Technol.* **2009,** *31*, 604-609.

22. Ramchandani, S.; Das, M.; Joshi, A.; Khanna, S. K., Effect of oral and parenteral administration of metanil yellow on some hepatic and intestinal biochemical parameters. *J. Appl. Toxicol.* **1997,** *17* (1), 85-91.

23. Sachdeva, S. M.; Mani, K. V.; Adaval, S. K.; Jalpota, Y. P.; Rasela, K. C.; Chadha, D. S., Acquired toxic methaemoglobinaemia. *J. Assoc.Physicians India* **1992,** *40* (4), 239-240.

24. Tiwari, H., Assessment of teratogenecity and embryo toxicity of dye wastewater untreated sludge from sanganer on swiss albino mice when administered during growth period of gestation. *Water Res. Dev.* **2012,** *2*, 48-53.

25. Adegoke, K. A.; Bello, O. S., Dye sequestration using agricultural wastes as adsorbents. *Water Resour. Ind.* **2015,** *12*, 8-24.

26. Sharma, S.; Rparelia, J.; Patel, M. L. In A general review on advanced oxidation processes for waste water treatment, Nirma University International Conference, Ahmedabad, Gujarat, **2011**.

27. Fujishima, A.; Honda, K., Electrochemical photolysis of water at a semiconductor electrode. *Nature* **1972,** *238* (5358), 37-8.

28. Liu, S. Q., Magnetic semiconductor nano-photocatalysts for the degradation of organic pollutants. *Environ. Chem. Lett.* **2012,** *10* (3), 209-216.

29. Dalrymple, O. K.; Stefanakos, E.; Trotz, M. A.; Goswami, D. Y., A review of the mechanisms and modeling of photocatalytic disinfection. *Appl. Catal., B* **2010,** *98* (1), 27-38.

30. Yao, H.; Fan, M.; Wang, Y.; Luo, G.; Fei, W., Magnetic titanium dioxide based nanomaterials: synthesis, characteristics, and photocatalytic application in pollutant degradation. *J. Mater. Chem. A* **2015,** *3* (34), 17511-17524.

31. Hiroshi, F.; Yukiko, H.; Michichiro, Y.; Shoichi, A., Magnetic photocatalyst. *JP 6154620 (A)* **1994**.

32. Atsuya T, M. S., Photocatalyst particles containing ferromagnetic metal particles and method for synthesis thereof. *U.S. Patent 5703002* **1997**.

33. Beydoun, D.; Amal, R.; Low, G. K. C.; McEvoy, S., Novel photocatalyst: titania-coated magnetite. activity and photodissolution. *J. Phys. Chem. B* **2000,** *104* (18), 4387-4396.

34. Hankare, P. P.; Patil, R. P.; Jadhav, A. V.; Garadkar, K. M.; Sasikala, R., Enhanced photocatalytic degradation of methyl red and thymol blue using titania–alumina–zinc ferrite nanocomposite. *Appl. Catal., B* **2011,** *107* (3–4), 333-339.

35. Chen, Y. H.; Chen, L. L.; Shang, N. C., Photocatalytic degradation of dimethyl phthalate in an aqueous solution with Pt-doped TiO_2-coated magnetic PMMA microspheres. *J. Hazard. Mater.* **2009,** *172* (1), 20-29.

36. Belessi, V.; Lambropoulou, D.; Konstantinou, I.; Zboril, R.; Tucek, J.; Jancik, D.; Albanis, T.; Petridis, D., Structure and photocatalytic performance of

magnetically separable titania photocatalysts for the degradation of propachlor. *Appl. Catal., B* **2009,** *87* (3–4), 181-189.

37. Deng, Y. H.; Wang, C. C.; Hu, J. H.; Yang, W. L.; Fu, S. K., Investigation of formation of silica-coated magnetite nanoparticles via sol–gel approach. *Colloids Surf., A* **2005,** *262* (1), 87-93.

38. Linic, S.; Christopher, P.; Ingram, D. B., Plasmonic-metal nanostructures for efficient conversion of solar to chemical energy. *Nat. Mater.* **2011,** *10* (12), 911-921.

39. Beydoun, D.; Amal, R., Implications of heat treatment on the properties of a magnetic iron oxide–titanium dioxide photocatalyst. *Mater. Sci. Eng., B* **2002,** *94* (1), 71-81.

40. Makovec, D.; Sajko, M.; Selisnik, A.; Drofenik, M., Low-temperature synthesis of magnetically recoverable, superparamagnetic, photocatalytic, nanocomposite particles. *Mater. Chem. Phys.* **2012,** *136* (1), 230-240.

41. Rana, S.; Srivastava, R.; Sorensson, M.; Misra, R., Synthesis and characterization of nanoparticles with magnetic core and photocatalytic shell: anatase TiO_2–$NiFe_2O_4$ system. *Mater. Sci. Eng., B* **2005,** *119* (2), 144-151.

42. Xu, J.; Ao, Y.; Fu, D.; Yuan, C., Low-temperature preparation of anatase titania-coated magnetite. *J. Phys. Chem. Solids* **2008,** *69* (8), 1980-1984.

43. Teng, Z.; Su, X.; Chen, G.; Tian, C.; Li, H.; Ai, L.; Lu, G., Superparamagnetic high-magnetization composite microspheres with $Fe_3O_4@SiO_2$ core and highly crystallized mesoporous TiO_2 shell. *Colloids Surf., A* **2012,** *402*, 60-65.

44. Huang, X.; Wang, G.; Yang, M.; Guo, W.; Gao, H., Synthesis of polyaniline-modified $Fe_3O_4/SiO_2/TiO_2$ composite microspheres and their photocatalytic application. *Mater. Lett.* **2011,** *65* (19), 2887-2890.

45. Yalcın, Y.; Kılıç, M.; Cınar, Z., The role of non-metal doping in TiO_2 photocatalysis. *J. Adv. Oxid. Technol.* **2010,** *13* (3), 281-296.

46. Aziz, A. A.; Yong, K. S.; Ibrahim, S.; Pichiah, S., Enhanced magnetic separation and photocatalytic activity of nitrogen doped titania photocatalyst supported on strontium ferrite. *J. Hazard. Mater.* **2012,** *199–200*, 143-150.

47. He, Z.; Hong, T.; Chen, J.; Song, S., A magnetic TiO_2 photocatalyst doped with iodine for organic pollutant degradation. *Sep. Purif. Technol.* **2012,** *96*, 50-57.

48. Shi, F.; Li, Y.; Zhang, Q.; Wang, H., Synthesis of $Fe_3O_4/C/TiO_2$ magnetic photocatalyst via vapor phase hydrolysis. *Int. J. Photoenergy* **2012,** *2012*.

49. Ao, Y.; Xu, J.; Fu, D.; Ba, L.; Yuan, C., Deposition of anatase titania onto carbon encapsulated magnetite nanoparticles. *Nanotechnology* **2008,** *19* (40), 405604.

50. Zhang, Q.; Meng, G.; Wu, J.; Li, D.; Liu, Z., Study on enhanced photocatalytic activity of magnetically recoverable $Fe_3O_4@C@TiO_2$ nanocomposites with core–shell nanostructure. *Opt. Mater.* **2015,** *46*, 52-58.

51. Xuan, S.; Jiang, W.; Gong, X.; Hu, Y.; Chen, Z., Magnetically separable Fe_3O_4/TiO_2 hollow spheres: fabrication and photocatalytic activity. *J. Phys. Chem. C* **2009,** *113* (2), 553-558.

52. Gupta, V. K.; Suhas., Application of low-cost adsorbents for dye removal – A review. *J. Environ. Manage.* **2009,** *90* (8), 2313-2342.

53. Li, Y.; Du, Q.; Liu, T.; Peng, X.; Wang, J.; Sun, J.; Wang, Y.; Wu, S.; Wang, Z.; Xia, Y.; Xia, L., Comparative study of methylene blue dye adsorption onto activated carbon, graphene oxide, and carbon nanotubes. *Chem. Eng. Res. Des.* **2013,** *91* (2), 361-368.

54.   Ai, L.; Zhang, C.; Liao, F.; Wang, Y.; Li, M.; Meng, L.; Jiang, J., Removal of methylene blue from aqueous solution with magnetite loaded multi-wall carbon nanotube: Kinetic, isotherm and mechanism analysis. *J. Hazard. Mater.* **2011,** *198*, 282-290.

55.   Yang, N.; Zhu, S.; Zhang, D.; Xu, S., Synthesis and properties of magnetic Fe_3O_4-activated carbon nanocomposite particles for dye removal. *Mater. Lett.* **2008,** *62* (4–5), 645-647.

56.   Wu, Q.; Feng, C.; Wang, C.; Wang, Z., A facile one-pot solvothermal method to produce superparamagnetic graphene-Fe_3O_4 nanocomposite and its application in the removal of dye from aqueous solution. *Colloids Surf., B* **2013,** *101*, 210-214.

57.   Moeinpour, F.; Alimoradi, A.; Kazemi, M., Efficient removal of Eriochrome black-T from aqueous solution using $NiFe_2O_4$ magnetic nanoparticles. *Journal J. environ. health sci. eng.* **2014,** *12*, 112.

58.   Afkhami, A.; Moosavi, R., Adsorptive removal of Congo red, a carcinogenic textile dye, from aqueous solutions by maghemite nanoparticles. *J. Hazard. Mater.* **2010,** *174* (1–3), 398-403.

59.   Wang, H.; Shen, Y.; Shen, C.; Wen, Y.; Li, H., Enhanced adsorption of dye on magnetic Fe_3O_4 via HCl-assisted sonication pretreatment. *Desalination* **2012,** *284*, 122-127.

60.   Hariani, P. L.; Faizal. M.; Setiabudidaya, D., Synthesis and properties of Fe_3O_4 nanoparticles by co-precipitation method to removal procion dye. *IJESD* **2013,** *4* (3), 336-340.

61.   Zhong, X.; Yang, J.; Chen, Y.; Qiu, X.; Zhang, Y., Synthesis of magnetically separable $MnFe_2O_4$ nanocrystals via salt-assisted solution combustion method

and their utilization as dye adsorbent. *J. Ceram. Soc. Jpn.* **2015,** *123* (1437), 394-398.

62.   Madrakian, T.; Afkhami, A.; Ahmadi, M.; Bagheri, H., Removal of some cationic dyes from aqueous solutions using magnetic-modified multi-walled carbon nanotubes. *J. Hazard. Mater.* **2011,** *196*, 109-114.

63.   Yang, K.; Xing, B., Adsorption of organic compounds by carbon nanomaterials in aqueous phase: Polanyi theory and its application. *Chem. Rev.* **2010,** *110* (10), 5989-6008.

64.   Yao, Y.; Yang, Z.; Zhang, D.; Peng, W.; Sun, H.; Wang, S., Magnetic $CoFe_2O_4$–graphene hybrids: facile synthesis, characterization, and catalytic properties. *Ind. Eng. Chem. Res* **2012,** *51* (17), 6044-6051.

65.   Debrassi, A.; Baccarin, T.; Demarchi, C.; Nedelko, N.; Slawska-Waniewska, A.; Dłużewski, P.; Bilska, M.; Rodrigues, C., Adsorption of Remazol Red 198 onto magnetic N-lauryl chitosan particles: equilibrium, kinetics, reuse and factorial design. *Environ. Sci. Pollut. Res.* **2012,** *19* (5), 1594-1604.

66.   Yan, H.; Li, H.; Yang, H.; Li, A.; Cheng, R., Removal of various cationic dyes from aqueous solutions using a kind of fully biodegradable magnetic composite microsphere. *Chem. Eng. J.* **2013,** *223*, 402-411.

67.   Xie, Y.; Qian, D.; Wu, D.; Ma, X., Magnetic halloysite nanotubes/iron oxide composites for the adsorption of dyes. *Chem. Eng. J.* **2011,** *168* (2), 959-963.

68.   Wu, D.; Zheng, P.; Chang, P. R.; Ma, X., Preparation and characterization of magnetic rectorite/iron oxide nanocomposites and its application for the removal of the dyes. *Chem. Eng. J.* **2011,** *174* (1), 489-494.

69.   Hashem, F., Adsorption of methylene blue from aqueous solutions using Fe$_3$O$_4$/Bentonite nanocomposite. *Hydrol. Current Res.* **2012**, doi:10.4172/ 2157 -7587.1000143

70.   Wu, Z.; Wu, J.; Xiang, H.; Chun, M. S.; Lee, K., Organosilane-functionalized Fe$_3$O$_4$ composite particles as effective magnetic assisted adsorbents. *Colloids Surf., A* **2006,** *279* (1–3), 167-174.

71.   Ge, F.; Ye, H.; Li, M.-M.; Zhao, B. X., Efficient removal of cationic dyes from aqueous solution by polymer-modified magnetic nanoparticles. *Chem. Eng. J.* **2012,** *198–199*, 11-17.

72.   Zhang, Y. R.; Wang, S. Q.; Shen, S. L.; Zhao, B. X., A novel water treatment magnetic nanomaterial for removal of anionic and cationic dyes under severe condition. *Chem. Eng. J.***2013,** *233*, 258-264.

73.   Rocher, V.; Bee, A.; Siaugue, J. M.; Cabuil, V., Dye removal from aqueous solution by magnetic alginate beads crosslinked with epichlorohydrin. *J. Hazard. Mater.* **2010,** *178* (1–3), 434-439.

74.   Oliveira, A. A. S.; Tristao, J. C.; Ardisson, J. D.; Dias, A.; Lago, R. M., Production of nanostructured magnetic composites based on Fe^0 nuclei coated with carbon nanofibers and nanotubes from red mud waste and ethanol. *Appl. Catal., B* **2011,** *105* (1–2), 163-170.

75.   Qiu, H.; Lu, L.; Bing, C. P.; Zhang, Q. J.; Zhang, W.M.; Zhang, Q. X., Critical review in adsorption kinetic models. *J. Zhejiang Univ.-SCI. A* **2009,** *10* (5), 716-724.

76.   Ho, Y.; Wase, D. J.; Forster, C., Batch nickel removal from aqueous solution by sphagnum moss peat. *Water Res.* **1995,** *29* (5), 1327-1332.

77.   Harsha, N.; Krishna, K. V. S.; Renuka, N. K.; Shukla, S., Facile synthesis of γ-Fe$_2$O$_3$ nanoparticles integrated H$_2$Ti$_3$O$_7$ nanotubes structure as a magnetically recyclable dye-removal catalyst. *RSC Adv.* **2015,** *5* (38), 30354-30362.

78.   Du, G.; Chen, Q.; Che, R.; Yuan, Z.; Peng, L. M., Preparation and structure analysis of titanium oxide nanotubes. *Appl. Phys. Lett.* **2001,** *79* (22), 3702-3704.

79.   Kasuga, T.; Hiramatsu, M.; Hoson, A.; Sekino, T.; Niihara, K., Formation of titanium oxide nanotube. *Langmuir* **1998,** *14* (12), 3160-3163.

80.   Wang, W.; Varghese, O. K.; Paulose, M.; Grimes, C. A.; Wang, Q.; Dickey, E. C., A study on the growth and structure of titania nanotubes. *J. Mater. Res.* **2004,** *19* (02), 417-422.

81.   Chen, Q.; Zhou, W.; Du, G.; Peng, L. M., Trititanate nanotubes made via a single alkali treatment. *Adv. Mater.* **2002,** *14* (17), 1208-1211.

82.   Sun, X.; Li, Y., Synthesis and characterization of ion-exchangeable titanate nanotubes. *Chem. Eur. J* **2003,** *9* (10), 2229-2238.

83.   Tsai, K. L.; Dye, J. L., Synthesis, properties, and characterization of nanometer-size metal particles by homogeneous reduction with alkalides and electrides in aprotic solvents. *Chem. Mater.* **1993,** *5* (4), 540-546.

84.   Wang, Y.; Hu, G.; Duan, X.; Sun, H.; Xue, Q., Microstructure and formation mechanism of titanium dioxide nanotubes. *Chem. Phys. Lett.* **2002,** *365* (5), 427-431.

85.   Razali, M. H.; Noor, A. F. M.; Mohamed, A. R.; Sreekantan, S., Morphological and structural studies of titanate and titania nanostructured materials obtained after heat treatments of hydrothermally produced layered titanate. *J Nanomater.* **2012,** *2012*, 18.

86. Chen, Q.; Du, G.; Zhang, S.; Peng, L. M., The structure of trititanate nanotubes. *Acta Crystallogr., Sect. B: Struct. Sci.* **2002,** *58* (4), 587-593.

87. Nakahira, A.; Kato, W.; Tamai, M.; Isshiki, T.; Nishio, K.; Aritani, H., Synthesis of nanotube from a layered $H_2Ti_4O_9 \cdot H_2O$ in a hydrothermal treatment using various titania sources. *J. Mater. Sci.* **2004,** *39* (13), 4239-4245.

88. Yang, J.; Jin, Z.; Wang, X.; Li, W.; Zhang, J.; Zhang, S.; Guo, X.; Zhang, Z., Study on composition, structure and formation process of nanotube $Na_2Ti_2O_4$ $(OH)_2$. *Dalton Trans.* **2003,** (20), 3898-3901.

89. Ma, R.; Bando, Y.; Sasaki, T., Nanotubes of lepidocrocite titanates. *Chem. Phys. Lett.* **2003,** *380* (5), 577-582.

90. Zhang, S.; Peng, L. M.; Chen, Q.; Du, G. H.; Dawson, G.; Zhou, W. Z., Formation mechanism of $H_2Ti_3O_7$ nanotubes. *Phys. Rev. Lett.* **2003,** *91* (25).

91. Lu, H.; Zhao, J.; Li, L.; Zheng, J.; Zhang, L.; Gong, L.; Wang, Z.; Zhu, Z., A systematic study on evolution mechanism of titanate nanostructures in the hydrothermal process. *Chem. Phys. Lett.* **2011,** *508* (4), 258-264.

92. Liu, W.; Wang, T.; Borthwick, A. G.; Wang, Y.; Yin, X.; Li, X.; Ni, J., Adsorption of Pb^{2+}, Cd^{2+}, Cu^{2+} and Cr^{3+} onto titanate nanotubes: competition and effect of inorganic ions. *Sci. Total Environ.* **2013,** *456*, 171-180.

93. Zhang, H.; Cao, L.; Liu, W.; Su, G., A new ion exchange behavior of protonated titanate nanotubes after deprotonation and the study on their morphology and optical properties. *Appl. Surf. Sci.* **2012,** *259*, 610-615.

94. Torrente-Murciano, L.; Lapkin, A. A.; Bavykin, D. V.; Walsh, F. C.; Wilson, K., Highly selective Pd/titanate nanotube catalysts for the double-bond migration reaction. *J. Catal.* **2007,** *245* (2), 272-278.

95.   Bavykin, D. V.; Lapkin, A. A.; Plucinski, P. K.; Friedrich, J. M.; Walsh, F. C., TiO$_2$ nanotube-supported ruthenium (III) hydrated oxide: A highly active catalyst for selective oxidation of alcohols by oxygen. *J. Catal.* **2005,** *235* (1), 10-17.

96.   Thazhe, L.; Shereef, A.; Shukla, S.; Pattelath Reshmi, C.; Varma, M. R.; Suresh, K. G.; Patil, K.; Warrier, K. G., Magnetic dye-adsorbent catalyst: processing, characterization, and application. *J. Am. Ceram. Soc.* **2010,** *93* (11), 3642-3650.

97.   Li, W.; Deng, Y.; Wu, Z.; Qian, X.; Yang, J.; Wang, Y.; Gu, D.; Zhang, F.; Tu, B.; Zhao, D., Hydrothermal etching assisted crystallization: a facile route to functional yolk-shell titanate microspheres with ultrathin nanosheets-assembled double shells. *J. Am. Chem. Soc.* **2011,** *133* (40), 15830-15833.

98.   Niu, H.; Zhang, S.; Zhang, X.; Cai, Y., Alginate-polymer-caged, C18-functionalized magnetic titanate nanotubes for fast and efficient extraction of phthalate esters from water samples with complex matrix. *ACS Appl. Mater. Interfaces* **2010,** *2* (4), 1157-1163.

99.   Zhou, L.; Xu, M.; Wei, G.; Li, L.; Chubik, M.; Chubik, M. P.; Gromov, A. A.; Han, W., Fe$_3$O$_4$@ titanate nanocomposites: novel reclaimable adsorbents for removing radioactive ions from wastewater. *J Mater Sci: Mater Electron* **2015,** *26* (5), 2742-2747.

100.   Dai, L.; Zheng, J.; Wang, L., Fabrication of titanate nanotubes/iron oxide magnetic composite for the high efficient capture of radionuclides: a case investigation of [109]Cd(II). *J. Radioanal. Nucl. Chem.* **2013,** *298* (3), 1947-1956.

101.   Zhang, L.; Wang, X.; Chen, H.; Jiang, F., Adsorption of Pb(II) using magnetic titanate nanotubes prepared via two-step hydrothermal method. *CLEAN – Soil, Air, Water* **2014,** *42* (7), 947-955.

102.   Liu, F.; Jin, Y. J.; Liao, H. B.; Cai, L.; Tong, M. P.; Hou, Y. L., Facile self-assembly synthesis of titanate/Fe_3O_4 nanocomposites for the efficient removal of Pb^{2+} from aqueous systems. *J. Mater. Chem. A* **2013,** *1* (3), 805-813.

103.   Papa, A.-L.; Maurizi, L.; Vandroux, D.; Walker, P.; Millot, N., Synthesis of titanate nanotubes directly coated with USPIO in hydrothermal conditions: a new detectable nanocarrier. *J. Phys. Chem. C* **2011,** *115* (39), 19012-19017.

104.   Kitano, M.; Nakajima, K.; Kondo, J. N.; Hayashi, S.; Hara, M., Protonated titanate nanotubes as solid acid catalyst. *J. Am. Chem. Soc.* **2010,** *132* (19), 6622-6623.

105.   Abkenar, S. D.; Khoobi, M.; Tarasi, R.; Hosseini, M.; Shafiee, A.; Ganjali, M. R., Fast removal of methylene blue from aqueous solution using magnetic-modified Fe_3O_4 nanoparticles. *Chem. Eng. J.* **2014,** *141* (1), 04014049.

106.   Venkatadri, R.; Peters, R. W., Chemical oxidation technologies - ultraviolet-light hydrogen-peroxide, fenton reagent, and titanium dioxide-assisted photocatalysis. *Hazard. Waste Hazard. Mater.* **1993,** *10* (2), 107-149.

107.   Lloyd, R. V.; Hanna, P. M.; Mason, R. P., The origin of the hydroxyl radical oxygen in the Fenton reaction. *Free Radical Biol. Med.* **1997,** *22* (5), 885-888.

108.   Kornweitz, H.; Burg, A.; Meyerstein, D., Plausible Mechanisms of the Fenton-like reactions, M = Fe(II) and Co(II), in the Presence of RCO_2- Substrates: are $OH^{\bullet}$ radicals formed in the process? *J. Phys. Chem. A* **2015,** *119* (18), 4200-4206.

109. Babuponnusami, A.; Muthukumar, K., A review on Fenton and improvements to the Fenton process for wastewater treatment. *J. Environ. Chem. Eng.* **2014,** *2* (1), 557-572.

110. Nidheesh, P., Heterogeneous Fenton catalysts for the abatement of organic pollutants from aqueous solution: a review. *RSC Adv.* **2015,** *5* (51), 40552-40577.

111. Pereira, M.; Oliveira, L.; Murad, E., Iron oxide catalysts: Fenton and Fenton-like reactions-a review. *Clay Miner.* **2012,** *47* (3), 285-302.

112. Pouran, S. R.; Raman, A. A. A.; Daud, W. M. A. W., Review on the application of modified iron oxides as heterogeneous catalysts in Fenton reactions. *J. Cleaner Prod.* **2014,** *64*, 24-35.

113. Wang, Y.; Liang, J. B.; Liao, X. D.; Wang, L.-s.; Loh, T. C.; Dai, J.; Ho, Y. W., Photodegradation of sulfadiazine by goethite−oxalate suspension under UV light irradiation. *Ind. Eng. Chem. Res.* **2010,** *49* (8), 3527-3532.

114. Blissett, R.; Rowson, N., A review of the multi-component utilisation of coal fly ash. *Fuel* **2012,** *97*, 1-23.

115. Chen, S.-h.; Du, D.-y., Degradation of n-butyl xanthate using fly ash as heterogeneous Fenton-like catalyst. *J. Cent. South Univ.* **2014,** *21* (4), 1448-1452.

116. Li, Y.; Zhang, F.-S., Catalytic oxidation of methyl orange by an amorphous FeOOH catalyst developed from a high iron-containing fly ash. *Chem. Eng. J.* **2010,** *158* (2), 148-153.

117. Zhang, A.; Wang, N.; Zhou, J.; Jiang, P.; Liu, G., Heterogeneous Fenton-like catalytic removal of p-nitrophenol in water using acid-activated fly ash. *J. Hazard. Mater.* **2012,** *201–202*, 68-73.

118. Nguyen, T. D.; Phan, N. H.; Do, M. H.; Ngo, K. T., Magnetic Fe_2MO_4 (M:Fe, Mn) activated carbons: Fabrication, characterization and heterogeneous Fenton oxidation of methyl orange. *J. Hazard. Mater.* **2011,** *185* (2–3), 653-661.

119. Yao, Y.; Wang, L.; Sun, L.; Zhu, S.; Huang, Z.; Mao, Y.; Lu, W.; Chen, W., Efficient removal of dyes using heterogeneous Fenton catalysts based on activated carbon fibers with enhanced activity. *Chem. Eng. Sci.* **2013,** *101*, 424-431.

120. Ghosh, P.; Kumar, C.; Samanta, A. N.; Ray, S., Comparison of a new immobilized Fe^{3+} catalyst with homogeneous Fe^{3+}–H_2O_2 system for degradation of 2,4-dinitrophenol. *J. Chem. Technol. Biotechnol.* **2012,** *87* (7), 914-923.

121. Li, Z.; Sheng, J.; Wang, Y.; Xu, Y., Enhanced photocatalytic activity and stability of alumina supported hematite for azo-dye degradation in aerated aqueous suspension. *J. Hazard. Mater.* **2013,** *254–255*, 18-25.

122. Zhong, X.; Xiang, L.; Royer, S.; Valange, S.; Barrault, J.; Zhang, H., Degradation of C.I. Acid Orange 7 by heterogeneous Fenton oxidation in combination with ultrasonic irradiation. *J. Chem. Technol. Biotechnol.* **2011,** *86* (7), 970-977.

123. Wu, J.; Zhao, J.; Du, F.; Han, Z., Development of environmentally friendly modified Fe-PAN fibrous catalyst and its application in degradation of dye. *J. Sustainable Dev.* **2009,** *2* (3), 214.

124. Nogueira, A.; #xe9; E.; Castro, I. A.; Giroto, A. S.; Magriotis, Z. M., Heterogeneous Fenton-like catalytic removal of methylene blue dye in water using magnetic nanocomposite (MCM-41/Magnetite). *J. Catal.* **2014,** *2014*, 6.

125.   Bokare, A. D.; Choi, W., Review of iron-free Fenton-like systems for activating H_2O_2 in advanced oxidation processes. *J. Hazard. Mater.* **2014,** *275,* 121-135.

126.   Jung, Y. S.; Lim, W. T.; Park, J. Y.; Kim, Y. H., Effect of pH on Fenton and Fenton-like oxidation. *Environ. Technol.* **2009,** *30* (2), 183-190.

127.   Wang, S., A Comparative study of Fenton and Fenton-like reaction kinetics in decolourisation of wastewater. *Dyes Pigm.* **2008,** *76* (3), 714-720.

128.   Angı, A.; Sanlı, D.; Erkey, C.; Birer, O., Catalytic activity of copper (II) oxide prepared via ultrasound assisted Fenton-like reaction. *Ultrason. Sonochem.* **2014,** *21* (2), 854-859.

129.   Bokare, A. D.; Choi, W., Zero-valent aluminum for oxidative degradation of aqueous organic pollutants. *Environ. Sci. Technol.* **2009,** *43* (18), 7130-7135.

130.   Heckert, E. G.; Seal, S.; Self, W. T., Fenton-like reaction catalyzed by the rare earth inner transition metal Cerium. *Environ. Sci. Technol.* **2008,** *42* (13), 5014-5019.

131.   Chaliha, S.; Bhattacharyya, K. G., Wet oxidative method for removal of 2,4,6-trichlorophenol in water using Fe(III), Co(II), Ni(II) supported MCM41 catalysts. *J. Hazard. Mater.* **2008,** *150* (3), 728-736.

132.   Ling, S. K.; Wang, S.; Peng, Y., Oxidative degradation of dyes in water using Co^{2+}/H_2O_2 and Co^{2+}/peroxymonosulfate. *J. Hazard. Mater.* **2010,** *178* (1–3), 385-389.

Chapter 2

Synthesis of TiO$_2$/γ-Fe$_2$O$_3$ Magnetic Photocatalyst with and without SiO$_2$ Interlayer and Their Photocatalytic Activity

Graphical Abstract
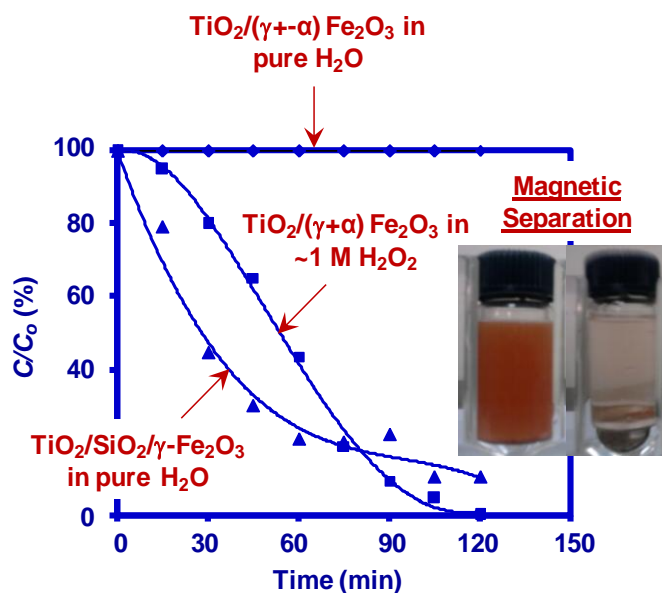
Highlights

- Magnetic photocatalyst synthesized via the combination of modified Stober and sol-gel methods.

- Effect of SiO$_2$ interlayer on the photo-dissolution process, photocatalytic activity, and magnetic separation of nanocomposite photocatalyst.

- Analysis of $^{\bullet}$OH generation from the magnetic photocatalysts through photoluminescence study.

- Enhancing the photocatalytic activity of γ-Fe$_2$O$_3$/TiO$_2$ magnetic photocatalyst in the presence of photo-dissolution process.

Abstract

Anatase-TiO_2-coated γ-Fe_2O_3 nanocomposite magnetic photocatalysts have been synthesized without and with the interlayer of SiO_2 coating. A combination of modified Stober and sol-gel methods involving the alkoxide-precursors has been employed for processing the magnetic photocatalysts. The photocatalytic activities of magnetic photocatalysts, prepared without and with the SiO_2 interlayer, have been measured under the UV radiation exposure using the MB as a model catalytic dye-agent. The free $^{\bullet}OH$ generated by the magnetic photocatalysts, under the UV-radiation exposure, has been measured via the $^{\bullet}OH$-trapping experiments using the photoluminescence (PL) spectrofluorometer. The amount of photo-dissolution of magnetic ceramic core, under the UV-radiation exposure, has been measured via the inductively coupled plasma atomic emission spectroscopy (ICP-AES). It has been shown that the SiO_2-coating as an interlayer between the anatase-TiO_2 shell and γ-Fe_2O_3 magnetic ceramic core plays a crucial role in controlling the number of parameters which directly affect the performance of nanocomposite particles as magnetic photocatalyst. The photocatalytic activity of TiO_2-γ-Fe_2O_3 core-shell magnetic photocatalyst is known to be severely affected by the photo-dissolution phenomenon in the absence of SiO_2 interlayer. We demonstrate here that the involvement of advance oxidation process, such as the Fenton-reaction, makes the same photo-dissolution process responsible for an enhanced photocatalytic activity.

2.1. Introduction

The nanocrystalline semiconductor anatase-titania has been the most commonly applied photocatalyst for the removal of organic synthetic-dyes from the aqueous solutions.[1] However, several issues have been associated in removing the nanocrystalline photocatalyst particles after the treatment of dye-solutions. The traditional methods for the separation such as the coagulation, flocculation, and sedimentation are tedious and expensive. Moreover, the requirements of additional chemicals and purification stage to wash the coagulant from the nanocrystalline photocatalyst particles make these processes expensive.[2-3] The approach to overcome these problems has been to facilitate the photocatalyst removal using an external magnetic field.[3] However, the nanocrystalline TiO_2-based photocatalysts are inherently non-magnetic and cannot be separated using this technique. Hence, the TiO_2-based photocatalysts have been modified into a "core-shell" nanocomposite structure, comprising the core of a magnetic particle and the shell of nanocrystalline TiO_2 particles. Such core-shell nanocomposite structure, which is termed as "magnetic photocatalyst", possesses both the magnetic and photocatalytic properties.

In a magnetic photocatalyst, various magnetic materials including Fe_3O_4 /γ-Fe_2O_3,[4-10] manganese ferrite,[11] nickel ferrite,[12] barium ferrite,[13] cobalt ferrite,[14] and nickel[15] have been used as a magnetic core. Among them Fe_3O_4 and γ-Fe_2O_3 have been reported most commonly due to its non toxic nature and ease of synthesis.[4, 9, 16-18] However, the TiO_2-coated iron oxide has been demonstrated to exhibit very low photocatalytic activity under the UV-radiation exposure due to two reasons. First, during the processing of TiO_2-coated γ-Fe_2O_3, the calcination treatment conducted at higher temperature causes the Fe^{3+} ions to diffuse into the TiO_2 lattice which then act as

trapping and/or annihilating centers for the photo-induced electrons and holes (e^-/h^+), thus enhancing or reducing the photocatalytic activity depending on the concentration of diffused Fe^{3+} ions.[19] Secondly, the Fe^{2+} ions formed via the reduction of Fe^{3+} ions present on the surface of TiO_2 photocatalyst get dissolved into the solution (the photo-dissolution process) during the measurement of photocatalytic activity. These dissolved Fe^{2+} ions can then react with the generated $^\bullet OH$ and transform them to hydroxyl ions (OH^-), thus reducing the photocatalytic activity. [20-21]

In order to avoid the diffusion of Fe^{3+} ions into the TiO_2 lattice during the calcination treatment and to avoid the electronic interaction of the magnetic oxide core and the photocatalyst shell during the photocatalytic activity measurements, the SiO_2 has been normally utilized as an interlayer between the core and the shell which enhances the photocatalytic activity under the UV-radiation exposure.[4-5,8] Generally, the photocatalytic activity of magnetic photocatalyst is less than that of the pure TiO_2 nanoparticles. The optimization of TiO_2 content in the magnetic photocatlyst is a real challenge and it cannot be obtained through a single step. Therefore, the present study focuses on the optimization of TiO_2 content in the magnetic photocatalyst in terms of coating thickness which has been varied with increasing number of sol-gel coating cycles.

The extent of photo-dissolution in TiO_2-coated iron oxide particles depends on the interface of coating and core, and TiO_2 coating thickness. There are no reports in the literature which demonstrate the enhancement in the photocatalytic activity of TiO_2-coated γ-Fe_2O_3 without the interlayer of SiO_2 typically under the occurrence of photo-dissolution process. Hence, the another major objective of this work is set to demonstrate a new approach, by simultaneously involving the AOP, to substantially

enhance the photocatalytic activity of TiO_2-coated γ-Fe_2O_3 magnetic photocatalyst under the UV-radiation exposure without the use of SiO_2 interlayer.

2.2 Experimental

2.2.1. Chemicals

Titanium(IV)-isopropoxide ($Ti(OC_3H_7)_4$, 97 %), nanocrystalline γ-Fe_2O_3 (<50 nm, 98 %) tetraethylorthosilicate (TEOS, 98 %), and terephthalic acid (TA, 98 %) were purchased from Sigma-Aldrich Chemicals, Bangalore, India; ammonium hydroxide (NH_4OH, 25 wt.%) from Qualigens Fine Chemicals, India; ethanol (99.9 % AR), 2-propanol (99.5 %, ACS reagent), sodium hydroxide (NaOH, Assay 97 %), methylene blue (MB, 96 %) from S.D. Fine-Chem Ltd., Mumbai, India; and commercial nanocrystalline anatase-TiO_2 from the Central Drug House (CDH) (P) Ltd., New Delhi, India. All chemicals were used as-received without any further purification and/or modification.

2.2.2. SiO₂ coating by modified Stober process

An insulating layer of SiO_2 was first deposited on the surface of nanocrystalline γ-Fe_2O_3 using the modified Stober process.[13, 22] To 2 g suspension of magnetic γ-Fe_2O_3 powder dispersed in 250 ml of ethanol, 14.5 ml of TEOS was slowly added and stirred for 1 h using an overhead stirrer (IKA RW 14, Sigma-Aldrich Labware, Bangalore, India). This was followed by the drop-wise addition of mixture of 2.3 ml of NH_4OH and 63.4 ml of water and the suspension was stirred for 12 h. The resulting product was collected via the magnetic separation (magnetic separator, Sigma-Aldrich Labware, Bangalore, India), washed first with 100 ml of ethanol and four times with distilled-water followed by drying in an oven at 60°C overnight. The SiO_2-coated

nanocrystalline γ-Fe_2O_3 particles were also prepared via similar procedure using 2-propanol as a solvent.

2.2.3. TiO$_2$ coating by sol-gel method

In order to deposit the nanocrystalline anatase-TiO_2, 2 g of as-received γ-Fe_2O_3 magnetic particles were suspended in a solution of 0.5 g of $Ti(OC_3H_7)_4$ dissolved in 125 ml of 2-propanol. To this suspension, a solution consisting 0.15 ml of distilled-water (R=5, defined as the ratio of molar concentration (final) of water to that of alkoxide-precursor) dissolved in 125 ml of 2-propanol, was added drop wise. The suspension was stirred for 12 h and the magnetically separated powder was washed with 100 ml of 2-propanol and then dried in an oven at 60°C overnight. The sol-gel process was repeated for different number of cycles (1 to 5) to control the thickness of amorphous-TiO_2 coating which is then converted to anatase-TiO_2 via the calcination treatment (heating rate = 3°C min^{-1}) of the dried-powder at 600°C for 2 h. The same procedure was followed to deposit the anatase-TiO_2 on the surface of SiO_2-coated γ-Fe_2O_3.

2.2.4. Characterization

The morphology of different products was examined using the transmission electron microscope (TEM, Tecnai G^2, FEI, The Netherlands) operated at 300 kV. The energy dispersive X-ray (EDX) analysis was conducted to confirm the chemical constituents in the samples and their relative concentrations. The selected-area electron diffraction (SAED) patterns were obtained to confirm the crystallinity of samples. The crystalline phases present were determined using the X-ray diffraction (XRD, PW1710 Phillips,

The Netherlands). The broad-scan analysis was typically conducted within the 2θ range of 10-80° using the Cu $K\alpha$ (λ_{Cu}=1.542 Å) X-radiation.

2.2.5. Measurement of photocatalytic activity

The photocatalytic activity was studied by monitoring the degradation of MB dye in an aqueous suspension containing the magnetic photocatalyst particles under the continuous UV-radiation exposure. 125 ml of aqueous suspension was prepared by completely dissolving 7.5 μM of MB dye and then dispersing 0.4 g l^{-1} of magnetic photocatalyst particles. The same solution was made using 3 wt% H_2O_2 for the Fenton reaction to enhance the activity of TiO_2-γ-Fe_2O_3 nanocomposite. The resulting suspension was ultra-sonicated for 5 min (Bandelin ultrasonic bath, Sigma-Aldrich Labware, Bangalore, India) and then stirred in the dark for 1 h using an overhead stirrer to stabilize the adsorption of MB dye over the surface of magnetic photocatalyst particles. The stable aqueous suspension was then irradiated with the UV-light using a Photoreactor (Luzchem Inc., Canada) containing 16 UVA tubes as the UV-source having the illuminance of 255 lm m^{-2} (lux) and emitting the radiation having the peak-wavelength at ~350 nm. Following the UV-radiation exposure, 8 ml aliquots were taken out of the UV-chamber after specific time interval for the total 2 h for obtaining the absorption spectra. After removing the aliquot, the remaining suspension was ultra-sonicated for 5 min before transferring it to the Photoreactor. The magnetic and non-magnetic photocatalyst particles were separated from the aliquots using either a magnetic separator or a centrifuge (Hettich EBA 20, Sigma-Aldrich Labware, Bangalore, India). The filtered solution was then examined using a UV-visible absorption spectrophotometer (UV-2401 PC, Shimadzu, Japan) to study the degradation kinetics of MB dye. The absorption spectra of MB dye solution were

obtained within the range of 200-800 nm as a function of UV-radiation exposure time. The intensity of main absorbance peak (A_t) of MB dye solution, located at ~656 nm, was taken as a measure of residual MB dye concentration (C_t). The UV-visible absorption spectrum of MB dye solution obtained after stirring the suspension for 1 h in the dark was regarded as a reference spectrum corresponding to the initial MB dye concentration (C_o). The normalized residual concentration of MB dye was calculated using the relationship of the form,

$$\left(\frac{C_t}{C_o}\right)_{MB} = \left(\frac{A_t}{A_o}\right)_{656\ nm} \tag{2.1}$$

The amount of MB dye adsorbed on the surface of magnetic photocatalyst particles after stirring the suspension in the dark for 1 h was calculated using the relationship of the form,

$$\left(\frac{C_{-60}-C_o}{C_{-60}}\right)_{MB} = \left(\frac{A_{-60}-A_o}{A_{-60}}\right)_{656\ nm} \tag{2.2}$$

where, C_{-60} and A_{-60} are the MB dye concentration and corresponding absorbance before the addition of magnetic photocatalyst particles. The photocatalytic activity measurement was also performed in the absence of magnetic photocatalyst particles to confirm the stability of MB dye in an aqueous solution under the continuous UV-radiation exposure. Under this condition, the initial MB dye concentration (C_{-60}) remained almost unchanged even after irradiating the sample for total 3 h. The cyclic nature of magnetic photocatalyst particles was confirmed by repeating the photocatalytic activity measurements using the best sample. During these tests, which were similar to the measurements as described above, the magnetic photocatalyst

particles were separated using the magnetic separator and dried in an oven at 80°C for 2 h before conducting the next-cycle of photocatalytic activity measurement.

2.2.6. Analysis of ˙OH generation

The radical trapping experiments were typically performed to trap the free ˙OH, using the TA, which were produced under the continuous UV-radiation exposure of magnetic photocatalyst particles in an aqueous solution. These experiments were similar to the one described above for the photocatalytic activity measurements except that the MB dye was replaced with 5×10^{-4} M of TA and 2×10^{-3} M NaOH in H_2O or H_2O_2.[23-25] The solubility of TA in the neutral and acidic water is relatively lower, which is enhanced by the addition of NaOH. Moreover, the TA is a non-fluorescent molecule; however, the trapping of free ˙OH by TA results in the formation of 2-hydroxyterephthalic acid which is a highly fluorescent molecule exhibiting a characteristic PL peak located in between ~422-428 nm at an excitation wavelength of ~315 nm. Hence, the PL spectra of 2-hydroxyterephthalic acid were recorded as a function of UV-radiation exposure time using the spectrofluorometer (Cary Eclipse, Varian, The Netherlands) at an excitation wavelength of ~315 nm. Through the analysis of the reports in the radiation-chemistry and sono-chemistry, it has been suggested that that the photo-generated O_2^-, $HO_2^˙$, and H_2O_2 do not interfere with the reaction between ˙OH and TA.[20] Moreover, the PL spectra generated in this investigation have the shape and wavelength corresponding to the maximum intensity (~422-428 nm) identical with those of 2-hydroxyterephthalic acid (~425 nm). It is also known that within the concentration range of 10^{-3}-10^{-4} M, the oxidation of TA preferentially takes place via the reaction with ˙OH instead of that with the photo-induced holes in the TiO_2 photocatalyst.[23] These results strongly suggest that the PL

intensity in the present investigation is originating specifically from the reaction between the $^\bullet$OH and TA. Hence, the intensity of PL peak is regarded here as the measure of amount of free $^\bullet$OH produced by the magnetic photocatalyst particles at a given time under the UV-radiation exposure. (Note: The TA molecule contains an aromatic ring having three double-bonds containing delocalized pi-electrons which are loosely bound to the ring. Hence, they can be excited with the external radiation (energy absorption). This is, however, not possible at the excitation wavelength of ~315 nm due to the relatively wider gaps in the energy levels. When the electron donating groups, such as –OH and –NH$_2$, are attached to the ring, they reduce the gaps between the energy levels, which in turn makes it possible to absorb the ~315 nm excitation wavelength, which subsequently leads to the maximum PL intensity at the emission wavelength within the range of ~422-428 nm).

2.2.7. Photo-dissolution

The photo-dissolution experiments were conducted using the as-received nanocrystalline γ-Fe$_2$O$_3$ and anatase-TiO$_2$-coated γ-Fe$_2$O$_3$ processed without and with the interlayer of SiO$_2$-coating. In these experiments, 0.4 g l^{-1} of magnetic photocatalyst particles were suspended in 125 ml of distilled-water having the dissolved-Fe below the detection limit. After sonicating for 5 min followed by stirring in the dark for 1 h, the suspension was subjected to a continuous UV-radiation exposure in a Photoreactor for 2 h. The photocatalyst particles were separated using either a magnetic separator or a centrifuge and the filtrate was then analyzed using the ICP-AES (Thermo Electron IRIS INTREPID II XSP DUO) for determining the Fe-content in the solution which is taken as a measure of the photo-dissolution occurring during the photocatalytic activity measurements.

2.3. Results and discussion

2.3.1. Morphological and structural characterization

 The TEM image of as-received nanocrystalline γ-Fe_2O_3 particles is shown in Fig. 2.1a and the corresponding EDX spectrum is presented in Fig. 2.1b. The size of as-received nanocrystalline γ-Fe_2O_3 particles is within the range of 15-25 nm with near-spherical morphology. The EDX spectrum confirms the presence of Fe and O within the particles. The SAED pattern, shown as an inset in Fig. 2.1a, exhibits the concentric rings pattern indicating the nanocrystalline nature of as-received γ-Fe_2O_3 particles in agreement with the TEM image.
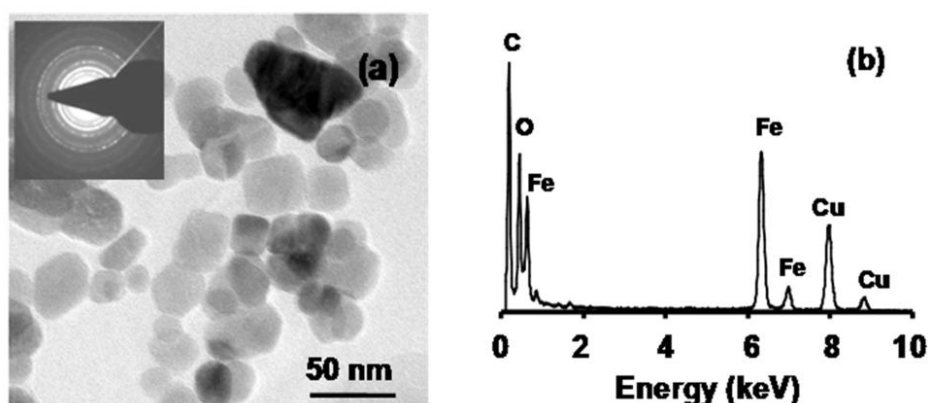
Fig. 2.1. TEM image (a) and EDX spectrum (b) of the as-received nanocrystaline γ-Fe_2O_3 particles.

The XRD patterns of as-received and calcined nanoparticles are presented in Fig. 2.2a and b. The as-received magnetic nanoparticles possess the γ-Fe_2O_3 structure; while, the calcined-sample possesses the α-Fe_2O_3 structure as confirmed after comparing the XRD patterns with the JCDPS card nos. 39-1346 and 24-0072.[18, 26] (Note: In Fig. 2.2a, all peaks are slightly shifted to higher diffraction angles relative to those of

Fe_3O_4 (JCPDS card no. 88-0866); hence, the diffraction pattern is assigned to γ-Fe_2O_3 instead of Fe_3O_4).
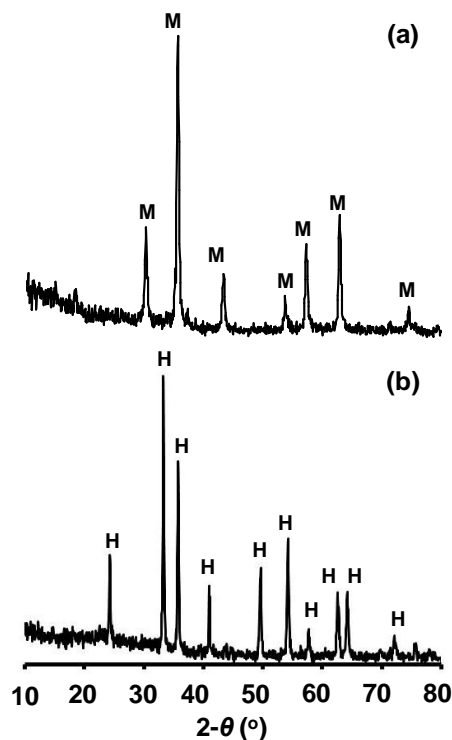
Fig. 2.2. XRD patterns of as-received nanocrystalline γ-Fe_2O_3 particles before (a) and after (b) calcination at 600^oC for 2 h. M and H refer to γ-Fe_2O_3 and α-Fe_2O_3 structures.

Due to the oxidation during the high temperature calcination treatment, the γ-Fe_2O_3 nanoparticles are transformed to the α-Fe_2O_3 nanoparticles which are ferromagnetic with the saturation magnetization of 0.57 emu g^{-1}.[27-28] As a result of small saturation magnetization, the α-Fe_2O_3 nanoparticles could not be separated from an aqueous solution using a moderate external magnetic field as demonstrated in Fig. 2.3. It is observed that the as-received nanocrystalline γ-Fe_2O_3 particles can be separated from an aqueous solution using a moderate external magnetic field, Fig. 2.3a. Hence, the phase transformation induced by the calcination treatment at 600^oC for 2 h is noted to destroy the magnetic properties of a core material.
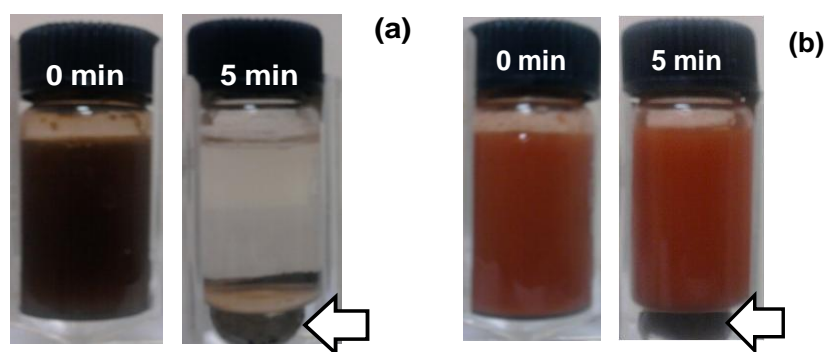
Fig. 2.3. Comparison of the effect of moderate external magnetic field on the magnetic separation of γ-Fe$_2$O$_3$ (a) and α-Fe$_2$O$_3$ (b) nanocrystalline particles from aqueous solutions. The arrows at the right-side show the position of a magnet.

The TEM images of nanocrystalline anatase-TiO$_2$-coated ($\gamma+\alpha$)-Fe$_2$O$_3$ particles, obtained after different number of TiO$_2$-coating cycles, are presented in Fig. 2.4a-c and the corresponding EDX spectra are presented in Fig. 2.4d-f. Comparison of Fig. 2.4a-c with Fig. 2.1a shows that, following the sol-gel anatase-TiO$_2$ coating, the particles become more aggregated and the aggregation tendency increases with the number of TiO$_2$-coating cycles. The EDX spectra, Fig. 2.4d-e, show increasing intensity of Ti-peak which suggests the deposition of increasing amount of TiO$_2$ with the number of TiO$_2$-coating cycles.

The corresponding XRD patterns of nanocrystalline anatase-TiO$_2$ coated nanocomposite particles are presented in Fig. 2.5. For the initial two cycles of TiO$_2$-coating, Fig. 2.5a and b, an increasing resistance to the γ-Fe$_2$O$_3$ to α-Fe$_2$O$_3$ phase transformation is observed. However, the resistance to the phase transformation is completely eliminated for the cycle-5 of TiO$_2$-coating indicating that larger thickness of anatase-TiO$_2$ coating is unable to avoid the complete phase transformation. The relative amount of α-Fe$_2$O$_3$ formed is qualitatively noted to be the highest for the

cycle-5 and the lowest for the cycle-3.The amount of anatase-TiO_2 deposited is seen to increase and the overall intensity of diffraction peaks of core magnetic ceramic particles is seen to decease with increasing number of TiO_2-coating cycles. In addition to this, the amorphous background is noted to be higher for the initial two cycles of TiO_2-coating which suggests greater resistance to the nucleation of anatase-phase from the amorphous-TiO_2 during the calcination treatment under these processing conditions.
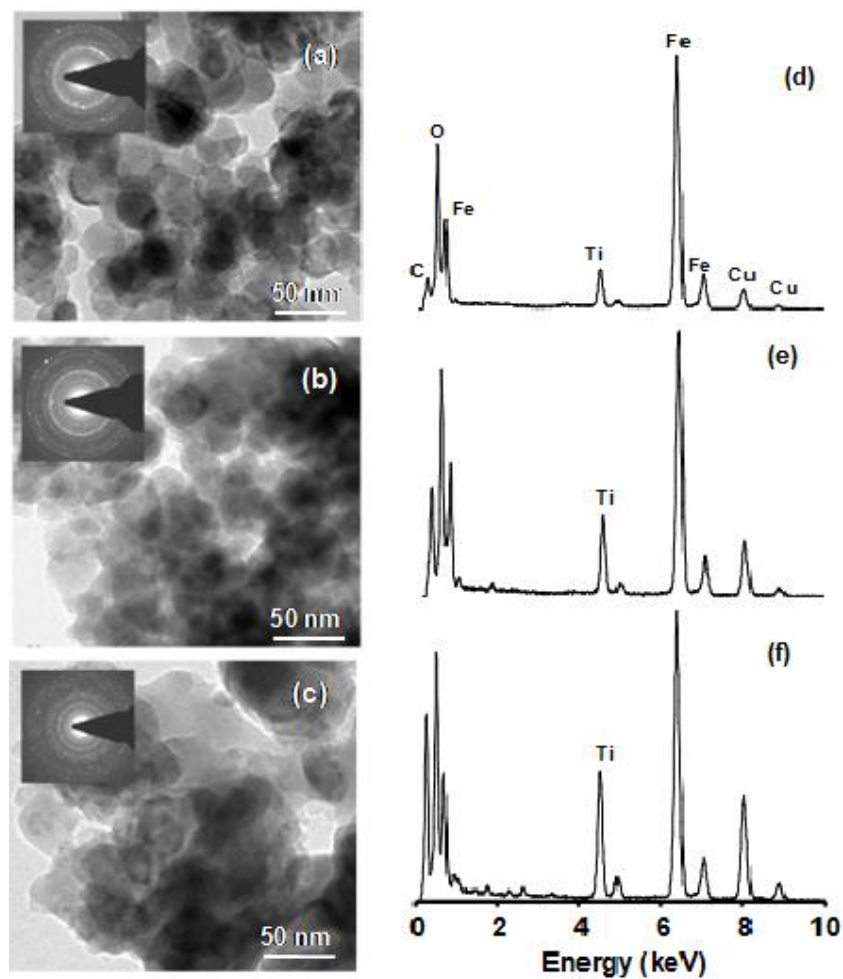
Fig. 2.4. TEM images of anatase-TiO_2-coated $(\gamma+\alpha)$-Fe_2O_3 nanocomposite particles processed with different number of sol-gel TiO_2-coating cycles – (a) cycle-1, (b) cycle-3, and (c) cycle-5. The insets show corresponding SAED patterns. Corresponding EDX spectra (d) cycle-1, (e) cycle-3, and (f) cycle-5.
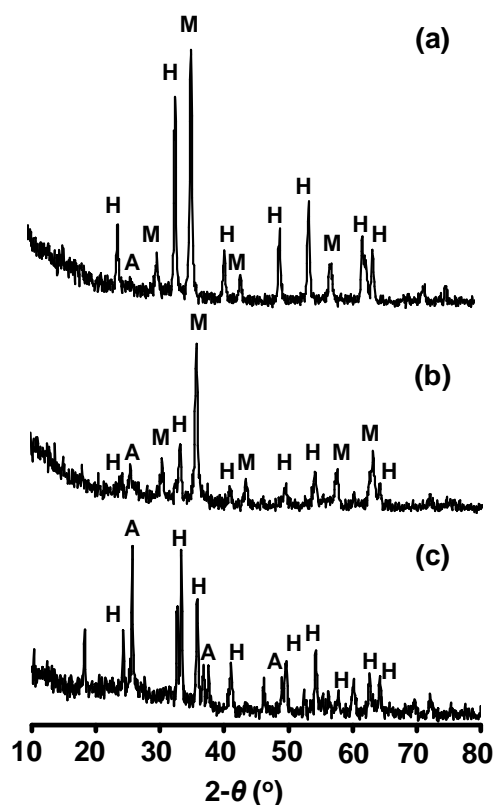
Fig. 2.5. XRD patterns of anatase-TiO_2-coated $(\gamma+\alpha)$-Fe_2O_3 nanocomposite particles processed with different number of sol-gel TiO_2-coating cycles – (a) cycle-1, (b) cycle-3, and (c) cycle-5.

The direct deposition of anatase-TiO_2, without the SiO_2 interlayer, can partially prevent the formation of anatse-TiO_2 with the increasing amount of latter due to the substrate-effect on the amorphous to anatase phase transformation (Fig. 2.5a and b). It is to be noted that the amorphous-TiO_2 is first deposited on the surface of magnetic ceramic particles via the sol-gel process which is then converted to the anatase-TiO_2 using the high temperature calcination treatment. The amorphous to anatase phase transformation is not completed for lower number of TiO_2-coating cycles which is referred here as the substrate-effect. The porous nature of amorphous TiO_2 cannot completely avoid the access of γ-Fe_2O_3 to the atmospheric oxygen which results in the partial phase transformation of magnetic core in the presence of TiO_2-coating.[7]

However, the substrate-effect is eliminated completely for the largest number of TiO_2-coating cycle investigated here (Fig. 2.5c) possibly leading to the complete formation of anatase-TiO_2. Since γ-Fe_2O_3 to α-Fe_2O_3 phase transformation begins at the surface,[29] the stability of interphase boundary between the amorphous-TiO_2 and γ-Fe_2O_3 plays a crucial role in the nucleation and growth of α-Fe_2O_3. As TiO_2 undergoes a phase transformation from the amorphous-to-anatase at about 400^oC,[30] the interphase boundary between the amorphous-TiO_2 and γ-Fe_2O_3 becomes weaker due to the atomic rearrangement taking place within the amorphous-TiO_2 at the interphase boundary, which allows an easy nucleation and growth of α-Fe_2O_3 phase. Hence, both the porous nature of amorphous-TiO_2 and amorphous-to-anatase phase transformation in TiO_2 at 400^oC are responsible for the complete phase transformation of magnetic ceramic core in the presence of the largest thickness of TiO_2-coating after the calcination treatment at 600^oC (Fig. 2.5c).

2.3.2. Effect of solvent on SiO_2 coating over γ-Fe_2O_3

The TEM images of SiO_2-coated nanocrystalline γ-Fe_2O_3 particles, processed using the ethanol and 2-propanol solvents, are shown in Fig. 2.6. Comparison of Fig. 2.6 with Fig. 2.1a shows that SiO_2-coating is very dense and highly continuous around the γ-Fe_2O_3 nanoparticles with the average thickness of 8 and 20 nm for the ethanol and 2-propanol solvents. Since the dielectric constants of ethanol and 2-propanol are 24.3 and 18.3, 2-propanol is relatively less polar protic solvent than ethanol.[31] The hydrogen bonding of 2-propnaol with water and hydroxyl-ion is, hence, relative weaker than that of ethanol, which increases the susceptibility of attack of water and hydroxyl-ions on the central Si^{4+} ions in the TEOS precursor. This enhances the rate of hydrolysis and condensation reactions of TEOS in 2-propanol relative to that in

ethanol. Although relatively large number of particles are nucleated in 2-propanol, they also tend to exhibit larger growth rates due to their smaller size. Moreover, the Debye screening length (as per the well-known DLVO theory (Derjaguin, Landau and Verwey, Overbeek)) is shorter for the particles nucleated in 2-propanol due to its lower dielectric constant which allows the particle-particle aggregation. Both of these two factors then lead to relatively rapid growth of nucleated particles in 2-propanol resulting in relatively large size particles and thicker-coating.[31] However, since thicker SiO_2-coating may affect the magnetic properties of nanocomposite photocatalyst, in the present investigation, the dense, continuous, and thin SiO_2-coating obtained using ethanol as a solvent is considered further as an interlayer between the anatase-TiO_2 shell and the magnetic ceramic core.
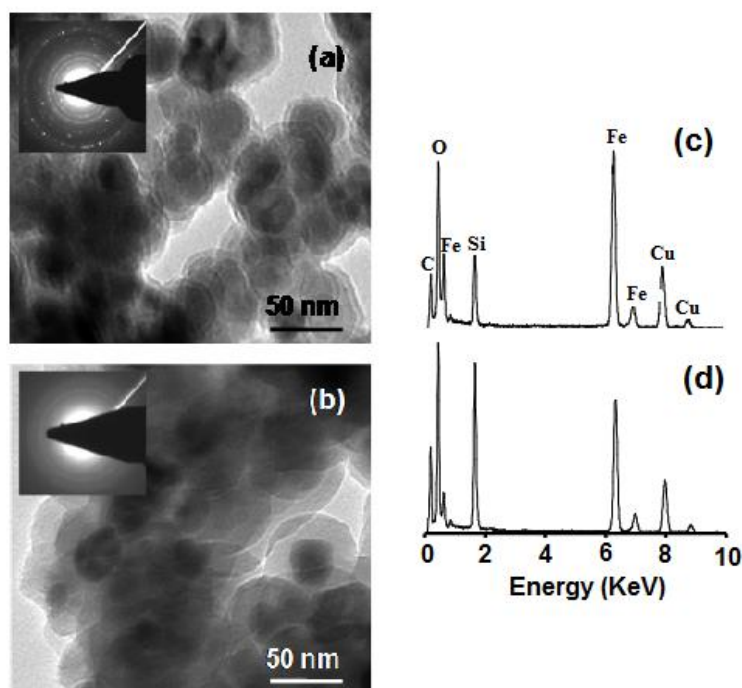
Fig. 2.6. TEM images of SiO_2-coated γ-Fe_2O_3 nanocomposite particles processed using ethanol (a) and 2-propanol (b) as solvents. The insets show corresponding SAED patterns and their respective EDX spectra (c) and (d).

The XRD patterns of SiO_2-coated nanocrystalline γ-Fe_2O_3 particles, processed using the ethanol and 2-propanol solvents, are presented in Fig. 2.7. In contrast to the effect of TiO_2-coating on the phase transformation of a magnetic ceramic core, it is observed that the SiO_2-coating results in the stabilization of both γ-Fe_2O_3 structure and the magnetic properties of SiO_2-coated nanocrystalline γ-Fe_2O_3 particles. The comparison of XRD patterns further reveals more amount of amorphous SiO_2 present in the case of 2-propanol solvent, which is in agreement with the TEM and EDX results. The SiO_2-coating, thus, remains amorphous even after the high temperature calcination treatment for both the solvents.
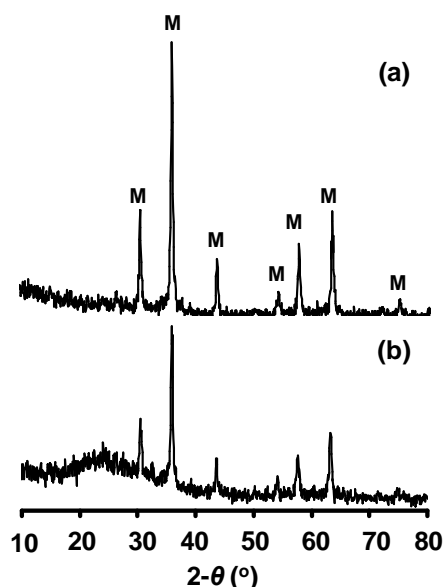
Fig. 2.7. XRD patterns of SiO_2-coated γ-Fe_2O_3 nanocomposite particles processed using ethanol (a) and 2-propanol (b) as solvents.

The TEM images of nanocrystalline anatase-TiO_2-coated SiO_2/γ-Fe_2O_3 nanocomposite particles, obtained after different number of TiO_2-coating cycles, are presented in Fig. 2.8a-c and the corresponding EDX spectra are also presented (2.8d-f). Comparison of Fig. 2.8 with Fig. 2.6a shows that, following the TiO_2-coating, the SiO_2/γ-Fe_2O_3 particles become more aggregated and the aggregation tendency

increases with the number of TiO$_2$-coating cycles. The EDX spectra, Fig. 2.8, show increasing intensity of Ti-peak which suggests the deposition of increasing amount of TiO$_2$ with the number of TiO$_2$-coating cycles.
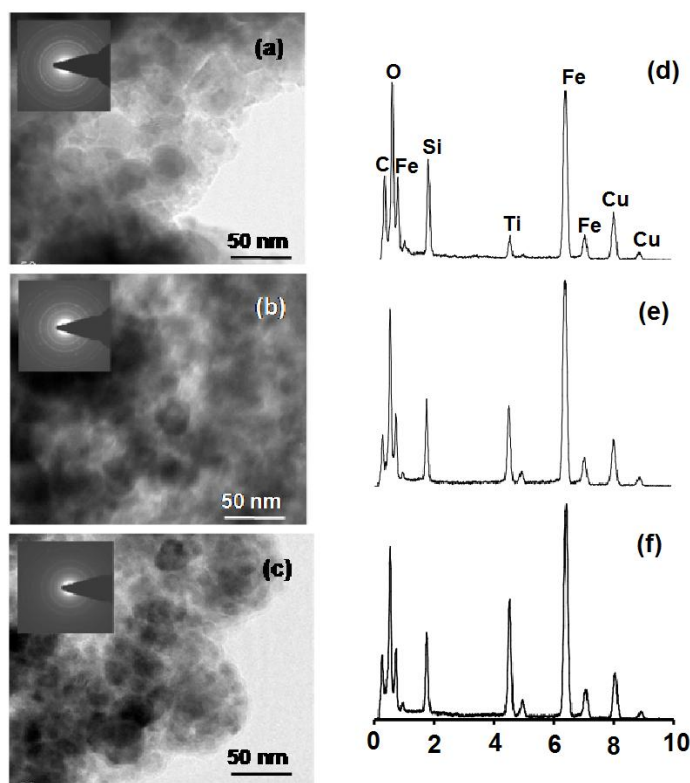
Fig. 2.8. TEM images of anatase-TiO$_2$-coated SiO$_2$/γ-Fe$_2$O$_3$ magnetic photocatalysts processed with different number of sol-gel TiO$_2$-coating cycles − (a) cycle-1, (b) cycle-3, and (c) cycle-5. The insets show corresponding SAED patterns. EDX spectra for different number of sol-gel TiO$_2$-coating cycles − (d) cycle-1, (e) cycle-3, and (f) cycle-5.

The corresponding XRD patterns of nanocrystalline anatase-TiO$_2$-coated SiO$_2$/γ-Fe$_2$O$_3$ particles are presented in Fig. 2.9. For all cycles, the stabilization of γ-Fe$_2$O$_3$ structure is observed indicating that the introduction of SiO$_2$-coating as an interlayer between the anatase-TiO$_2$ and γ-Fe$_2$O$_3$ is effective in avoiding the phase transformation of magnetic ceramic core. The amount of anatase-TiO$_2$ deposited is

seen to increase and the overall intensity of diffraction peaks of core magnetic ceramic particles is seen to decrease with increasing number of TiO_2-coating cycles.
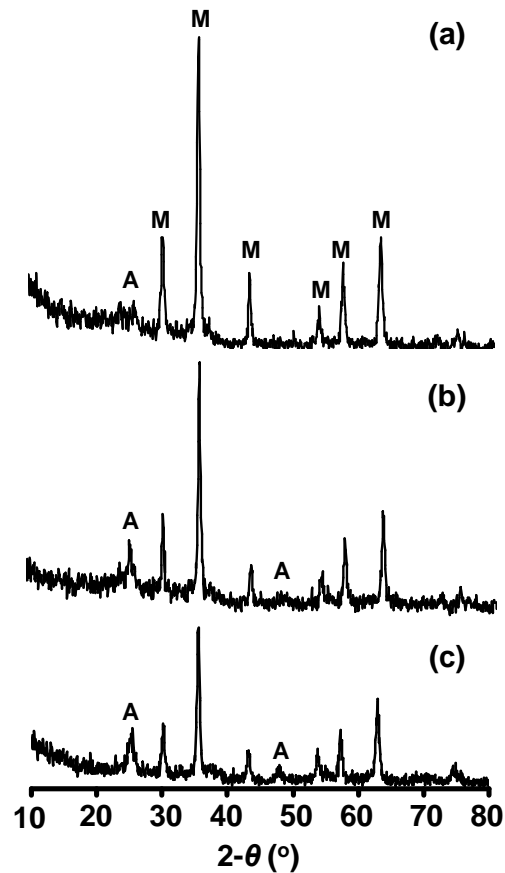
Fig. 2.9. XRD patterns of anatase-TiO_2-coated SiO_2/γ-Fe_2O_3 magnetic photocatalysts processed with different number of sol-gel TiO_2-coating cycles − (a) cycle-1, (b) cycle-3, and (c) cycle-5.

In Fig. 2.10, the effect of stabilization of γ-Fe_2O_3 on the magnetic separation of these nanocomposite particles is compared with that of anatase-TiO_2-coated γ-Fe_2O_3 nanocomposite particles (without SiO_2-coating) typically for the cycle-5 of TiO_2-coating. It is observed that the TiO_2-coated SiO_2/γ-Fe_2O_3 nanocomposite particles can be separated from an aqueous solution using a moderate external magnetic field; however, the magnetic separation is not possible in the absence of an interlayer SiO_2-

coating. Thus, the introduction of SiO_2-coating as an interlayer between the anatase-TiO_2 shell and the γ-Fe_2O_3 magnetic ceramic core has successfully stabilized the magnetic γ-Fe_2O_3 structure of the core resulting in the successful magnetic separation of TiO_2-coated SiO_2/γ-Fe_3O_4 magnetic nanocomposite particles from an aqueous solution.
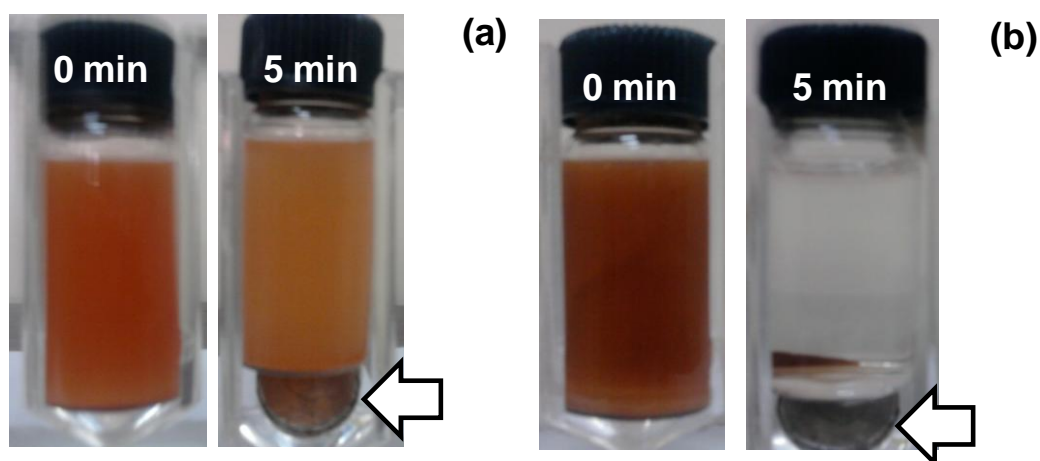
Fig. 2.10. Comparison of effect of a moderate external magnetic field on the magnetic separation of nanocomposite particles from aqueous solutions – (a) anatase-TiO_2-coated $(\gamma+\alpha)$-Fe_2O_3 (cycle-5) and (b) anatase-TiO_2-coated SiO_2/γ-Fe_2O_3 (cycle-5). The arrows at the right-side bottom show the position of a magnet.

2.3.3. Comparison of $^{\bullet}OH$ generation

The variation in the PL intensity of 2-hydroxyterephthalic acid as a function of UV-radiation exposure time as observed for the anatase-TiO_2-coated $(\gamma+\alpha)$-Fe_2O_3 nanocomposite particles (cycle-3) and that observed for the anatase-TiO_2-coated SiO_2/γ-Fe_2O_3 nanocomposite particles (cycles-1, 3, and 5) are presented in Figs. 2.11 and 2.12.
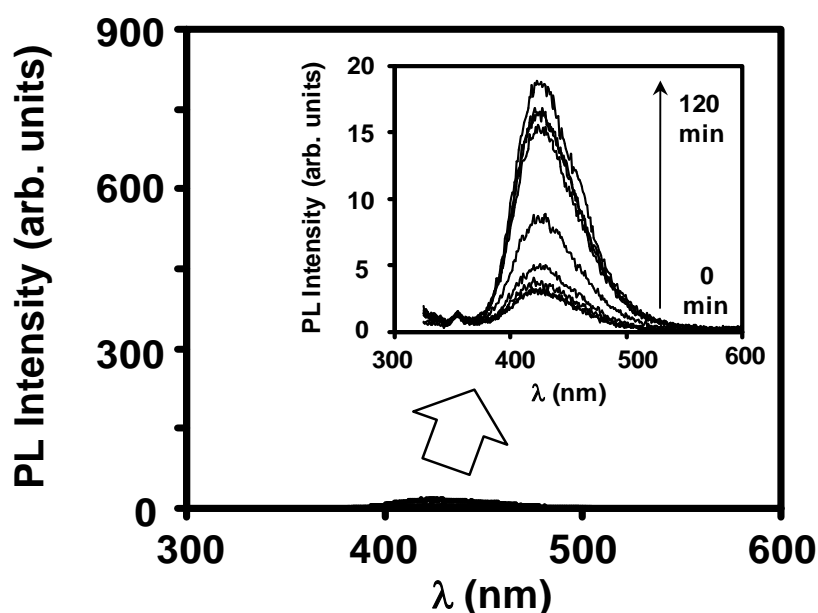
Fig. 2.11. Variation in the PL intensity associated with the formation of 2-hydroxyterphthalic acid as a function of UV-radiation exposure time as obtained for the anatase-TiO$_2$-coated $(\gamma+\alpha)$-Fe$_2$O$_3$ (cycle-3) nanocomposite particles. The inset shows an enlarged view of the graph.

It is observed that the anatase-TiO$_2$-coated $(\gamma+\alpha)$-Fe$_2$O$_3$ nanocomposite particles (cycle-3) does not generate an appreciable concentration of free $^\bullet$OH under the UV-radiation exposure. (Note: Although not shown here, this behavior is also followed by the as-received nanocrystalline γ-Fe$_2$O$_3$ and the anatase-TiO$_2$-coated $(\gamma+\alpha)$-Fe$_2$O$_3$ particles processed under other conditions (cycle-1 and 5)). On the other hand, the comparison shows that large concentration of free $^\bullet$OH are produced by the anatase-TiO$_2$-coated SiO$_2$/γ-Fe$_2$O$_3$ nanocomposite particles (cycle-1, 3, and 5). Moreover, the concentration of free $^\bullet$OH produced is noted to increase with the number of TiO$_2$-coating cycles at a given time of UV-radiation exposure.
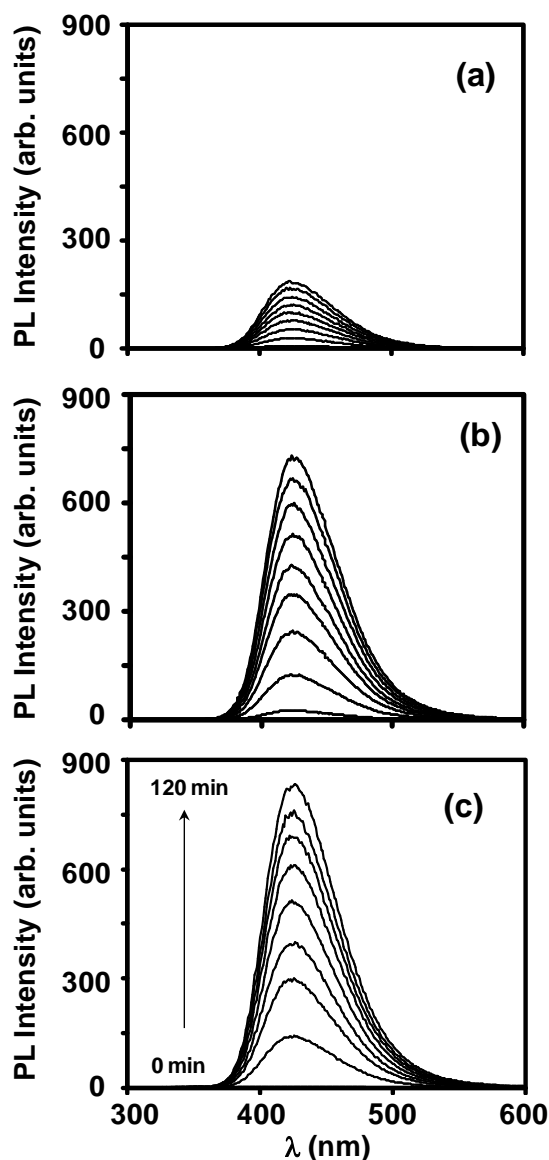
Fig. 2.12. Variation in the PL intensity associated with the formation of 2-hydroxyterphthalic acid as a function of UV-radiation exposure time as obtained for the anatase-TiO_2-coated SiO_2/ γ-Fe_2O_3 magnetic photocatalysts processed with different number of sol-gel TiO_2-coating cycles – (a) cycle-1, (b) cycle-3, and (c) cycle-5.

As demonstrated in Table 1, the rate of formation of free $^\bullet OH$ ($k_{OH^\bullet}$) under the UV-radiation exposure is higher only for the nanocomposite particles processed with the SiO_2-coating as an interlayer. Moreover, the value of $k_{OH^\bullet}$ is noted to increase with the

number of TiO_2-coating cycles. Thus, the introduction of SiO_2-coating as an interlayer between the anatase-TiO_2 shell and the magnetic ceramic core results not only in the generation of large concentration of free $^\bullet OH$ but also in higher rate of their formation under the UV-radiation exposure.

Table 2.1 The amount of photo-dissolution of Fe and the values of photocatalytic activity related parameters as obtained for the nanocomposite magnetic photocatalysts processed under different conditions without and with the interlayer SiO_2 coating.

Sample		$k_{\bullet OH}$ (min^{-1})	MB adsorbed in dark (%)	k_{app} (min^{-1})	Photo-dissolution of Fe (ppm)
Distilled-water		--	--	--	bdl*
γ-Fe_2O_3	As-received	0.08	0	0	0.03
Anatase-TiO_2-coated (γ+α)-Fe_2O_3	Cycle-1	0.04	0	0	0.89
	Cycle-3	0.15	18	0.001	0.17
	Cycle-5	0.07	30	0.001	0.02
Anatase-TiO_2-coated SiO_2/ γ-Fe_2O_3	Cycle-1	1.5	67	0.02	0.03
	Cycle-3	5.9	38	0.106	0.01
	Cycle-5	6.9	45	0.126	0.02

2.3.4. Photocatalytic activity of TiO_2/SiO_2/γ-Fe_2O_3 and TiO_2/(γ+α)-Fe_2O_3

The variations in the normalized residual MB dye concentration as a function of UV-radiation exposure time as obtained using the anatase-TiO_2-coated (γ+α)-Fe_2O_3 and the anatase-TiO_2-coated γ-Fe_2O_3 nanocomposite particles, processed without and with the SiO_2-coating as an interlayer with the different number of TiO_2-coating cycles, are presented in Fig. 2.13a and b. The corresponding values of MB dye adsorbed on the surface of magnetic photocatalyst particles after stirring the suspension in the dark for

1 h and the calculated apparent first-order-reaction rate-constant (k_{app}) are tabulated in Table 2.1.
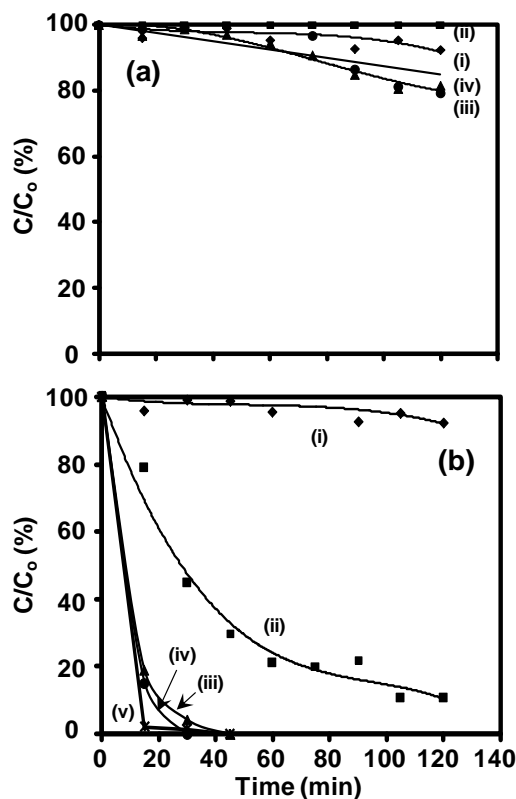
Fig. 2.13. (a) Variation in the normalized residual MB dye concentration as a function of UV-radiation exposure time as obtained for the anatase-TiO_2-coated ($\gamma+\alpha$)-Fe_2O_3 nanocomposite particles processed with different number of sol-gel TiO_2-coating cycles – (i) γ-Fe_2O_3, (ii) cycle-1, (iii) cycle-3, and (iv) cycle-5. (b) Similar graphs as obtained for the anatase-TiO_2-coated SiO_2/γ-Fe_2O_3 magnetic photocatalysts processed with different number of sol-gel TiO_2-coating cycles – (i) γ-Fe_2O_3, (ii) cycle-1, (iii) cycle-3, (iv) cycle-5, and (v) commercial (CDH) nanocrystalline anatase-TiO_2.

It is noted that as-received nanocrystalline γ-Fe_2O_3 particles does not show any dye-adsorption on the surface and photocatalytic activity. Comparison further reveals that k_{app} values are the largest for the anatase-TiO_2-coated SiO_2/γ-Fe_2O_3 nanocomposite

particles. The maximum photocatalytic activity is exhibited by the anatase-TiO_2-coated SiO_2/γ-Fe_2O_3 nanocomposite particles (cycle-5), which is comparable with that (0.17 min^{-1}) of commercial (CDH) nanocrystalline anatase-TiO_2. Thus, the introduction of SiO_2-coating as an interlayer between the outer TiO_2 shell and the magnetic ceramic core particle results in higher photocatalytic activity under the UV-radiation exposure which can be correlated with higher values of $k_{OH\bullet}$.

2.3.5. Recyclability of magnetic photocatalyst

The cyclic nature of anatase-TiO_2-coated SiO_2/γ-Fe_2O_3 nanocomposite particles (cycle-5), as obtained via the photocatalytic activity measurements, is demonstrated in Fig. 2.14. Although the MB dye is observed to be decomposed completely for all the cycles, the k_{app} value is noted to decrease as 0.126, 0.061, 0.035 min^{-1} with the increasing number of photocatalytic activity measurement cycles (1, 2, and 3).
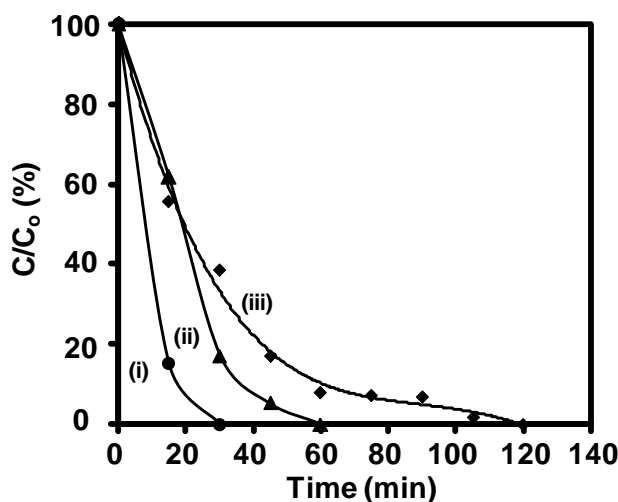
Fig. 2.14. Variation in the normalized residual MB dye concentration as a function of UV-radiation exposure time as obtained for the anatase-TiO_2-coated SiO_2/γ-Fe_2O_3 magnetic photocatalyst (cycle-5) for the different number of photocatalytic activity measurement cycles – (i) cycle-1, (ii) cycle-2, and (iii) cycle-3.

2.3.6. Enhanced activity of TiO$_2$/(γ+α)-Fe$_2$O$_3$ system undergoing photo-dissolution

The amount of Fe detected via the ICP-AES analyses conducted using the aqueous solutions, obtained as a result of the photo-dissolution of γ-Fe$_2$O$_3$ magnetic ceramic core under the UV-radiation exposure, are tabulated in Table 2.1 for the magnetic photocatalyst particles processed under the different conditions. It is noted that the photo-dissolution is maximum for the anatase-TiO$_2$-coated (γ+α)-Fe$_2$O$_3$ nanocomposite particles; while, it is minimum for the as-received nanocrystalline γ-Fe$_2$O$_3$ and anatase-TiO$_2$-coated SiO$_2$/γ-Fe$_2$O$_3$ nanocomposite particles. Thus, the interlayer of SiO$_2$-coating appears to inhibit significantly the photo-dissolution of γ-Fe$_2$O$_3$ magnetic ceramic core under the UV-radiation exposure. Typically, for the anatase-TiO$_2$-coated (γ+α)-Fe$_2$O$_3$ nanocomposite particles, the amount of photo-dissolved Fe is noted to decrease with the increasing amount of sol-gel deposited anatase-TiO$_2$.

The variation in the normalized residual MB dye concentration as a function of UV-radiation exposure time in pure H$_2$O, as obtained for the anatase-TiO$_2$-coated (cycle-1) (γ+α)-Fe$_2$O$_3$ and γ-Fe$_2$O$_3$ nano-composite particles processed without and with the SiO$_2$ interlayer, is presented in Fig. 2.15a. Similar variation as obtained for the anatase-TiO$_2$-coated (cycle-1) (γ+α)-Fe$_2$O$_3$ nano-composite particles in 1 M H$_2$O$_2$ is also shown. The corresponding qualitative variation in the concentration of $^\bullet$OH produced as a function of UV-radiation exposure time, as obtained via the PL analysis under the above test-conditions, is presented in Fig. 2.16. As observed in Fig. 2.15a, the anatase-TiO$_2$-coated (cycle-1) (γ+α)-Fe$_2$O$_3$ nano-composite particles do not exhibit any photocatalytic activity (k_{app}=0 min^{-1}) in pure H$_2$O. This has been attributed to the photo-induced e$^-$/h$^+$ pair transfer from the anatase-TiO$_2$ to (γ+α)-Fe$_2$O$_3$ and their

lower mobility in (γ+α)-Fe$_2$O$_3$ resulting in the rapid rate of recombination which is aided by narrow band-gap energy values of these semiconductor oxides.[4, 16]
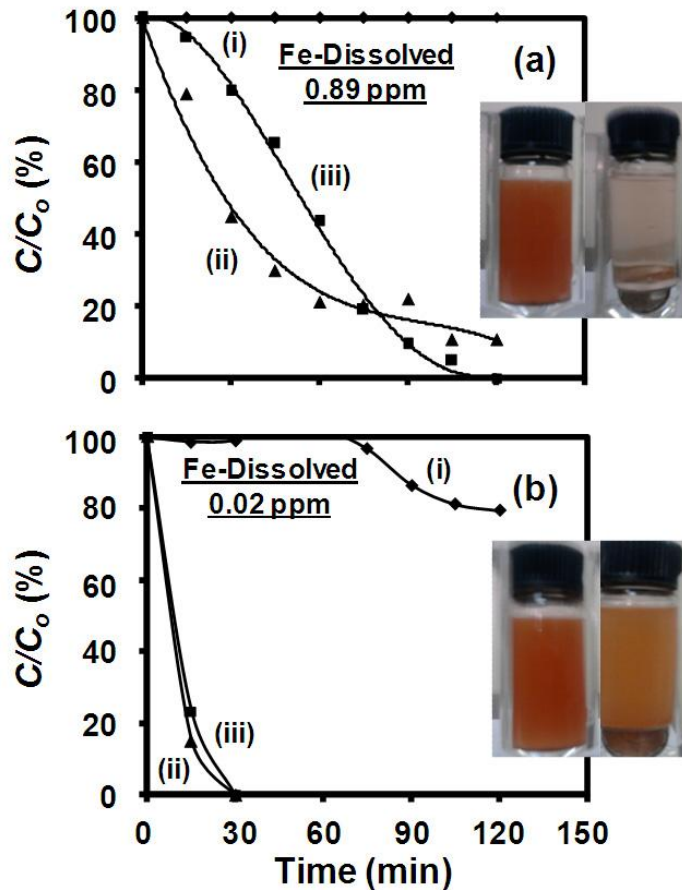
Fig. 2.15. Variation in the normalized residual MB dye concentration as a function of UV-radiation exposure time as obtained for the anatase-TiO$_2$-coated (γ+α)-Fe$_2$O$_3$, γ-Fe$_2$O$_3$, and α-Fe$_2$O$_3$ nano-composite particles processed with different number of sol-gel TiO$_2$ coating-cycles − 1 (a) and 5 (b). (i) and (iii) correspond to the samples processed without the SiO$_2$ interlayer; while, (ii) corresponds to those processed with the SiO$_2$ interlayer. The photocatalytic activity measurements are conducted in pure H$_2$O (i, ii) and ~1 M H$_2$O$_2$ (iii).

Since the conduction-band and valence-band energy levels of anatase-TiO$_2$ are higher and lower than those of (γ+α)-Fe$_2$O$_3$ respectively,[16] the photo-induced e$^-$/h$^+$ pairs

generated in the anatase-TiO_2 can easily escape into $(\gamma+\alpha)$-Fe_2O_3 nanoparticles and

get annihilated before they can produce the $^\bullet OH$ in the surrounding aqueous solution

which are responsible for the degradation of MB dye. As a result, for the anatase-

TiO_2-coated (cycle-1) $(\gamma+\alpha)$-Fe_2O_3 nano-composite particles, the concentration of $^\bullet OH$

produced is significantly lower as observed in Fig. 2.16a. Moreover, it is to be noted

that under an exposure to the UV-radiation, the photo-induced electrons in the

anatase-TiO_2 result in the formation of Fe^{2+} ions via the reduction of Fe^{3+} ions which

are already diffused into the anatase-TiO_2 lattice during the calcination treatment.
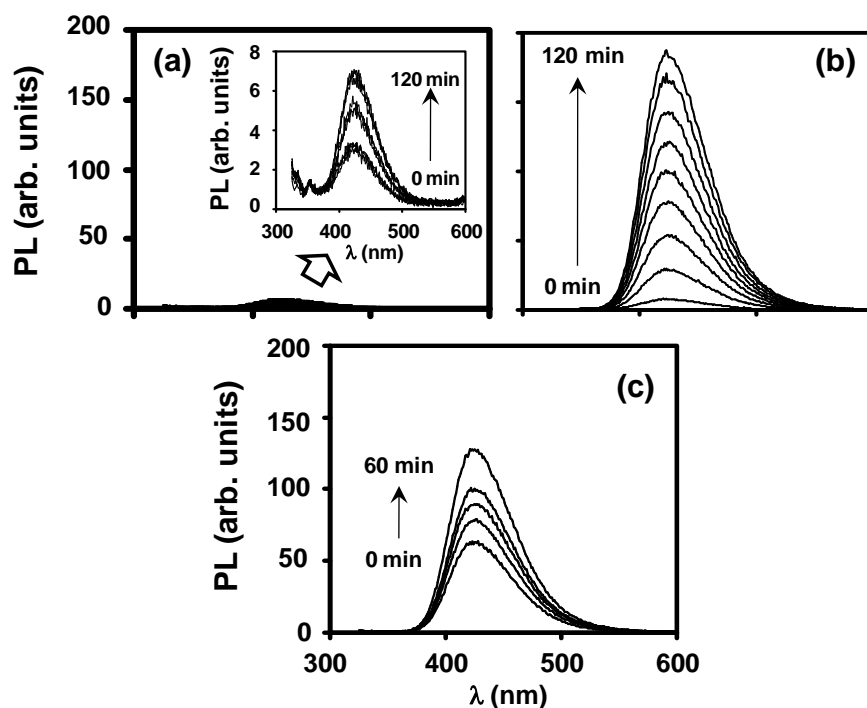
Fig. 2.16. Variation in the PL intensity associated with the formation of 2-hydroxyterphthalic acid as a function of UV-radiation exposure time as obtained for the anatase-TiO_2-coated (cycle-1) $(\gamma+\alpha)$-Fe_2O_3 (a,c) and γ-Fe_2O_3 (b) nano-composite particles. (a) and (c) correspond to the samples processed without the SiO_2 interlayer; while, (b) corresponds to the sample processed with the SiO_2 interlayer. The PL measurements are conducted in pure H_2O (a,b) and ~ 1 M H_2O_2 (c).

For the present sample, due to the smallest thickness of anatase-TiO_2 shell as obtained via a single sol-gel TiO_2 coating-cycle, the former is highly concentrated with the diffused Fe^{3+} cations after the calcination treatment at 600^oC for 2 h. Due to their larger size the Fe^{2+} ions, which are newly formed at the surface under the UV-radiation exposure, get immediately dissolved into the surrounding aqueous solution[6, 16] (termed here as the "photo-dissolution process"). The Fe^{2+} ions thus generated in an aqueous solution, however, can decrease the concentration of $^•OH$ produced via the following reaction [20-21].

$$Fe^{2+} + {}^•OH \rightarrow Fe^{3+} + OH^- \qquad (2.3)$$
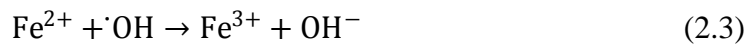
The amount of photo-dissolved Fe for the present sample is 0.89 ppm which is ~30 times larger than that (0.03 ppm) observed for the as-received γ-Fe_2O_3 nanoparticles. Hence, the photo-dissolved Fe^{2+} ions do play a major role in minimizing both the concentration of $^•OH$ produced by this sample, and hence, its photocatalytic activity, Fig. 2.15a.

In order to enhance the photocatalytic activity of anatase-TiO_2-coated (cycle-1) ($\gamma+\alpha$)-Fe_2O_3 nano-composite particles, two different approaches are investigated here. In the first approach, the amorphous-SiO_2 is introduced as an interlayer between the magnetic oxide core and the anatase-TiO_2 shell. Since the band-gap energy of amorphous-SiO_2 is larger (9.0 eV) with its conduction-band and valence-band energy levels above and below those of anatase-TiO_2,[32-33] it significantly hinders the transfer of photo-induced e^-/h^+ pairs from the anatase-TiO_2 to γ-Fe_2O_3. As a result, a drastic increase in the concentration of $^•OH$ produced is noted after the introduction of SiO_2 interlayer, Fig. 2.16b, due to the following redox reactions taking place on the surface

of nanocomposite particles with the corresponding increase in the dye-degradation

kinetics ($k_{app} = 0.02$ min^{-1}), Fig. 2.15a.[30]
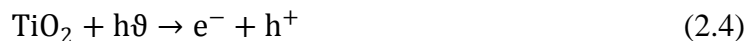
$$TiO_2 + h\vartheta \rightarrow e^- + h^+ \tag{2.4}$$

$$OH^- + h^+ \rightarrow {}^{\bullet}OH \tag{2.5}$$

$$O_2 + e^- \rightarrow O_2^- \tag{2.6}$$

$$2O_2^- + 2H^+ \rightarrow H_2O_2 + O_2 \tag{2.7}$$

$$H_2O_2 + e^- \rightarrow {}^{\bullet}OH + OH^- \tag{2.8}$$

The amount of photo-dissolved Fe, in the case of anatase-TiO$_2$-coated (cycle-1) SiO$_2$/γ-Fe$_2$O$_3$ nanoparticles, is measured to be 0.03 ppm which is equal to that obtained for the as-received γ-Fe$_2$O$_3$ nanoparticles. Hence, for the present sample, the effect of photo-dissolution of Fe^{2+} on the photocatalytic activity can be assumed to be minimum. The enhancement in the photocatalytic activity is, hence, attributed to the effect of interlayer SiO$_2$ in agreement with the several other reports in the literature which show an increase in the photocatalytic activity obtained via the introduction of SiO$_2$ as an interlayer between the magnetic oxide core and the photocatalyst shell. The SiO$_2$ interlayer avoids not only the diffusion of Fe^{3+} ions from the core to the shell during the calcination treatment but also the electronic interaction between the two during the measurement of photocatalytic activity under the UV-radiation exposure.[8-10,17,34] In support of this, the concentration of $^{\bullet}$OH produced by the anatase-TiO$_2$-coated (cycle-1) SiO$_2$/γ-Fe$_2$O$_3$ nanoparticles is noted to be higher and also to increase gradually with the UV-radiation exposure time, Fig. 2.16b.

In the second approach which is novel to enhance the photocatalytic activity of anatase-TiO_2-coated (cycle-1) ($\gamma+\alpha$)-Fe_2O_3 nano-composite particles, photocatalytic activity measurements are conducted in ~1 M H_2O_2 solution without the SiO_2 interlayer. It is well-known that the concentration of $^\bullet OH$ produced in an aqueous solution can be enhanced via the following "Fenton-reaction" even without an exposure to the external UV-radiation.[20-21]

$$Fe^{2+} + H_2O_2 \rightarrow Fe^{3+} + OH^- + {}^\bullet OH \qquad (2.9)$$
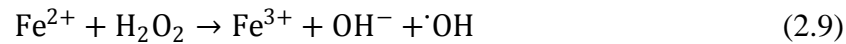
It appears that the addition of H_2O_2 to an aqueous solution is beneficial in increasing the concentration of $^\bullet OH$ produced during the simultaneous occurrence of photo-dissolution of Fe^{2+} ions under the UV-radiation exposure. As mentioned earlier, the amount of photo-dissolved Fe, in the case of anatase-TiO_2-coated (cycle-1) ($\gamma+\alpha$)-Fe_2O_3 nano-composite particles, is very high (0.89 ppm). Interestingly, the same sample exhibits very high MB dye degradation kinetics (k_{app}=0.023 min^{-1}) in ~1 M H_2O_2 solution which is comparable with that (k_{app}=0.02 min^{-1}) obtained in pure H_2O via the introduction of SiO_2 interlayer and significantly larger than that (k_{app}=0 min^{-1}) obtained in pure H_2O without the use of SiO_2 interlayer, Fig. 2.15a. In support of this, the concentration of $^\bullet OH$ produced is seen to increase gradually in the first 60 min of UV-radiation exposure time, Fig. 2.16c, for the anatase-TiO_2-coated (cycle-1) ($\gamma+\alpha$)-Fe_2O_3 nano-composite particles in ~1 M H_2O_2. However, it tends to decrease thereafter with further increase in the UV-radiation exposure time within the interval of 60-120 min (not shown in Fig. 6c for clarity) due to the consumption of $^\bullet OH$ produced as a result of their interaction with the Fe^{3+} cations and H_2O_2, Eqs. 2.3 and 3.10.

$$^\bullet OH + H_2O_2 \rightarrow {}^\bullet OOH + H_2O \qquad (2.10)$$

The nanocrystalline γ-Fe_2O_3 particles are ferrimagnetic with the saturation magnetization of 74 emu g^{-1} and α-Fe_2O_3 nanoparticles are ferromagnetic with the saturation magnetization of 0.57 emu g^{-1}.[7] As a result, the anatase-TiO_2-coated (cycle-1) $(\gamma+\alpha)$-Fe_2O_3 nano-composite particles, consisting of mixed γ-Fe_2O_3 and α-Fe_2O_3 as magnetic oxide core, could be quickly separated from an aqueous solution using a moderate external magnetic field as shown in the right-side inset of Fig. 2.15a.

Similar to the previous case, the photocatalytic activity measurements are also conducted using the anatase-TiO_2-coated (cycle-5) α-Fe_2O_3 or γ-Fe_2O_3 nano-composite particles, without and with the SiO_2 interlayer, in pure H_2O and ~1 M H_2O_2 solution. The corresponding photocatalytic activity graphs are presented in Fig. 2.15b. It is again noted that the dye-degradation kinetics (k_{app}=0.1 min^{-1}) obtained using the anatase-TiO_2-coated (cycle-5) α-Fe_2O_3 nano-composite particles in ~1 M H_2O_2 solution is comparable with that (k_{app}=0.13 min^{-1}) obtained in pure H_2O using the SiO_2 interlayer. Moreover, the use of ~1 M H_2O_2 solution is also seen to enhance significantly the photocatalytic activity of anatase-TiO_2-coated (cycle-5) α-Fe_2O_3 nano-composite particles relative to that (k_{app}=0.001 min^{-1}) obtained in pure H_2O. In this case well, although the Fenton-reaction, Eq. 2.9, is held responsible for an enhanced photocatalytic activity, it differs from the previous case in the manner it takes place under the UV-radiation exposure. For the present sample, the thickness of anatase-TiO_2 shell is relatively larger than that in the previous case due to the more number of sol-gel TiO_2 coating-cycles. Due to the increased diffusion distance, the amount of Fe-dissolved into the solution under the UV-radiation exposure is hence measured to be as low as 0.02 ppm. This suggests that for the present sample, the anatase-TiO_2 shell remains highly doped with Fe^{3+} ions during the photocatalytic

activity measurements. It is known that if the concentration of Fe^{3+} ions doped in the nanocrystalline anatase-TiO_2 is either below or above a critical value, then they act either as trapping or annihilating sites for the photo-induced e^-/h^+ pairs.[19] Lower photocatalytic activity of anatase-TiO_2-coated (cycle-5) α-Fe_2O_3 nano-composite particles as observed in pure H_2O, Fig. 2.15b, is hence contributed by the doped-Fe^{3+} ions which possibly act as annihilating centers for the photo-induced e^-/h^+ pairs. However, in the presence of ~1 M H_2O_2 in the surrounding medium, it appears that the same doped-Fe^{3+} cations, typically present at the surface, act as effective trapping sites and transfer the photo-induced electrons to H_2O_2 within the solution to produce large concentration of $^\bullet OH$, Eq. 2.9. The generated $^\bullet OH$ are then responsible for an enhanced photocatalytic activity of anatase-TiO_2-coated (cycle-5) α-Fe_2O_3 nano-composite particles. The dynamics in the variation of the concentration of $^\bullet OH$ produced, as observed earlier in Fig. 2.16a, is also noted for the present sample in pure H_2O and 1 M H_2O_2 solution, Fig. 2.17a and c. Since the Fe^{3+} diffusion into the anatase-TiO_2 is possible only without the SiO_2 interlayer, it appears that the oscillating variation in the concentration of $^\bullet OH$ produced, as observed for the two different samples processed without the SiO_2 interlayer, further supports the generation of $^\bullet OH$ via the Fenton-reaction either in the presence of photo-dissolution process or in the presence of Fe^{3+}/Fe^{2+} cations on the surface of nano-composite particles. As shown in the inset of Fig. 2.15b, the present sample could not be separated using an external magnetic field due to the presence of only α-Fe_2O_3 which has the minimum saturation magnetization.
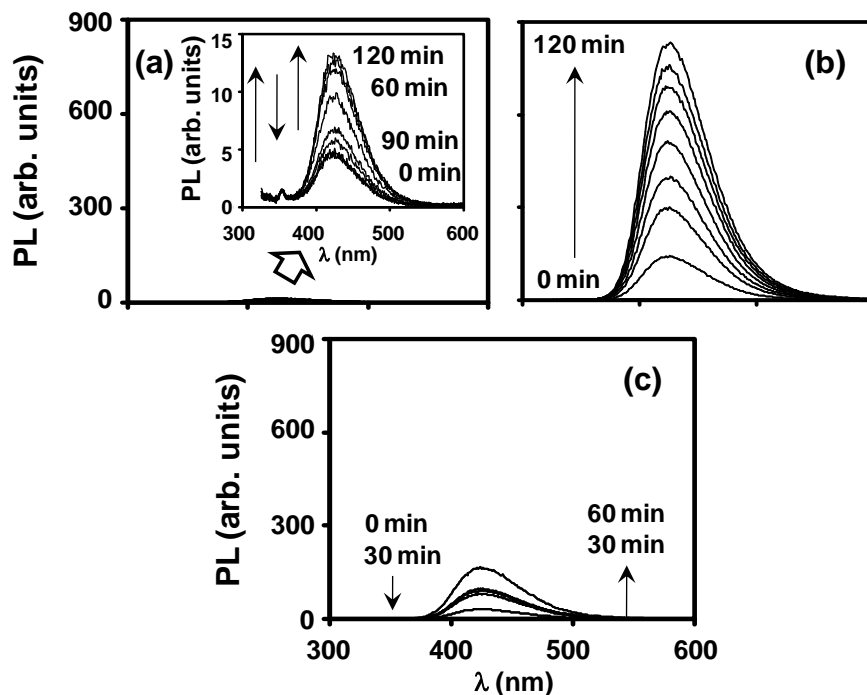
Fig. 2.17. Variation in the PL intensity associated with the formation of 2-hydroxyterephthalic acid as a function of UV-radiation exposure time as obtained for the anatase-TiO_2-coated (cycle-5) α-Fe_2O_3 (a,c) and γ-Fe_2O_3 (b) nano-composite particles. (a) and (c) correspond to the samples processed without the SiO_2 interlayer; while, (b) corresponds to the sample processed with the SiO_2 interlayer. The PL measurements are conducted in pure H_2O (a, b) and ~1 M H_2O_2 (c).

It is noted that the weight-fraction of anatase-TiO_2 is not same for a specific number of sol-gel TiO_2 coating-cycles (either 1 or 5) when a given amount of magnetic nano-composite particles are processed without and with the SiO_2 interlayer. The amount of anatase-TiO_2 in the shell is always higher when the magnetic photocatalyst is processed without the interlayer of SiO_2 compared with that processed with the interlayer of SiO_2. Nevertheless, in spite of higher amount of anatase-TiO_2 the photocatalytic activity of magnetic nano-composite, processed without the SiO_2 interlayer, is almost negligible in the absence of Fenton-reaction for both the number

of sol-gel TiO_2 coating-cycles, Fig. 2.15a and b. Hence, the difference in the weight-fraction of anatase-TiO_2 does not appear to be a critical factor in determining the observed difference in the photocatalytic activity under the given test-conditions. Since the main purpose here is to demonstrate the combined effect of photo-dissolution and Fenton-reaction, the effect of difference in the amount of anatase-TiO_2 within the shell of magnetic nano-composite particles, processed without and with the SiO_2 interlayer, has been neglected.

In addition to this, the concentration of H_2O_2 within the solution is also an important parameter which needs to be considered in further detail to understand precisely the combined effect of photo-dissolution and Fenton-reaction on the photocatalytic activity. It is anticipated that with the same amount of TiO_2, the photocatalytic activity would be relatively superior when the measurements are conducted in pure H_2O with the use of SiO_2 interlayer than those conducted in 3 wt.% H_2O_2 without the use of SiO_2 interlayer. However, the results may significantly differ if the concentration of H_2O_2 is increased above 3 wt%.

Overall, it is clearly shown here that the addition of H_2O_2 during the photocatalytic activity measurements of anatase-TiO_2-coated $(\gamma+\alpha)$-Fe_2O_3 or α-Fe_2O_3 magnetic nano-composite particles, under the UV-radiation exposure, is beneficial to utilize the photo-dissolution process as a source of Fe^{2+} ions within the solution leading to the large concentration of $^{\bullet}OH$ produced, and hence higher photocatalytic activity, via the Fenton-reaction which is an advanced oxidation process.[35-36] Thus, the present work when combined with the reports available in the literature would allow to increase the photocatalytic activity of anatase-TiO_2-coated $(\gamma+\alpha)$-Fe_2O_3 or α-Fe_2O_3 magnetic nano-composite particles, under the UV-radiation exposure, without and with the

occurrence of photo-dissolution phenomenon. In other words, the addition of H_2O_2 in the surrounding medium is a new alternative for the conventional use of SiO_2 interlayer.

2.4 Conclusions

When the magnetic photocatalyst is processed using the γ-Fe_2O_3 as a magnetic ceramic core, the SiO_2-coating as an interlayer between the anatase-TiO_2 shell and the γ-Fe_2O_3 magnetic ceramic core plays a crucial role in enhancing the concentration of free $^\bullet OH$ produced, their rate of formation, the thermal stability against the phase transformation of magnetic ceramic core, the efficiency of magnetic separation using a moderate external magnetic field, and the stability of magnetic ceramic core against the photo-dissolution under the UV-radiation exposure. As a result of the combined effect of all these factors, the best magnetic photocatalyst is observed to be the anatase-TiO_2-coated SiO_2/γ-Fe_2O_3 (cycle-5). The anatase-TiO_2-coated $(\gamma+\alpha)$-Fe_2O_3 and α-Fe_2O_3 nano-composites particles (magnetic and non-magnetic) exhibit very low photocatalytic activity under the UV-radiation exposure which has been contributed by either the photo-dissolution of Fe^{2+} ions into the solution or the doping of TiO_2 with Fe^{3+} ions in large concentration. Both of the latter effects reduce substantially the concentration of $^\bullet OH$ produced under the UV-radiation exposure, and hence, the photocatalytic activity. However, the addition of H_2O_2 to the surrounding aqueous medium significantly enhances the concentration of $^\bullet OH$ produced under the UV-radiation exposure, and hence the photocatalytic activity, via the advanced oxidation process involving the Fenton-reaction. Within the investigated range of experimental parameters, the photocatalytic activity is observed to be comparable with that obtained using the SiO_2 interlayer. Thus, the photo-dissolution process which severely

affects the photocatalytic activity in the absence of SiO_2 interlayer is beneficial in enhancing the same when combined with the Fenton-reaction.

References

1. Fujishima, A.; Rao, T. N.; Tryk, D. A., Titanium dioxide photocatalysis. *J. Photochem. Photobiol., C* **2000,** *1* (1), 1-21.

2. Kagaya, S.; Shimizu, K.; Arai, R.; Hasegawa, K., Separation of titanium dioxide photocatalyst in its aqueous suspensions by coagulation with basic aluminium chloride. *Water Res.* **1999,** *33* (7), 1753-1755.

3. Beydoun, D.; Amal, R.; Scott, J.; Low, G.; McEvoy, S., Studies on the mineralization and separation efficiencies of a magnetic photocatalyst. *Chem. Eng. Technol.* **2001,** *24* (7), 745-748.

4. Chen, F.; Zhao, J., Preparation and photocatalytic properties of a novel kind of loaded photocatalyst of $TiO_2/SiO_2/\gamma\text{-}Fe_2O_3$. *Catal. Lett.* **1999,** *58* (4), 246-247.

5. Chen, F.; Xie, Y.; Zhao, J.; Lu, G., Photocatalytic degradation of dyes on a magnetically separated photocatalyst under visible and UV irradiation. *Chemosphere* **2001,** *44* (5), 1159-1168.

6. Beydoun, D.; Amal, R.; Low, G.; McEvoy, S., Occurrence and prevention of photodissolution at the phase junction of magnetite and titanium dioxide. *J. Mol. Catal. A: Chem.* **2002,** *180* (1), 193-200.

7. Beydoun, D.; Amal, R., Implications of heat treatment on the properties of a magnetic iron oxide–titanium dioxide photocatalyst. *Mater. Sci. Eng., B* **2002,** *94* (1), 71-81.

8. Xu, M. W.; Bao, S. J.; Zhang, X. G., Enhanced photocatalytic activity of magnetic TiO_2 photocatalyst by silver deposition. *Mater. Lett.* **2005,** *59* (17), 2194-2198.

9. Song, X.; Gao, L., Fabrication of Bifunctional titania/silica-coated magnetic spheres and their photocatalytic activities. *J. Am. Ceram. Soc.* **2007,** *90* (12), 4015-4019.

10. Gad-Allah, T. A.; Kato, S.; Satokawa, S.; Kojima, T., Role of core diameter and silica content in photocatalytic activity of $TiO_2/SiO_2/Fe_3O_4$ composite. *Solid State Sci.* **2007,** *9* (8), 737-743.

11. Xiao, H. M.; Liu, X. M.; Fu, S. Y., Synthesis, magnetic and microwave absorbing properties of core-shell structured $MnFe_2O_4/TiO_2$ nanocomposites. *Compos. Sci. Technol.* **2006,** *66* (13), 2003-2008.

12. Rana, S.; Rawat, J.; Sorensson, M.; Misra, R., Antimicrobial function of Nd^{3+}-doped anatase titania-coated nickel ferrite composite nanoparticles: a biomaterial system. *Acta Biomater.* **2006,** *2* (4), 421-432.

13. Lee, S.W.; Drwiega, J.; Mazyck, D.; Wu, C.-Y.; Sigmund, W. M., Synthesis and characterization of hard magnetic composite photocatalyst—Barium ferrite/silica/titania. *Mater. Chem. Phys.* **2006,** *96* (2), 483-488.

14. Thazhe, L.; Shereef, A.; Shukla, S.; Pattelath Reshmi, C.; Varma, M. R.; Suresh, K. G.; Patil, K.; Warrier, K. G., Magnetic dye-adsorbent catalyst: processing, characterization, and application. *J. Am. Ceram. Soc.* **2010,** *93* (11), 3642-3650.

15. Jiang, J.; Gao, Q.; Chen, Z.; Hu, J.; Wu, C., Syntheses, characterization and properties of novel nanostructures consisting of Ni/titanate and Ni/titania. *Mater. Lett.* **2006,** *60* (29), 3803-3808.

16.   Beydoun, D.; Amal, R.; Low, G. K. C.; McEvoy, S., Novel photocatalyst: titania-coated magnetite. activity and photodissolution. *J. Phys. Chem. B* **2000,** *104* (18), 4387-4396.

17.   Watson, S.; Beydoun, D.; Amal, R., Synthesis of a novel magnetic photocatalyst by direct deposition of nanosized TiO$_2$ crystals onto a magnetic core. *J. Photochem. Photobiol., A* **2002,** *148* (1), 303-313.

18.   Gao, Y.; Chen, B.; Li, H.; Ma, Y., Preparation and characterization of a magnetically separated photocatalyst and its catalytic properties. *Mater. Chem. Phys.* **2003,** *80* (1), 348-355.

19.   Zhang, Z.; Wang, C. C.; Zakaria, R.; Ying, J. Y., Role of particle size in nanocrystalline TiO$_2$-based photocatalysts. *J. Phys. Chem. B* **1998,** *102* (52), 10871-10878.

20.   Cruz-Gonzalez, K.; Torres-Lopez, O.; Garcia-Leon, A.; Guzman-Mar, J.; Reyes, L.; Hernandez-Ramirez, A.; Peralta-Hernandez, J., Determination of optimum operating parameters for Acid Yellow 36 decolorization by electro-Fenton process using BDD cathode. *Chem. Eng. J.* **2010,** *160* (1), 199-206.

21.   Jeong, J.; Yoon, J., pH effect on OH radical production in photo/ferrioxalate system. *Water Res.* **2005,** *39* (13), 2893-2900.

22.   Deng, Y. H.; Wang, C. C.; Hu, J. H.; Yang, W. L.; Fu, S. K., Investigation of formation of silica-coated magnetite nanoparticles via sol–gel approach. *Colloids Surf., A* **2005,** *262* (1), 87-93.

23.   Ishibashi, K. I.; Fujishima, A.; Watanabe, T.; Hashimoto, K., Quantum yields of active oxidative species formed on TiO$_2$ photocatalyst. *J. Photochem. Photobiol., A* **2000,** *134* (1), 139-142.

24.   Xiao, Q.; Ouyang, L., Photocatalytic activity and hydroxyl radical formation of carbon-doped TiO_2 nanocrystalline: effect of calcination temperature. *Chem. Eng. J.* **2009,** *148* (2), 248-253.

25.   Hirakawa, T.; Nosaka, Y., Properties of O^{2-} and ·OH formed in TiO_2 aqueous suspensions by photocatalytic reaction and the influence of H_2O_2 and some ions. *Langmuir* **2002,** *18* (8), 3247-3254.

26.   Xu, S.; Shangguan, W.; Yuan, J.; Shi, J.; Chen, M., Preparations and photocatalytic degradation of methyl orange in water on magnetically separable $Bi_{12}TiO_2$ supported on nickel ferrite. *Sci. Technol. Adv. Mater.* **2007,** *8* (1), 40-46.

27.   Nasrazadani, S.; Raman, A., The application of infrared spectroscopy to the study of rust systems—II. Study of cation deficiency in magnetite (Fe_3O_4) produced during its transformation to maghemite (γ-Fe_2O_3) and hematite (α- Fe_2O_3). *Corros. Sci.* **1993,** *34* (8), 1355-1365.

28.   Okada, I.; Ozaki, M.; Matijevic, E., Magnetic interactions between platelet-type colloidal particles. *J. Colloid Interface Sci.* **1991,** *142* (1), 251-256.

29.   Lagoeiro, L., Transformation of magnetite to hematite and its influence on the dissolution of iron oxide minerals. *J. Metamorph. Geol.* **1998,** *16* (3), 415-423.

30.   Baiju, K.; Shukla, S.; Sandhya, K.; James, J.; Warrier, K., Photocatalytic activity of sol-gel-derived nanocrystalline titania. *J. Phys. Chem. C* **2007,** *111* (21), 7612-7622.

31.   Sadasivan, S.; Dubey, A. K.; Li, Y.; Rasmussen, D. H., Alcoholic solvent effect on silica synthesis—NMR and DLS investigation. *J. Sol-Gel Sci. Technol.* **1998,** *12* (1), 5-14.

32.　　Zhang, X.; Yang, H.; Zhang, F.; Chan, K. Y., Preparation and characterization of Pt–TiO_2–SiO_2 mesoporous materials and visible-light photocatalytic performance. *Mater. Lett.* **2007,** *61* (11), 2231-2234.

33.　　Cho, K.; Chang, H.; Park, J. H.; Kim, B. G.; Jang, H. D., Effect of molar ratio of TiO_2/SiO_2 on the properties of particles synthesized by flame spray pyrolysis. *J. Ind. Eng. Chem.* **2008,** *14* (6), 860-863.

34.　　Watson, S.; Scott, J.; Beydoun, D.; Amal, R., Studies on the preparation of magnetic photocatalysts. *J. Nanopart. Res.* **2005,** *7* (6), 691-705.

35.　　Munter, R., Advanced oxidation processes–current status and prospects. *Proc. Estonian Acad. Sci. Chem* **2001,** *50* (2), 59-80.

36.　　Zazo, J.; Casas, J.; Mohedano, A.; Gilarranz, M.; Rodriguez, J., Chemical pathway and kinetics of phenol oxidation by Fenton's reagent. *Environ. Sci. Technol.* **2005,** *39* (23), 9295-9302.

Chapter 3

Synthesis of Hydrogen Titanate Nanotubes via Hydrothermal and Their Dye Adsorption Properties

Graphical Abstract
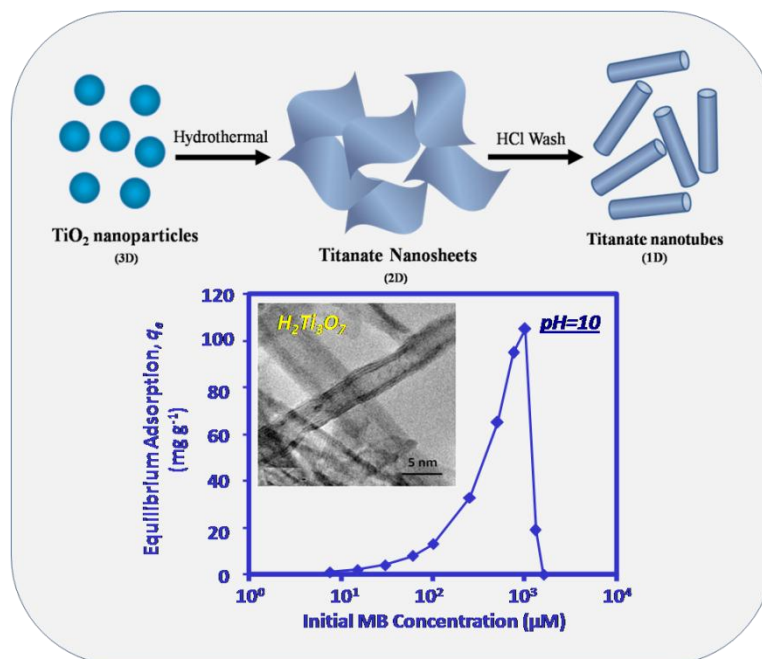
Highlights

- Hydrogen titanate nanotubes (HTN) of high surface area are synthesized via hydrothermal method.

- HTN exhibit MB adsorption capacity of 105 mg g^{-1}.

- MB adsorption on HTN follows pseudo-second-order kinetics and Langmuir /DKR isotherm models depending on the initial solution-pH.

Abstract

Hydrothermally processed hydrogen titanate nanotubes (HTN) have been utilized for the removal of MB dye from an aqueous solution via surface-adsorption mechanism. The HTN have been characterized using different analytical techniques such as the scanning electron microscope (SEM), transmission electron microscope (TEM), selected-area electron diffraction (SAED), X-ray diffraction (XRD), and Brunauer-Emmett-Teller (BET) specific surface-area measurement techniques. The amount of MB dye adsorbed on the surface of HTN at equilibrium (q_e) has been examined as a function of contact time, initial dye-concentration, and initial solution-pH. A new model has been proposed to explain the observed variation in q_e as a function of above variables. Within the investigated range of initial solution-pH (2.5-11), the MB adsorption on the surface of HTN has been observed to follow the pseudo-second-order kinetics with the dye-adsorption capacity of 105 mg g^{-1} observed at the initial solution-pH of ~10. The adsorption equilibrium follows the Langmuir isotherm in a highly acidic solution (initial solution-pH~2.5) and Dubinin-Kaganer-Radushkevich (DKR) isotherm in a highly basic solution (initial solution-pH~11); while, within the intermediate range of initial solution-pH (~7.5 and 10), it exhibits a transition from the Langmuir to DKR isotherm.

3.1. Introduction

Industrial wastewater containing organic synthetic-dyes present a serious environmental problem due to their high toxicity which leads to ground-water and surface-water pollution. The discharge of colored effluents into water bodies affects the sunlight penetration and oxygen solubility which decrease the photosynthesis activity and life-sustainability. Moreover, due to their strong color even at lower concentrations, organic synthetic-dyes cause serious aesthetic problems in the wastewater disposal. Therefore, the removal of organic synthetic-dyes from the industry effluents is of prime importance. Photocatalysis using the nanocrystalline semiconductor TiO_2 has been explored for the removal of organic synthetic-dyes from the industry wastewater.[1] In this technique, the nanocrystalline particles of TiO_2 are suspended in an aqueous solution containing a dye and exposed to the external-radiation generating the electron/hole (e^-/h^+) pairs within the particle volume. These e^-/h^+ pairs in turn form the $^\bullet OH$ radicals on the particle surface, which attack the surface-adsorbed dye molecules degrading them into non-toxic species. The photocatalysis process, however, suffers from major drawbacks such as the limited surface-adsorption of dye molecules, requirement of exposure to the external-radiation, doping of foreign elements to reduce the band-gap energy, aggregation of nanoparticles which affects their specific surface-area, and need for the development of magnetic photocatalyst to overcome the difficulties in the separation of photocatalyst from the treated effluent at the end of the photocatalysis process as demonstrated in the Chapter-2.

As an alternative, the removal of organic synthetic-dyes via the surface-adsorption mechanism in the dark-condition (that is, without any exposure to the external-

radiation) have been reported. Various adsorbents including zeolite,[2] flyash,[3] activated carbon,[4] orange peel,[5] rice husk,[6] pillard clays,[7] perlite,[8] and coconut shell[9] has been investigated for this purpose. Recently, the nanotubes of anatase-TiO_2 and hydrogen titanate (HTN, $H_2Ti_3O_7$) have also been reported to be suitable for this application.[10-17] However, there are only few reports in the literature investigating the dye-adsorption characteristics of these nanotubes as a function of initial solution-pH.[14] Moreover, the effect of initial solution-pH on the adsorption kinetics and equilibrium isotherm has not been investigated so far for the HTN. To clarify this further, in this investigation, we process the $H_2Ti_3O_7$ nanotubes and systematically study their dye-adsorption properties as a function of initial solution-pH. The obtained results have been explained using a new model proposed here.

3.2. Experimental

3.2.1. Chemicals

Sodium hydroxide (NaOH, Assay 97 %) and methylene blue (MB, >96 %) were purchased from S.D. Fine-Chem Limited, India; hydrochloric acid (HCl, 35 wt.%) from Ranbaxy Fine-Chemicals, India; ammonium hydroxide (NH_4OH, 25 wt.%) from Fisher Scientific, India; and anatase-TiO_2 from the Central Drug House (CDH) Laboratory (P) Limited, India. All chemicals and powders were used as-received without any further purification.

3.2.2. Synthesis of HTN

3 g of as-received anatase-TiO_2 was suspended in a highly alkaline aqueous solution, containing 10 M NaOH, filled up to 84 vol% of a Teflon-beaker placed in a stainless-steel (SS 316) vessel of 200 ml capacity. The process was carried out with continuous

stirring in an autoclave (Amar Equipment Pvt. Ltd., Mumbai, India) at 120^oC for 30 h

under an autogenous pressure. The autoclave was allowed to cool naturally to room

temperature and the hydrothermal product was separated by decanting the top

solution. The product was washed using 100 ml of 1 M HCl solution for 1 h followed

by washing using 100 ml of pure distilled water for 1 h. The product obtained was

then subjected to another washing-cycle consisting washing using 100 ml of 1 M HCl

for 1 h and then multiple times (#8-9) using 100 ml of pure distilled water for 1 h till

pH (Hanna HI 2210 Bench Top, Sigma-Aldrich, India) of the filtrate became almost

constant or neutral. The washed-product was then separated from the solution using a

centrifuge and dried in an oven at 800^oC overnight (termed as the final hydrothermal

product).

3.2.3. Characterizations

The morphology of the final hydrothermal product was examined using the scanning

electron microscope (SEM, JEOL JSM-5600LV, Japan) operated at 15 kV and

transmission electron microscope (TEM, Tecnai G2, FEI, The Netherlands) operated

at 300 kV. The selected-area electron diffraction (SAED) patterns were obtained to

confirm the crystallinity and structure of the final hydrothermal product. The

crystalline phases present were determined using the X-ray diffraction (XRD,

PW1710 Phillips, The Netherlands). The broad-scan analysis was typically conducted

within the 2-θ range of 10-80° using the Cu Kα (λCu=1.542 Å) X-radiation. The

specific surface-area was measured using the Brunauer-Emmett-Teller (BET) specific

surface-area measurement technique (Micrometrics Gemini 2375 Surface Area

Analyzer, U.S.A.) via nitrogen (N_2) adsorption, using the multi-point method, after

degassing the powder in flowing N_2 at 200°C for 2 h.

3.2.4. Adsorption measurements

The dye-adsorption experiments in the dark were conducted using the MB as a model catalytic dye-agent. 7.5-1300 μM of MB dye was dissolved in an aqueous solution, having an initial solution-pH within the range of 2.5-11 adjusted using the HCl and NH_4OH solutions, to prepare total 125 ml dye solution. 2.4 g l^{-1} of HTN (final hydrothermal product) was then dispersed in this solution and the resulting suspension was stirred continuously in the dark for 180 min using a magnetic stirrer (C MAG HS 7, IKA, Germany). 8 ml aliquot was separated after each 10 or 30 min time interval for obtaining the absorption spectra, using the ultraviolet (UV)-visible absorption spectrophotometer (UV-2401 PC, Shimadzu, Japan), of the filtrate obtained after separating HTN using the centrifuge. The normalized concentration of the surface-adsorbed MB dye was calculated using the equation of the form,

$$\%MB_{adsorbed} \ = \left(\frac{C_0 - C_t}{C_o}\right)_{MB} \times 100 \qquad\qquad (3.1)$$

which is equivalent of the form,

$$\%MB_{adsorbed} \ = \left(\frac{A_o - A_t}{A_o}\right)_{MB} \times 100 \qquad\qquad (3.2)$$

where, C_0 (mg l^{-1}) and C_t (mg l^{-1}) correspond to the MB dye concentration at the start and after stirring time t (min) with the corresponding absorbance of A_0 and A_t.

Results and discussion

3.3.1. Morphological, structural and surface characteristics of HTN

The SEM image of the final hydrothermal product is presented in Fig. 3.1a, where highly porous morphology of aggregated nanofibers is observed. The fiber diameter is measured to be ~50-100 nm.
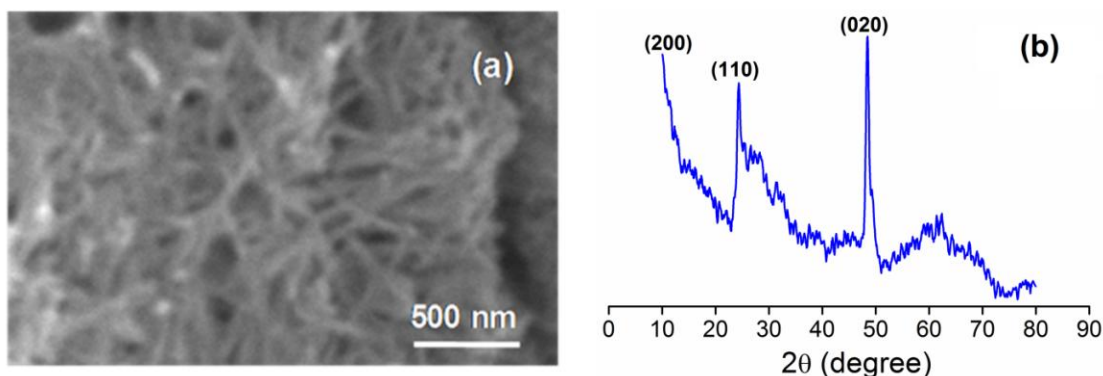
Fig. 3.1. SEM image (a) and XRD pattern (b) obtained using the final hydrothermal product.

The powder XRD pattern of this product is presented in Fig. 3.1b, which suggests its crystalline nature. The XRD peaks have been indexed according to those of HTN.[12] The TEM images of the final hydrothermal product are shown in Fig. 3.2 at different magnifications. It appears that the nanofiber morphology observed in Fig. 3.1a consists of nanotubes of average length, internal and outer diameters, and wall-thickness of 100, 2.3, 4.2, and 0.96 nm respectively.

The SAED pattern as obtained using the final hydrothermal product is presented in Fig. 3.2a as an inset. The SAED pattern confirms the crystalline nature of the product

and has been indexed as HTN,[10-18] also in accordance with the XRD pattern obtained here.
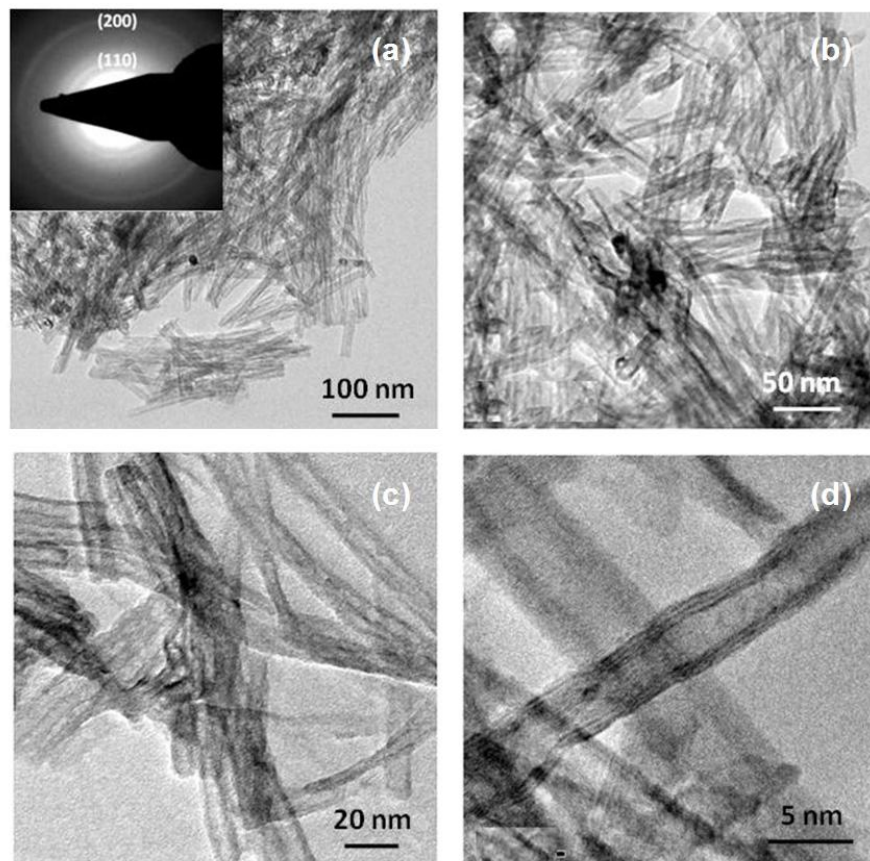
Fig. 3.2. TEM images obtained using the final hydrothermal product at different magnifications. The SAED pattern is shown as an inset in (a).

The N_2 adsorption/desorption isotherms obtained using HTN are presented in Fig. 3.3a. The isotherms exhibit typical hysteresis behavior of type H3 (at $P/P_0>0.6$) indicating the mesoporous nature of HTN. The observed hysteresis is extended to $P/P_0\approx0.9$, which suggests the presence of long unfilled pores.[10,19] The BET analysis shows that HTN have a specific surface-area as high as 330 m^2g^{-1}.Considering the nanotube morphology of the final product, it appears that these mesopores possibly correspond to the internal pores of HTN and the pore size is equal to the average

internal diameter of nanotubes, which is measured to be ~2.3 nm from the TEM image, Fig. 3.2d. The pore-size distribution curve (Barret-Joyner-Halenda (BJH) plot) obtained using the HTN is presented in Fig. 3.3b. The graph shows a plateau at ~2.5 nm which is comparable with the measured internal diameter of HTN. A small peak is also seen at ~4.5 nm which suggests HTN having slightly higher internal diameter. A larger peak is likely to be present close to ~20 nm which corresponds to the intra-aggregate porosity of HTN which is clearly observed in Fig. 3.2b and c. Overall, the above results suggest that the final hydrothermal product consists of high surface-area HTN which are aggregated into mesoporous powder.
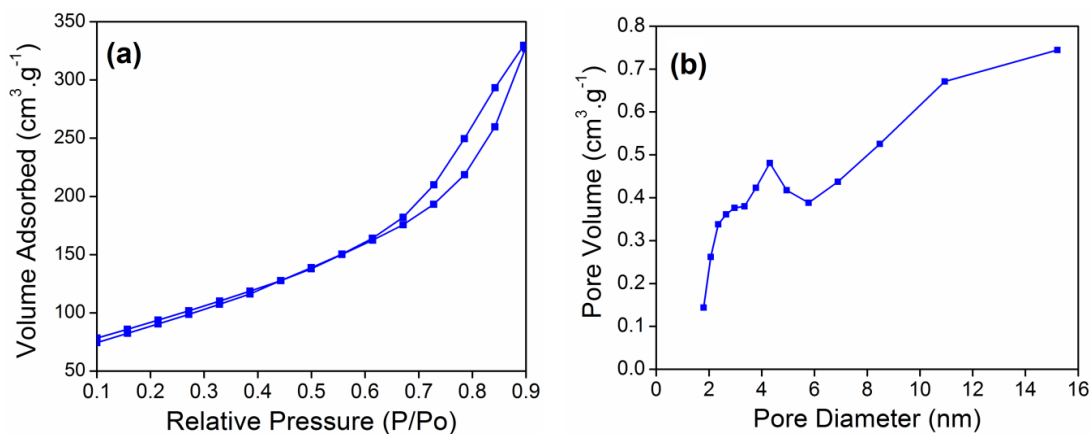
Fig. 3.3. The N_2 adsorption/desorption isotherms (a) and BJH pore-size distribution curve (b) obtained using the HTN.

3.3.2. Adsorptive removal of MB and kinetic-isotherm studies

The variations in the normalized concentration of MB dye adsorbed on the surface of HTN as a function of contact time, obtained for different initial MB dye concentrations and initial solution-pH, are presented in Fig. 3.4. It is observed that the normalized concentration of MB dye adsorbed on the surface of HTN increases rapidly within first 10 min of contact time and then tends to attain an equilibrium with

increasing contact time. For the initial solution-pH within the range of 2.5-10, the

normalized concentration of MB dye adsorbed at equilibrium on the surface of HTN

reaches almost 100% at the lowest initial MB dye concentration and decreases with

increase in the latter, Fig. 3.4a-c. Comparison however shows that the trend is

reversed in a highly basic solution (pH~11), Fig. 3.4d. Under this condition, the

normalized concentration of MB dye adsorbed at equilibrium increases with the initial

MB dye concentration within the range of 7.5-100 μM. Above this range, the

normalized concentration of MB dye adsorbed at equilibrium is noted to decrease.

This reverse trend observed in a highly basic solution has been explained using the

model proposed here later.

The adsorption data presented in Fig. 3.4 is utilized to calculate the amount of MB

dye adsorbed on the surface at equilibrium per unit mass of HTN, q_e (mg g^{-1}), using

the equation of the form,[20]

$$q_e = \frac{(C_o - C_e) \times V}{m_{HTN}} \qquad (3.3)$$

where, C_e (mg l^{-1}) is the MB dye concentration within the solution at equilibrium (that

is, after the contact time of 180 min), V (l) the initial volume of MB dye solution, and

m_{HTN} (g) the amount of HTN used as a dye-adsorbent. The obtained variation in q_e as a

function of initial MB dye concentration is presented in Fig. 3.5 for different initial

solution-pH values.
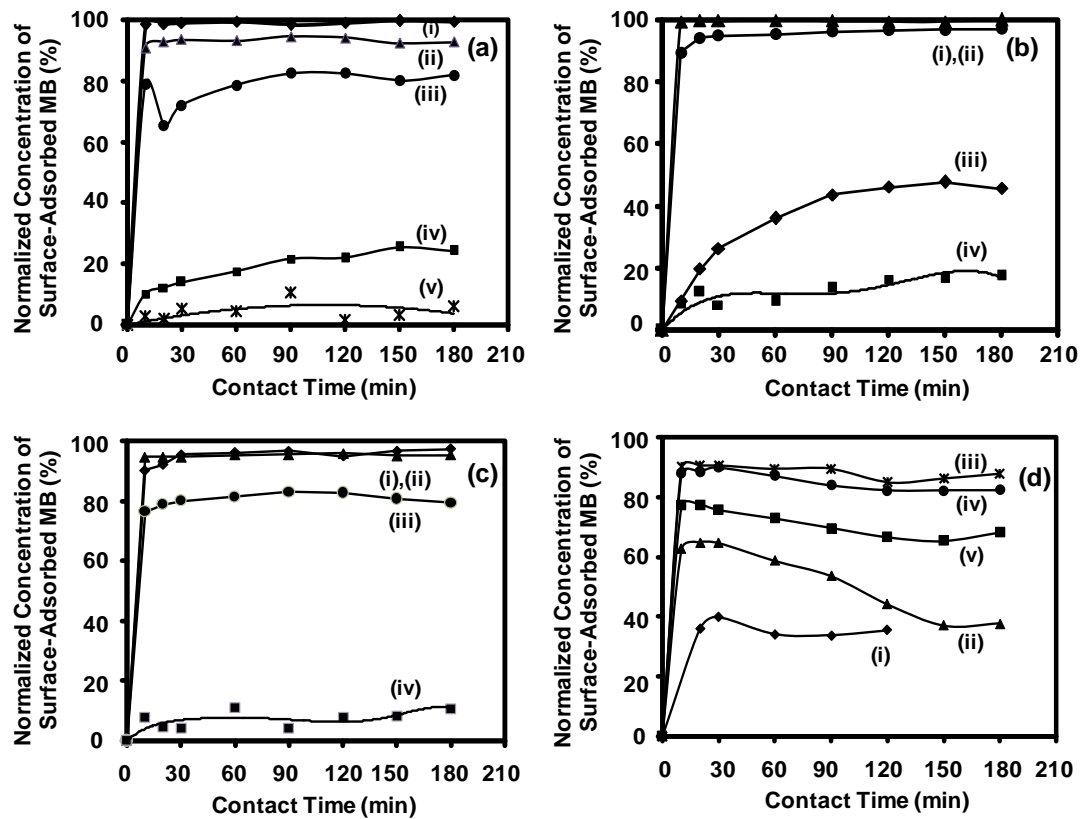
Fig. 3.4. Typical variations in the normalized concentration of surface-adsorbed MB as a function of contact time obtained using the HTN for different initial solution-pH: 2.5 (a), 7.5 (b), 10 (c), and 11 (d). In (a), the initial MB dye concentration is varied as 7.5 (i), 60 (ii), 100 (iii), 250 (iv) and 500 (v) µM; in (b), 30 (i), 250 (ii), 500 (iii), and 750 µM (iv); in (c), 7.5 (i), 750 (ii), 1000 (iii), and 1300 (iv) µM; and in (d), 15 (i), 30 (ii), 100 (iii), 250 (iv), and 750 (v) µM. (Note: For clarity, the graphs are shown only for the selected initial MB dye concentrations).

It is noted that at a given initial solution-pH, q_e increases with the initial MB dye concentration, reaches a maximum value (q_m (mg g^{-1})), termed here as a maximum dye-adsorbed at equilibrium per unit mass of HTN corresponding to a monolayer coverage for a given initial solution-pH, and then decreases with further increase in the initial MB dye concentration. It is also noted that q_m increases within the initial solution-pH range of 2.5-10, reaches the largest value (termed here as the dye-

adsorption capacity of HTN) at the initial solution-pH of 10, and then decreases in a highly basic solution. Interestingly, slight delay in increase in the slope of the graph is noted at lower initial MB dye concentrations for the highest initial solution-pH of 11, Fig. 3.5d. It appears that the initial solution-pH has a significant effect on q_m, and as a result, the dye-adsorption capacity of HTN is noted to be 105 mg g^{-1} at the initial solution-pH of 10 which is comparable with that of 133 mg g^{-1} as reported for HTN by others.[15] The recycling of HTN via photocatalytic dye-degradation has also been demonstrated which suggests their catalytic nature.[17]
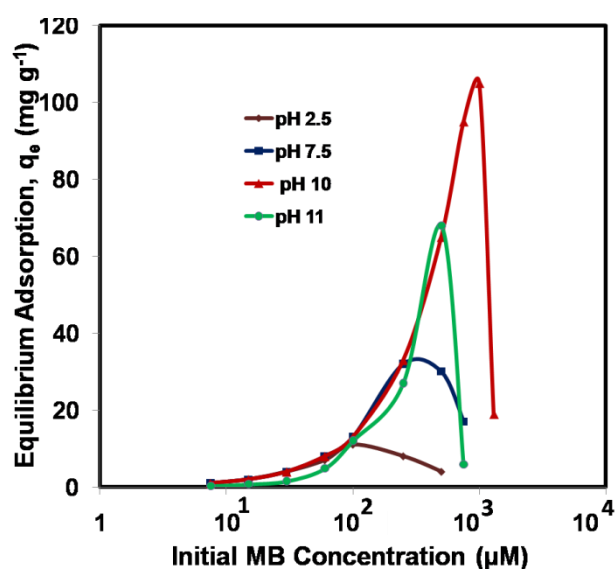
Fig. 3.5. Variation in q_e as a function of initial MB dye concentration for different initial solution-pH: 2.5, 7.5, 10 and 11.

The observed variation in q_e and q_m as a function of initial MB dye concentration and initial solution-pH can be explained using the model proposed in Fig. 3.6. It is to be noted that, as described in the experimental section, the HTN are added to the solution having a definite initial MB dye concentration and initial-pH. Accordingly, following assumptions have been made in the proposed model. It is assumed that the adsorption

of OH⁻ ions from an aqueous solution provides a negative charge on the surface of HTN which electrostatically attracts the cationic MB dye molecules resulting in the dye-adsorption.[21] The maximum number of potential surface-sites available for the dye-adsorption is a function of both the initial solution-pH and mutual interaction between the cationic MB dye molecules and OH⁻ ions within the solution. When the concentration of either MB dye or OH⁻ ions within the solution is very high, then their mutual interaction within the solution strongly affects the surface-adsorption of other specie.

In Fig. 3.6a, the adsorption of MB dye on the surface of HTN is considered as resembling the conditions existing at the lowest initial solution-pH (~2.5). Under this condition, the surface of HTN is relatively less negatively charged and provides minimum number of potential sites for the MB dye adsorption. At the beginning, the concentration of MB dye is also very low and only fraction of the total number of potential sites on the surface of HTN are occupied by the MB dye. With increasing initial MB dye concentration, more number of dye molecules is adsorbed which increases q_e. At a particular initial MB dye concentration, nearly all potential sites are occupied by the MB dye molecules. This situation corresponds to q_m as observed in Fig. 3.5. If the initial MB dye concentration is increased further, q_e is noted to decrease. According to the present model, at higher initial MB dye concentrations, the interaction between the cationic MB dye molecules and OH⁻ ions within the solution becomes stronger which reduces the adsorption of latter on the surface of HTN, Fig. 3.6a. This in turn reduces both the amount of negative surface-charge and MB dye adsorbed on the surface of HTN.
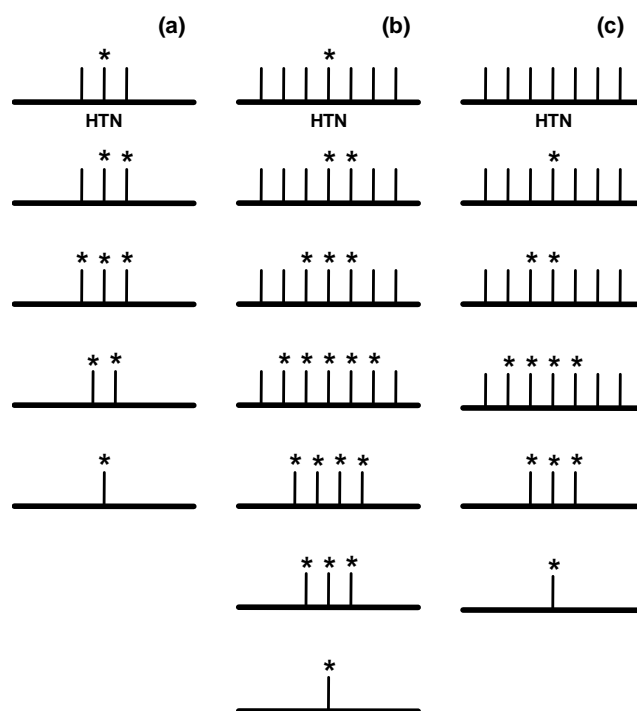
Fig. 3.6. A model proposed to explain the nature of graphs presented in Fig. 3.5a-c represent the hypothetical conditions at the initial solution-pH of 2.5, 7.5-10, and 11 respectively. The vertical lines and ∗ represent the potential sites on the surface of HTN available for dye-adsorption and the MB dye molecule. The initial MB dye concentration increases from top to bottom at a given initial solution-pH.

Similar situation also exists at relatively higher initial solution-pH, Fig. 3.6b, which resembles the conditions existing at the initial solution-pH of ~7.5 and 10. In Fig. 3.6b, initially the surface of HTN is shown to possess relatively more number of potential surface-sites for the MB dye adsorption, which increases q_e, q_m, and the initial MB dye concentration associated with the latter. Surprisingly, the trend is reversed in a highly basic solution (pH~11), where q_m is noted to decrease suddenly. According to the present model, under the highly basic condition, excess OH⁻ ions remain in the solution after their adsorption on the surface of HTN up to the full capacity, Fig. 3.6c. These excess OH⁻ ions within the solution interact with the MB

dye and reduce its effective concentration available for the surface-adsorption, which in turn reduces both q_e and q_m. This also explains the reverse trend as observed in Fig. 3.4d and slight delay in increase in the slope of the graph for pH 11 (Fig. 3.5).

The rate at which the MB dye is adsorbed from an aqueous solution on the surface of HTN is analyzed using three different kinetics models: Lagergren pseudo-first-order, pseudo-second-order, and intra-particle diffusion.[3,20] The adsorption data presented in Fig. 3.4 is utilized to fit the above kinetics models at different initial solution-pH and the values of different parameters derived from the slopes and intercepts of the best-fitted straight-lines, Fig. 3.7, are tabulated in Tables 3.1-3.4.

Table 3.1. Kinetics constants for MB adsorption on the surface of HTN at the initial solution-pH of 2.5.

MB (μM)	q_e (Exp)	Pseudo First-Order			Pseudo-Second-Order			Pseudo Second-Order		
		q_e (mg g^{-1})	k_1 (min^{-1})	r^2	q_e (mg g^{-1})	k_2 (mg g^{-1} min^{-1})	r^2	k_{id} (mg g^{-1} min$^{-0.5}$)	C (mg g^{-1})	r^2
7.5	1	0.034	0.018	0.199	0.99	5.34	0.999	0	0.982	0.341
15	2	0.061	0.016	0.191	1.98	1.13	0.999	0	1.961	0.02
30	4	0.17	0.031	0.564	3.95	1.49	1.000	0	3.972	0.074
60	7	0.31	0.016	0.168	7.5	-0.46	0.999	0.009	7.351	0.144
100	11	2.27	0.016	0.470	11.1	0.03	0.998	0.141	9.165	0.446
250	8	6.38	0.018	0.959	9.4	0.004	0.987	0.501	1.936	0.970
500	4	1.92	0	0.001	2.6	0.045	0.438	0.122	1.990	0.060

Table 3.2. Kinetics constants for MB adsorption on the surface of HTN at the initial solution-pH of 7.5.

MB] (µM)	q_e (Exp)	Pseudo-First-Order			Pseudo-Second-Order			Intra-Particle Diffusion		
		q_e (mg g^{-1})	k_1 (min^{-1})	r^2	q_e (mg g^{-1})	k_2 (mg g^{-1} min^{-1})	r^2	k_{id} (mg g^{-1} min$^{-0.5}$)	C (mg g^{-1})	r^2
7.5	1	0.0001	0.044	0.071	0.94	143	0.999	0.003	0.97	0.284
15	2	0.09	0.016	0.197	1.97	-	0.999	0	1.97	0.001
30	4	0.07	0.014	0.137	3.98	4.9	1	0	3.97	0.074
60	8	0.17	0.018	0.281	8	1.56	1	0.003	7.93	0.523
100	13	0.16	0.025	0.319	13.3	5.63	1	0.003	13.2	0.379
250	32	4.51	0.030	0.767	33.3	0.031	1	0.183	30.1	0.714
500	30	34	0.032	0.974	40	0.001	0.983	2.4	2.77	0.901
750	17	14.5	0.016	0.853	20.9	0.001	0.917	0.892	5.23	0.766

Table 3.3. Kinetics constants for MB adsorption on the surface of HTN at the initial solution-pH of 10.

MB (µM)	q_e (Exp)	Pseudo-First-Order			Pseudo-Second-Order			Intra-Particle Diffusion		
		q_e (mg g^{-1})	k_1 (min^{-1})	r^2	q_e (mg g^{-1})	k_2 (mg g^{-1} min^{-1})	r^2	k_{id} (mg g^{-1} min$^{-0.5}$)	C (mg g^{-1})	r^2
7.5	1	0.11	0.02	0.525	0.97	1.11	0.999	0.050	0.90	0.667
15	2	0.18	0.06	0.374	1.99	1.72	0.999	0.004	1.94	0.657
30	4	0.14	0.02	0.354	3.98	1.80	1.000	0.003	3.93	0.430
60	8	0.16	0.03	0.159	7.87	0.77	1.000	0.002	7.80	0.194
100	13	0.36	0.02	0.231	13.3	-0.70	1.000	-0.001	13.27	0.065
250	33	0.77	0.01	0.184	33.3	0.22	1.000	0.011	32.65	0.136
500	65	1.20	0.02	0.149	66.7	0.22	1.000	0.028	64.75	0.336
750	95	0.48	0.004	0.083	100	---	1.000	0.081	94.24	0.532
1000	105	82.41	0.26	0.973	111	---	0.999	0.430	103.2	0.302
1300	19	11.94	0.005	0.397	18	0.002	0.677	0.586	7.80	0.215

Table 3.4. Kinetics constants for MB adsorption on the surface of HTN at the initial solution-pH of 11.

MB (μM)	q_e (Exp)	Pseudo-First-Order			Pseudo-Second-Order			Intra-Particle Diffusion		
		q_e (mg g^{-1})	k_1 (min^{-1})	r^2	q_e (mg g^{-1})	k_2 (mg g^{-1} min^{-1})	r^2	k_{id} (mg g^{-1} min$^{-0.5}$)	C (mg g$^-$)	r^2
7.5	0.26	---	---	---	0.3	-0.24	0.856	-.004	0.45	0.020
15	0.7	0.55	0.034	0.859	0.7	0.51	0.996	-0.063	1.27	0.433
30	1.5	---	---	---	1.4	-0.05	0.977	-0.118	3.11	0.902
60	4.8	---	---	---	4.6	-0.03	0.993	-0.223	7.53	0.931
100	12	11.3	0.028	0.996	11.5	-0.08	0.999	-0.058	12.3	0.610
250	27	23.4	0.044	0.961	27	-0.017	0.999	-0.257	30.6	0.845
750	68	58.5	0.023	0.887	67	-0.005	0.998	-1.215	81.7	0.905

It is noted that the regression correlation coefficient (r^2) values are the highest and closest to 1 for the pseudo-second-order kinetics model. Moreover, the values of q_e estimated using this model are comparable with the experimentally determined values of q_e. Hence, it appears that the adsorption of MB dye on the surface of HTN follows the pseudo-second-order kinetics.[14] The adsorption data at equilibrium, derived using Fig. 3.4, is fitted using the Langmuir, Freundlich, and DKR-isotherms.[3,14,20]

The values of different parameters of the three isotherm models obtained from slopes and intercepts of the best-fitted straight-lines, Figs. 3.8-3.11, as well as those of ε, E, ΔG^0, and R_L are tabulated in Table 3.5 for initial different initial solution-pH.
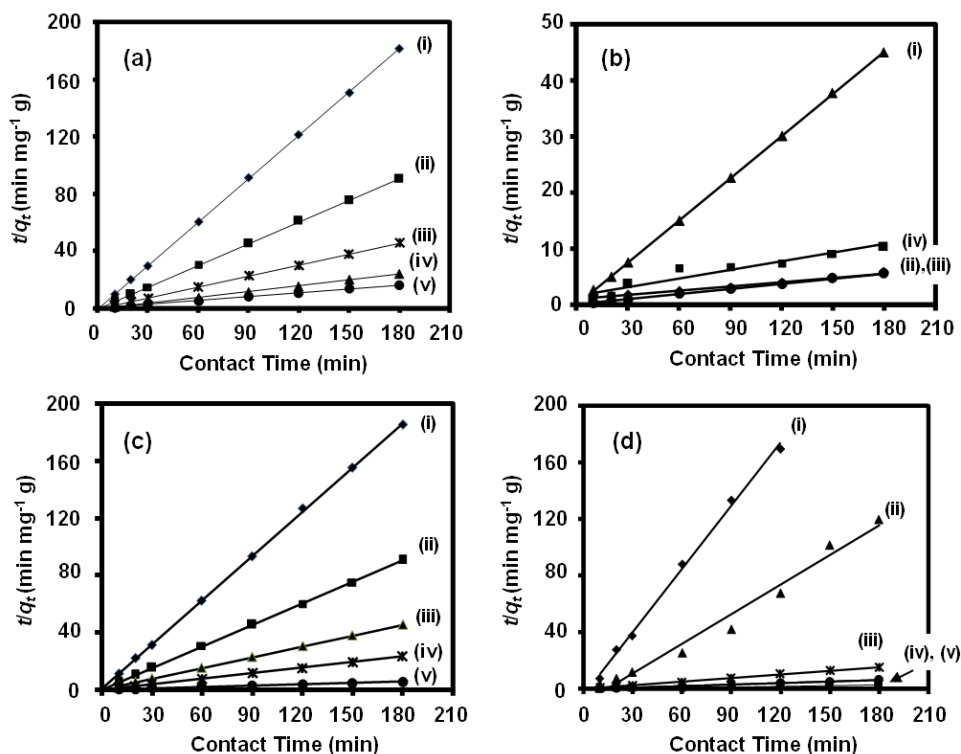
Fig. 3.7. Typical pseudo-second-order kinetics plots for the adsorption of MB dye on the surface of HTN for different initial solution-pH: 2.5 (a), 7.5 (b), 10 (c), and 11 (d). In (a), the initial MB dye concentration is varied as 7.5 (i), 15 (ii), 30 (iii), 60 (iv), and 100 (v) μM; in (b), 30 (i), 250 (ii), 500 (iii), and 750 (iv) μM; in (c), 7.5 (i), 15 (ii), 30 (iii), 60 (iv), and 250 (v) μM; and in (d), 15 (i), 30 (ii), 100 (iii), 250 (iv), and 750 (v) μM. (Note: For clarity, the graphs are shown only for the selected initial MB dye concentrations).
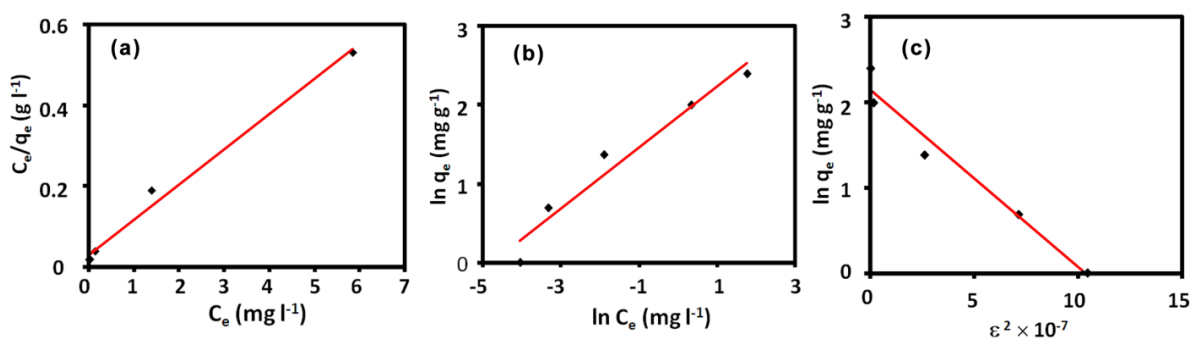
Fig. 3.8. Langmuir (a), Freundlich (b), and DKR (c) isotherm plots for the adsorption of MB dye on the surface of HTN for the initial solution-pH of 2.5.
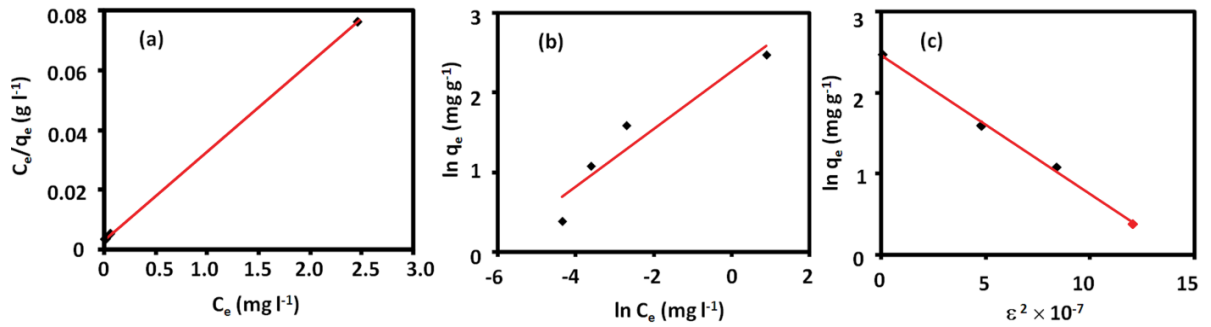
Fig. 3.9. Langmuir (a), Freundlich (b), and DKR (c) isotherm plots for the adsorption of MB dye on the surface of HTN for the initial solution-pH of 7.5.
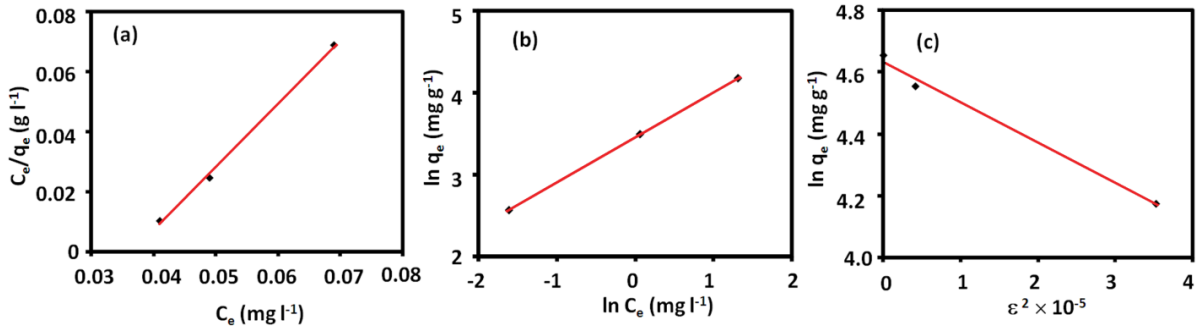
Fig. 3.10. Langmuir (a), Freundlich (b), and DKR (c) isotherm plots for the adsorption of MB dye on the surface of HTN for the initial solution-pH of 10.
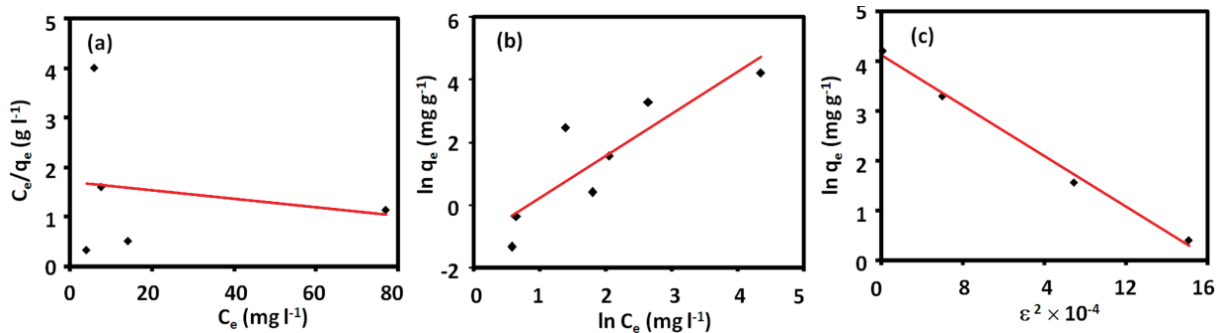
Fig. 3.11. Langmuir (a), Freundlich (b), and DKR (c) isotherm plots for the adsorption of MB dye on the surface of HTN for the initial solution-pH of 11.

Table 3.5. Equilibrium isotherm constants, standard Gibb's free energy change, and R_L for MB adsorption on the surface of HTN determined by varying the initial MB concentration at different initial solution-pH.

pH	q_m (EXP)	Langmuir					Freundlich			DKR			
		q_m	K_L	r^2	R_L	ΔG^0	n	K_F	r^2	q_m	β	r^2	E
2.5	11	11.5	3.1	0.99	0.002-0.12	-37.6	2.6	6.3	0.952	8.6	-2×10^{-8}	0.967	5
7.5	32	34.5	14.5	1	0.003-0.03	-41.5	3.4	26	0.969	32.2	-2×10^{-8}	0.997	5
10	105	0.47	---	0.997	---	---	1.81	31.7	0.999	103	-1×10^{-6}	0.991	0.7
11	68	-125	-213	0.031	-0.002	---	0.74	3.1	0.761	63	-3×10^{-5}	0.994	0.13

It is noted that for highly acidic solution (pH~2.5), the $<r^2>$ value is the highest and closest to 1 for the Langmuir isotherm. Moreover, the value of q_m estimated using this model is comparable with the experimentally determined value of q_m. Hence, the equilibrium adsorption of MB dye on the surface of HTN follows the Langmuir isotherm in a highly acidic solution, which is also supported by the calculated values of ΔG^0 and R_L.[20,22-23] For the neutral solution-pH (~7.5), it appears that the equilibrium adsorption follows both the Langmuir and DKR models. The $<r^2>$ value is the highest and equal to 1 for the Langmuir isotherm; however the value of q_m estimated using this model, although close, is slightly larger than the experimentally determined value. On the other hand, the $<r^2>$ value is slightly lower than 1 for the DKR isotherm; however, the value of q_m estimated using this model matches with the experimentally determined value of q_m. For the initial solution-pH in the basic region (~10), an

interesting observation has been made which is not noted in the previous two cases. The equilibrium adsorption data under this condition could not be fitted using any of the above three isotherm models. In contrary, different isotherm models are noted to be followed in different ranges of initial MB dye concentration, Figs. 3.5 (pH 10) and 3.10. Typically, within the initial MB dye concentration range of 7.5-30, 100-500, and 750-1300 μM, the Langmuir, Freundlich, and DKR isotherm models are obeyed respectively. Moreover, the value of q_m estimated using the DKR model is comparable with the experimentally determined value, Table 3.5. Hence, at the initial solution-pH of ~10, the equilibrium adsorption data follows the Langmuir, Freundlich, and DKR isotherms depending on the initial MB dye concentration. For a highly basic solution (pH~11), the $<r^2>$ value is the highest and closest to 1 for the DKR isotherm and the value of q_m estimated using this model is also comparable with the experimentally determined value of q_m, Table 3.5. Hence, under this condition, the adsorption equilibrium data follows only the DKR model. It is also noted that for the conditions when the DKR model is obeyed, the calculated adsorption energy values are within the range of 0.13-5 kJ mol^{-1}. It is known that for the E values within the range of 8-16 kJ mol^{-1}, the adsorption is governed by the ion-exchange mechanism.[22] Since in this investigation, the E values are below 8 kJ mol^{-1}, the adsorption of MB dye on the surface of HTN is possibly governed by the electrostatic forces, which is supported by the fact that the q_m is highly sensitive to the variation in the initial solution-pH. Overall, we note that the adsorption equilibrium follows the Langmuir isotherm in a highly acidic solution and DKR isotherm in a highly basic solution; while, in the intermediate initial solution-pH range, it exhibits a transition from the Langmuir to DKR isotherm.

3.3.3. Surface coverage by dye molecules

The variation in the maximum fraction of the surface-area of HTN covered by the MB dye at equilibrium, calculated using the following equation (Eq.3.4), is presented in Fig. 3.12 as a function of initial solution-pH.

$$\text{Coverage (\%)} = \frac{q_m \times N_{AV} \times SA_{MB}}{MW_{MB} \times S_{HTN} \times 10} \tag{3.4}$$

where, N_{AV} is the Avogadro's number (6.023×10^{23} molecules mole^{-1}), MW_{MB} the molecular weight of MB dye (319.85 g mole^{-1}), SA_{MB} and S_{HTN} the surface-area (m^2) of a single MB dye molecule (8.723×10^{-19} m^2; dimensions: 1.43 nm $\times$ 0.61 nm $\times$ 0.4 nm)[23] and the specific surface-area (330 m^2 g^{-1}) of HTN (Note: In Eq.3.4, q_m has the unit of mg g^{-1}). It is noted that MB dye covers 5-52 % of the surface-area of HTN within the investigated range of initial solution-pH with the maximum coverage obtained at the initial solution-pH of 10.
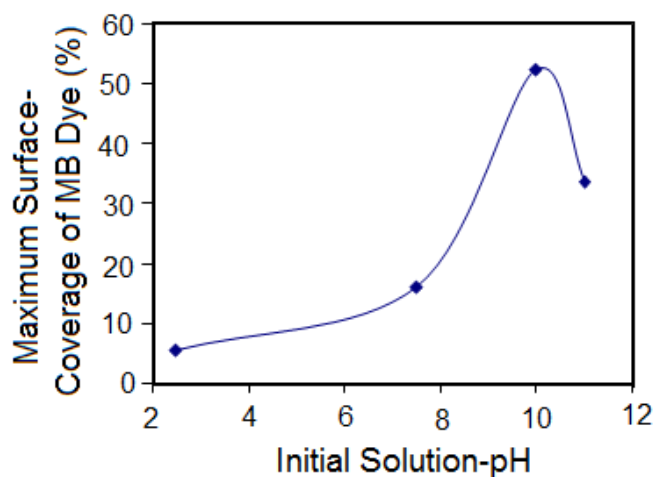
Fig. 3.12. Variation in the maximum coverage of MB dye adsorbed on the surface of HTN as a function of initial solution-pH.

3.4. Conclusions

The HTN processed via hydrothermal have been successfully utilized for the removal of MB dye from an aqueous solution via surface-adsorption mechanism. The dye-adsorption on the surface of HTN at equilibrium is strongly governed by the contact time, initial MB dye concentration, and initial solution-pH. The dye-adsorption capacity of HTN is observed to be 105 mg g^{-1} at the initial solution-pH of ~10. A new model has been proposed to explain the observed variation in q_e and q_m as a function of initial MB dye concentration and solution-pH. According to this model, such dependence is governed by the interaction between the cationic MB dye molecules and OH$^-$ ions within the solution, which in turn control their respective adsorption on the surface of HTN, thus affecting the q_e, q_m, and initial MB dye concentration associated with the latter. The MB dye-adsorption on the surface of HTN follows the pseudo-second-order kinetics within the entire range of initial solution-pH investigated here. The adsorption equilibrium follows the Langmuir isotherm in a highly acidic solution and DKR isotherm in a highly basic solution; while in the intermediate initial solution-pH range, it exhibits a transition from the Langmuir to DKR isotherm.

References

1. Fujishima, A.; Rao, T. N.; Tryk, D. A., Titanium dioxide photocatalysis. *J. Photochem. Photobiol., C* **2000,** *1* (1), 1-21.

2. Wang, S.; Li, H.; Xu, L., Application of zeolite MCM-22 for basic dye removal from wastewater. *J. Colloid Interface Sci.* **2006,** *295* (1), 71-78.

3. Kumar, K. V.; Ramamurthi, V.; Sivanesan, S., Modeling the mechanism involved during the sorption of methylene blue onto fly ash. *J. Colloid Interface Sci.* **2005,** *284* (1), 14-21.

4. Gomez, V.; Larrechi, M.; Callao, M., Kinetic and adsorption study of acid dye removal using activated carbon. *Chemosphere* **2007,** *69* (7), 1151-1158.

5. Sivaraj, R.; Namasivayam, C.; Kadirvelu, K., Orange peel as an adsorbent in the removal of acid violet 17 (acid dye) from aqueous solutions. *Waste Manage.* **2001,** *21* (1), 105-110.

6. Han, R.; Wang, Y.; Yu, W.; Zou, W.; Shi, J.; Liu, H., Biosorption of methylene blue from aqueous solution by rice husk in a fixed-bed column. *J. Hazard. Mater.* **2007,** *141* (3), 713-718.

7. Gil, A.; Assis, F.; Albeniz, S.; Korili, S., Removal of dyes from wastewaters by adsorption on pillared clays. *Chem. Eng. J.* **2011,** *168* (3), 1032-1040.

8. Dogan, M.; Alkan, M., Removal of methyl violet from aqueous solution by perlite. *J. Colloid Interface Sci.* **2003,** *267* (1), 32-41.

9. Bhatnagar, A.; Vilar, V. J.; Botelho, C. M.; Boaventura, R. A., Coconut-based biosorbents for water treatment—a review of the recent literature. *Adv. Colloid Interface Sci.* **2010,** *160* (1), 1-15.

10. Baiju, K.; Shukla, S.; Biju, S.; Reddy, M.; Warrier, K., Hydrothermal processing of dye-adsorbing one-dimensional hydrogen titanate. *Mater. Lett.* **2009,** *63* (11), 923-926.

11. Harsha, N.; Ranya, R.; Shukla, S.; Biju, S.; Reddy, M.; Warrier, K., Effect of silver and palladium on dye-removal characteristics of Anatase-titania nanotubes. *J. Nanosci. Nanotechnol.* **2011,** *11* (3), 2440-2449.

12. Harsha, N.; Ranya, K.; Babitha, K.; Shukla, S.; Biju, S.; Reddy, M.; Warrier, K., Hydrothermal processing of hydrogen titanate/anatase-titania nanotubes and their application as strong dye-adsorbents. *J. Nanosci. Nanotechnol.* **2011,** *11* (2), 1175-1187.

13. Lee, C. K.; Liu, S. S.; Juang, L. C.; Wang, C. C.; Lyu, M. D.; Hung, S. H., Application of titanate nanotubes for dyes adsorptive removal from aqueous solution. *J. Hazard. Mater.* **2007,** *148* (3), 756-760.

14. Lee, C. K.; Lin, K. S.; Wu, C. F.; Lyu, M. D.; Lo, C. C., Effects of synthesis temperature on the microstructures and basic dyes adsorption of titanate nanotubes. *J. Hazard. Mater.* **2008,** *150* (3), 494-503.

15. Xiong, L.; Yang, Y.; Mai, J.; Sun, W.; Zhang, C.; Wei, D.; Chen, Q.; Ni, J., Adsorption behavior of methylene blue onto titanate nanotubes. *Chem. Eng. J.* **2010,** *156* (2), 313-320.

16. Xu, S.; Ng, J.; Zhang, X.; Bai, H.; Sun, D. D., Adsorption and photocatalytic degradation of Acid Orange 7 over hydrothermally synthesized mesoporous TiO_2 nanotube. *Colloids Surf., A* **2011,** *379* (1), 169-175.

17. Prado, A. G.; Costa, L. L., Photocatalytic decouloration of malachite green dye by application of TiO_2 nanotubes. *J. Hazard. Mater.* **2009,** *169* (1), 297-301.

18. Mao, Y.; Kanungo, M.; Hemraj-Benny, T.; Wong, S. S., Synthesis and growth mechanism of titanate and titania one-dimensional nanostructures self-assembled into hollow micrometer-scale spherical aggregates. *J. Phys. Chem. B* **2006,** *110* (2), 702-710.

19.   Bavykin, D. V.; Parmon, V. N.; Lapkin, A. A.; Walsh, F. C., The effect of hydrothermal conditions on the mesoporous structure of TiO_2 nanotubes. *J. Mater. Chem.* **2004,** *14* (22), 3370-3377.

20.   Matheswaran, M.; Karunanithi, T., Adsorption of Chrysoidine R by using fly ash in batch process. *J. Hazard. Mater.* **2007,** *145* (1), 154-161.

21.   Bavykin, D. V.; Redmond, K. E.; Nias, B. P.; Kulak, A. N.; Walsh, F. C., The effect of ionic charge on the adsorption of organic dyes onto titanate nanotubes. *Aust. J. Chem.* **2010,** *63* (2), 270-275.

22.   Belessi, V.; Lambropoulou, D.; Konstantinou, I.; Zboril, R.; Tucek, J.; Jancik, D.; Albanis, T.; Petridis, D., Structure and photocatalytic performance of magnetically separable titania photocatalysts for the degradation of propachlor. *Appl. Catal., B* **2009,** *87* (3–4), 181-189.

23.   Pelekani, C.; Snoeyink, V. L., Competitive adsorption between atrazine and methylene blue on activated carbon: the importance of pore size distribution. *Carbon* **2000,** *38* (10), 1423-1436.

Synthesis of $H_2Ti_3O_7/\gamma$-Fe_2O_3 Magnetic Nanocomposites *via* Hydrothermal and Their Dye Adsorption/ Decomposition Properties

Graphical Abstract
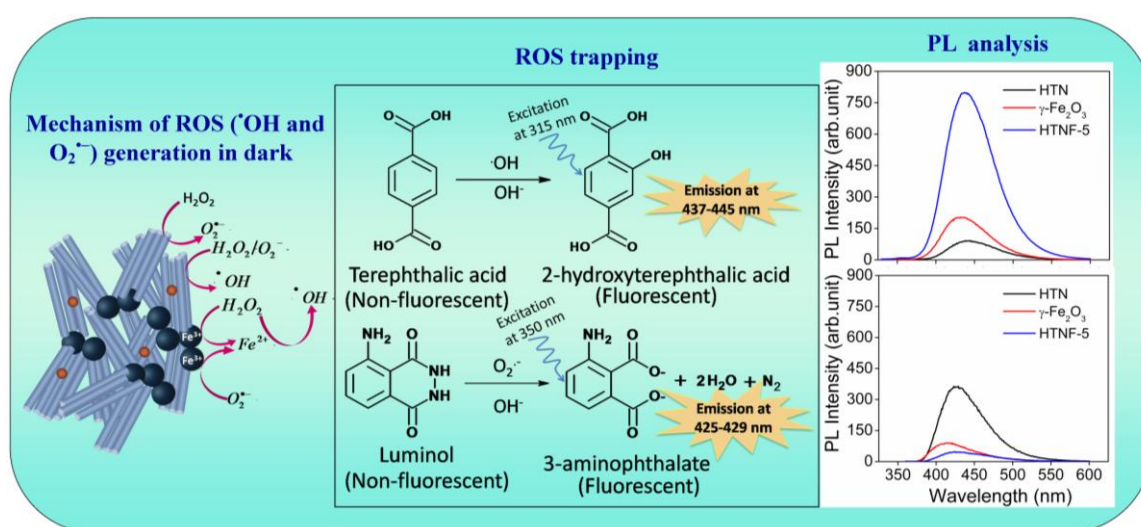
Highlight

- $TiO_2/SiO_2/\gamma$-Fe_2O_3 magnetic photocatalyst has been synthesized via Stober/sol-gel.

- $H_2Ti_3O_7/\gamma$-Fe_2O_3 (HTNF) magnetic nanocomposite processed via hydrothermal.

- TiO_2 coating thickness, substrate effect, and Si pick-up direct $H_2Ti_3O_7$ morphology.

- HTNF-5 sample exhibits highest adsorption capacity with magnetic separatebility.

- Recycling is demonstrated via H_2O_2 activation and elucidated using ROS trapping.

Abstract

Magnetic nanocomposite (HTNF) composed of hydrogen titanate ($H_2Ti_3O_7$) nanotubes/nanosheets (HTN) and γ-Fe_2O_3 nanoparticles have been processed by subjecting the core-shell γ-Fe_2O_3/SiO_2/TiO_2 (TSF) magnetic photocatalyst, having varying amount of TiO_2, to the hydrothermal conditions. It has been demonstrated that the morphological variations in the $H_2Ti_3O_7$ has been governed by the roll-up mechanism superimposed with the substrate and Si pick-up effects. The HTNF magnetic nanocomposite having 31 wt% $H_2Ti_3O_7$, typically having the 100% nanotube morphology with the highest specific surface-area (133 m^2 g^{-1}) and pore-volume (0.22 cm^3 g^{-1}), exhibits the highest capacity (74 mg g^{-1}) for the adsorption of cationic MB dye from an aqueous solution involving the electrostatic attraction mechanism and pseudo-second-order kinetics. Very fast magnetic separation (less than a minute) and the recyclability of HTNF magnetic nanocomposite have been demonstrated for the consecutive six adsorption/decomposition cycles accomplished through the catalytic decomposition of the previously adsorbed dye on its surface via the H_2O_2 activation in the dark. The underlying mechanism of dye-decomposition, involving the generation and attack of ROS, such as the $O_2^{\bullet-}$ and $^{\bullet}OH$ has been revealed which confirms, for the first time, the synergy effect between the constituents of HTNF magnetic nanocomposite.

4.1. Introduction

In the photocatalytic degradation of organic pollutants, the magnetic photocatalyst based on the core-shell TSF nanocomposite has been the most commonly reported system in which the photocatalytic and magnetic properties are provided by TiO_2 and γ-Fe_2O_3.[1] The interlayer of SiO_2 avoids the direct electrical contact between the core (γ-Fe_2O_3) and the shell (TiO_2) which enhances the photocatalytic activity. It also avoids the transformation of magnetic γ-Fe_2O_3 to the non-magnetic hematite (α-Fe_2O_3) during the high temperature calcination treatment. Moreover, it prevents the photo-dissolution of Fe^{2+} ions into the surrounding aqueous solution during the photocatalysis process without affecting the photocatalytic activity.[2] However, to overcome some of the limitations of the magnetic photocatalyst, the development of adsorbents-based magnetic nanocomposites has been initiated.[3] It has been demonstrated that the hydrothermal treatment of TiO_2-coated SiO_2-based flyash particles results in the stabilization of the nanosheets of hydrogen titanate which exhibit enhanced adsorption properties compared to that of the nanotube morphology.[4] Hence, it is interesting to investigate the morphological evolution of the titanate-based magnetic adsorbents via the hydrothermal treatment of γ-Fe_2O_3/SiO_2/TiO_2 magnetic photocatalyst and their subsequent adsorption properties, which are still not reported in the literature.

Thazhe et al.[5] first derived the titanate-based magnetic nanocomposite via the hydrothermal treatment of sol-gel derived core-shell cobalt ferrite ($CoFe_2O_4$)/SiO_2/TiO_2 which was subsequently modified by Li et al.[6], Zhou et al.[7], and Papa et al.[8] demonstrated the hydrothermal treatment of magnetic nanoparticles dispersed along with TiO_2 in an alkali solution with the formation of magnetic

titanates which is also the modification of the former method. Recently, we demonstrated that the formation of hydrogen titanate $(H_2Ti_3O_7)/\gamma$-Fe_2O_3 magnetic nanocomposites involves a strong ion-exchange bond formation at the interface between the magnetic nanoparticles and the titanate nanotubes.[9] In spite of these earlier efforts in the conversion of the core-shell magnetic photocatalyst to the magnetic dye-adsorbent catalyst via hydrothermal, the precise morphological evolution during the hydrothermal treatment of γ-Fe_2O_3/SiO_2/TiO_2 magnetic photocatalyst as a function of the amount of TiO_2 (or the shell-thickness) and its effect on the adsorption characteristics of the newly developed products have not been systematically studied in the literature. Hence, these have been set as the major objectives of this investigation.

Relative to the costlier carbon-based[10] and low-cost adsorbents,[11] the titanate-based adsorbents, as investigated in this work, concurrently offer several advantages in the dye-removal application such as the operation of ion-exchange and electrostatic attraction mechanisms for the adsorption,[12-13] easy tailoring of the surface chemistry to increase the adsorption capacity,[14] easy solid-liquid separation using an external magnetic field by attaching them to the magnetic nanoparticles, and lastly, the fast regeneration of the catalyst via the H_2O_2 activation process conducted in the dark.[15-17] In this investigation, we demonstrate the magnetic separation of HTNF magnetic nanocomposite from an aqueous dye solution followed by its regeneration via the H_2O_2 activation. The underlying mechanism of dye-decomposition, involving the generation and attack of ROS, such as $O_2^{\bullet-}$ and $^{\bullet}OH$, is revealed for the first time via the radical-trapping experiments.

4.2. Experimental

4.2.1. Chemicals

Titanium(IV)-isopropoxide ($Ti(OC_3H_7)_4$, 97%), tetraethylorthosilicate (TEOS, 98%), nanocrystalline γ-Fe_2O_3 (<50 nm, 98%) magnetic powder, and terephthalic acid (TA, 98%) were purchased from Sigma-Aldrich Chemicals, Bengaluru, India; hydrochloric acid (HCl, 35 wt%) from Ranbaxy Fine-Chemicals, India; ammonium hydroxide (NH_4OH, 25 wt%) from Qualigens Fine Chemicals, India; ethanol (99.9% AR), 2-propanol (99.5%, ACS reagent), sodium hydroxide (NaOH, Assay 97%), MB (96%), H_2O_2 (30 wt%) from S.D. Fine-Chem Ltd., Mumbai, India; and Luminol (5-Amino-2,3-dihydro-pthalazine-1,4-dione) from Merck Specialties Pvt. Ltd., India. All listed chemicals were used as-received without any further purification and/or modification.

4.2.2. Sol-gel synthesis of TSF magnetic photocatalyst

The core-shell γ-Fe_2O_3/SiO_2/TiO_2 nanocomposites of different TiO_2 weight-fractions were prepared by the combination of modified Stober and sol-gel methods similar to that described in second chapter. Briefly, a continuous uniform coating of SiO_2 over γ-Fe_2O_3 nanoparticles was obtained via the controlled hydrolysis of TEOS using NH_4OH solution in the ethanol medium. The product obtained was washed with distilled water, then with ethanol, and finally dried at room temperature. The TiO_2 coating over the SiO_2/γ-Fe_2O_3 nanocomposite was performed via the hydrolysis of $Ti(OC_3H_7)_4$ in 2-propanol in several number of cycles (1, 3, 5, and 7 cycles) in order to get TiO_2 coated SiO_2/γ-Fe_2O_3 which are denoted as TSF-1, TSF-3, TSF-5, and TSF-7 respectively. The theoretical calculations show that the fraction of anatase-TiO_2 in TSF-1, TSF-3, TSF-5, and TSF-7 samples varies as 6, 17, 26, and 33 wt%

respectively (Note: it is to be noted that for the precise determination of the amount of TiO_2 deposited on the surface of γ-Fe_2O_3/SiO_2, the final weight of the γ-Fe_2O_3/SiO_2/TiO_2 magnetic nanocomposite obtained is considered for the calculations instead of the amount of $Ti(OC_3H_7)_4$ used).

4.2.3. Hydrothermal synthesis of $H_2Ti_3O_7$/γ-Fe_2O_3 magnetic nanocomposites

2 g of TSF sample was suspended in a highly alkaline NaOH solution (10 M) taken in a Teflon beaker (84 vol%) which was placed in a stainless-steel (SS 316) vessel of 200 ml capacity. The hydrothermal reaction was carried out in an autoclave at 120°C for 30 h. The autoclave was allowed to cool naturally to room temperature and the product was collected by decanting the top solution. Then, the latter was first washed using 100 ml of 1 M HCl solution for 1 h followed by that using 100 ml of pure distilled water for 1 h for multiple times till pH of the filtrate became almost neutral. The washed-product was then separated from the solution using a centrifuge and dried in an oven at 80°C (termed as the final hydrothermal product). Depending on the precursor used, the final hydrothermal product was denoted as HTNF-1, HTNF-3, HTNF-5, and HTNF-7 respectively. The theoretical calculations show that the fraction of HTN in the HTNF-1, HTNF-3, HTNF-5, and HTNF-7 magnetic nanocomposites varies as 8, 21, 31, and 39 wt% respectively.

4.2.4. Characterization

The morphology of the samples was examined using the transmission electron microscope (TEM) (Tecnai G^2, FEI, The Netherlands) operated at 300 kV and the nanocrystalline nature was confirmed from the selected-area electron diffraction (SAED) patterns. The chemical constituents of the different samples were identified

using the energy dispersive X-ray (EDX) analysis. The crystal structure was determined using the X-ray diffraction (XRD, PW1710 Phillips) technique by utilizing the Cu*Kα* X-radiation (λ_{Cu}=1.5406 Å). The XRD patterns were obtained at room temperature over the 2θ values within the range of $10\text{-}80^{\circ}$. The specific surface-area of the samples, average pore size and its distribution were measured via the Brunauer-Emmett-Teller (BET) surface-area measurement technique (Micrometrics Gemini 2375 Surface Area Analyzer) by using nitrogen (N_2) adsorption-desorption multi-point method. The samples were degassed in the flowing N_2 atmosphere at 200°C before the measurements. The magnetic properties were analyzed using a vibrating sample magnetometer (VSM) attached to a Physical Property Measurement System (PPMS, Quantum Design, Dynacool, U.S.A.). The zeta-potential measurements were performed using the electrophoretic light scattering in the pH range from 2 to 10 using a Zetasizer Nano Series-Zen 3600 (Malvern Instruments, U.K.).

4.2.5. Dye-Adsorption characteristics of $H_2Ti_3O_7/\gamma\text{-}Fe_2O_3$ magnetic nanocomposite

The time dependent adsorption of MB on the surface of HTNF samples was carried out via the procedure already described in third chapter (section 3.2.4). The measurements were conducted using the initial MB concentration within the range of ~7.5-250 μM, at the initial solution-pH of ~10 adjusted using the NH$_4$OH solution, with the adsorbent concentration of 0.4 g l^{-1}. (Note: the dye-adsorption measurements as discussed in chapter-3 for the pure-HTN suggest that, within the initial solution-pH range of 2.5-11, the maximum adsorption capacity is obtained at the initial solution-pH of ~10).[18] The aliquots collected at the definite time intervals were analyzed by recording the absorption spectra obtained using the UV-visible spectrophotometer.

4.2.6. Recycling of HTNF magnetic nanocomposite by the decomposition of surface-adsorbed MB dye

The recycling was achieved via the magnetic separation of MB dye adsorbed HTNF sample and its surface-cleaning via catalytic decomposition of dye molecules through H_2O_2 activation in an aqueous solution in the dark-condition. The recycling was demonstrated using the HTNF-5 magnetic nanocomposite (0.4 g l^{-1}) in 125 ml aqueous solution of MB dye having the initial concentration of ~30 µM at the initial solution-pH of ~10. After the first cycle of MB adsorption, a bar magnet was placed outside the container to attract the magnetic nanocomposite on its walls and the treated solution was decanted. The bar magnet was removed and fresh ~10 ml distilled H_2O was poured into the container to collect the magnetic nanocomposite sticking on the walls of container. The aqueous suspension of magnetic nanocomposite was then dried in an oven at $80^{o}C$ overnight and the dried sample was utilized for the second-cycle of dye-adsorption measurement conducted under the similar test-conditions. Total six successive cycles of dye-adsorption measurements were conducted without the use of any intermediate surface-cleaning treatment. Later, the dye-adsorption experiments were repeated with the involvement of surface-cleaning treatment which was conducted after the end of each cycle of dye-adsorption. In the latter, the dried HTNF-5 sample with the MB dye adsorbed on its surface was dispersed in the 100 ml of 15 wt% H_2O_2 solution (obtained via the dilution method) and stirred using an overhead stirrer (IKA, Eurostar Digital, Germany) for 3 h. The surface-cleaned powder was separated from the aqueous solution using an external magnetic field provided by a small bar magnet; and after drying in an oven at $80^{o}C$ overnight, it was recycled for the next-cycle of dye-

adsorption. Total six successive cycles of dye-adsorption measurements were conducted with the use of intermediate surface-cleaning treatment.

4.2.7. Detection of ROS ($O_2^{•-}$ and $^•OH$)

Luminol was used as a chemiluminescent probe for the detection of generated $O_2^{•-}$. 0.278 g l^{-1} of Luminol was dissolved in 125 ml of alkaline (0.4 g l^{-1} NaOH) H_2O_2 (15 wt%) solution. After 1 h of overhead stirring, 0.4 g l^{-1} of HTNF-5 sample was added with the continued stirring. 8 ml aliquot was then collected after 10 min of contact time. The magnetic nanocomposite was separated from the sample suspension using a bar magnet and the filtrate obtained was immediately subjected to the PL emission spectral analysis (Cary Eclipse, Varian, The Netherlands). The luminol molecules react with the generated $O_2^{•-}$ species and produce 3-aminophthalate (AP) which exhibits a characteristic broad PL peak normally located at ~420 nm at an excitation wavelength of ~350 nm, the intensity of which is taken as the measure of generated amount of $O_2^{•-}$ species.[19] In the present work, this emission peak was located within the wavelength range of 425-429 nm. (Note: The H_2O_2 solution, in the absence of magnetic nanocomposite, also contains small amount of $O_2^{•-}$ species. The intensity of PL peak obtained from this blank solution is considered as a reference peak (background) and is subtracted from the PL intensity observed in the presence of a magnetic nanocomposite.

For the $^•OH$ detection, an alkaline solution of TA was used which upon excitation at 315 nm normally provides an emission peak at ~425 nm due to the formation of 2-hydroxyterephthalic acid as a result of the reaction between TA and generated free $^•OH$.[20] In the present work, this emission peak was located within the wavelength

range of 437-445 nm. The experiments were similar to the previous case except that the concentration of NaOH and TA were changed to 0.08 g l^{-1} and 0.058 g l^{-1} respectively. Similar to the previous case, the background subtraction is conducted in this case as well using the blank solution. The $O_2^{\bullet-}$ and $^{\bullet}OH$ trapping experiments were also conducted using the pure HTN (0.124 g l^{-1}) and pure γ-Fe$_2$O$_3$ (0.276 g l^{-1}) nanoparticles. For these typical experiments, the concentration of respective catalyst was determined from its weight-fraction in the HTNF-5 sample. All other experimental parameters were similar to those as described above.

4.3. Results and discussion

4.3.1. Morphological, chemical and structural evolution of hydrothermally processed H$_2$Ti$_3$O$_7$/γ-Fe$_2$O$_3$ magnetic nanocomposite

The TSF magnetic nanocomposites having varying amount of TiO$_2$ are obtained via multiple sol-gel TiO$_2$ coating cycles. The calculated fraction of TiO$_2$ in TSF-1, TSF-3, TSF-5, and TSF-7 samples vary as 6, 17, 26, and 33 wt% respectively. The morphologies of TSF magnetic nanocomposites as observed by the TEM analysis have been already reported by us[21] and also by others.[22-24] Typical morphologies of the HTNF magnetic nanocomposites evolved subsequent to the hydrothermal treatment of TSF samples, as observed using the TEM images obtained at lower and higher magnifications, are presented in Figs. 4.1 and 4.2. The corresponding EDX patterns are shown in Fig. 4.3, it is noted that the core-shell TSF magnetic nanocomposite is the combination of three components - γ-Fe$_2$O$_3$, SiO$_2$, and anatase-TiO$_2$.
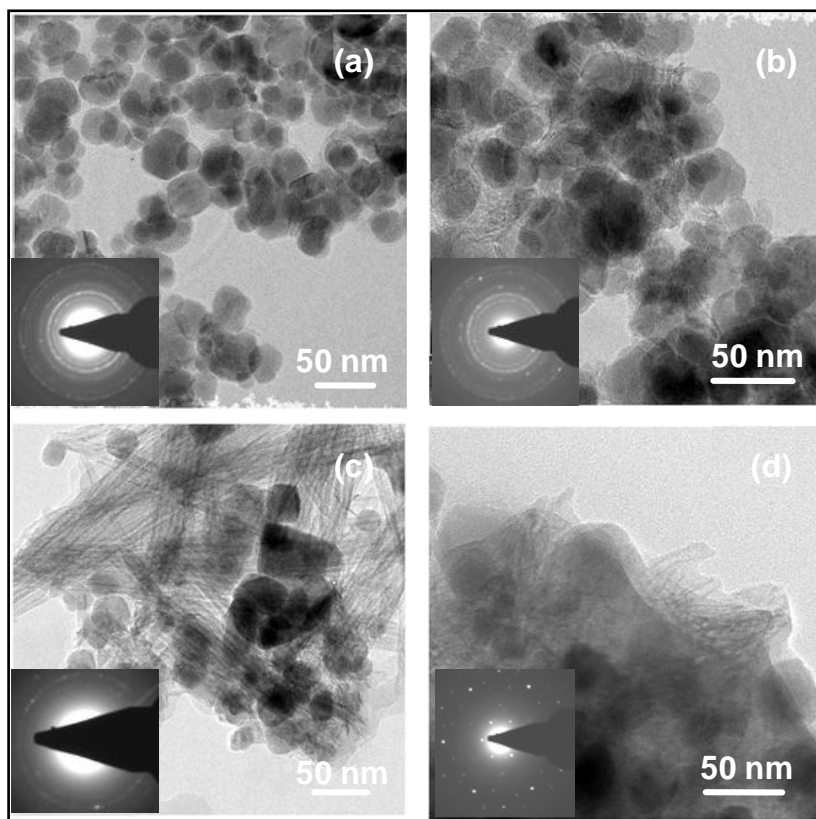
Fig. 4.1. Low magnification TEM images of HTNF-1 (a), HTNF-3 (b), HTNF-5 (c), and HTNF-7 (d) samples. The lower-left corner insets show the corresponding SAED patterns.

Among these components, γ-Fe_2O_3 is inactive under the hydrothermal conditions and remains intact in the final hydrothermal products. On the other hand, the SiO_2 and TiO_2 layers undergo chemical reactions in a highly alkaline hydrothermal conditions forming the SiO_4^{4-} ions and nanosheets/nanotubes of hydrogen titanate respectively which remain dissolved or suspended in the surrounding aqueous solution.[4,6] In Fig. 4.1a, the average size of γ-Fe_2O_3 nanoparticles is noted to be ~25 nm with no direct evidence of the presence of $H_2Ti_3O_7$ phase. However, the EDX pattern presented in Fig. 4.3 does show the existence of tiny amount of Ti in this sample along with the significant presence of Fe and Cu (Note: Cu originates from the grid used for the

TEM analysis). For the HTNF-3 sample, Fig. 4.1b, the γ-Fe_2O_3 nanoparticles are observed to be surrounded by the nanosheets of $H_2Ti_3O_7$ which are also clearly seen in Fig. 4.2a at higher magnification. The formation of nanotube morphology of $H_2Ti_3O_7$ is not evident in these images. On the contrary, for the HTNF-5 sample, Fig. 4.1c, the γ-Fe_2O_3 nanoparticles are observed to be surrounded by the nanotubes of $H_2Ti_3O_7$, having the average length of ~150 nm and average inner diameter of ~4 nm, which are undoubtedly seen in Fig. 4.2b at higher magnification.
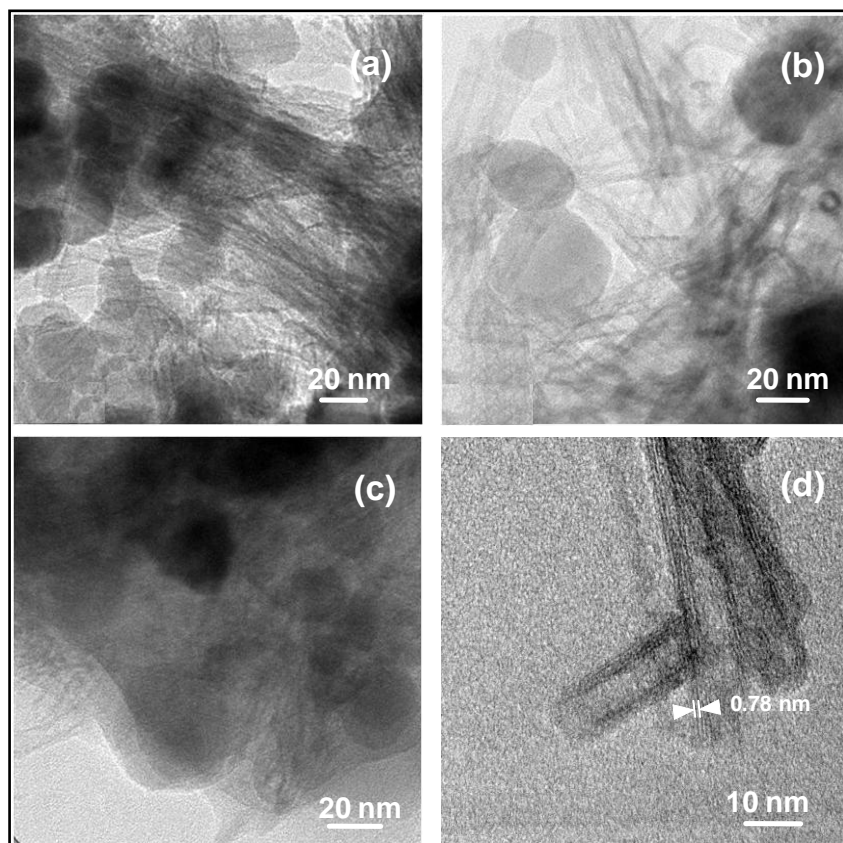
Fig. 4.2. High magnification TEM images of HTNF-3 (a), HTNF-5 (b), HTNF-7 (c). (d) HRTM image of pure HTN showing the average spacing between the lattice fringes.
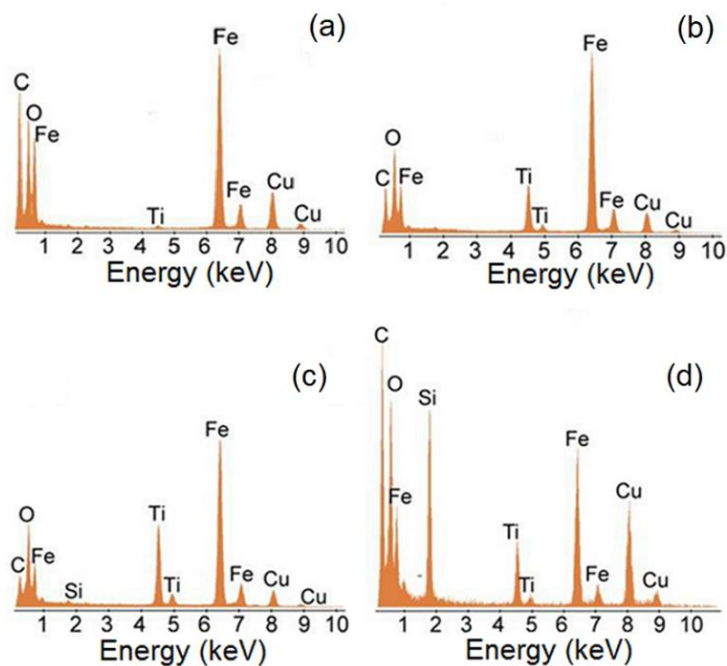
Fig. 4.3. EDX analyses of HTNF-1 (a), HTNF-3 (b), HTNF-5 (c), and HTNF-7 (d) samples.

In contrast to the previous samples, the formation of nanosheet morphology of $H_2Ti_3O_7$ is not noticeable in these images. However, for the HTNF-7 sample, Fig. 4.1d, the γ-Fe_2O_3 nanoparticles are observed to be surrounded by the mixed nanosheets and nanotubes of $H_2Ti_3O_7$ which are also evident in Fig. 4.2c at higher magnification. Moreover, the layered structured $H_2Ti_3O_7$ nanosheets are observed to be formed in a relatively larger amount and exhibit a highly aggregated morphology. The corresponding EDX patterns reveal a gradual increase in the Ti content (2, 15, and 25 atomic %) with the increasing number of sol-gel TiO_2 coating cycles (Fig. 4.3a-c). However, for the HTNF-7 sample, a decrease in Ti content (11 atomic %) is observed which is attributed to the pick-up of large amount of Si by this sample (Fig. 4.3). No free islands of $H_2Ti_3O_7$ nanotubes or nanosheets are observed in all the TEM images presented in Figs. 4.1 and 4.2 suggesting the formation of a nanocomposite

instead of the mixture of former with the γ-Fe$_2$O$_3$ nanoparticles. Moreover, the high-resolution TEM (HRTEM) image presented in Fig. 4.2d shows the average interlayer spacing of 0.78 nm which is close to that of (200) plane of H$_2$Ti$_3$O$_7$.[25]

The XRD patterns of as-received γ-Fe$_2$O$_3$ nanoparticles and HTNF samples are shown in Fig. 4.4a. It is noted that all the HTNF samples strongly exhibit the XRD pattern of γ-Fe$_2$O$_3$ nanoparticles according to the JCPDS card no. 39-1346. Small intensity XRD peaks of HTN, located at the 2θ values of 24.5^o and 48.5^o, are assigned to either pure H$_2$Ti$_3$O$_7$ (in agreement with the HRTEM analysis) or lepidocrocite-type titanate.[26] It is to be noted that the variation in the intensity of XRD peaks corresponding to H$_2$Ti$_3$O$_7$, Fig. 4.4a, is not commensurate with the weight-fraction of HTN in the HTNF samples which is due to the very low peak intensities of HTN relative to those of γ-Fe$_2$O$_3$ nanoparticles. However, such correlation can be easily established from the EDX analysis presented in Fig. 4.3 except for the HTNF-7 sample for which the interference of large amount of Si pick-up has been observed.

The N$_2$ adsorption-desorption isotherms of pure HTN and HTNF magnetic nanocomposites are shown in Fig. 4.5a. The isotherms are recognized as type II while the hysteresis loops correspond to type H3 which are the characteristics of slit-shaped mesopores. The Barret–Joyner–Halenda (BJH) pore-size distribution curves for the above samples are shown in Fig. 4.5b. It is observed that narrow and small peaks in the pore-size distribution curve appear in between ~2-6 nm region ascribed to the inner diameter of HTN consistent with the TEM results. The continuous increase in the pore volume after 6 nm pore size is related to the aggregates of nanotubes having non-uniform pore volume in between them.
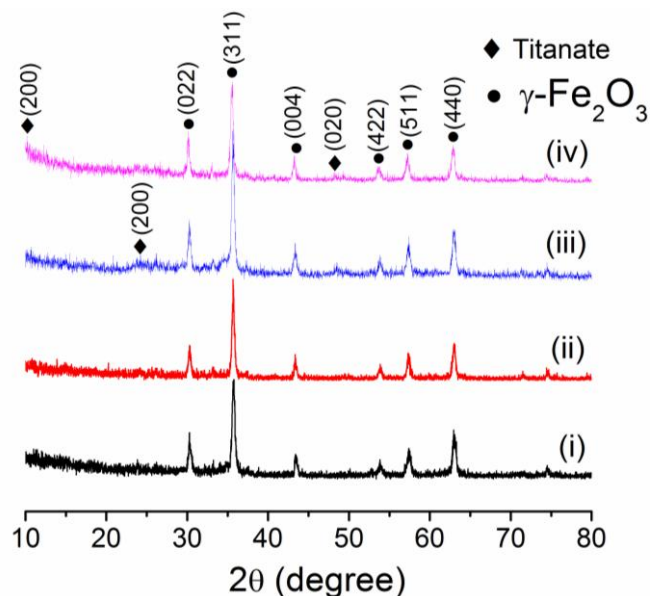
Fig. 4.4. XRD patterns of HTNF-1 (i), HTNF-3 (ii), HTNF-5 (iii), and HTNF-7 (iv).
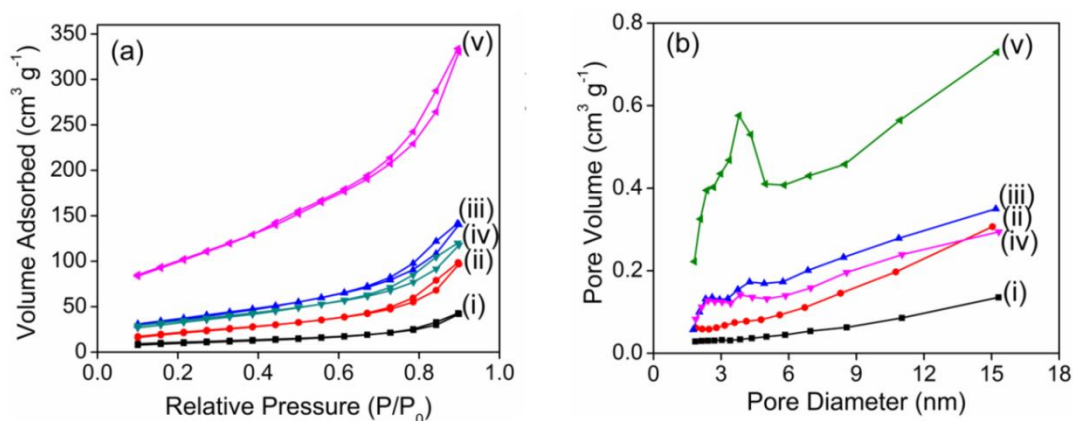
Fig. 4.5. N_2 adsorption-desorption isotherms (a) and BJH pore-size distribution curves (b) as obtained for the HTNF-1 (i), HTNF-3 (ii), HTNF-5 (iii), HTNF-7 (iv), and pure HTN (v) samples.

The BET specific surface-area of 38, 81, 133, 121 m^2 g^{-1} and the pore volume of 0.07, 0.15, 0.22, 0.19 cm^3 g^{-1} are respectively observed for the HTNF-1, HTNF-3, HTNF-5, and HTNF-7 samples. The values of these parameters for the pure γ-Fe_2O_3 nanoparticles and pure HTN are noted to be 32, 362 m^2 g^{-1} and 0.00045, 0.53 cm^3 g^{-1}

respectively. Both the specific surface-area and pore volume of HTNF samples, thus, fall in between those of pure γ-Fe_2O_3 nanoparticles and pure HTN. It is noted that both the specific surface-area and pore volume increase with the number of sol-gel TiO_2 coating cycles, except for the cycle-7 where a decrease in the values of these parameters is noted which is attributed to the highly aggregated nature of relatively large number of layered structured $H_2Ti_3O_7$ nanosheets as obtained under this processing condition. Thus, the attachment of non-magnetic HTN to the magnetic γ-Fe_2O_3 using the hydrothermal reactions results in a net increase in the specific surface-area (from 32 m^2 g^{-1} to 38-121 m^2 g^{-1}) and pore volume (from 0.00045 cm^3 g^{-1} to 0.07-0.22 cm^3 g^{-1}) of the HTNF magnetic nanocomposites which have been attributed to the higher specific surface-area and pore volume of pure HTN compared with those of γ-Fe_2O_3 nanoparticles.

4.3.2. Mechanism for morphological evolution of hydrothermally processed HTNF magnetic nanocomposite

The mechanism of morphological evolution of HTNF samples along with the changes in their structural and chemical-constituents as a function of number of sol-gel TiO_2 coating cycles, as confirmed via the TEM, EDX, XRD, and BET analyses, are summarized in the model proposed in the Scheme 4.1. As shown in the model, the γ-Fe_2O_3 nanoparticles are coated with SiO_2 via the modified Stober process followed by the sol-gel coating of TiO_2 over the SiO_2/γ-Fe_2O_3 nanocomposite particles. The amount of TiO_2 (that is, the average thickness of TiO_2 coating) is controlled by increasing the number of sol-gel TiO_2 coating cycles. Moreover, the average aggregate size of SiO_2/γ-Fe_2O_3 nanocomposite particles over which TiO_2 coating takes place is assumed to increase with the number of sol-gel TiO_2 coating cycles.[7,18]

For the cycles-1 and 3, the final hydrothermal products contain the nanosheets of $H_2Ti_3O_7$. It appears that the average TiO_2 thickness under these processing conditions is below the critical thickness required to avoid the substrate effect which is the result of a strong bond formation at the interface of γ-Fe_2O_3 nanoparticles and $H_2Ti_3O_7$ phase via the ion-exchange reactions.[9] (Note: This further supports the presence of a nanocomposite of γ-Fe_2O_3 nanoparticles and $H_2Ti_3O_7$ instead of their mixture in the final hydrothermal product). It is well-known that the nanocrystalline particles of anatase-TiO_2 in a free standing powder are converted to the nanotubes of $H_2Ti_3O_7$ via the roll-up mechanism involving the sequential transformation of nanoparticles to nanosheets, and then, to nanotubes.[27] It appears that when the thickness of sol-gel TiO_2 coating is below the critical thickness, the substrate effect does not allow the roll-up mechanism to go to completion resulting in the stabilization of the intermediate nanosheet morphology. As per the TEM analysis, Figs. 4.1a and b, and the model presented in the Scheme 4.1, this is particularly observed for the TSF-1 and TSF-3 samples. Since, the amount of Si pick up is minimum (Fig. 4.3a and b), the effect of Si pick-up on the stabilization of nanosheet morphology is ruled out for these two samples. For the TSF-5 sample, the sol-gel TiO_2 coating is assumed to be relatively larger than the critical thickness. In this case, as a result of the minimization of substrate effect and minimum Si pick-up by this sample (Fig. 4.3c), the nanocrystalline TiO_2 coating is effectively converted to the nanotubes of $H_2Ti_3O_7$ via the roll-up mechanism without any stabilization of intermediate nanosheet morphology. The gradual increase in the specific surface-area and pore volume from the HTNF-1 to HTNF-5 sample is attributed to the corresponding increase in the weight-fraction of HTN in these samples.
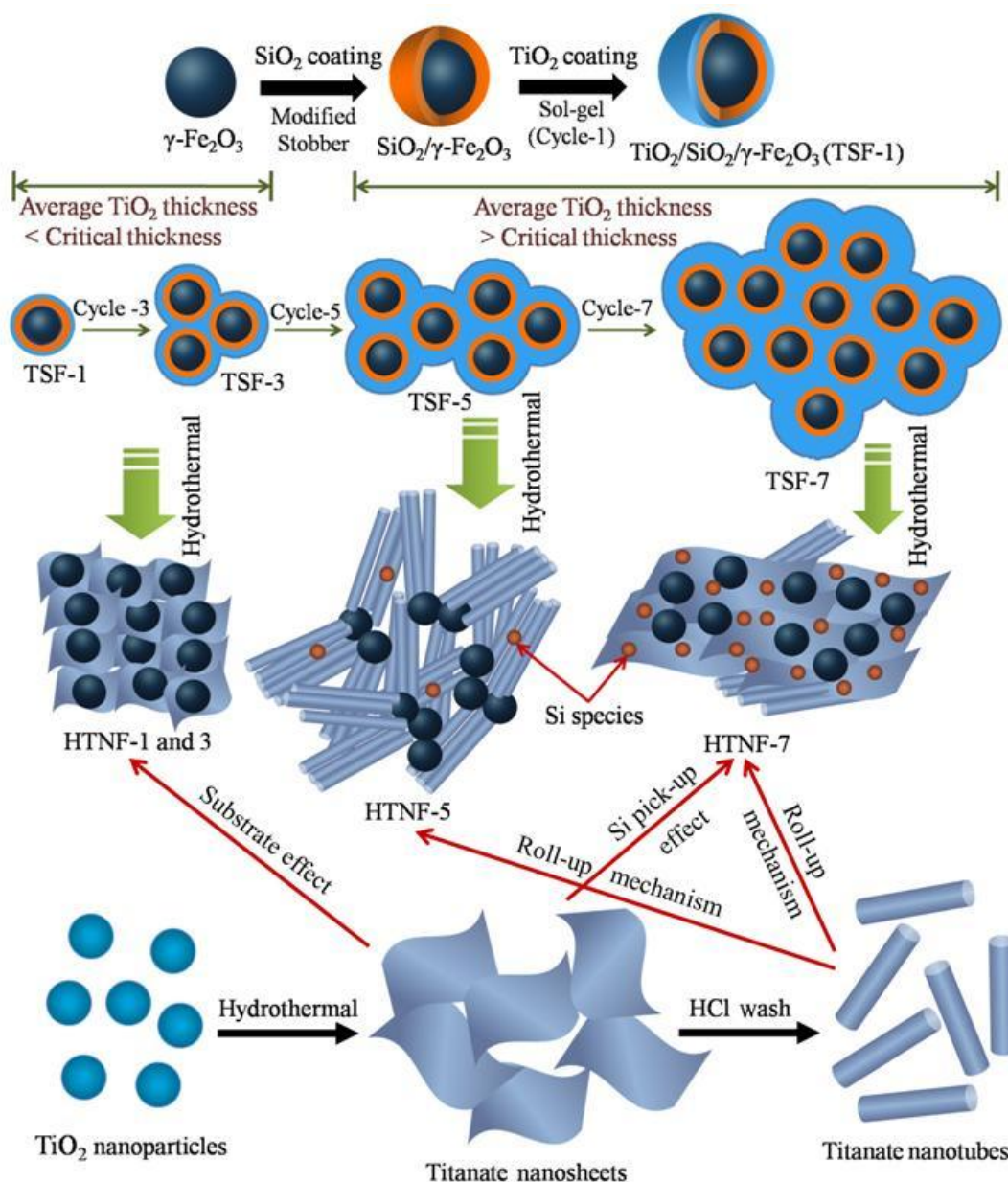
Scheme 4.1. Model describing the morphological evolution of HTNF magnetic nanocomposites hydrothermally processed using TSF samples synthesized with different of number of sol-gel TiO_2 coating cycles.

Since for the TSF-7 sample, the average sol-gel TiO_2 coating thickness is also assumed to be larger than the critical thickness (Scheme 1) required to avoid the substrate effect, similar to the previous case, the formation of only nanotube

morphology is expected for this sample as well. In contrast to this, the formation of both nanosheets and nanotubes (predominantly nanosheets) is observed, Figs 4.1d and 4.2c. The formation of mixed morphologies in the case of HTNF-7 sample is the result of large amount of Si pick-up by this sample (Fig. 4.3d), which is possibly due to the intercalation of SiO_4^{4-} ions within the layered structure of highly aggregated nanosheets of $H_2Ti_3O_7$. The stabilization of the intermediate nanosheet morphology of $H_2Ti_3O_7$ by the surface-adsorption of Si species during the hydrothermal treatment has been reported earlier in the literature.[4] There is also a strong possibility of the contribution of non-uniform distribution of Si species which may allow the formation of nanotubes at the specific locations where the concentration of Si species is relatively lower allowing the nanosheets to roll-up forming the nanotubes. The decrease in the specific surface-area and pore volume of this sample compared with those of HTNF-5 sample is ascribed to the effect of strong aggregation tendency of nanosheets and their large fraction in the nanocomposite relative to that of nanotubes, which is superimposed on the magnetic effect.

Thus, the formation of either nanosheets, nanotubes, or mixed morphologies for the hydrothermally processed HTNF magnetic nanocomposite as a function of number of sol-gel TiO_2 coating cycles is primarily governed by the roll-up mechanism superimposed with the substrate and Si pick-up effects.

4.3.3. MB dye-adsorption characteristics of HTNF magnetic nanocomposites

The adsorption performance of HTNF magnetic nanocomposites is studied by varying the initial MB concentration within the range of ~7.5-250 µM. The time dependent

variations in the normalized concentration of surface-adsorbed MB at the initial

solution-pH of ~10 are presented in Fig. 4.6 for the different HTNF samples.
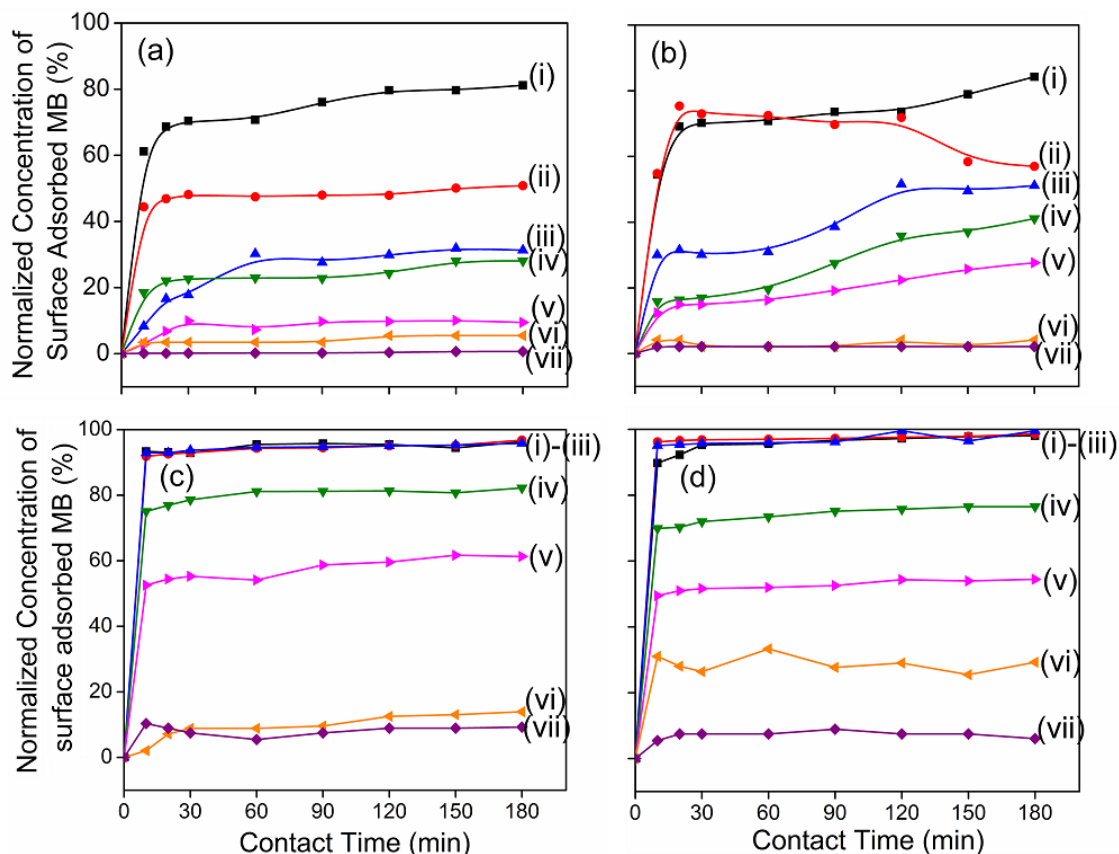
Fig. 4.6. Variations in the normalized concentration of surface-adsorbed MB as a

function of contact time as obtained for the HTNF-1 (a), HTNF-3 (b), HTNF-5 (c),

and HTNF-7 (d) samples. The initial MB dye concentration is varied as 7.5 (i), 30 (ii),

60 (iii), 90 (iv), 150 (v), 200 (vi), and 250 μM (vii).

The calculated values of q_e for the various HTNF samples at the different initial MB

concentrations are plotted in Fig. 4.7. It is noted that the q_e increases initially with the

initial MB concentration, reaches the maximum value within the initial MB

concentration range of ~90-150 μM, and then reduces with further increase in the

initial MB concentration. The initial rise in q_e is attributed to the greater driving force

for the gradual consumption of more number of active surface-sites available on the

surface of HTNF samples. The decrease in q_e values at higher initial MB concentration is ascribed to the decrease in the negative charge present on the surface of adsorbent as a result of reduction in the adsorption of OH$^-$ ions on its surface due to their strong interaction with the cationic MB molecules within the solution.[19]
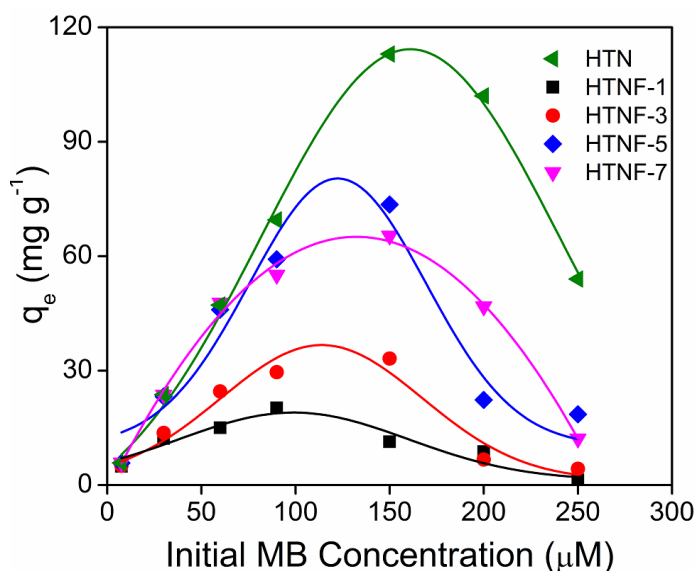
Fig. 4.7. Variation in q_e as a function of initial MB dye concentration as obtained for the HTNF samples.

The MB adsorption capacity (q_m) is estimated to be 20, 33, 74, and 65 mg g^{-1} for the HTNF-1, HTNF-3, HTNF-5, and HTNF-7 samples respectively. The MB adsorption capacity of γ-Fe$_2$O$_3$ nanoparticles and HTN is determined to be 13 and 113 mg g^{-1}.[9] Thus, the attachment of non-magnetic HTN to the magnetic γ-Fe$_2$O$_3$ nanoparticles via the hydrothermal reactions results in a net increase in the MB adsorption capacity of the HTNF magnetic nanocomposites from 13 to 20-74 mg g^{-1} which has been attributed to the higher MB adsorption capacity of pure HTN compared with that of γ-Fe$_2$O$_3$ nanoparticles. Moreover, the zeta-potential measurements in Fig. 4.8 suggest that the point-of-zero charge for the pure HTN, pure γ-Fe$_2$O$_3$ nanoparticles, and

HTNF-5 samples is 4.7, 5.0, and 5.3 respectively. Typically, at the initial solution-pH of 8.0, they exhibit the surface-potential of -22.7, -11.9, and -30 mV respectively. It appears that at the initial solution-pH of 10, the surface of HTNF-5 magnetic nanocomposite is highly negatively charged which is contributed by the adsorption of hydroxyl ions (OH⁻) and the Bronsted acidic nature of titanate surface resulting from the dissociation of $H_2Ti_3O_7$ as per the following reaction.[13,28]

$$H_2Ti_3O_7 \leftrightarrow 2H^+ + Ti_3O_7^- \tag{4.1}$$
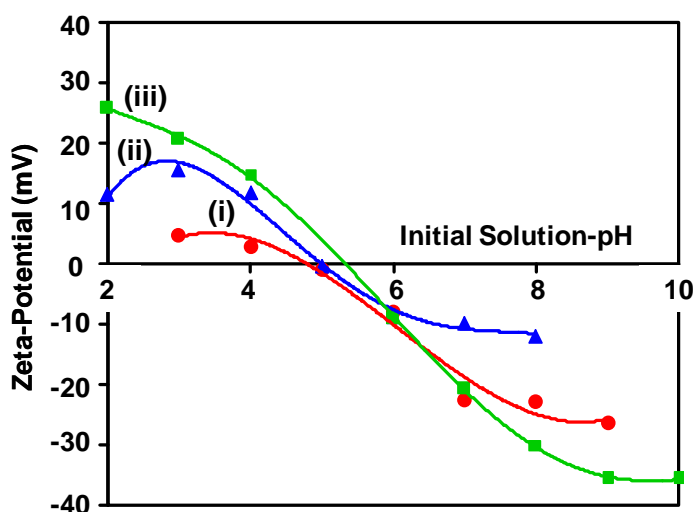
Fig. 4.8. Variation in the zeta-potential of pure HTN (i), pure $\gamma\text{-}Fe_2O_3$ nanoparticles (ii), and HTNF-5 (iii) samples as a function of initial solution-pH.

It is noted that the MB adsorption capacity of HTNF samples lie in between that of pure $\gamma\text{-}Fe_2O_3$ nanoparticles and pure HTN. It is further noted that with the increasing HTN content of the magnetic nanocomposite samples, the MB adsorption capacity is increased which is attributed to the corresponding increase in the specific surface-area and pore volume of the samples. However the dye-adsorption capacity is noted to decrease suddenly for the HTNF-7 sample which is ascribed to its lower specific

surface-area and pore volume compared with that of HTNF-5 sample. The maximum MB adsorption capacity (74 mg g^{-1}) is, thus, exhibited by the HTNF-5 sample which appears to be the most optimum one.

The time dependent MB adsorption over the HTNF surface is analyzed using two different kinetics models – Lagergren pseudo-first-order and pseudo-second-order. The linear forms of the above kinetics models are provided in the chapter 1.The linear plots (Fig. 4.9) with the regression correlation coefficient, $<r^2>$, approximately equal to one and the q_e values approximately equal to that of experimentally observed values, q_e (Exp), (Table 4.1) suggest that the MB adsorption on the surface of HTNF magnetic nanocomposites follows the pseudo-second-order kinetics.
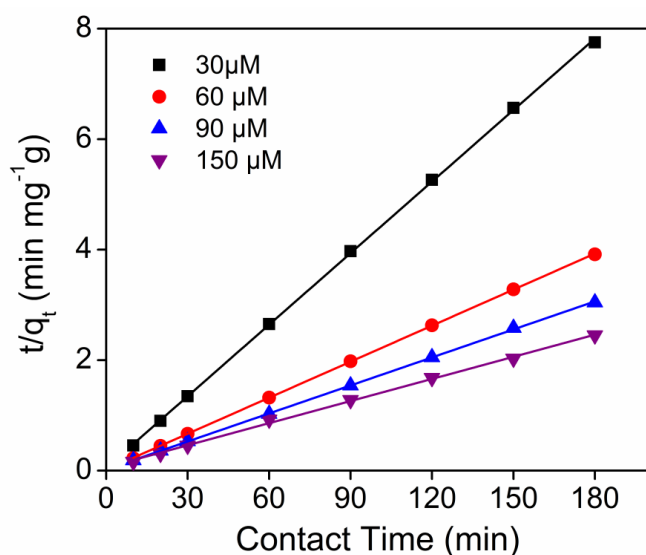
Fig. 4.9. Typical pseudo-second-order kinetics plots as obtained for the HTNF-5 sample for the different initial MB dye concentrations.

Adsorption isotherm study is very important to understand the nature of the adsorbate-adsorbent interaction. The equilibrium adsorption of MB on the surface of HTNF samples is analyzed using three well known adsorption isotherm models - Langmuir, Freundlich, and DKR. The fitted curves for the equilibrium MB adsorption on the

surface of HTNF-5 sample obtained using the above isotherm models are shown in Fig. 4.10.

Table 4.1. Various parameters of pseudo-second-order kinetics model as obtained for the different HTNF samples.

Samples	Initial MB Concentration	q_e *(Exp)*	q_e	k_2	r^2
HTNF-1	7.5	4.86	4.98	0.035	0.998
	60	15.0	17.9	0.002	0.988
	90	20.2	20.8	0.004	0.984
	150	11.3	13.0	0.005	0.976
HTNF-3	7.5	5.10	5.00	0.025	0.992
	60	24.5	27.8	0.001	0.950
	90	29.6	33.3	0.008	0.990
	150	33.2	30.3	0.002	0.990
HTNF-5	7.5	5.80	5.78	0.302	0.999
	60	45.9	47.6	0.03	1
	90	59.2	62.5	0.013	0.999
	150	73.5	71.4	0.007	0.990
HTNF-7	7.5	5.9	5.9	0.124	1
	60	47.8	47.6	0.018	0.999
	90	55.1	55.6	0.009	0.999
	150	65.3	66.7	0.007	0.999
HTN	7.5	5.84	5.88	0.22	0.999
	60	47.2	47.6	0.11	1
	90	69.5	71.4	---	1
	150	113	125	0.003	0.999
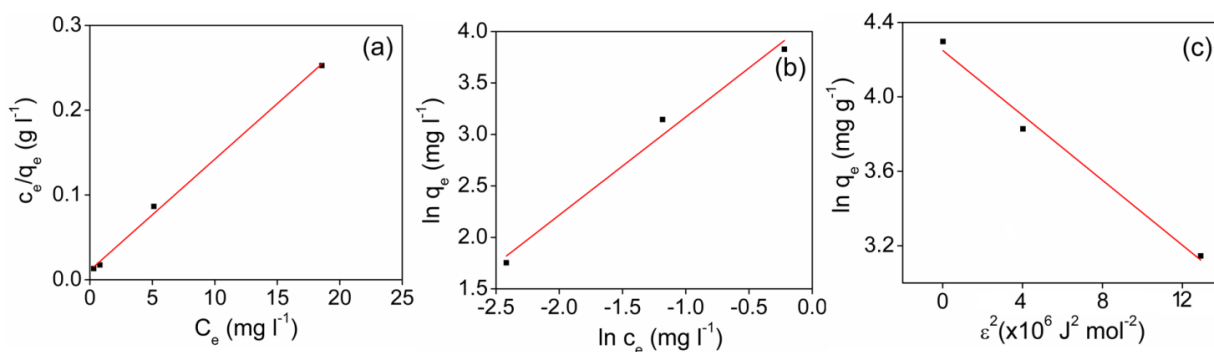
Fig. 4.10. Typical Langmuir (a), Freundlich (b), and DKR (c) plots as obtained for the HTNF-5 sample.

The calculated values of different parameters of these equilibrium isotherm models are listed in the Table 4.2. The superior matching of q_m values as obtained via the Langmuir and DKR models with the experimentally observed values (q_m (Exp)), along with the $<r^2>$ values close to unity, strongly suggest the validity of these isotherm models. Hence, in the present investigation, the equilibrium adsorption of MB on the surface of HTNF magnetic nanocomposites follows both the Langmuir and DKR models which is in good agreement with that observed for the pure HTN as discussed in the previous chapter.[9,19] Moreover, the degree of suitability of HTNF samples towards the adsorption of MB is estimated from the values of separation factor (R_L). The adsorption process is unfavorable if $R_L > 1$, linear if $R_L = 1$, favorable if $0 < R_L < 1$, or irreversible if $R_L = 0$. The R_L values for the MB adsorption on the surface of both pure HTN and HTNF magnetic nanocomposites lie in between 0.002-0.55, which indicates that the adsorption process is favorable. Further, the spontaneity of MB adsorption on the surface of HTNF samples can be tested from the values of change in the Gibb's free energy (ΔG^0, J mol^{-1}). Both the negative values of ΔG^0 and E values less than 8 kJ mol^{-1} (Table 2), strongly suggest the spontaneous monolayer MB adsorption on the

surface of HTNF samples via the electrostatic attraction mechanism (and not via the ion-exchange mechanism).

Table 4.2. Values of parameters of different equilibrium adsorption isotherm models as obtained for the different HTNF samples.

Samples	q_m (Exp)	Langmuir					Freundlich			DKR			
		q_m	k_L	R_L	ΔG	r^2	n	k_F	r^2	q_m	β	E	r^2
HTNF-1	11.3	22	0.33	0.09-0.55	-31	0.951	2.8	6.6	0.986	17.5	-2×10^{-7}	1.6	0.961
HTNF-3	33.2	39	0.21	0.05-0.5	-32	0.984	2.3	7.9	0.979	31.6	-3×10^{-6}	0.4	0.980
HTNF-5	73.5	77	1.18	0.02-0.2	-35	0.997	4.0	1.3	0.857	66.0	-8×10^{-8}	2.5	0.971
HTNF-7	65.3	67	2.14	0.01-0.16	-36	0.997	4.9	35.8	0.995	62.4	-4×10^{-8}	3.5	0.988
HTN	113	143	2.33	0.002-0.15	-36	0.979	1.9	81.6	0.944	129	-6×10^{-8}	2.9	0.987

4.3.4. Magnetic separation, regeneration (surface-cleaning), and reuse (recycling) of HTNF magnetic nanocomposite

The magnetic hysteresis loops obtained for the HTNF samples at room temperature are displayed in the Fig. 4.11. The S-like hysteresis loops, very low values of remanence field and coercivity indicate the superparamagnetic nature of the nanocomposites. The magnetic nanoparticles of γ-Fe_2O_3 possess relatively higher saturation magnetization value of 71 emu g^{-1}. It is noted that the magnetization of HTNF nanocomposites is gradually decreased from HTNF-1 to HTNF-7 sample due to decrease in the weight-fraction of γ-Fe_2O_3 nanoparticles. The saturation magnetization values are noted to be 62, 52, 36, and 34 emu g^{-1} for the HTNF-1, HTNF-3, HTNF-5, and HTNF-7 samples respectively. Appreciable magnetization values enable their fast separation from the treated aqueous solution in less than a

minute. The digital photograph of the separation process as demonstrated for the HTNF-5 magnetic nanocomposite particles, after the surface-adsorption of MB dye in an aqueous solution, is presented as an inset in Fig. 4.11.
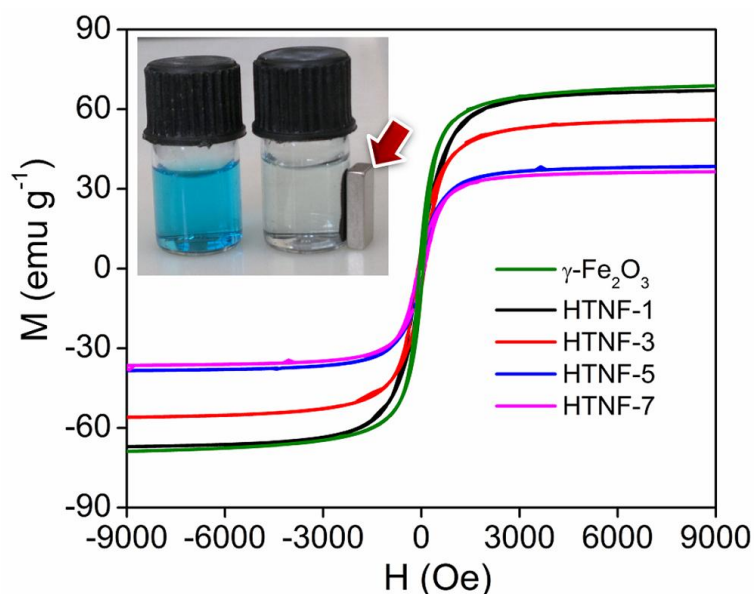
Fig. 4.11. Magnetization curves as obtained for the pure γ-Fe$_2$O$_3$ nanoparticles and HTNF samples. The inset in upper-left corner shows the magnetic separation of HTNF-5 sample in an aqueous solution using an external bar magnet which is indicated by an arrow.

In the dye-removal application, the regeneration of adsorption sites is generally achieved by desorbing the adsorbent molecules using organic solvents such as acetone, ethanol, acrylonitrile, and ethyl acetate.[29] In the case of acidic and basic dyes, this has been accomplished by adjusting the solution-pH using the NaOH and HCl solutions respectively.[30] However, these techniques merely transfer the organics from the catalyst-surface to the desorption medium; thus, creating a secondary pollution. The other most commonly employed techniques for the regeneration of adsorbents are the thermal decomposition, photocatalytic and chemical oxidation which are energy-

157

sensitive techniques.[31-33] In this respect, the recycling of titanate nanotubes via the oxidative catalytic process involving the activation of H_2O_2, as recently demonstrated by us,[15] and followed by others,[34-35] is highly noteworthy since the surface-adsorbed organics are completely decomposed in an aqueous solution in the dark. Although the dynamics of the radical-ions generation and their role in the dye-decomposition process have been thoroughly investigated in the case of the photocatalysis mechanism,[36] such study in the case of H_2O_2 activation using the semiconductor-oxides nanostructures, such as the titanate nanotubes, is very limited. Hence, the recyclability of HTNF magnetic nanocomposite is demonstrated here through the catalytic decomposition of the surface-adsorbed dye molecules via the H_2O_2 activation.

The obtained variation in the amount of MB dye adsorbed on the surface of HTNF-5 sample for the six successive cycles of dye-adsorption, conducted without and with the involvement of surface-cleaning treatment, is shown as a bar diagram in Fig. 4.12. It is clearly observed that without the surface-cleaning treatment, the MB adsorption on the surface of HTNF-5 sample decreases almost by ~89%. Comparison, however, shows that only a marginal decrease of 1.5% is observed with the involvement of surface-cleaning treatment conducted in the H_2O_2 solution. This strongly suggests that without the surface-cleaning treatment, more number of potential sites available for MB adsorption on the surface of HTNF-5 sample is consumed resulting in a progressive decrease in the amount of MB dye adsorbed after each cycle of dye-adsorption. The surface-cleaning treatment conducted in the H_2O_2 solution, however, decomposes the dye already adsorbed in the previous cycle resulting in the restoration of total number of potential sites available for MB adsorption on the catalyst surface.

As a result, the amount of MB dye adsorbed remains very high for each successive cycle of dye-adsorption.
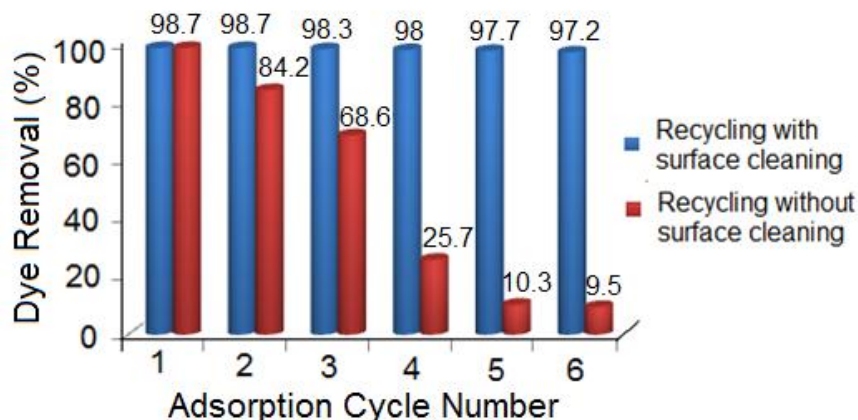
Fig. 4.12. Variation in the normalized concentration of MB dye adsorbed after 1 h of contact time as a function of dye-adsorption cycle number as obtained for the HTNF-5 sample without and with the involvement of surface-cleaning treatment conducted after each dye-adsorption cycle. The initial MB dye concentration is ~30 μM and the initial H_2O_2 concentration used for the surface-cleaning treatment is 15 wt%.

4.3.5. Mechanism of MB degradation on the surface of HTNF magnetic nanocomposite via H_2O_2 activation

The HTNF-5 magnetic nanocomposite essentially contains 31 wt% of HTN and balance γ-Fe_2O_3 nanoparticles as the major constituents. It is generally accepted that the degradation of an organic synthetic-dye, such as MB, via the Fenton-like reactions takes place by the generation and attack of ROS such as $O_2^{\bullet-}$ and $^{\bullet}OH$.[37] In the case of MB, the dye decomposition reactions can be written as given below,[38]

$$C_{16}H_{18}N_3S^+ + 102\,^{\bullet}OH \xrightarrow{\text{HTNF}} 16CO_2 + 3NO_3^- + SO_4^{2-} + 6H^+ + 57H_2O \qquad (4.2)$$

$$2C_{16}H_{18}N_3S^+ + 51O_2^- \xrightarrow{\text{HTNF}} 32CO_2 + 6NO_3^- + 2SO_4^{2-} + 12H^+ + 12H_2O + 102e^- \qquad (4.3)$$
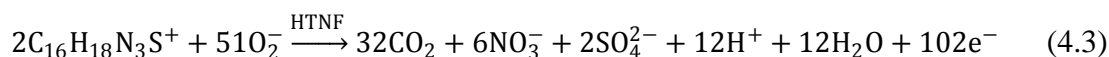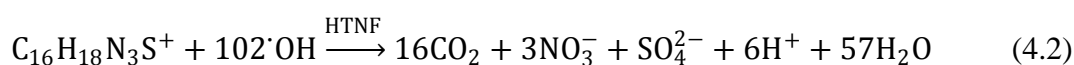
(Note: the generated electrons in Eq. 4.3 may be picked by the dissolved oxygen). Hence, in order to confirm the proposed mechanism of decomposition of MB dye on the surface of HTNF-5 magnetic nanocomposite via the activation of H_2O_2 and also to elucidate the precise role of individual catalyst components, the $O_2^{\bullet-}$ and $^{\bullet}OH$ were trapped using two different radical trapping agents. The obtained variation in the concentration of $^{\bullet}OH$ produced after 10 min of contact time for the different catalysts is presented and compared in Fig. 4.13. It is noted that both pure HTN and pure γ-Fe_2O_3 nanoparticles produce relatively lower concentration of $^{\bullet}OH$. Moreover, the concentration of $^{\bullet}OH$ produced by pure γ-Fe_2O_3 nanoparticles is relatively higher than that produced by pure HTN. However, the concentration of $^{\bullet}OH$ generated by the HTNF-5 magnetic nanocomposite is much higher than that produced by the individual components and their cumulative effect which strongly suggests a positive synergy effect in between them. It has been proposed that the activation of H_2O_2 in the presence of pure HTN results in the generation of $^{\bullet}OH$ via the following sequence of chemical reactions which includes the well-known Haber-Weiss reaction.[39]

$$H_2O_2 \xrightarrow{\text{HTN}} O_2^{\bullet-} + 2H^+ + e^- \tag{4.4}$$

$$H_2O_2 + O_2^{\bullet} \xrightarrow{\text{HTN}} {}^{\bullet}OH + OH^- + O_2 \tag{4.5}$$

$$O_2 + e^- \xrightarrow{\text{HTN}} O_2^{\bullet-} \tag{4.6}$$
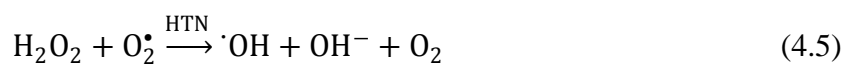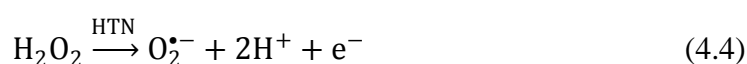
Moreover, the pure γ-Fe_2O_3 nanoparticles are also responsible for the generation $^{\bullet}OH$ via the following Fenton-like reactions.[40]

$$Fe^{3+} + H_2O_2 \xrightarrow{\gamma-Fe_2O_3} Fe^{2+} + {}^{\bullet}OOH + H^+ \tag{4.7}$$

$$Fe^{2+} + H_2O_2 \xrightarrow{\gamma-Fe_2O_3} Fe^{3+} + \cdot OH + OH^- \tag{4.8}$$

$$Fe^{3+} + O_2^{\bullet-} \xrightarrow{\gamma-Fe_2O_3} Fe^{2+} + O_2 \tag{4.9}$$
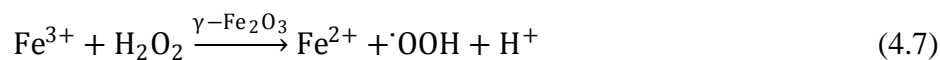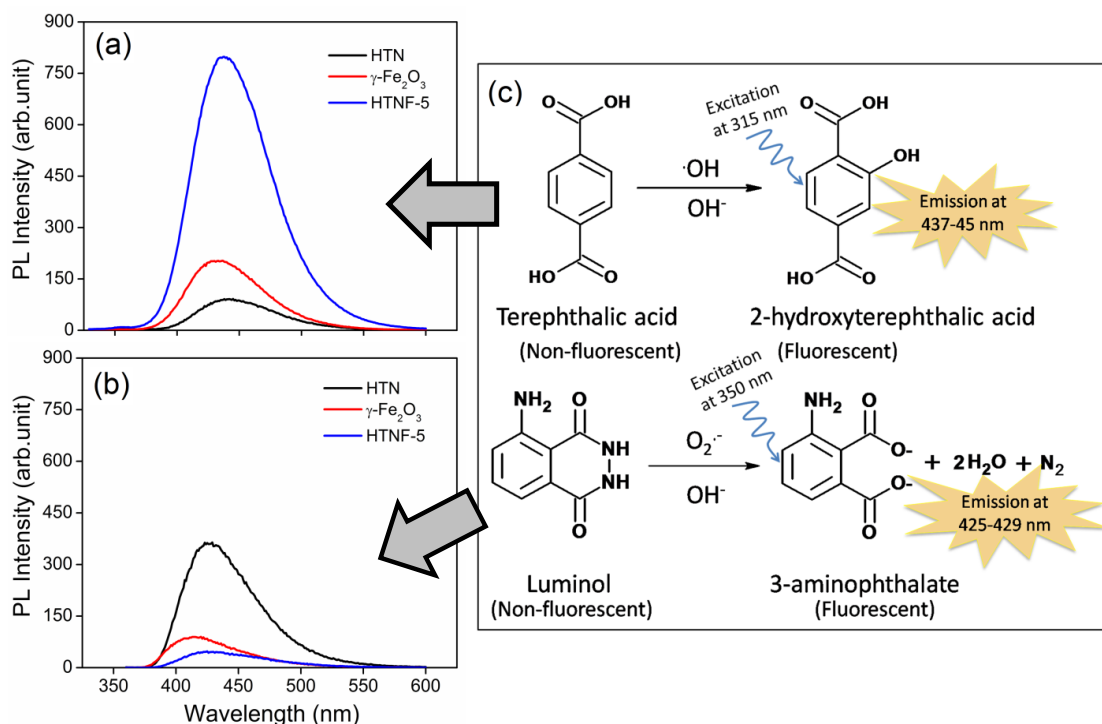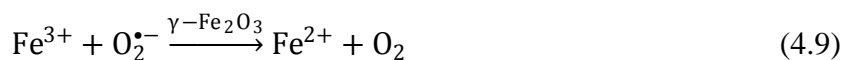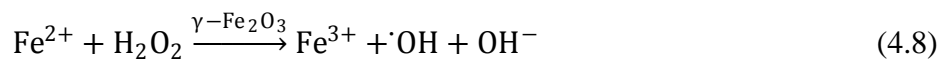
Fig. 4.13. PL intensities in the visible range associated with 2-hydroxyterpthalic acid (a) and 3-aminophthalate (b) formed as a result of radical trapping (c), after the contact time of 10 min, as observed for the different catalysts at the excitation wavelengths of ~315 and ~350 nm respectively. PL intensities observed in (a) and (b) are proportional to the concentration of $\cdot OH$ and $O_2^{\bullet-}$ produced as a result of the activation of H_2O_2 using the different catalysts.

The positive synergy effect between the HTN and $\gamma-Fe_2O_3$ nanoparticles in the generation of $\cdot OH$ can be explained based on the chemical reactions presented in the Eqs. 4.4-4.6, 4.8 and 4.9. It appears that large amount of $O_2^{\bullet-}$ are produced by HTN alone (Eqs. 4.4 and 4.6) which drive the chemical reaction presented in Eq. 4.9 in the

forward direction when both the HTN and γ-Fe_2O_3 nanoparticles are simultaneously present in the H_2O_2 solution in the form of HTNF-5 magnetic nanocomposite. As a consequence, for the HTNF-5 magnetic nanocomposite, the concentration Fe^{2+} ions is relatively higher than that of pure γ-Fe_2O_3 nanoparticles which results in the generation of relatively higher concentration of $^{\bullet}OH$ via the chemical reaction presented in the Eqs. 4.5 and 4.8 as noted in Fig. 4.13.

It, hence, appears that during the operation of above mechanism involving the activation of H_2O_2 using the magnetic HTNF-5 sample, the concentration of $O_2^{\bullet-}$ produced by the latter must be lower than that of pure HTN. In order to confirm this hypothesis, the $O_2^{\bullet-}$ trapping experiments were conducted and the obtained variation in the concentration of $O_2^{\bullet-}$ produced after 10 min of contact time for the different catalysts is presented and compared in Fig. 4.13b. It is clear that both pure HTN and pure γ-Fe_2O_3 nanoparticles produce $O_2^{\bullet-}$. Using the electron paramagnetic resonance (EPR) and X-ray photoelectron spectroscope (XPS) spectroscope analyses, Lorencon et al.[34] and Zhou et al.[35] also confirmed that the $O_2^{\bullet-}$ are generated via the H_2O_2 activation using the pure HTN in the dark-condition (that is, without the UV-irradiation) and are responsible for the decomposition of MB and Rhodamine B dyes. In Fig. 4.13b, the concentration of $O_2^{\bullet-}$ produced by the pure HTN is observed to be relatively higher than that produced by the pure γ-Fe_2O_3 nanoparticles. However, the concentration of $O_2^{\bullet-}$ generated by the HTNF-5 magnetic nanocomposite is lower than that produced by the individual components and much lower than their cumulative effect. Thus, a negative synergy effect is undoubtedly observed in between the HTN and γ-Fe_2O_3 nanoparticles for the generation of $O_2^{\bullet-}$ which strongly supports the mechanism proposed above for the generation of $^{\bullet}OH$ via the activation of H_2O_2 using

the HTNF-5 magnetic nanocomposite. Hence, in the case of HTNF-5 magnetic nanocomposite, the generated $O_2^{\cdot-}$ are rapidly consumed and converted to $^{\cdot}OH$ as a consequence of the synergy effect of two components. The net result is that the concentration of $^{\cdot}OH$ produced by the activation of H_2O_2 using the HTNF-5 sample is very high; while, that of $O_2^{\cdot-}$ is very low.

Based on the above results, the degradation of MB dye on the surface of HTNF-5 sample (that is, the surface-cleaning treatment) is attributed to the predominance of chemical reaction presented in Eq. 4.2 over that presented in Eq. 4.3. This is in contrast to pure HTN for which the degradation of MB dye on their surfaces appears to be predominantly due to the chemical reaction presented in Eq. 4.3 than that presented in Eq. 4.2. It is further noted that, in the present investigation, the activation of H_2O_2 is achieved using the combination of magnetic γ-Fe_2O_3 nanoparticles and the non-magnetic nanotubes of $H_2Ti_3O_7$ typically in the dark-condition which is in contrast to the activation of H_2O_2 normally reported under the UV-radiation exposure for the semiconductor-oxides (such as TiO_2) based photocatalysis mechanism.[41] Thus, the precise role of ROS, and hence, the underlying dye-decomposition mechanism are elucidated here using the different radical trapping agents via PL studies which, for the first time, clearly reveal the synergy effect of the constituents of HTNF magnetic nanocomposite. The present dye removal method provide a systematic approach for the dye-removal, magnetic separation, regeneration, and reuse of the magnetic nanocomposite for its successive use as a catalyst and the possible scale-up of the new technology in the near-future to meet the industrial requirement, which is schematically represented in Scheme. 4.2.
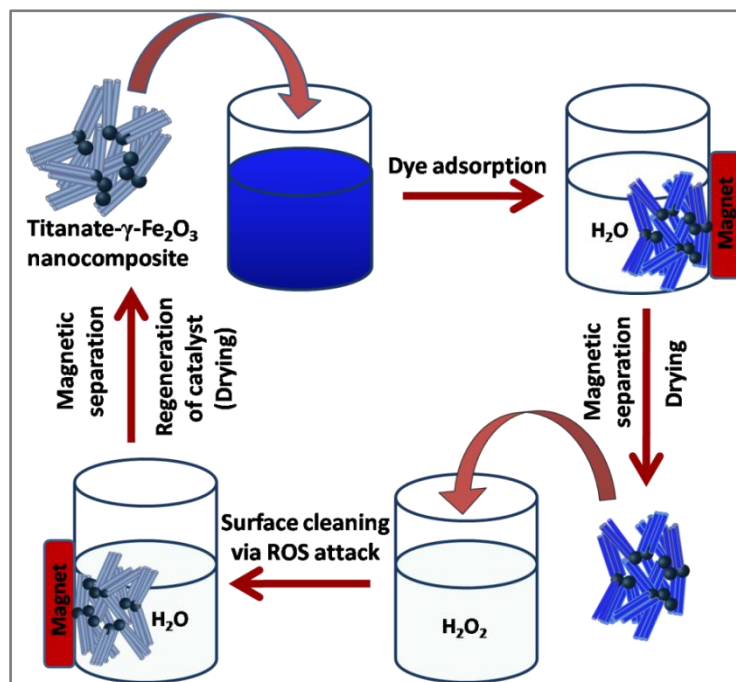
Scheme 4.2. The envisioned dye-removal technology based on the hydrothermally processed HTNF magnetic nanocomposite suitable for the treatment of industrial effluents containing organic synthetic-dyes.

4.4. Conclusions

The mesoporous magnetic nanocomposite consisting of $H_2Ti_3O_7$ nanosheets/ nanotubes and γ-Fe_2O_3 nanoparticles are successfully synthesized with a varying HTN weight-fraction via the hydrothermal transformation of the core-shell γ-Fe_2O_3/SiO_2/TiO_2 magnetic photocatalyst. Lower amounts of sol-gel coated (cycles-1 to 3) TiO_2 in the magnetic photocatalyst results in the formation of titanate nanosheets; whereas, relatively higher amount (cycle-5) leads to the rolling of nanosheets to the nanotube morphology. For the highest amount of TiO_2 (cycle-7), mixed morphologies are observed to form. Such variations in the observed morphologies of $H_2Ti_3O_7$ in the HTNF magnetic nanocomposite as a function of increasing amount of TiO_2 is attributed to the roll-up mechanism superimposed with

the substrate and Si pick-up effects. The magnetic HTNF-5 sample containing 31 wt% HTN exhibits the highest MB adsorption capacity (74 mg g^{-1}) which is ascribed to its higher specific surface-area and pore volume. The equilibrium adsorption of MB dye on the surface of HTNF-5 magnetic nanocomposite follows the pseudo-second-order kinetics and Langmuir and DKR isotherm models. The recyclability (that is, the regeneration and reuse) of HTNF-5 sample in the dye-removal application is achieved by the magnetic separation in less than a minute and decomposing the previously adsorbed MB dye on the surface via the H_2O_2 activation in which the contribution of $^\bullet OH$ dominates that of $O_2^{\bullet -}$ as a result of the newly observed synergy effect between the constituents of HTNF magnetic nanocomposite.

Reference

1.   Liu, S. Q., Magnetic semiconductor Nano-Photocatalysts for the degradation of organic pollutants. *Environ. Chem. Lett. 10(3)*, 209-216.

2.   Beydoun, D.; Amal, R.; Low, G.; McEvoy, S., Occurrence and prevention of photodissolution at the phase junction of magnetite and titanium dioxide. *J. Mol. Catal. A: Chem.* **2002**, *180*(1-2), 193-200.

3.   Sivashankar, R.; Sathya, A.; Vasantharaj, K.; Sivasubramanian, V., M agnetic composite an environmental super adsorbent for dye sequestration–a Review. *Environ. Nanotechnol. Monit. Manage.* **2014**, *1*, 36-49.

4.   Hareesh, P.; Babitha, K. B.; Shukla, S., Processing fly ash stabilized hydrogen titanate nanosheets for industrial dye-removal application. *J. Hazard. Mater.* **2012**, *229–230*, 177-182.

5.   Thazhe, L.; Shereef, A.; Shukla, S.; Pattelath Reshmi, C.; Varma, M. R.; Suresh, K. G.; Patil, K.; Warrier, K. G., Magnetic dye-adsorbent catalyst:

processing, characterization, and application. *J. Am. Ceram. Soc.* **2010**, *93*(11), 3642-3650.

6.   Li, W.; Deng, Y.; Wu, Z.; Qian, X.; Yang, J.; Wang, Y.; Gu, D.; Zhang, F.; Tu, B.; Zhao, D., Hydrothermal etching assisted crystallization: a facile route to functional yolk-shell titanate microspheres with ultrathin nanosheets-assembled double shells. *J. Am. Chem. Soc.* **2011**, *133*(40), 15830-15833.

7.   Zhou, L.; Xu, M.; Wei, G.; Li, L.; Chubik, M.; Chubik, M. P.; Gromov, A. A.; Han, W., Fe_3O_4@ Titanate nanocomposites: novel reclaimable adsorbents for removing radioactive ions from wastewater. *J Mater Sci: Mater Electron* **2015**, *26*(5), 2742-2747.

8.   Papa, A. L.; Maurizi, L.; Vandroux, D.; Walker, P.; Millot, N., Synthesis of titanate nanotubes directly coated with USPIO in hydrothermal conditions: a new detectable nanocarrier. *J. Phys. Chem. C* **2011**, *115*(39), 19012-19017.

9.   Harsha, N.; Krishna, K. V. S.; Renuka, N. K.; Shukla, S., Facile synthesis of γ-fe_2o_3 nanoparticles integrated $H_2Ti_3O_7$ nanotubes structure as a magnetically recyclable dye-removal catalyst. *RSC Adv.* **2015**, *5*(38), 30354-30362.

10.   Gracia-Espino, E.; Lopez-Urias, F.; Terrones, H.; Terrones, M.; Tascon, J., Novel nanocarbons for adsorption. Elsevier: Oxford, UK: 2012; pp 3-35.

11.   Gupta, V. K.; Suhas, Application of low-cost adsorbents for dye removal – a review. *J. Environ. Manage.* **2009**, *90*(8), 2313-2342.

12.   Lee, C. K.; Lin, K. S.; Wu, C. F.; Lyu, M. D.; Lo, C. C., Effects of synthesis temperature on the microstructures and basic dyes adsorption of titanate nanotubes. *J. Hazard. Mater.* **2008**, *150*(3), 494-503.

13. Bavykin, D. V.; Redmond, K. E.; Nias, B. P.; Kulak, A. N.; Walsh, F. C., The effect of ionic charge on the adsorption of organic dyes onto titanate nanotubes. *Aust. J. Chem.* **2010**, *63*(2), 270-275.

14. Lee, C. K.; Fen, S. K.; Chao, H. P.; Liu, S. S.; Huang, F. C., Effects of pore structure and surface chemical characteristics on the adsorption of organic vapors on titanate nanotubes. *Adsorption* **2012**, *18*(5-6), 349-357.

15. Babitha, K. B.; Warrier, K. G.; Shukla, S., Decolorization of aqueous solution containing organic synthetic-dye via dark-catalysis process using hydrothermally synthesized semiconductor-oxides nanotubes. *Adv. Sci., Eng. Med.* **2014**, *6*(2), 173-183.

16. Shukla, S.; Warrier, K. G. K.; Babu, B. K., A process for decomposition of organic synthetic-dyes using semiconductor-oxides nanotubes via dark-catalysis. *World Intellectual Property Organization (WIPO) Publication Number WO/2014/027364,* **20-February-2014**..

17. Shukla, S.; Oturan, M. A., Dye Removal Using Electrochemistry and Semiconductor Oxide Nanotubes. *Environ Chem Lett* **2015**, *13*(2), 157-172.

18. Narayani, H.; Kunniveetil, S. P.; Shukla, S., Effect of solution-ph on methylene blue dye adsorption on hydrogen titanate nanotubes processed via hydrothermal method. *Adv. Sci., Eng. Med.* **2013**, *5*(1), 63-72.

19. Nosaka, Y.; Yamashita, Y.; Fukuyama, H., Application of chemiluminescent probe to monitoring superoxide radicals and hydrogen peroxide in TiO_2 photocatalysis. *J. Phys. Chem. B* **1997**, *101*(30), 5822-5827.

20. Ishibashi, K. I.; Fujishima, A.; Watanabe, T.; Hashimoto, K., Detection of active oxidative species in TiO_2 photocatalysis using the fluorescence technique. *Electrochem. Commun.* **2000**, *2*(3), 207-210.

21. Narayani, H.; Arayapurath, H.; Shukla, S., Significance of silica interlayer in magnetic photocatalyst having γ-Fe$_2$O$_3$ as a magnetic ceramic core. *Sci. Adv. Mater.* **2013**, *5*(8), 1060-1073.

22. Abramson, S.; Srithammavanh, L.; Siaugue, J. M.; Horner, O.; Xu, X.; Cabuil, V., Nanometric core-shell-shell γ-Fe$_2$O$_3$/SiO$_2$/TiO$_2$ particles. *J. Nanopart. Res.* **2009**, *11*(2), 459-465.

23. Yu, X.; Liu, S.; Yu, J., Superparamagnetic γ-Fe$_2$O$_3$@SiO$_2$@TiO$_2$ composite microspheres with superior photocatalytic properties. *Appl. Catal. B* **2011**, *104*(1-2), 12-20.

24. Wang, C.; Yin, L.; Zhang, L.; Kang, L.; Wang, X.; Gao, R., Magnetic (Fe$_2$O$_3$@SiO$_2$@TiO$_2$) functional hybrid nanoparticles with actived photocatalytic ability. *J. Phys. Chem. C* **2009**, *113*(10), 4008-4011.

25. Wu, D.; Liu, J.; Zhao, X.; Li, A.; Chen, Y.; Ming, N., Sequence of events for the formation of titanate nanotubes, nanofibers, nanowires, and nanobelts. *Chem. Mater.* **2006**, *18*(2), 547-553.

26. Kitano, M.; Wada, E.; Nakajima, K.; Hayashi, S.; Miyazaki, S.; Kobayashi, H.; Hara, M., Protonated titanate nanotubes with lewis and brønsted acidity: relationship between nanotube structure and catalytic activity. *Chem. Mater.* **2013**, *25*(3), 385-393.

27. Lu, H.; Zhao, J.; Li, L.; Zheng, J.; Zhang, L.; Gong, L.; Wang, Z.; Zhu, Z., A Systematic study on evolution mechanism of titanate nanostructures in the hydrothermal process. *Chem. Phys. Lett.* **2011**, *508*(4), 258-264.

28. Bavykin, D. V.; Friedrich, J. M.; Lapkin, A. A.; Walsh, F. C., Stability of aqueous suspensions of titanate nanotubes. *Chem. Mater.* **2006**, *18*(5), 1124-1129.

29.   Konicki, W.; Sibera, D.; Mijowska, E.; Lendzion-Bielun, Z.; Narkiewicz, U., Equilibrium and kinetic studies on acid dye acid red 88 adsorption by magnetic ZnFe$_2$O$_4$ spinel ferrite nanoparticles. *J. Colloid Interface Sci.* **2013**, *398*, 152-160.

30.   Zhang, Y. R.; Wang, S. Q.; Shen, S. L.; Zhao, B. X., A Novel water treatment magnetic nanomaterial for removal of anionic and cationic dyes under severe condition. *Chem. Eng. J.* **2013**, *233*, 258-264.

31.   Teixeira, T. P. F.; Aquino, S. F.; Pereira, S. I.; Dias, A., Use of calcined layered double hydroxides for the removal of color and organic matter from textile effluents: kinetic, equilibrium and recycling studies. *Braz. J. Chem. Eng.* **2014**, *31*, 19-26.

32.   Haitham, K.; Razak, S.; Nawi, M., Kinetics and Isotherm Studies of Methyl Orange Adsorption by a Highly Recyclable Immobilized Polyaniline on a Glass Plate. *Arabian J. Chem.* **2014**.

33.   Lin, S.; Wang, C., Adsorption and catalytic oxidation of phenol in a new ozone reactor. *Environ. Technol.* **2003**, *24*(8), 1031-1039.

34.   Lorencon, E.; Brandao, F. D.; Krambrock, K.; Alves, D. C. B.; Silva, J. C. C.; Ferlauto, A. S.; Lago, R. M., Generation of reactive oxygen species in titanates nanotubes induced by hydrogen peroxide and their application in catalytic degradation of methylene blue dye. *J. Mol. Catal. A* **2014**, *394*, 316-323.

35.   Zhou, C.; Luo, J.; Chen, Q.; Jiang, Y.; Dong, X.; Cui, F., Titanate nanosheets as highly efficient non-light-driven catalysts for degradation of organic dyes. *Chem. Commun.* **2015**, *51*(54), 10847-10849.

36.   Schneider, J.; Matsuoka, M.; Takeuchi, M.; Zhang, J.; Horiuchi, Y.; Anpo, M.;
       Bahnemann, D. W., Understanding TiO_2 photocatalysis: mechanisms and
       materials. *Chem. Rev.* **2014**, *114*(19), 9919-9986.

37.   Wu, Q.; Feng, C.; Wang, C.; Wang, Z., A Facile one-pot solvothermal method
       to produce superparamagnetic graphene-fe_3o_4 nanocomposite and its
       application in the removal of dye from aqueous solution. *Colloids Surf., B*
       2013, *101*, 210-214.

38.   Houas, A.; Lachheb, H.; Ksibi, M.; Elaloui, E.; Guillard, C.; Herrmann, J.-M.,
       Photocatalytic degradation pathway of methylene blue in water. *Appl. Catal.,
       B* **2001**, *31*(2), 145-157.

39.   Costa, R. C.; Lelis, M.; Oliveira, L.; Fabris, J.; Ardisson, J. D.; Rios, R.; Silva,
       C.; Lago, R., Novel active heterogeneous fenton system based on Fe_3- XM
       XO_4 (Fe, Co, Mn, Ni): the role of M^{2+} species on the reactivity towards H_2O_2
       reactions. *J. Hazard. Mater.* **2006**, *129*(1), 171-178.

40.   Wang, C.; Liu, H.; Sun, Z., Heterogeneous photo-Fenton reaction catalyzed by
       nanosized iron oxides for water treatment. *Int. J. Photoenergy* **2012**, *2012*.

41.   Wong, C.; Chu, W., The Hydrogen peroxide-assisted photocatalytic
       degradation of alachlor in TiO_2 suspensions. *Environ. Sci. Technol.* **2003**,
       37(10), 2310-2316.

Synthesis of H₂Ti₃O₇/γ-Fe₂O₃ Magnetic Nanocomposite *via* Ion-exchange Mechanism and Its Dye-Adsorption/Decomposition Characteristics

Graphical Abstract
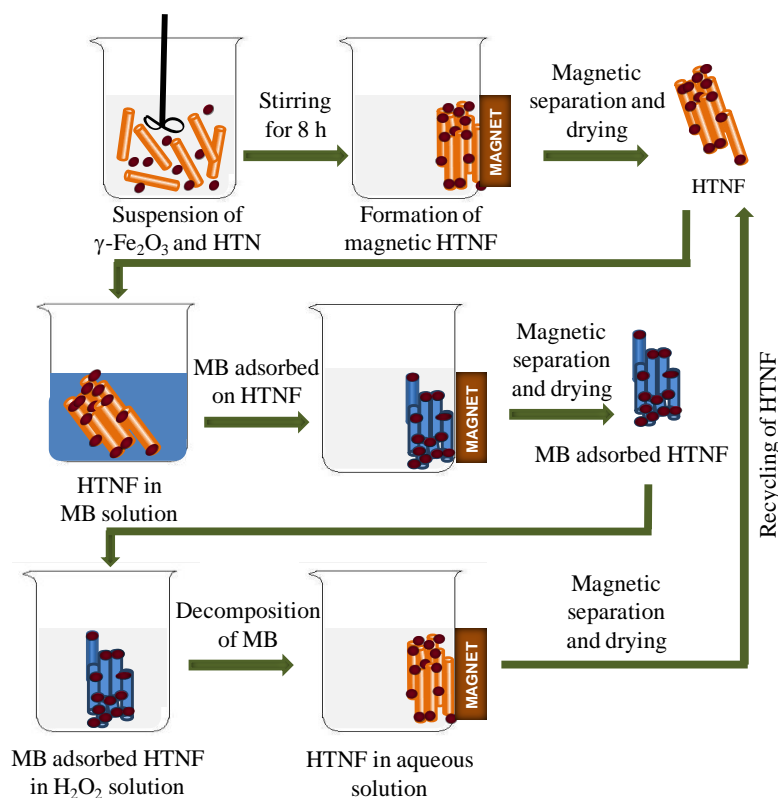
Highlights

- γ-Fe₂O₃–HTN synthesized using simple strategy involving the combination of hydrothermal treatment and mechanical mixing.

- The unique nanostructures of HTNF composites in which γ-Fe₂O₃ nanoparticles typically attached to the ends of HTN bundles.

- The MB dye-adsorption characteristics of HTNF nanocomposites have been investigated by varying the amount of γ -Fe₂O₃ (0–25 wt%).

Abstract

The nanocomposites consisting of γ-Fe_2O_3 nanoparticles incorporated hydrogen titanate ($H_2Ti_3O_7$) nanotubes (HTNF) have been synthesized through a simple strategy involving the combination of hydrothermal treatment followed by an ion-exchange process both conducted in the aqueous media. The resulting nanocomposites reveal high efficiency in dye-adsorption capacity, magnetic separability from an aqueous solution, and recyclability. The unique nanostructures of HTNF composites are composed of γ-Fe_2O_3 nanoparticles typically attached to the ends of HTN bundles rather than along the surface and exhibit high magnetic separability in an aqueous medium using a moderate external magnetic field. The MB dye-adsorption characteristics of HTNF nanocomposites have been investigated by varying the amount of γ-Fe_2O_3 (0-25 wt.%) and initial MB concentration (~7.5-250 μM) at the initial solution-pH of ~10. The HTNF nanocomposite with 5 wt% γ-Fe_2O_3 shows relatively higher MB dye adsorption capacity (99 mg g^{-1}) along with reasonable magnetic separability (2 min) from an aqueous solution. The MB adsorption on the surface of HTNF nanocomposites follows the pseudo-second-order kinetics model and the equilibrium adsorption isotherm follows both the Langmuir and Dubinin-Kaganer-Radushkevich (DKR) models. The recyclability of HTNF magnetic nanocomposite in the dye-removal application has been demonstrated by decomposing the previously adsorbed MB dye via the surface-cleaning treatment conducted in H_2O_2 solution.

5.1. Introduction

There is a growing interest in the development of magnetic nanocomposites of various structures and compositions in diverse fields such as biomedical, catalysis, drug delivery, adsorption, and others.[1-4] These materials have magnetic properties in addition to the properties of constituents which enables their easy separation under an external magnetic field; thus, overcoming the limitations of conventional separation techniques such as the filtration and centrifugation. High specific surface-area and mesoporous nature of certain magnetic nanocomposites allow an effective utilization of these materials in the field of environmental purification due to their effectiveness and recyclability in the process. Two magnetic materials of significant interest in this field are the photocatalysts and adsorbents. The use of magnetic photocatalysts having the core-shell structure has been demonstrated for the degradation of various organic species.[5] However, they suffer from two main drawbacks. First, the time required for the processing of thick TiO_2 coating (which cannot be obtained through a single-cycle) is very large; and second, the efficiency towards the decomposition of complex aromatic systems is lower. In this respect, the adsorption appears to be the most effective method due to its simplicity in operation, lower cost, and higher efficiency.

Magnetically assisted removal of water pollutant using high surface-area carbon based composites has been proposed with different nanostructures, involving nanocarbon, carbon nanotubes, and graphene.[6-8] However, such materials on the industry scale pose major limitations such as higher cost, difficult synthetic route, and lower yield. Moreover, certain functional groups are necessary to be loaded on their surfaces in order to make them hydrophilic. Recently, the hydrothermally processed titanate nanotubes of high specific surface-area have been shown to exhibit high adsorption-

capacity towards different pollutants mainly the organic-synthetic-dyes and toxic heavy metal-cations.[9-10] Their processing involves neither expensive experimental set-up nor excessive chemicals. As a result of their unique surface characteristics, the titanate nanostructures have been reported to be efficient for the removal of most of organic-synthetic-dyes. So far four different methods have been employed to load the magnetic nanoparticles on the titanate nanostructures. The first method involves the hydrothermal reaction involving the magnetic nanoparticles dispersed along with TiO_2 in an alkali solution.[11] However, in this method, the magnetic nanoparticles may get dissolved during the subsequent acid-washing step. Niu *et al.* reported an ion-exchange reaction for the adsorption of Fe^{3+}/Fe^{2+} ions on the surface of titanate nanostructures which were converted to magnetite (Fe_3O_4) nanoparticles via co-precipitation.[10] Liu *et al.* reported the self-assembly of titanate and magnetic nanoparticles in an acidic aqueous medium.[12] Lastly, Thazhe *et al.* derived the magnetic nanocomposite via the hydrothermal treatment of sol-gel derived core-shell structured magnetic photocatalyst particles.[13]

Herein, we report the easiest pathway for the synthesis of titanate-based magnetic nanocomposite without the use of any binding species which is the modification of process reported by Liu *et al.*[12] The as prepared magnetic nanocomposite is expected to be an excellent adsorbent because of large number of free adsorption sites on the surface of nanotubes due to the predominant attachment of magnetic nanoparticles to the ends of nanotubes. Although reusable magnetic adsorbent systems have been reported for the removal of metal-cations and organics,[14-20] to the best of our knowledge, there is no report available in the literature yet on the effect of addition of magnetic property on the dye-adsorption capacity of the titanate-based magnetic nanocomposites synthesized via the novel ion-exchange mechanism. The advantage

of using these nanocomposite materials for the present application involves the dye-removal in the dark condition, their separation from the treated aqueous solution using an external magnetic field with no loss in the amount of catalyst recovered, and their regeneration and reuse for the multiple cycles of dye-adsorption. We demonstrate here both a simplest route for the processing of titanate-based magnetic nanocomposite and its recyclability in the dye-removal application involving the surface-cleaning treatment conducted via a novel strategy by using the cationic MB dye as a substrate.

5.2. Experimental

5.2.1. Chemicals

Sodium hydroxide (NaOH, Assay 97 %) and methylene blue (MB, >96 %) were purchased from S.D. Fine-Chem Limited, India; hydrochloric acid (HCl, 35 wt.%) from Ranbaxy Fine-Chemicals, India; ammonium hydroxide (NH_4OH, 25 wt.%) from Fisher Scientific, India; nanocrystalline γ-Fe_2O_3 (<50 nm, 98%) magnetic powder from Sigma-Aldrich Chemicals, Bengaluru, India; and anatase-TiO_2 from the Central Drug House (CDH) Laboratory (P) Limited, India. All chemicals and powders were used as received without any further purification.

5.2.2. Synthesis of pure HTN and HTN/γ-Fe_2O_3 (HTNF) magnetic nanocomposites

The HTN were synthesized via the hydrothermal method as described in the chapter-3. The HTNF magnetic nanocomposites having varying fractions (0-25 wt%) of γ-Fe_2O_3 nanoparticles (Aldrich Chemicals, Bengaluru, India) were synthesized via the self-assembly process without the use of an acid-catalyst.[12] In this method, appropriate quantities of γ-Fe_2O_3 nanoparticles and HTN were dispersed separately in equal quantities of two different aqueous solutions at the neutral solution-pH (~6.5)

using an ultra-sonication bath (Bandelin Sonorex Super with Built-In Heating, Aldrich Labware, Bengaluru, India). The two suspensions were then mixed together to form total 1 g of solid particles suspended in 125 ml aqueous solution at the neutral solution-pH which was stirred vigorously using an overhead stirrer (IKA RW 14, Aldrich Labware, Bengaluru, India) for 8 h at 600 rpm. The brownish product formed was separated using an external magnetic field provided by a small bar magnet and dried in an oven at 80$^{\text{o}}$C overnight. The different magnetic nanocomposites are designated as HTNF-X where X represents the weight-percentage of γ-Fe_2O_3 in the magnetic nanocomposite.

5.2.3. Characterization of pure HTN and HTNF magnetic nanocomposites

The morphology and average size of different samples were determined using the transmission electron microscope (TEM, Tecnai G^2, FEI, The Netherlands) operated at 300 kV. (Note: The samples were ultrasonically dispersed in 30 ml acetone for 20 min in which the carbon-coated Cu-grid (Ted Pella, Inc., U.S.A.) of 3 mm diameter was dipped for the TEM sample preparation). The nanocrystalline nature of samples was confirmed via obtaining the selected-area electron diffraction (SAED) patterns. The crystalline phases present were determined using the X-ray diffraction (XRD, PW1710 Phillips, The Netherlands). The broad-scan analysis was typically conducted within the 2θ range of 5-80$^{\text{o}}$ using the Cu$K\alpha$ (λ_{Cu}=1.542 Å) X-radiation. The specific surface-area and pore-size distribution were measured using the Brunauer-Emmett-Teller (BET) surface-area measurement technique (Micrometrics Gemini 2375 Surface Area Analyzer, U.S.A.) via nitrogen (N_2) adsorption using the multi-point method after degassing the samples in flowing N_2 at 200°C for 2 h. The magnetic properties of different samples were measured using a vibrating sample magnetometer

(VSM) attached to a Physical Property Measurement System (PPMS, Quantum Design, Dynacool, U.S.A.). The pristine samples were subjected to different magnetic field strengths (H) and the induced magnetization (M) was measured at 298 K. The external magnetic field was reversed on saturation and the hysteresis loop was traced. The zeta-potential measurements were performed using the electrophoretic light scattering in the pH range from 2 to 9 using a Zetasizer Nano Series-Zen 3600 (Malvern Instruments, U.K.).

5.2.4. Dye-adsorption characteristics of pure HTN and HTNF magnetic nanocomposites

The dye-adsorption measurements were carried out using the MB dye via the procedure already described in the third chapter (section 3.2.4). These measurements were conducted in 125 ml aqueous solutions at the initial solution-pH of ~10 adjusted using the ammonium hydroxide (NH_4OH) solution (25% NH_3, Qualigens Fine Chemicals Pvt. Ltd., Mumbai, India) containing ~7.5-250 µM of MB dye and 0.4 g l^{-1} of adsorbent. The HTNF magnetic nanocomposites were separated from the aqueous solutions using an external magnetic field provided by a small bar magnet. The normalized concentration of surface-adsorbed MB dye was calculated using the Eqs. 3.1 and 3.2.

5.2.5. Surface-cleaning treatment and recycling of HTNF magnetic nanocomposite in the dye-removal application

The HTNF-5 sample was selected for the demonstration of surface-cleaning treatment and recycling in the dye-adsorption experiments. 0.4 g l^{-1} of HTNF-5 was added to 125 ml aqueous solution of MB dye having the initial concentration of

~90 μM at the initial solution-pH of ~10. The dye-adsorption measurement was then conducted using the procedure similar to the one described in the previous section. The HTNF-5 sample with the surface-adsorbed MB dye, after the separation from the aqueous solution using an external magnetic field provided by a small bar magnet and subsequent drying in an oven at 80°C overnight, was utilized for the second-cycle of dye-adsorption measurement conducted under the similar test-conditions. Total three successive cycles of dye-adsorption measurements were conducted. The HTNF-5 sample, with the MB dye adsorbed on its surface, was utilized for the surface-cleaning treatment. For this purpose, the former was added to 100 ml of 30 wt% H_2O_2 solution (S.D. Fine-Chem Ltd., Mumbai, India) and stirred continuously using an overhead stirrer for 3 h. The surface-cleaned powder was separated from the aqueous solution using an external magnetic field provided by a small bar magnet, and after drying in an oven at 80°C overnight, it was recycled for the fourth-cycle of dye-adsorption.

5.3. Results and discussion

5.3.1. Morphology, structure, and specific surface-area of pure HTN and HTNF magnetic nanocomposites

Fig. 5.1a shows the TEM image of pure HTN which are observed to form the bundles of nanotubes having the average length of ~100 nm and average inner diameter of ~4 nm. The cross-section of one of the nanotubes is shown as an inset (upper-left corner) in Fig. 5.1a where the thickness of cross-section is noted to be different on the opposite sides, which suggests that the nanotubes are formed via the roll-up mechanism.[21] The HTNF-5 sample presented in Fig. 5.1b shows that γ-Fe_2O_3 nanoparticles are firmly attached to the HTN bundles typically at the ends of nanotubes. Moreover, no free γ-Fe_2O_3 nanoparticles are observed for this sample. The

HTNF-10 sample, Fig. 5.1c, clearly exhibits relatively larger fraction of γ-Fe_2O_3

nanoparticles attached to the ends of aggregated HTN (see upper-left corner inset of

Fig. 5.1c) without the presence of free γ-Fe_2O_3 nanoparticles. In contrast to this, the

HTNF-25 sample shows both free (marked as encircled nanoparticles) as well as large

number of γ-Fe_2O_3 nanoparticles attached to the HTN bundles, Fig. 5.1d. The SAED

patterns (lower-right corner insets in Fig. 5.1) show the continuous ring patterns

which suggest the nanocrystalline nature of all samples.
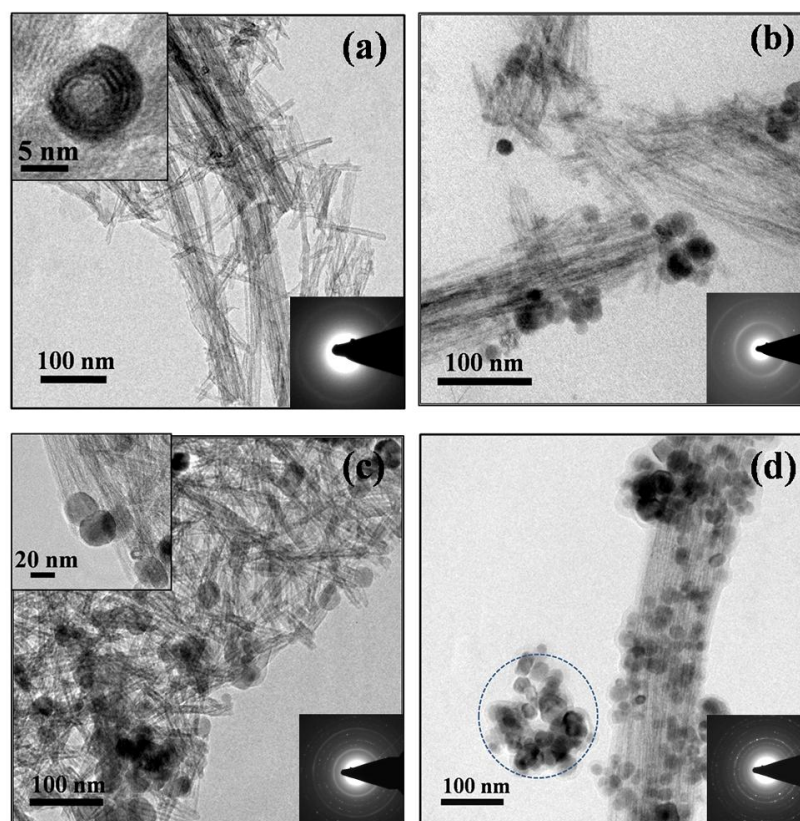
Fig. 5.1. TEM images of pure HTN (a), HTNF-5 (b), HTNF-10 (c), and HTNF-25 (d)

samples.The lower-right corner insets show the corresponding SAED patterns.

The site at which γ-Fe_2O_3 nanoparticles are attached to the HTN strongly indicate the

nature of interaction between the two. Liu *et al.* observed the deposition of γ-Fe_2O_3

nanoparticles all along the surface of HTN when the two were dispersed in an acidic

aqueous solution.[12] In contrast to this, as seen in the TEM images, most of the γ-Fe$_2$O$_3$ nanoparticles are attached to the ends of nanotubes where the surface energy is maximum since the ends of nanotubes are the edges of nanosheets from which the nanotubes are evolved. Although such interaction is also possible along the outer surface of titanate nanotubes, it is possibly inhibited due to the bundled nature of nanocomposites. There exists a predominant force of electrostatic interaction among the titanate nanotubes and γ-Fe$_2$O$_3$ nanoparticles in an acidic environment.[12] In the case of present nanocomposites, however, there is no extra charge on the surface of HTN since the nanocomposites are synthesized in the neutral solution-pH. (Note: The term "extra" here refers to the charge created by the external addition of acid or base into the system.) Under such situation, the chemisorption of OH$^-$ ions as well as Bronsted acidic nature of titanate surface develop a negative potential which involves the dissociation of H$_2$Ti$_3$O$_7$ as,[22]

$$H_2Ti_3O_7 \leftrightarrow 2H^+ + Ti_3O_7^{2-} \tag{5.1}$$
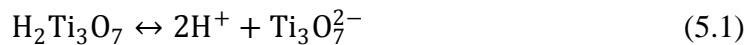
The zeta-potential measurements indiacte that the point-of-zero charge of γ-Fe$_2$O$_3$ nanoparticles and HTN is 5.0 and 4.7. Considering this, it is obvious that at the neutral solution-pH, they have the negative surface-potential of -10.8 and -22.6 mV and the chemisorbed OH$^-$ ions are primarily responsible for the negative surface-potential of γ-Fe$_2$O$_3$ nanoparticles. Although, initially the negative surface-potentials of both the solid surfaces would repel each other, the negative surface-charge on the γ-Fe$_2$O$_3$ nanoparticles may get neutralized due to the Bronsted acidic hydrogen titanate which may shift the equilibrium of Eq. 5.1 in the forward direction. This in turn can expose the surface of γ-Fe$_2$O$_3$ nanoparticles for the closest approach of HTN. The attachment of HTN to γ-Fe$_2$O$_3$ nanoparticles predominantly occurs on a highly

energetic site such as the ends of nanotubes. In our view, there is a strong possibility of ion-exchange reaction contributing to the actual bond formation of HTN with the surface of γ-Fe_2O_3 nanoparticles through the intercalation of surface Fe^{3+} ions typically at the nanotubes openings since the HTN can adsorb the metal-cations from an aqueous solution via the ion-exchange reaction.[23] Moreover, the concept of bond formation via the ion-exchange mechanism has been carefully demonstrated in detail by us elsewhere.[24] As a result, the bond which actually holds the nanotubes to the surface of γ-Fe_2O_3 nanoparticles is ion-exchange in nature. This is also evident from the report of Niu *et al.* where the strong interaction between Fe_3O_4 nanoparticles and $H_2Ti_3O_7$ nanotubes has been demonstrated.[10] Furthermore, the titanate also behaves as Lewis acid (Ti^{4+} site) which may favor the nanotubes attachment to the surface of γ-Fe_2O_3 nanoparticles.[25] (Note: In Fig. 5.1d, the γ-Fe_2O_3 nanoparticles appear to be attached to the surface of HTN bundles). This is attributed to the two possible reasons. First, the HTN bundle contains large number of nanotubes, and hence, large number of nanotube openings (that is, the ends of nanotubes) all along its surface which can attract the γ-Fe_2O_3 nanoparticles via the ion-exchange mechanism. Second, as shown in Fig. 5.2, each individual nanotube is formed via the roll-up mechanism; it has a complete edge of nanosheet running along its length which can also attract γ-Fe_2O_3 nanoparticles via the ion-exchange mechanism.

The XRD patterns of γ-Fe_2O_3 nanoparticles, HTN, and HTNF samples synthesized with varying weight-fractions of γ-Fe_2O_3 nanoparticles are presented in Fig. 5.3. The XRD pattern of HTN is assigned to pure $H_2Ti_3O_7$ or lepidocrocite-type titanate or $H_2Ti_2O_4(OH)$-type structure as evident from the 2θ values at 9.5, 25, and 48.1° which are allocated to the (200), (110), and (020) planes respectively.[21,26] Also, the

diffraction peaks at the 2θ values of 30.2, 35.6, 43.3, 53.7, 57.3, and 62.8^o are assigned to (220), (311), (400), (422), (511), and (440) planes of γ-Fe$_2$O$_3$ in the pure form and within the nanocomposite as per the JCPDS card number 39-1346.[27]
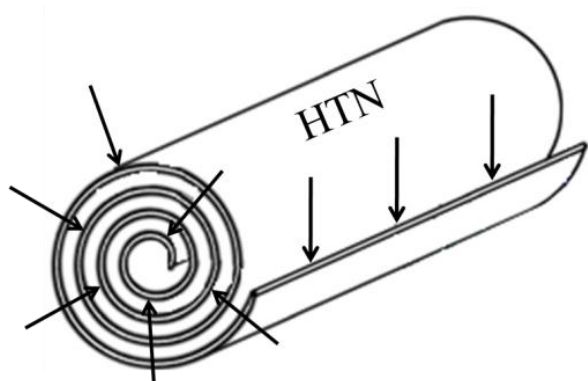
Fig. 5.2. Potential sites for the operation of ion-exchange mechanism as indicated by the arrows.
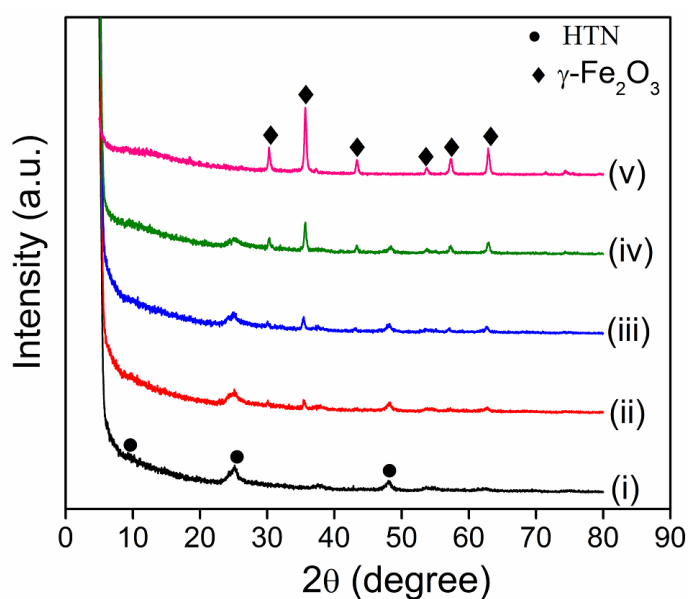
Fig. 5.3. XRD patterns of pure HTN (i), HTNF-5 (ii), HTNF-10 (iii), HTNF-25 (iv), and pure γ-Fe$_2$O$_3$ nanoparticles (v) samples.

The intensity of peaks corresponding to γ-Fe$_2$O$_3$ phase is observed to increase gradually with its weight-fraction. It is to be noted that, in the present investigation,

the HTNF magnetic nanocomposites are synthesized after the formation of HTN via the hydrothermal treatment. One of the advantages of synthesizing the HTNF magnetic nanocomposites through this strategy is the presence of only pure HTN phase in the final nanocomposite. However, if the TiO_2 and γ-Fe_2O_3 nanoparticles are mixed together before the hydrothermal treatment, the final product may also consist of sodium titanate phase.[28]

The N_2 adsorption-desorption isotherms of pure HTN and HTNF magnetic nanocomposites are shown in Fig. 5.4a. The isotherms are of type II while the hysteresis loop is of type H3 which are the characteristics of slit-shaped pores. The BET specific surface-area of 362, 311, 220, 243 m^2 g^{-1} and the pore volume of 0.53, 0.46, 0.34, 0.38 cm^3 g^{-1} are respectively observed for the HTN, HTNF-5, HTNF-10, and HTNF-25 samples.
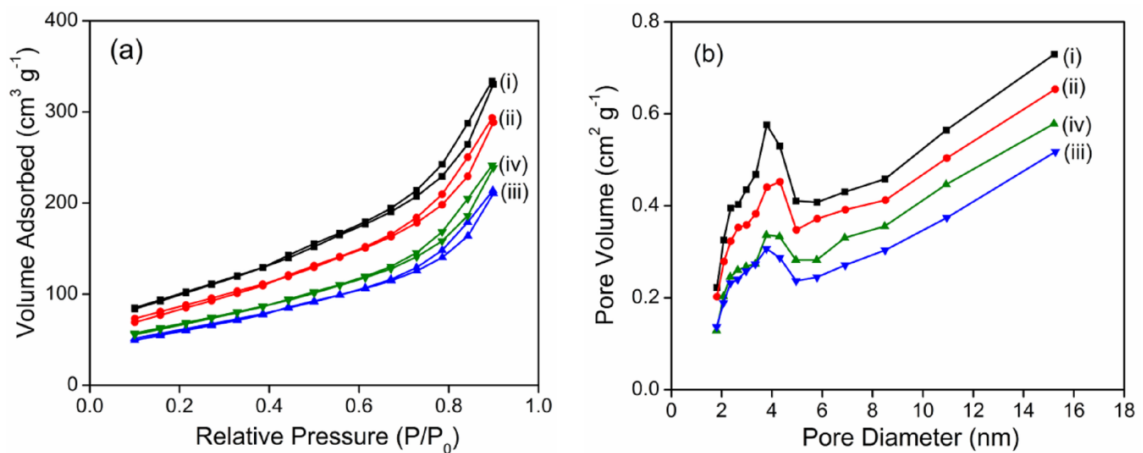
Fig. 5.4. N_2 adsorption-desorption isotherms (a) and BJH pore-size distribution curves (b) as obtained for the pure HTN (i), HTNF-5 (ii), HTNF-10 (iii), and HTNF-25 (iv) samples.

Both the specific surface-area and pore volume are, thus, noted to be reduced with the increasing weight-fraction of γ-Fe_2O_3 nanoparticles (except for the HTNF-25 sample

which may be attributed to the repulsive forces created by the magnetic γ-Fe$_2$O$_3$ nanoparticles which can reduce the aggregation of HTN) since the values of these parameters are relatively lower (32 m^2 g^{-1} and 0.00045 cm^3 g^{-1}) for the γ-Fe$_2$O$_3$ nanoparticles compared with those of pure HTN. The Barret–Joyner–Halenda (BJH) pore-size distribution curves for the above samples are shown in Fig. 5.4b. It is observed that a narrow peak in the pore-size distribution curve lies in between ~2-5 nm region which is attributed to the average inner diameter of pure HTN consistent with the TEM results. The broad distribution of pore-size in higher range corresponds to the non-uniform pore volume present in between the nanotubes within the bundles.

5.3.2. *MB dye-adsorption characteristics of pure HTN and HTNF magnetic nanocomposites*

The dye adsorption studies using the pure HTN and HTNF magnetic nanocomposites are carried out using the aqueous solutions of MB with the initial dye-concentration varying in the range of ~7.5-250 μM. The obtained variations in the normalized concentration of MB dye adsorbed as a function of contact time, at the initial solution-pH of ~10, are presented in Fig. 5.5 for the different samples. It is noted that the adsorption equilibrium is reached within 10 min. The normalized equilibrium concentration of MB adsorbed on the surface of adsorbent is noted to decrease with the increasing initial MB dye concentration which is due to the dominance of increase in the factor C_o appearing in the denominator of Eq. 3.1(Chapter 3). The electrostatic interaction between the negatively charged surface of HTN and cationic MB molecules plays a major role in the adsorption of latter on the surface of former. The negative surface-potential of HTN is further enhanced by adjusting the initial solution-pH to ~10.[29]
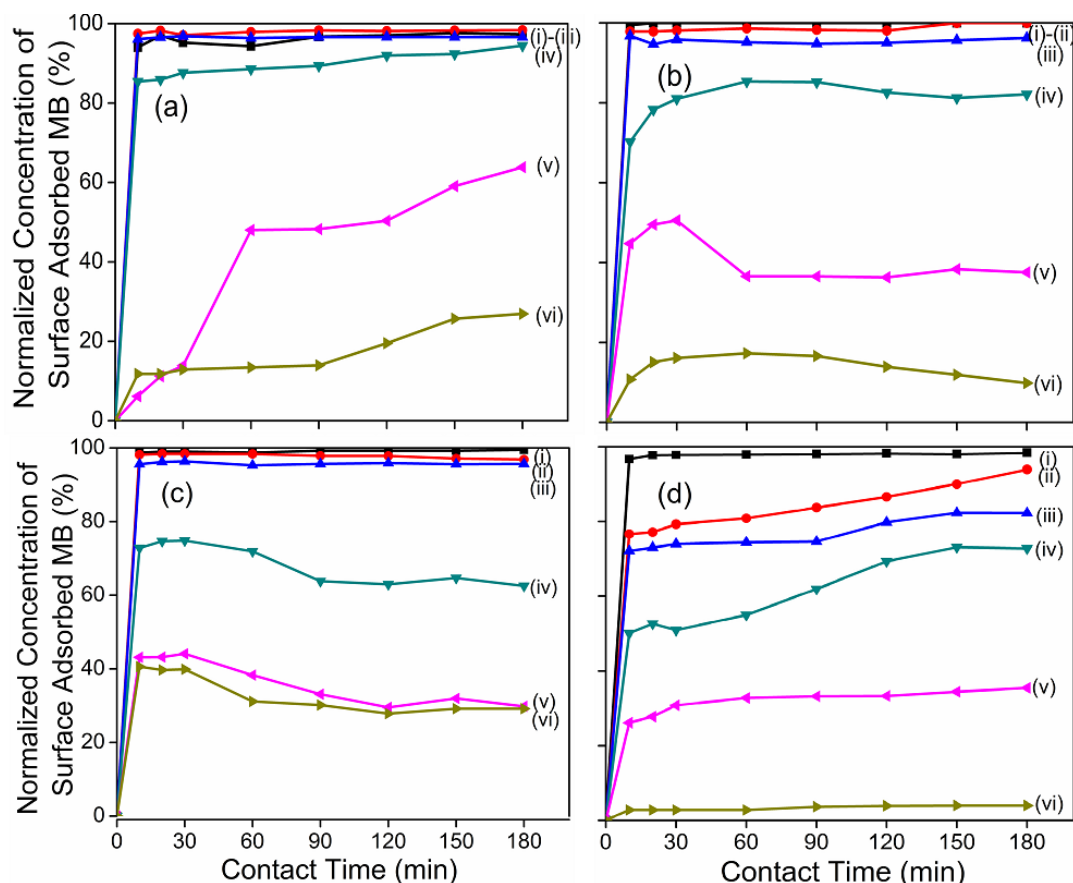
Fig. 5.5. Variations in the normalized concentration of surface-adsorbed MB as a function of contact time as obtained for the pure HTN (a), HTNF-5 (b), HTNF-10 (c), and HTNF-25 (d) samples. The initial MB dye concentration is varied as 7.5 (i), 60 (ii), 90 (iii), 150 (iv), 200 (v), and 250 μM (vi).

The increase in q_e with the initial MB dye concentration, within the range of 7.5-150 μM, is due to the gradual consumption of more number of active surface-sites available for the dye-adsorption. The decrease in q_e at higher initial MB concentration has been attributed to the strong interaction of cationic MB molecules with the OH$^-$ ions within the solution which restricts the adsorption of latter on the surface of adsorbent, thus reducing the negative surface-charge developed on the surface of adsorbent under these test-conditions.[30] The MB adsorption capacity (q_m) is estimated to be 113, 99, 75, and 66 mg g^{-1} for the HTN, HTNF-5, HTNF-10, and HTNF-25

samples respectively. Within the investigated range of initial MB concentration, the MB dye-adsorption capacity of γ-Fe$_2$O$_3$ nanoparticles at the initial solution-pH of ~10 is determined to be very small (~13 mg g^{-1}) which is attributed to their lower specific surface-area and pore volume.[31] Hence, it is noted that the introduction of magnetic property to the non-magnetic HTN results in a decrease in the dye-adsorption capacity of HTNF magnetic nanocomposites which is ascribed to the reduction in both the weight-fraction of HTN and the specific surface-area with the increasing amount of γ-Fe$_2$O$_3$. Among all the HTNF samples which possess the magnetic property, the maximum MB adsorption capacity is shown by the HTNF-5 sample which appears to be the most optimum one.
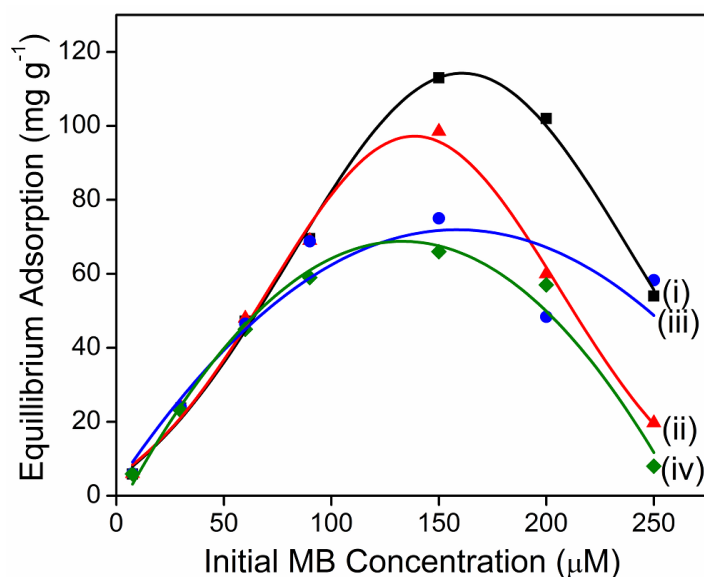
Fig. 5.6. Variation in q_e as a function of initial MB dye concentration as obtained for the pure HTN (i), HTNF-5 (ii), HTNF-10 (iii), and HTNF-25 (iv) samples.

The time dependent adsorption of MB dye on the surface of pure HTN and HTNF magnetic nanocomposites is studied using two different kinetics models – Lagergren pseudo-first-order and pseudo-second-order. The linear plots with the regression correlation coefficient, $<r^2>$, approximately equal to 1 and the q_e values

approximately equal to that of experimentally observed values, Table 5.1, indicate that the MB adsorption on the surface of pure HTN and HTNF magnetic nanocomposites follows the pseudo-second-order kinetics which is in agreement with that reported by Lee *et al.*.[32]

Table 5.1. Values of parameters of pseudo-second-order kinetics model as obtained for the different samples.

Sample	[MB] μM	q_e (Exp.) mg g^{-1}	q_e mg g^{-1}	k_2 g mg^{-1} min^{-1}	r^2
HTN	7.5	5.84	5.88	0.22	0.99
	60	47.2	47.6	0.11	1
	90	69.5	71.4	-	1
	150	113	125	0.003	0.99
HTNF-5	7.5	6	6.1	1.58	1
	60	48	50	0.027	0.99
	90	69	71.4	0.039	0.99
	150	98.5	100	-	0.99
HTNF-10	7.5	6	6	0.9	1
	60	46.5	47.6	-0.04	1
	90	68.8	71.4	-	1
	150	75	77	-0.003	0.99
HTNF-25	7.5	5.9	5.9	0.864	1
	60	45	45.4	0.003	0.99
	150	59	62.5	0.003	0.99
	250	66	71.4	0.002	0.99

The equilibrium adsorption of MB on the surface of HTN and HTNF samples is further studied using three different adsorption isotherm models-Langmuir, Freundlich, and DKR. The values of different parameters estimated after fitting the three equilibrium isotherm models, Fig. 5.7, are listed in the Table 5.2. Evidently, the q_m values obtained via the Langmuir and DKR models are observed to be in

agreement with the experimentally observed values. Moreover, the $<r^2>$ values obtained from the Langmuir and DKR plots are nearly equal to one which suggests that the equilibrium adsorption of MB on the surface of pure HTN and HTNF magnetic nanocomposites follows these two models.
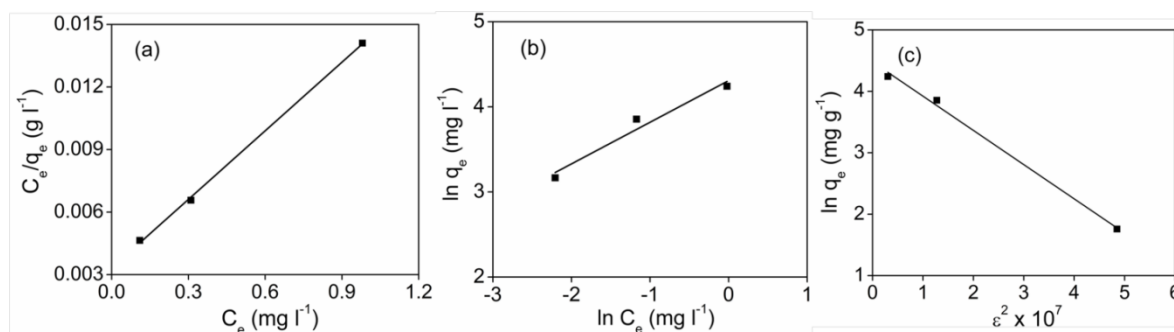
Fig. 5.7. Langmuir (a), Freundlich (b), and DKR (c) plots as obtained for the HTNF-5 sample.

Table 5.2. Values of parameters of different equilibrium adsorption isotherm models as obtained for the different samples.

Sample	q_m (Exp)	Langmuir					Fruendlich			DKR			
		q_m	K_L	r^2	R_L	ΔG	n	K_F	r^2	q_m	β	r^2	E
HTN	113	143	2.3	0.97	0.002 -0.15	-36.3	1.9	81.6	0.94	129	-6×10^{-8}	0.98	2.9
HTNF-5	98.5	91	3.7	0.99	0.006 -0.1	-37.5	2.0	74.2	0.96	88	-6×10^{-8}	0.99	2.9
HTNF-10	75	77	3.2	0.99	0.006 -0.11	-2.9	6.5	45	0.97	72.8	10^{-8}	0.99	7.1
HTNF-25	66	71.4	1.6	0.99	0.012 -0.2	-35	2.6	28.4	0.89	61.6	10^{-7}	0.98	2.2

It has been demonstrated that in a highly acidic (initial solution-pH~2.5) and basic (initial solution-pH~11) solutions, the equilibrium adsorption of MB on the surface of pure HTN follows the Langmuir and DKR models; while, it exhibits a transition from the Langmuir to DKR models within the intermediate range of initial solution-pH.[31]

In the present investigation, the equilibrium adsorption of MB on the surface of pure HTN and HTNF magnetic nanocomposites follows both the Langmuir and DKR models at the initial solution-pH of ~10 which is in agreement with the reported trend. Also, the Langmuir isotherm can decide whether the adsorption process is favorable (< 1) or unfavorable (> 1). The R_L value for the MB adsorption on the surface of both pure HTN and HTNF magnetic nanocomposites lies in between 0.002-0.2 which indicates that the adsorption process is favorable. Further, the spontaneity of adsorption process can be predicted from the change in Gibb's free energy (ΔG_0, J mol^{-1}). The appreciable negative values of ΔG^0 as observed for all samples, Table 5.2, along with the E values less than 8 kJ mol^{-1} strongly suggest the spontaneous MB adsorption via the electrostatic attraction on the surface of HTN and HTNF samples which justify the nature of graph as observed in Fig. 5.5.

5.3.3. Magnetic characteristics of HTNF magnetic nanocomposites

Since the pure HTN is non-magnetic in nature, their separation from an aqueous solution is a difficult process. However, by attaching the super paramagnetic γ-Fe$_2$O$_3$ nanoparticles to the ends of HTN, the latter can be separated from the aqueous solution by applying a moderate external magnetic field. The magnetization curves of HTNF samples as measured at room temperature are presented in Fig. 5.8. The magnetic hysteresis loops are S-like curves. The saturation magnetization values for the γ-Fe$_2$O$_3$, HTNF-5, HTNF-10, and HTNF-25 samples are 71, 4, 9, and 17 emu g^{-1} respectively. Extremely small hysteresis loop and lower coercivity (57 Oe, see upper-left corner inset in Fig. 5.8) are the typical characteristics of super paramagnetic particles.
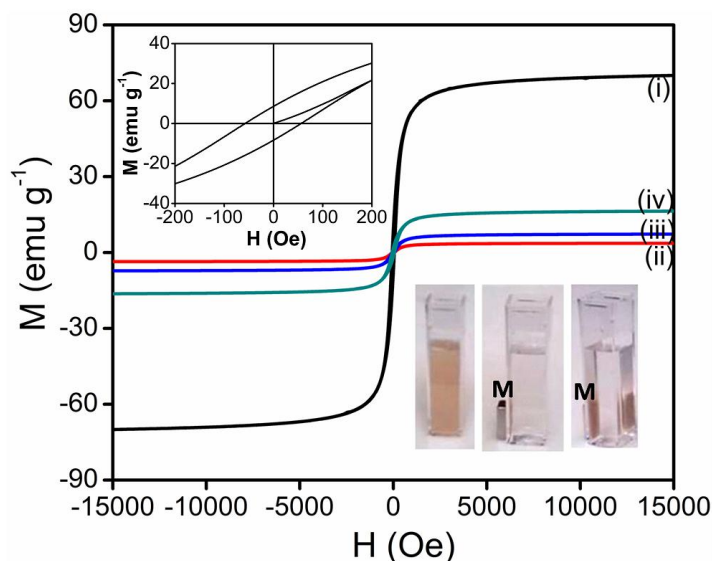
Fig. 5.8. Magnetization curves as obtained for the pure γ-Fe$_2$O$_3$ nanoparticles (i), HTNF-5 (ii), HTNF-10 (iii), and HTNF-25 (iv) samples. The inset in lower-right corner shows the magnetic separation of HTNF-5 sample from an aqueous solution; while, that in upper-left corner shows the low-field magnetization curve for γ-Fe$_2$O$_3$ nanoparticles.

The efficiency of magnetic separation of these nanocomposites from an aqueous solution is dependent on the weight-fraction of γ-Fe$_2$O$_3$ present in the nanocomposite. It is noted that HTNF-5 sample is separated within ~2 min whereas; very fast (~10 sec) magnetic separation is possible for the HTNF-10 and HTNF-25 samples. As demonstrated in the previous section, due to the introduction of magnetic property via the attachment of HTN to the γ-Fe$_2$O$_3$ nanoparticles, the HTNF samples exhibit some loss in the dye-adsorption capacity. In comparison with pure HTN, the reduction in MB dye adsorption capacity of magnetic nanocomposites is calculated to be 13, 33, and 42% for HTNF-5, HTNF-10, and HTNF-25 samples respectively. On the basis of both the effectiveness of magnetic separability and reduction in MB dye adsorption capacity, the optimum magnetic nanocomposite is found to be HTNF-5.

5.3.4. Surface-cleaning and recyclability of HTNF magnetic nanocomposite

 Finally, the HTNF-5 magnetic nanocomposite is used to demonstrate its recyclability in the dye removal application. For this, the MB dye is first adsorbed on the surface of HTNF-5 sample via three successive dye-adsorption cycles, which is then subjected to the surface-cleaning treatment using 30 wt% H_2O_2 solution. This is in turn followed by the fourth cycle of dye-adsorption. The obtained variations in the normalized concentration of surface-adsorbed MB as a function of contact time as obtained for the different cycles of dye-adsorption, conducted before and after the surface-cleaning treatment, are presented in Fig. 5.9.
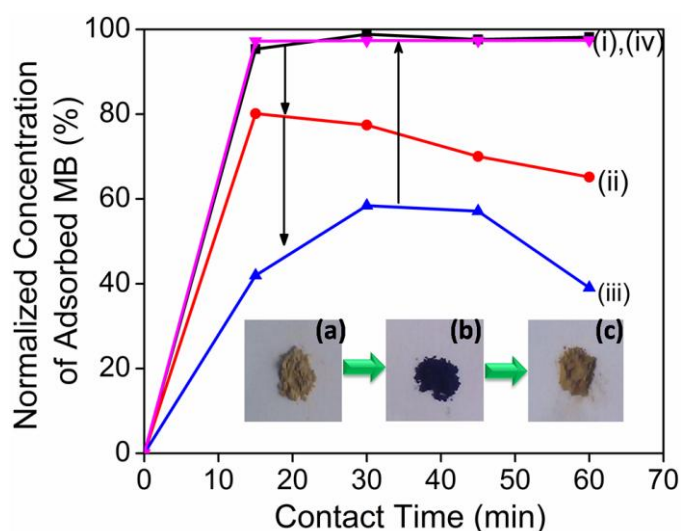
Fig. 5.9. Variation in the normalized concentration of MB dye adsorbed as a function of contact time as obtained under the different test-conditions for the HTNF-5 sample. The successive dye-adsorption cycles-1 to 3 (i-iii) and cycle-4 (iv) are conducted before and after the surface-cleaning treatment. For each dye-adsorption cycle, the initial MB dye concentration is ~90 μM. The inset shows change in the color of original magnetic nanocomposite (a) after the completion of both dye-adsorption cycle-3 (b) and the surface-cleaning treatment (c).

It is noted that, before the surface-cleaning treatment, the amount of dye-adsorbed on the surface of HTNF-5 sample decreases with the increasing number of dye-adsorption cycles. The surface-cleaning treatment conducted after the cycle-3 is successful in decomposing the MB on the surface of HTNF-5 sample. The proposed mechanism of dye-decomposition in the dark using H_2O_2 as a strong oxidizer involves the generation of O_2^- and/or $^{\bullet}OH$ which attack and decompose the dye adsorbed on the surface of nanotubes.[33]

$$H_2O_2 \xrightarrow{H_2T_3O_7} O_2^- + 2H^+ + e^-$$ 5.2

$$H_2O_2 + O_2^- \xrightarrow{H_2Ti_3O_7} \,^{\cdot}OH + OH^- + O_2$$ 5.3
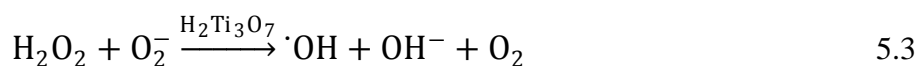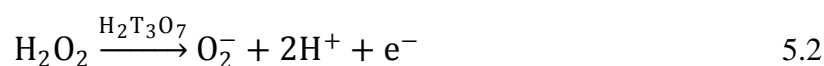
As a result, the surface of nanotubes is free of MB dye after the surface-cleaning treatment and can be recycled for the next successive cycle of dye-adsorption. The original amount of dye-adsorption is also restored in the fourth cycle of dye-adsorption, Fig. 5.9. The inset of Fig. 5.9 illustrates the variation in the color of HTNF-5 sample as observed at the different stages of recycling process which supports the adsorption and decomposition of MB dye before and after the surface-cleaning treatment.

5. 4. Conclusions

The HTN/γ-Fe$_2$O$_3$ hybrid nanostructures are successfully synthesized with varying γ-Fe$_2$O$_3$ weight-fraction. The γ-Fe$_2$O$_3$ nanoparticles are observed to be invariably attached to the ends of nanotubes possibly via the ion-exchange mechanism. The as-synthesized HTNF samples show high dye-adsorption capacity and effective magnetic separability. The introduction of magnetic property is observed to result in

the loss of dye-adsorption capacity of HTN depending on the weight-fraction of γ-Fe_2O_3 nanoparticles. Based on both the effectiveness of magnetic separability and reduction in the dye-adsorption capacity, the optimum magnetic nanocomposite is found to be HTNF-5. The MB adsorption on the surface of HTNF nanocomposites follows the pseudo-second-order kinetics model and the equilibrium adsorption isotherm follows both the Langmuir and DKR models at the initial solution-pH of ~10. By decomposing the previously adsorbed MB dye using the H_2O_2 solution, the HTNF magnetic nanocomposite can be recycled for the next-cycle of dye-adsorption with the restoration of original higher value of dye-adsorption capacity.

References

1.   Corr, S. A.; Rakovich, Y. P.; Gun'ko, Y. K., Multifunctional magnetic-fluorescent nanocomposites for biomedical applications. *Nanoscale Res. Lett.* **2008,** *3* (3), 87-104.

2.   Wang, X.; Cui, Y.; Wang, Y.; Song, X.; Yu, J., Fabrication and catalytic performance of highly stable multifunctional core–shell zeolite composites. *Inorg. Chem.***2013,** *52* (19), 10708-10710.

3.   Pan, D.; Zhang, H.; Fan, T.; Chen, J.; Duan, X., Nearly monodispersed core-shell structural Fe_3O_4@DFUR-LDH submicro particles for magnetically controlled drug delivery and release. *Chem. Comm.* **2011,** *47* (3), 908-910.

4.   Thanikaivelan, P.; Narayanan, N. T.; Pradhan, B. K.; Ajayan, P. M., Collagen based magnetic nanocomposites for oil removal applications. *Sci. Rep.* **2012,** *2*, 230.

5.   Liu, S. Q., Magnetic semiconductor nano-photocatalysts for the degradation of organic pollutants. *Chem. Lett*. **2012,** *10* (3), 209-216.

6.   Ai, L.; Huang, H.; Chen, Z.; Wei, X.; Jiang, J., Activated carbon/CoFe$_2$O$_4$ composites: Facile synthesis, magnetic performance and their potential application for the removal of malachite green from water. *Chem. Eng. J.* **2010,** *156* (2), 243-249.

7.   Han, X.; Zhang, L.; Li, C., Preparation of polydopamine-functionalized graphene–Fe$_3$O$_4$ magnetic composites with high adsorption capacities. *RSC RSC Adv.* **2014,** *4* (58), 30536-30541.

8.   Madrakian, T.; Afkhami, A.; Ahmadi, M.; Bagheri, H., Removal of some cationic dyes from aqueous solutions using magnetic-modified multi-walled carbon nanotubes. *J. Hazard. Mater.* **2011,** *196*, 109-114.

9.   Wang, T.; Liu, W.; Xu, N.; Ni, J., Adsorption and desorption of Cd(II) onto titanate nanotubes and efficient regeneration of tubular structures. *J. Hazard. Mater.* **2013,** *250–251*, 379-386.

10.   Niu, H.; Zhang, S.; Zhang, X.; Cai, Y., Alginate-polymer-caged, C18-functionalized magnetic titanate nanotubes for fast and efficient extraction of phthalate esters from water samples with complex matrix. *ACS Appl. Mater. Interfaces* **2010,** *2* (4), 1157-1163.

11.   Papa, A. L.; Maurizi, L.; Vandroux, D.; Walker, P.; Millot, N., Synthesis of titanate nanotubes directly coated with USPIO in hydrothermal conditions: a new detectable nanocarrier. *J. Phys. Chem. C* **2011,** *115* (39), 19012-19017.

12.   Liu, F.; Jin, Y. J.; Liao, H. B.; Cai, L.; Tong, M. P.; Hou, Y. L., Facile self-assembly synthesis of titanate/Fe$_3$O$_4$ nanocomposites for the efficient removal of Pb^{2+} from aqueous systems. *J. Mater. Chem. A* **2013,** *1* (3), 805-813.

13.   Thazhe, L.; Shereef, A.; Shukla, S.; Pattelath Reshmi, C.; Varma, M. R.; Suresh, K. G.; Patil, K.; Warrier, K. G., Magnetic dye-adsorbent catalyst:

processing, characterization, and application. *J. Am. Ceram. Soc*. **2010,** *93* (11), 3642-3650.

14.   Krishna, B.; Mahadevaiah, N.; Murty, D.; Prakash, B. J., Surfactant immobilized interlayer species bonded to montmorillonite as recyclable adsorbent for lead ions. *J. Colloid Interface Sci.* **2004,** *271* (2), 270-276.

15.   Zhang, Y.; Cheng, Y.; Chen, N.; Zhou, Y.; Li, B.; Gu, W.; Shi, X.; Xian, Y., Recyclable removal of bisphenol A from aqueous solution by reduced graphene oxide–magnetic nanoparticles: Adsorption and desorption. *J. Colloid Interface Sci.* **2014,** *421* (0), 85-92.

16.   Liu, X.; Hu, Q.; Fang, Z.; Zhang, X.; Zhang, B., Magnetic chitosan nanocomposites: a useful recyclable tool for heavy metal ion removal. *Langmuir* **2008,** *25* (1), 3-8.

17.   Kharissova, O. V.; Dias, H. R.; Kharisov, B. I., Magnetic adsorbents based on micro-and nano-structured materials. *RSC Adv.***2015,** *5* (9), 6695-6719.

18.   Liao, M. H.; Wu, K. Y.; Chen, D. H., Fast removal of basic dyes by a novel magnetic nano-adsorbent. *Chem. Lett.* **2003,** *32* (6), 488-489.

19.   Gong, J. L.; Wang, B.; Zeng, G. M.; Yang, C. P.; Niu, C. G.; Niu, Q. Y.; Zhou, W. J.; Liang, Y., Removal of cationic dyes from aqueous solution using magnetic multi-wall carbon nanotube nanocomposite as adsorbent. *J. Hazard. Mater.* **2009,** *164* (2), 1517-1522.

20.   Li, J.; Hou, Y.; Chen, X.; Ding, X.; Liu, Y.; Shen, X.; Cai, K., Recyclable heparin and chitosan conjugated magnetic nanocomposites for selective removal of low-density lipoprotein from plasma. *J Mater Sci: Mater Med* **2014,** *25* (4), 1055-1064.

21.   Nakahira, A.; Kato, W.; Tamai, M.; Isshiki, T.; Nishio, K.; Aritani, H., Synthesis of nanotube from a layered $H_2Ti_4O_9$ center dot H_2O in a hydrothermal treatment using various titania sources. *J. Mater. Sci.* **2004,** *39* (13), 4239-4245.

22.   Bavykin, D. V.; Friedrich, J. M.; Lapkin, A. A.; Walsh, F. C., Stability of aqueous suspensions of titanate nanotubes. *Chem. Mater.* **2006,** *18* (5), 1124-1129.

23.   Liu, W.; Wang, T.; Borthwick, A. G.; Wang, Y.; Yin, X.; Li, X.; Ni, J., Adsorption of Pb^{2+}, Cd^{2+}, Cu^{2+} and Cr^{3+} onto titanate nanotubes: competition and effect of inorganic ions. *Sci. Total Environ.* **2013,** *456*, 171-180.

24.   Shukla, S. V.; Padinhattayil, H.; Narayani, H.; Jose, M.; Karunakaran, R.; Hareesh, P.; Harsha, N.; Manu, J.; Remya, K.; Vishnu, S. S. Composite particles used for removal of dye from e.g. aqueous solution, comprise metal-cations or protons-sensitized fly ash particles, and nanotubes of semiconductor-oxides deposited on surface of metal-cations or fly ash particles. WO2014188448-A1; IN201301563-I1.

25.   Kitano, M.; Wada, E.; Nakajima, K.; Hayashi, S.; Miyazaki, S.; Kobayashi, H.; Hara, M., Protonated titanate nanotubes with lewis and brønsted acidity: relationship between nanotube structure and catalytic activity. *Chem. Mater.* **2013,** *25* (3), 385-393.

26.   Mozia, S.; Borowiak-Palen, E.; Przepiorski, J.; Grzmil, B.; Tsumura, T.; Toyoda, M.; Grzechulska-Damszel, J.; Morawski, A. W., Physico-chemical properties and possible photocatalytic applications of titanate nanotubes synthesized via hydrothermal method. *J. Phys. Chem. Solids* **2010,** *71* (3), 263-272.

27.   Dutta, A. K.; Maji, S. K.; Adhikary, B., γ-Fe$_2$O$_3$ nanoparticles: an easily recoverable effective photo-catalyst for the degradation of rose bengal and methylene blue dyes in the waste-water treatment plant. *Mater. Res. Bull.* **2014,** *49* (0), 28-34.

28.   Cao, X.; Xue, X.; Zhu, L.; Chen, P.; Song, Y.; Chen, M., Ultrasensitive Na$^+$ exchanging performance of free-standing Fe$_3$O$_4$@Na$_2$Ti$_3$O$_7$ nanosheets indicated by fluorescein. *J. Mater. Chem.* **2010,** *20* (12), 2322-2328.

29.   Bavykin, D. V.; Redmond, K. E.; Nias, B. P.; Kulak, A. N.; Walsh, F. C., The effect of ionic charge on the adsorption of organic dyes onto titanate nanotubes. *Aust. J. Chem.* **2010,** *63* (2), 270-275.

30.   Narayani, H.; Kunniveetil, S. P.; Shukla, S., Effect of solution-ph on methylene blue dye adsorption on hydrogen titanate nanotubes processed via hydrothermal method. *Adv. Sci. Eng. Med.* **2013,** *5* (1), 63-72.

31.   Xie, G.; Xi, P.; Liu, H.; Chen, F.; Huang, L.; Shi, Y.; Hou, F.; Zeng, Z.; Shao, C.; Wang, J., A facile chemical method to produce superparamagnetic graphene oxide-Fe$_3$O$_4$ hybrid composite and its application in the removal of dyes from aqueous solution. *J. Mater. Chem.* **2012,** *22* (3), 1033-1039.

32.   Lee, C. K.; Lin, K. S.; Wu, C. F.; Lyu, M. D.; Lo, C. C., Effects of synthesis temperature on the microstructures and basic dyes adsorption of titanate nanotubes. *J. Hazard. Mater.* **2008,** *150* (3), 494-503.

33.   Belessi, V.; Lambropoulou, D.; Konstantinou, I.; Zboril, R.; Tucek, J.; Jancik, D.; Albanis, T.; Petridis, D., Structure and photocatalytic performance of magnetically separable titania photocatalysts for the degradation of propachlor. *Appl. Catal., B* **2009,** *87* (3–4), 181-189.

34. Babitha, K. B.; Warrier, K. G.; Shukla, S., Decolorization of aqueous solution containing organic synthetic-dye via dark-catalysis process using hydrothermally synthesized semiconductor-oxides nanotubes. *Adv. Sci. Eng. Med.* **2014,** *6* (2), 173-183.

Chapter 6

Synthesis of Pd Supported Non-magnetic/Magnetic Catalysts and Their Dye Removal Application *via* Fenton-like Reaction

Graphical Abstract
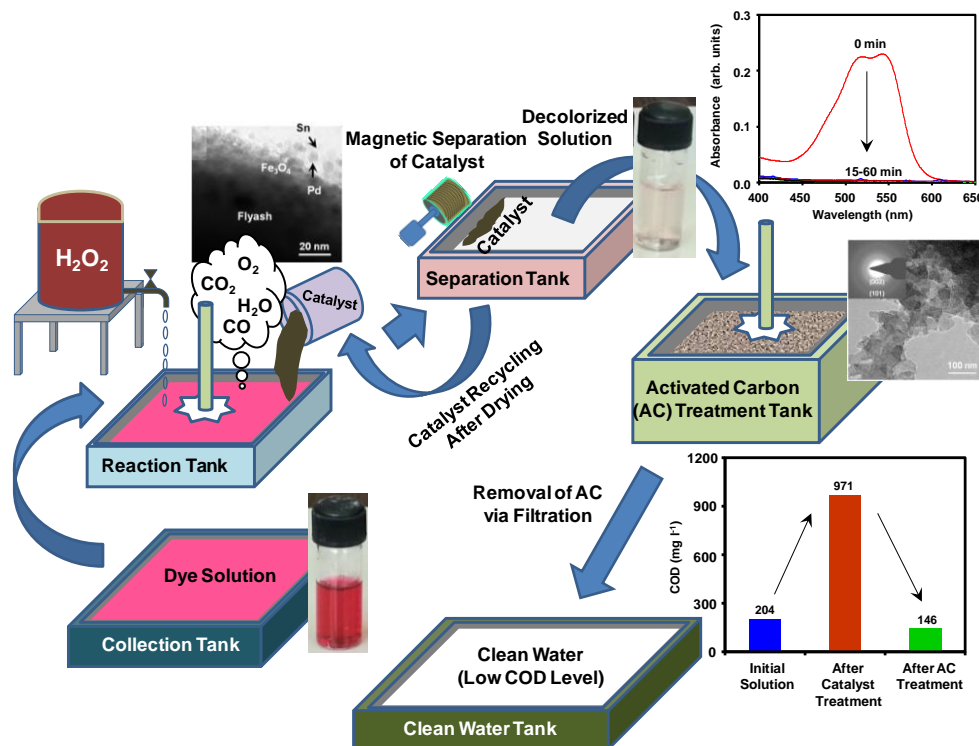
Highlights

- Pd-flyash and Pd-Fe$_3$O$_4$-flyash activate H$_2$O$_2$ for decolorizing aqueous solutions.

- Basic and industrial azo reactive dyes are removed by this technique.

- Magnetic separation of Pd-Fe$_3$O$_4$-flyash catalyst is achieved.

- Activated carbon reduces significantly the final COD level via adsorption.

- Technology bridges the gap between thermal power plants and dye-related industries.

Abstract

The palladium (Pd)-flyash composite particles have been conventionally used for obtaining copper (Cu) or silver (Ag)-coated flyash particles as fillers for manufacturing the conducting polymers. We demonstrate that the involvement of Fenton-like reactions (AOPs), makes the same composite particles useful as catalyst for the decoloration of aqueous solutions containing the organic synthetic-dyes. The non-magnetic Pd-flyash and magnetic Pd-(Fe_3O_4)-flyash composite particles have been processed for this purpose, for the first time, using the combination of electroless and inverse co-precipitation techniques. The dye-removal characteristics of the catalysts have been investigated in the dark-condition via the Fenton-like reactions involving the activation of H_2O_2 to generate the $^\bullet OH$ in the aqueous solutions containing the basic and industrial azo reactive dye. The initial dye, H_2O_2, and catalyst concentrations have been varied within the range of 0.003-0.4 g l^{-1}, 3-50 wt%, and 40-100 g l^{-1} respectively. Within the investigated test-conditions, the Pd-flyash composite particles show higher dye-removal rates than those associated with the Pd-Fe_3O_4-flyash composite particles due to the higher amounts of surface-deposited Pd and reduced concentration of Fe^{2+} ions leached into the surrounding acidic medium from the catalyst-surface. Conversely, the Pd-Fe_3O_4-flyash composite particles exhibit effective magnetic separation after the dye-decoloration process which is not possible without the presence of intermediate layer of Fe_3O_4. For both the catalysts, the chemical oxygen demand (COD) levels of the decolorized aqueous solutions are observed to be increased after the catalyst-treatment of initial dye-solutions. Nevertheless, the increased COD levels are easily controlled by the post treatment with the high surface-area AC which strongly adsorbs the intermediate products of the dye-decoloration and carbon leached out from the surface of flyash particles. Hence,

the Fenton-like reactions backed up with the AC-based adsorption process appear to be effective combination for the fast and efficient removal of organic synthetic-dyes from the aqueous solutions.

6.1. Introduction

Recently a novel dark-catalysis process has been developed for the removal of organic synthetic-dyes from the industry effluents and aqueous solutions.[1-6] The process involves the dye removal via the chemical activation of hydrogen peroxide (a strong oxidizer) using two different methods. In the first method, the dye is adsorbed from the aqueous solution on the surface of a catalyst and then decomposed in another aqueous solution containing H_2O_2. In the second method, the dye is adsorbed and decomposed in an aqueous solution containing both the catalyst and H_2O_2. For the chemical activation of H_2O_2, the hydrothermally synthesized nanotubes of hydrogen titanate ($H_2Ti_3O_7$) and anatase-TiO_2 are revealed to be suitable as the catalysts. The main advantage of the dark-catalysis process is that it is a non-radiation driven dye-removal process. Moreover, it is relatively simpler, faster, safer to conduct and does not involve any sludge formation.

The mechanism of decomposition of organic synthetic-dyes via the dark-catalysis process using the nanotubes of semiconductor-oxides involves the AOPs such as the Fenton-like reactions. In the well-known homogeneous Fenton-reaction, the reaction between Fe^{2+} ions and H_2O_2 is known to generate the Fe^{3+} ions and $^\bullet OH$.[7] However, the toxicity of some intermediates can be higher than that of the initial compound such as phenol.[7] The unsupported and supported nanoparticles of pure metal, metal-oxides and metal-sulfides have also been reported to be useful as heterogeneous catalysts in the removal of harmful organics via the Fenton-like reactions.[8-9]

Lately, the supported metal/metal-oxides nanoparticles consisting of the heterogeneous Pd/Al_2O_3 catalyst system, synthesized via the impregnation method, has been developed for the in-situ generation of H_2O_2 using the formic acid and O_2 for the phenol degradation in an aqueous solution.[10-11] Moreover, the multi-component $Pd/PdO/Fe_2O_3$ nanoparticles highly dispersed in the porous SBA-15 support has also been reported for the decomposition of Acid Red 73 dye using the Fenton-like reactions via the in-situ generation of H_2O_2.[12] However, considering that H_2O_2 is widely available commercially, the advantages of in-situ generation of this reagent have been strongly questioned.[8] Moreover, in our view, the in-situ generation of H_2O_2 leads to lower kinetics of dye-degradation. In addition to this, there is also a need to replace the costlier SBA-15 support with the cheaply available material for the cost-reduction of the new dye-removal technology based on the AOPs.

In the perspective of these limitations, the Pd-flyash where the Pd nanoparticles are deposited on the surface of flyash particles via the facile electroless process, involving the Sn-Pd catalyst-system,[13] appears to be an attractive composite material for further investigation of the removal of organic synthetic-dyes from the aqueous solutions. The flyash is a waste by-product of thermal power plants and is cheaply available around the world. The Pd-flyash composite particles have been utilized as fillers for the manufacturing of conducting polymers useful in the electromagnetic interference (EMI) shielding application.[13] However, other potential industrial applications of this composite material are limited. Recently, the use of flyash-supported cobalt oxide (Co_3O_4) catalysts for the removal of phenol from an aqueous solution via the activation of peroxymonosulfate has been reported.[14] However, the reported catalyst was not utilized for the quick and easy magnetic separation possibly due to its non-magnetic nature. Considering these earlier reports, it appears that the demonstration of

utilizing the non-magnetic Pd-flyash as well as the magnetic Pd-Fe_3O_4-flyash composite particles for the removal of organic synthetic-dyes from the aqueous solutions via the activation of a strong oxidant and their subsequent magnetic separation for the effective regeneration are still lacking in the literature. Such successful demonstration would also offer a new pathway of utilizing flyash as a cheap catalyst-support for the novel chemical reactions involving AOPs in the dye-removal application providing a new strategy for the solid waste management. Hence, the first major objective of the present investigation has been set to synthesize the Pd-nanoparticles deposited non-magnetic and magnetic flyash-based composite particles via the combination of electroless and inverse co-precipitation processes. The second major objective of the present investigation has been set to demonstrate and compare the use of these composite materials in the removal of organic synthetic-dyes (basic and industrial azo reactive) via the Fenton-like reactions (that is, the non-radiation driven activation of H_2O_2) involving the magnetic separation of flyash-based composite particles.

6.2. Experimental

6.2.1. Chemicals

Terephthalic acid (TA, 98%) and H_2O_2 (3 wt%) were purchased from Sigma-Aldrich Chemicals, Bengaluru, India; sodium acetate (CH_3COONa, 98%) from NICE chemicals Pvt. Ltd., Kochi, India; H_2O_2 (30 and 50 wt%), ferric chloride anhydrous ($FeCl_3$, 96%), ferrous sulphate ($FeSO_4 \cdot 7H_2O$, 99.5%), methylene blue (MB) ($C_{16}H_{18}N_3SCl \cdot nH_2O$, 96%), hydrochloric acid (HCl, 35 wt%), tin(II) chloride ($SnCl_2 \cdot 2H_2O$, 97%), ethanol (C_2H_5OH, 99.9 %), palladium(II) chloride ($PdCl_2$, 99.0%, Pd 59-60%), sodium hydroxide (NaOH, 97%), and activated charcoal

(carbon) (AC) (AR grade, phosphorous free) from S.D. Fine-Chem Ltd., Mumbai, India. The azo reactive dye, Corafix Red ME4B was received from the Colourtex Industries Limited, Surat, India; and flyash (diameter ~ 1-3 μm) from the National Thermal Power Corporation (NTPC), Ramagundam, India. All chemicals and materials were used as-received without any further purification.

6.2.2. Synthesis of Pd deposited flyash

The as-received flyash particles were utilized for the surface-deposition of Pd catalyst via the conventional electroless process.[13,15] 5 g of as-received flyash particles were first stirred in 250 ml of distilled aqueous solution containing 40 g l^{-1} of $SnCl_2 \cdot 2H_2O$ and 40 ml l^{-1} of HCl for 2 h. The suspension was filtered and the surface-sensitized flyash particles (that is, particles with the surface-adsorbed Sn^{2+} ions) obtained as the residue were activated by stirring them for 1 h in 250 ml aqueous solution containing 1.0 g l^{-1} of $PdCl_2$ and 5 ml l^{-1} of HCl. The suspension is filtered and the surface-activated flyash particles (that is, particles with the surface-deposited Pd nanoparticles) obtained as the residue were dried in an oven at $80^{o}C$ overnight. Theoretical calculations show that the Pd-flyash composite particles obtained by this method contain 1.44 wt% Pd with the balance being the weight of Sn-flyash particles.

6.2.3. Synthesis of Fe₃O₄ coated flyash

The magnetic composite particles consisting of flyash and Fe_3O_4 were synthesized via the inverse co-precipitation technique.[16] First, the desired amount of $FeSO_4 \cdot 7H_2O$ and $FeCl_3$ were dissolved in 120 ml distilled water at the neutral solution-pH (~6.7) (referred as solution A). (Note: during the processing of magnetic Fe_3O_4-flyash composite particles having 40 wt% Fe_3O_4, a gradual decrease in the solution-pH is

observed (4.41 and 3.04) after the dissolution of $FeSO_4 \cdot 7H_2O$ followed by that of $FeCl_3$ precursors which is possibly due to the formation of iron(II) hydroxide precipitate. It is noted that the resulting solution is not highly transparent but remains slightly murky after the dissolution of the two precursors). The final concentration of the two precursors is varied in the range of 2.0×10^{-3}-1.9×10^{-2} M (0.56-5.3 g l^{-1}) and 4.0×10^{-3}- 3.85×10^{-2} M (0.65-6.2 g l^{-1}) respectively such that the Fe^{3+} to Fe^{2+} mole ratio (final) is always equal to 2. (Note: in Fe_3O_4, the oxidation state of O ion is -2. Since there are 4 oxygen ions, the total negative charge is -8. For the charge neutrality, the total positive charge in Fe_3O_4 must be +8. Since there are 3 Fe ions, the total positive charge of +8 can be obtained provided the mole ratio of Fe^{3+} to Fe^{2+} is 2:1). Separately, the solution B was prepared by dissolving certain amounts of NaOH and CH_3COONa (with the constant NaOH to Fe and CH_3COONa to Fe mole ratios (final) of 2.67 and 10 respectively) in 80 ml distilled H_2O. Then, the specific amount of flyash particles were suspended into the solution B such that the final concentration of the as-synthesized composite particles formed would be 5 g l^{-1}. The solution A was then added dropwise to the solution B under the continuous mechanical stirring. The resulting composite particles were then separated via filtration, washed with distilled H_2O and ethanol several times, then dried in an oven at 60^oC overnight. By this procedure, the magnetic Fe_3O_4-flyash composite particles with the weight-fraction of Fe_3O_4 varying in the range of 10-90 wt% were processed. Pure Fe_3O_4 magnetic powder was also synthesized as a reference material.

6.2.4. Synthesis of Pd-Fe$_3$O$_4$-flyash

The Pd-Fe_3O_4-flyash composite particles having both the magnetic and catalytic properties were prepared via the combination of inverse co-precipitation and

electroless deposition techniques. In the electroless process, as described above, the as-received flyash particles were replaced with the magnetic Fe_3O_4-flyash composite particles having 40 wt% Fe_3O_4 for the surface-deposition of Pd nanoparticles. Theoretical calculations show that the final magnetic Pd-Fe_3O_4-flyash composite particles contain 1.44 wt% Pd and 19 wt% Fe_3O_4 with the balance weight of Sn-flyash particles.

6.2.5. Characterizations

The morphology of the different products were examined using the transmission electron microscope (TEM, Tecnai G^2, FEI, The Netherlands) operated at 300 kV. The chemical constituents in the different samples were analyzed using the energy dispersive X-ray (EDX) analysis. The crystalline phases present were analyzed using the X-ray diffraction (XRD, PW1710 Phillips, The Netherlands) technique. The broad-scan analysis was typically conducted within the 2θ range of 10-80° using the Cu$K\alpha$ (λ_{Cu}=1.542 Å) X-radiation. The magnetic properties of the samples were measured using a vibrating sample magnetometer (VSM) attached to a Physical Property Measurement System (PPMS, Quantum Design, Dynacool, U.S.A.). The pristine samples were subjected to different magnetic field strengths (*H*) and the induced magnetization (*M*) was measured at 298 K. The external magnetic field was reversed on saturation and the hysteresis loop was traced.

6.2.6. Removal of basic and industrial azo reactive dyes from aqueous solutions

The non-magnetic Pd-flyash and magnetic Pd-Fe_3O_4-flyash composite particles were then utilized for the decomposition of cationic MB dye in an aqueous solution under the dark-condition in the presence of a strong-oxidizer such as the H_2O_2. In 125 ml of

3 wt% H_2O_2 solution (equivalent of ~1 M H_2O_2), 60-1250 μM (0.0192-0.4 g l^{-1}) of MB dye was dissolved completely under the continuous overhead stirring (IKA Eurostar Digital, Germany). 40 g l^{-1} of composite particles were then dispersed in the above dye-solution and the resulting suspension was stirred for 1 h in the dark-condition. 8 ml aliquots were collected after 5-30 min time interval and the catalyst particles were separated from the solution using a centrifuge (R23, Remi Instruments Ltd., Mumbai, India) operated at 3000 rpm. The solutions were then used for obtaining the UV-visible absorption spectra (UV-2401 PC, Shimadzu, Japan) to determine the amount of MB dye decomposed at a given time. Similar dye-decomposition experiments were also conducted using the higher initial H_2O_2 concentrations (15, 30, and 50 wt%) at the constant initial MB dye concentration of 1250 μM (0.4 g l^{-1}) and 500 μM (0.16 g l^{-1}) for the non-magnetic Pd-flyash and magnetic Pd-Fe_3O_4-flyash composite particles respectively. (Note: the initial concentrations of 1250 μM (0.4 g l^{-1}) and 500 μM (0.16 g l^{-1}) represent the approximate maximum limits of initial MB concentrations decolorized by the two catalysts).

The cyclic-tests for the MB decomposition in the dark-condition were conducted for the consecutive 30 and 10 cycles at the initial MB concentration of 7.5 μM (0.0024 g l^{-1}) and initial H_2O_2 concentration of 3 wt% using the non-magnetic Pd-flyash and magnetic Pd-Fe_3O_4-flyash composite particles (catalyst concentration of 40 g l^{-1}) respectively. After the completion of each cycle of dye-decomposition, the catalyst was separated from the treated solution using either a centrifuge or a magnetic separator (Sigma-Aldrich Labware, Bengaluru, India) and then dried in an

oven at 80°C for 12 h. The dried-catalyst thus obtained was used for the next-cycle of MB degradation conducted in the dark-condition.

The dye-decomposition experiments involving the industrial azo reactive dyes Corafix Red ME4B, via the activation of H_2O_2 using the non-magnetic Pd-flyash and magnetic Pd-Fe$_3$O$_4$-flyash composite particles were also conducted in the dark-condition. These experiments were typically conducted in 100 ml of 50 wt% H_2O_2 solution using the 100 g l^{-1} of composite particles with the initial concentrations of azo reactive dye varying in the range of 0.003-0.3 g l^{-1}. (Note: it is to be noted that the initial catalyst concentration is higher for the industrial dyes compared with that used for the MB dye since the industrial dyes are azo reactive dyes which are more stable than the cationic (basic) MB dye. Since the time for the dye-decoloration is kept constant at 60 min, the initial catalyst concentration is enhanced for the industrial dyes to achieve their sufficient decoloration comparable with that of the MB dye).

6.2.7. COD measurement on treated dye solutions

For the measurements of the COD levels, as per the procedure already described elsewhere[17], typical dye-decomposition experiments were conducted in 100 ml of 30 wt% H_2O_2 solution using the initial MB concentration of 7.5 (0.0024) and 60 μM (0.0192 g l^{-1}) and the catalyst (non-magnetic Pd-flyash composite particles) concentration of 50 g l^{-1} with the contact time of 1 h. The filtrate solutions obtained from these experiments were utilized for the measurement of COD levels, before and after the treatment with the AC. For the latter treatment, 50 g l^{-1} of AC was added to the total 100 ml of filtrate solution and the suspension was mechanically stirred for the contact time of 5 h. The AC was separated from the treated solution via the filtration method instead of using the centrifuge. Similar experiments were also

conducted using the Corafix Red ME4B dye using the non-magnetic Pd-flyash and magnetic Pd-Fe$_3$O$_4$-flyash composite particles. For these experiments, the initial dye, initial H$_2$O$_2$, and catalyst concentrations were 0.003 g l^{-1}, 50 wt%, and 100 g l^{-1} respectively.

6.2.8. Gas chromatograph (GC) analysis

For the GC analysis, 100 ml of 30 wt% H$_2$O$_2$ solution without and with the MB dye, having the initial dye concentrations of 30 (0.0096) and 500 μM (0.16 g l^{-1}), was taken in a two-neck round-bottom flask through an open neck which was closed with a lid. 50 g l^{-1} of Pd-flyash particles were then transferred to the flask. After 5 min of contact time, the emanating gases were collected in a 20 ml syringe through the main neck. In the case of an industrial dye Corafix Red ME4B, the initial dye, initial H$_2$O$_2$, and catalyst concentrations were changed to 0.003 g l^{-1}, 50 wt%, and 100 g l^{-1}. The gas samples were analyzed in a GC (Perkin Elmer, Clarus 580, U.S.A.) equipped with a Flame Ionization Detector (FID) and Electron Capture Detector (ECD) to determine the concentrations (in ppm by volume) of CO, CO$_2$, CH$_4$, and N$_2$O. Isothermal separation was performed at 35°C in a 30 m long and 0.53 mm internal diameter Elite-PLOT Q column with N$_2$ as a carrier gas. These were then analyzed for O$_2$ concentration in percentage by volume on a thermal conductivity detector (TCD) equipped GC (NUCON 5700, New Delhi, India) with a 5 m long PORAPAK Q (80/100 mesh) packed column and N$_2$ as a carrier gas.

6.2.9. $^{\bullet}$OH trapping

The $^{\bullet}$OH trapping experiments were typically performed using the TA which were produced under the continuous overhead stirring in an aqueous solution in the

presence of a catalyst and H_2O_2.[18-20] These experiments were similar to the one described above for the dye-decomposition measurements conducted in the dark-condition for the MB dye except that the dye was replaced with 5×10^{-4} M of TA and 2×10^{-3} M of NaOH. The solubility of TA in the neutral and acidic water is relatively lower which is enhanced by the addition of NaOH. Moreover, the TA is a non-fluorescent molecule; however, the trapping of free $^{\bullet}OH$ by TA results in the formation of 2-hydroxyterephthalic acid which is a highly fluorescent molecule. In the present investigation, the latter exhibits a characteristic photoluminescence (PL) (Cary Eclipse, Varian, The Netherlands) peak located in between ~442-459 nm and ~438-445 nm at an excitation wavelength of ~315 nm for the experiments conducted typically in 3 wt% H_2O_2 solution using the non-magnetic Pd-flyash and magnetic Pd-Fe$_3$O$_4$-flaysh composite particles respectively. The variation in the solution-pH (HI1131B Refillbale, Combinaton pH Electrode, Hanna Equipments (India) Pvt. Ltd., Navi Mumbai, India) was typically measured for the non-magnetic Pd-flyash composite particles in the absence of TA and MB dye.

6.3. Results and discussion

6.3.1. Morphological, chemical, and structural analyses of catalysts

The TEM image, Fig. 6.1a, shows that the surface of as-received flyash particle is smooth and featureless. The EDX analysis, Fig. 6.1b, confirms the presence of O, Si, Al, Ca, and Fe, with the concentration of 32, 32, 20, 13, and 3 atomic % respectively, as the major constituents on the surface of as-received flyash. (Note: the Cu and C-peaks originate from the grid used for obtaining the TEM images). Moreover, the intensity of carbon peak as a contamination is very weak since the latter is confined to the top surface layer only which cannot be detected using the EDX which is the bulk

analysis technique). The TEM image of non-magnetic Pd-flyash composite particle is presented in Fig. 6.2a where a non-uniform layer consisting of Pd-nanoparticles deposited on the surface of flyash particle is clearly seen. The high magnification image, Fig. 6.2b, of the surface-layer suggests the presence of Pd-nanoparticles of size in the range of 20-60 nm formed within the protective layer of Sn.[21] The comparison of EDX spectrum, Fig. 6.2c, with that presented in Fig. 6.1b confirms the deposition of Pd (13 atomic %) nanoparticles on the surface of as-received flyash particles. The presence of large quantity of surface-adsorbed Sn (40 atomic %) and small quantity of Fe (2 atomic %) are also detected in the EDX spectrum presented in Fig. 6.2c.
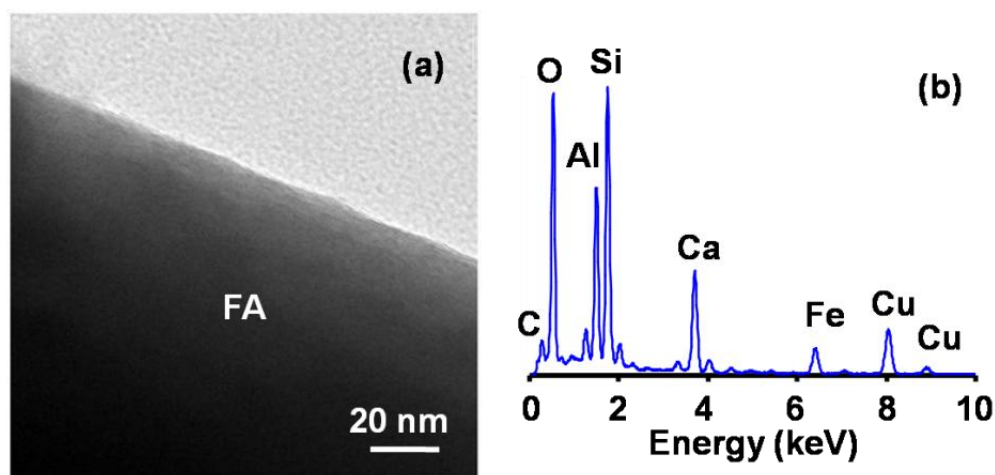
Fig. 6.1. Typical TEM image of the surface of as-received flyash particle (a) and the corresponding EDX spectrum (b). (FA – flyash).
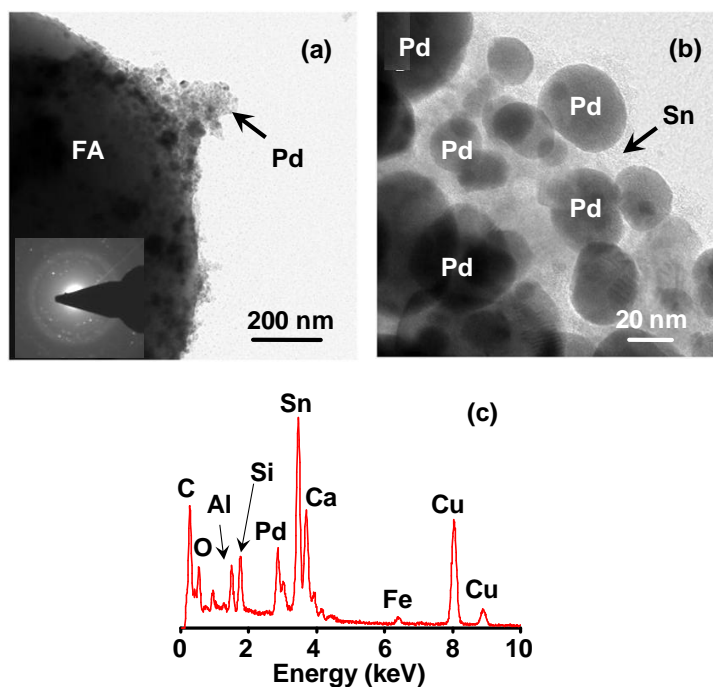
Fig. 6.2. Typical TEM images of the surface of Pd-flyash composite particle at lower (a) and higher (b) magnifications and the corresponding EDX spectrum (c).(FA – flyash).

The TEM image of one of the magnetic Fe_3O_4-flyash composite particle, Fig. 6.3a, shows a non-uniform but continuous deposition of Fe_3O_4 on the surface of as-received flyash particles with the thickness varying in the range of 10-50 nm. On the other hand, the TEM image of the interface of magnetic Pd-Fe_3O_4-flyash composite particle, Fig. 6.3b, suggests the incorporation of Pd nanoparticles within the protective layer of Sn which are deposited on the surface of magnetic Fe_3O_4-flysh composite particles. For both of these samples, the corresponding EDX spectra, Fig. 6.3c and d, suggest an increase in the concentration of Fe (8 and 12 atomic % respectively) on the surface compared with that (2 and 3 atomic %) measured on the surface of non-magnetic Pd-flyash composite and as-received flyash particles. This strongly suggests the successful deposition of Fe_3O_4 on the surface of magnetic composite particles. Moreover, the presence of Pd (5 atomic %) nanoparticles within the protective layer

of Sn (7 atomic %) deposited on the surface of magnetic Fe_3O_4-flysh composite particles is also confirmed via the EDX analysis, Fig. 6.3d. Thus, although the theoretical calculation suggests that the amount of Pd on the surface of both the non-magnetic Pd-flyash and magnetic Pd-Fe_3O_4-flyash composite particles is the same (1.44 wt% Pd), the actual measurements via the EDX analysis suggests that the amount of Pd on the surface of former (13 atomic %) is higher (more than double) than that (5 atomic %) on the surface of latter. It, hence, appears that the TEM and EDX analyses successfully demonstrate the formation of non-magnetic Pd-flyash and magnetic Pd-Fe_3O_4-flyash composite particles via the combination of electroless and inverse co-precipitation methods.
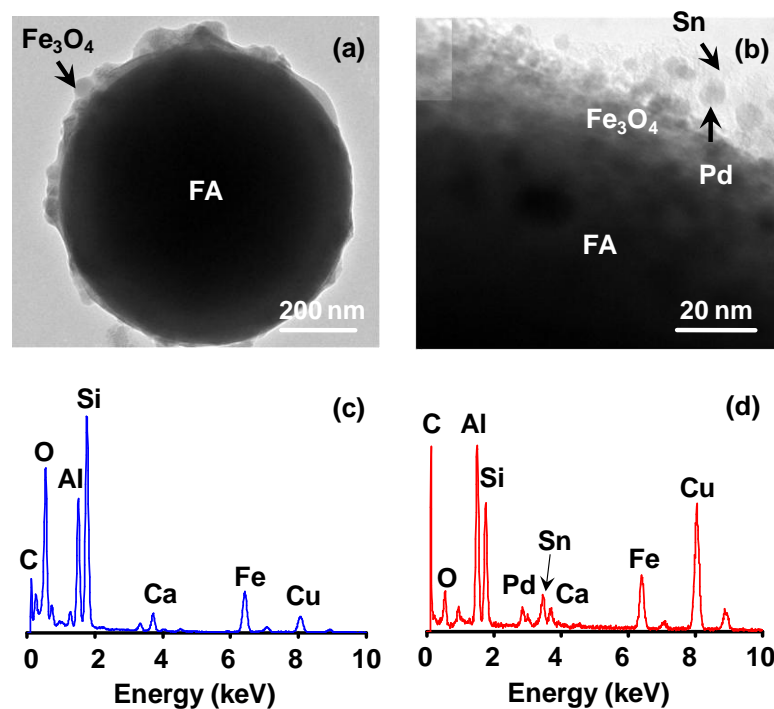
Fig. 6.3. Typical TEM images of the magnetic Fe_3O_4-flyash (a) and the interface of magnetic Pd-Fe_3O_4-flyash (b) composite particles at lower (a) and higher (b) magnifications respectively. The corresponding EDX spectra are presented in (c) and (d) respectively. FA - flyash.

The broad-scan XRD patterns as obtained using the different catalyst samples are presented in Fig. 6.4. The various phases identified in the XRD patterns of these samples, along with the observed diffraction angles, and the matching JCPDS card numbers are tabulated in the Table 6.1. The XRD pattern of as-received flyash particles, suggests that these particles are primarily composed of silica, mullite, and hematite, Table 6.1, which is in accordance with the EDX analysis, Fig. 6.1b. The presence of CaO is, however, not detected in the XRD pattern of the as-received flyash which is in contrast to the presence of Ca which is observed in the EDX spectrum, Fig. 6.1b. The successful deposition of Fe_3O_4 and Pd nanoparticles, as obtained via the inverse co-precipitation and electroless deposition techniques respectively, is confirmed here using the XRD analysis.
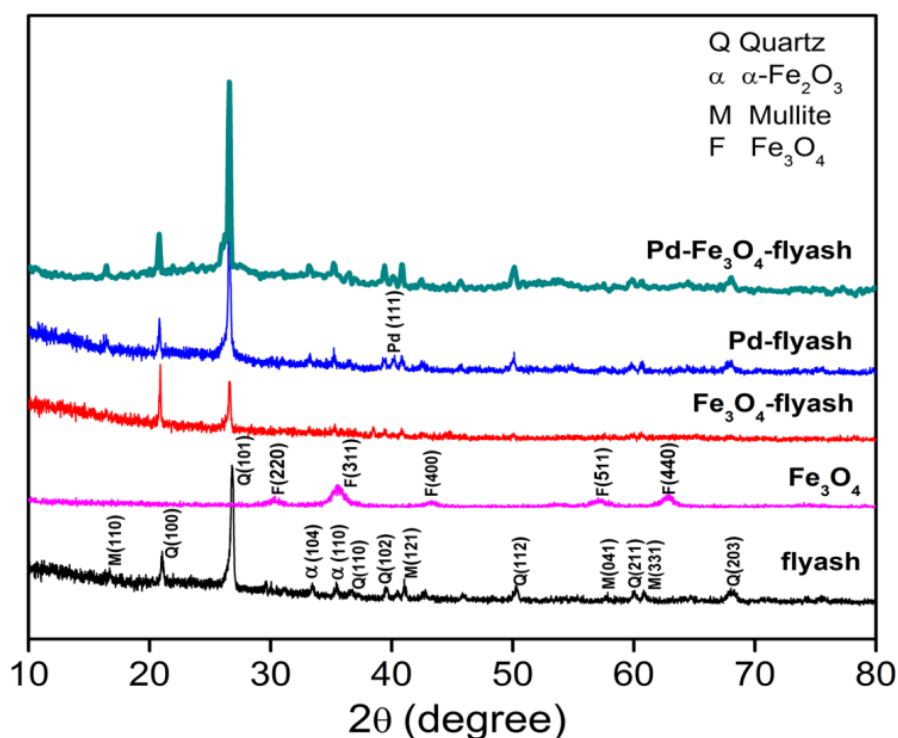
Fig. 6.4. XRD patterns obtained using the different catalyst samples.

Table 6.1. Summary of the various phases identified in the XRD patterns of different catalyst samples, as presented in Fig. 6.4, along with the observed diffraction angles, diffracting planes, and the matching JCPDS card numbers.

Identified Phase	Diffraction Angle 2θ (Degree) (Diffracting Plane)	JCPDS Card No.
SiO_2 (Quartz)	20.81 (100)	46-1015
	26.59 (101)	
	36.52 (110)	
	39.43 (102)	
	50.06 (112)	
	59.97 (211)	
	68.04 (203)	
$Al_6Si_2O_{13}$ (Mullite)	16.42 (110)	15-0776
	40.89 (121)	
	57.56 (041)	
	60.74 (331)	
α-Fe_2O_3 (Hematite)	33.16 (104)	33-0664
	35.21 (110)	
Fe_3O_4 (Magnetite)	30.1 (220)	85-1436
	35.4 (311)	
	43.05(400)	
	57.02(511)	
	62.62(440)	
Pd (Palladium)	40.13(111)	46-1043

6.3.2. Dye-decoloration via Fenton-like reactions using non-magnetic Pd-flyash composite particles

The electroless deposition of Pd nanoparticles on the surface of flyash particles occurs via the redox reaction, Eq. 6.1.[13,15]

$$Sn^{2+} + Pd^{2+} \rightarrow Pd^0 + Sn^{4+} \tag{6.1}$$
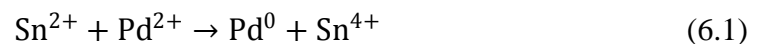
The X-ray photoelectron spectroscope (XPS) analysis of the as-received flyash surface-modified with the electroless process suggests that the Pd exists in 0 and +2 oxidation states with the predominance of former state; on the other hand, the Sn is present only in the +4 oxidation state.[13] From the well-known Fenton-reaction

($Fe^{2+} + H_2O_2 \rightarrow Fe^{3+} + {}^\bullet OH$), it is evident that if the elemental catalyst can possess the multiple oxidation-states, then in the lower oxidation state, it can be directly utilized for the activation of H_2O_2 to generate the ${}^\bullet OH$ responsible for the dye-degradation in the dark-condition. As a result, in the present investigation, due to the predominance of Pd with the zero oxidation state, the Pd^0 nanoparticles appear to be an effective catalyst which are supported by either as-received flyash or magnetic Fe_3O_4-flyash composite particles for the generation of ${}^\bullet OH$ via the H_2O_2 activation through the Fenton-like pathways.[22]

Hence, the non-magnetic Pd-flyash composite particles are utilized first for the degradation of a basic dye such as the MB. In the present investigation, the as-received flyash and Sn-flyash composite particles are ineffective in the decomposition of MB dye via the Fenton-like reactions. The variation in the normalized MB dye concentration decomposed as a function of contact time as obtained for the different initial MB concentrations varying in the range of 100-1250 µM (0.032-0.4 g l^{-1}), at the constant initial H_2O_2 concentration of 3 wt%, is presented in Fig. 6.5a. It is noted that the dye-degradation rate is maximum for the initial MB concentration of 100 µM (0.032 g l^{-1}); however, the former decreases with increasing the latter. Moreover, the amount of MB dye decomposed after 1 h of contact time is observed to decrease from 100% to 16% with the increasing initial MB concentration. Hence, in order to enhance the MB degradation rate and the amount of MB dye decomposed after 1 h of contact time, typically at the highest initial MB concentration (1250 µM (0.4 g l^{-1})), the initial H_2O_2 concentration is increased in between the range of 3-50 wt%. The obtained variation in the normalized MB concentration decomposed as

a function of contact time as obtained for the different initial H_2O_2 concentration, at a constant initial MB concentration of 1250 μM (0.4 g l^{-1}), is presented in Fig. 6.5b.
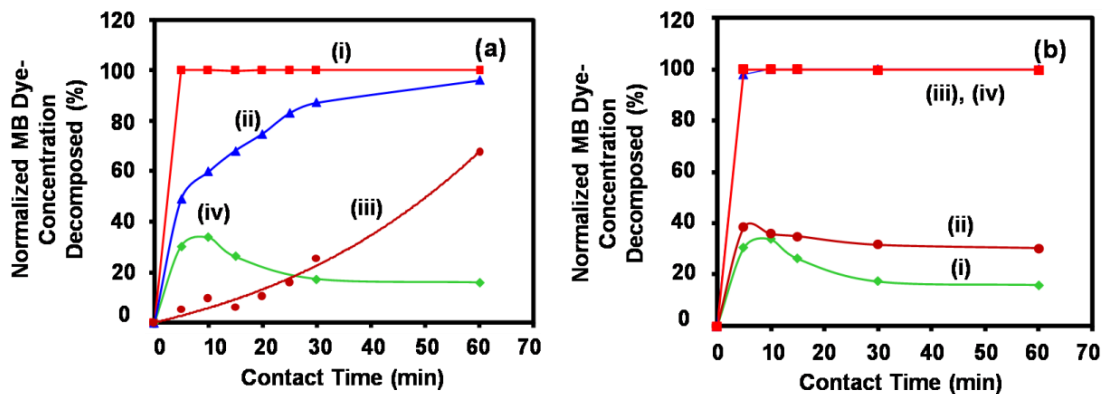
Fig. 6.5. Variation in the normalized MB dye-concentration decomposed in the dark-condition as a function of contact time (a,b) as obtained using the Pd-flyash composite particles (40 g l^{-1}). In (a), the initial MB dye-concentration varies as 100 (0.032) (i), 250 (0.08) (ii), 500 (0.16) (iii), and 1250 μM (0.4 g l^{-1}) (iv) at the initial H_2O_2 concentration of 3 wt%. In (b), the initial H_2O_2 concentration is varied as 3 (i), 15 (ii), 30 (iii), and 50 wt% (iv) at the initial MB concentration of 1250 μM (0.4 g l^{-1}).

It is noted that the rate of MB decomposition increases with the initial H_2O_2 concentration. Moreover, the amount of MB dye decomposed after 1 h of contact time also increases from 16% to 100% with the initial H_2O_2 concentration. The 100% MB decomposition is observed for the initial H_2O_2 concentration of 30 and 50 wt%. Hence, it is inferred that for the decoloration of highly concentrated solution of MB dye, the initial concentration of H_2O_2 is also required to be very high.

It is proposed here that the decoloration of MB dye solution through the H_2O_2 activation using the non-magnetic Pd-flyash composite particles as catalyst occurs via the following Fenton-like chemical reaction, Eq. 6.2.

$$Pd^o + 2H_2O_2 \rightarrow Pd^{2+} + 2\,^{\cdot}OH + 2OH^- \tag{6.2}$$

This is in contrast to the mechanisms proposed by Choudhary et al.[23] and Yuan et al.[24] for the generation of $^{\cdot}OH$ using the $Pd-Al_2O_3$ and Pd/C composite systems. Choudhary et al.[23] proposed the hemolytic decomposition of H_2O_2 on the surface of Pd^o nanoclusters, Eq. 6.3

$$Pd^o + 2H_2O_2 \Leftrightarrow Pd^o + 2\,^{\cdot}OH \tag{6.3}$$

On the other hand, Yuan et al.[24] generated H_2O_2 via the electrolysis of water which was then adsorbed on the surface of Pd^o nanoparticles. Subsequently, the latter catalyzed the Fenton reaction involving Fe^{2+} ions to generate the $^{\cdot}OH$ responsible for the dye (Rhodamine B) degradation. Choudhary et al.[23] also demonstrated that the decomposition of H_2O_2 can occur on the surface of PdO (Pd oxidation state of +2) nanoclusters and suggested that the conversion of Pd^{2+} to Pd^o at the initial stages was responsible for the catalytic activity of PdO nanoclusters. In the present investigation, due to the absence of homogeneous catalyst, the $^{\cdot}OH$ are possibly generated via the combination of chemical reactions presented in Eqs. 6.2 and 6.3 which subsequently attack and decompose the MB dye molecules, Eq. 6.4. [25-26]

$$C_{16}H_{18}N_3S^+ + 102\,^{\cdot}OH \rightarrow 16CO_2 + 3NO_3^- + SO_4^- + 6H^+ + 57H_2O \tag{6.4}$$
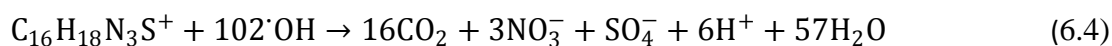
As demonstrated in Fig. 6.6, vigorous chemical reaction occurs in the dark-condition following the addition of catalyst (non-magnetic Pd-flyash composite particles) to the MB dye-solution containing H_2O_2 which emanates the white-fumes after approximately 15 min from the catalyst-addition typically for 3 wt% H_2O_2 solution. This time is further noted to decrease with the increasing initial H_2O_2 concentration within the range of 3-50 wt% for a given initial MB concentration.
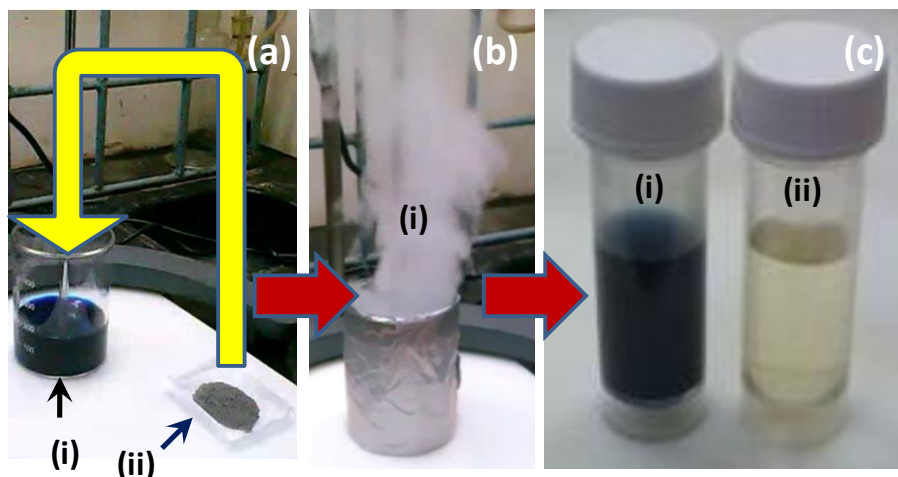
Fig. 6.6. Demonstration of the decomposition of MB dye as obtained typically in the dark-condition using the non-magnetic Pd-flyash composite particles (100 g l^{-1}) in 100 ml of 30 wt% H_2O_2 solution. In (a), (i) and (ii) represent the initial MB dye solution with the initial dye concentration of 1000 μM (0.32 g l^{-1}) and the non-magnetic Pd-flyash composite particles. In (b), (i) represents the strong fumes emanating from the dye-solution after the addition of catalyst-particles to the dye-solution. In (c), (i) and (ii) represent the comparison between the initial and final (obtained after 1 h of contact time) solutions.

Based on the chemical reaction presented in Eq. 6.4, it appears that the white-fumes may be composed of C, N, S, and O containing gases. Although its exact composition is not determined, the present GC analysis confirms the presence of large amount of O_2 gas along with the CO and CO_2 gases in the different proportions depending on the nature and concentration of organic synthetic-dye used (Table 6.2). In spite of the successful decoloration of MB dye solution with the removal of organic contaminants via the formation of CO and CO_2 gases as the contents of emanating gaseous stream, it is observed that the COD levels of the aqueous solutions treated with the catalyst are higher than those of the initial dye-solutions, Fig. 6.7. We attribute this to the

leaching of large amount of carbon already present on the surface of non-magnetic Pd-flyash composite particles and the possible presence of intermediate products of the degradation of MB dye.

Table 6.2. The contents of gaseous stream emanating from the aqueous solutions containing the non-magnetic Pd-flyash composite particles under the different test-conditions.

Test- Condition	Gas Concentration (ppm)				Gas Concentration (Vol%)
	CO	CO_2	CH_4	N_2O	O_2
Air	4.2	459	1.2	0.16	21
(Blank) Pd-flyash (50 g l^{-1}) + 30 wt% H_2O_2	94	192	0.46	0.1	79.3
Pd-flyash (50 g l^{-1}) + 30 wt% H_2O_2 + 30 μM (0.0096 g l^{-1}) MB	101	144	0.44	0.05	90.2
Pd-flyash (50 g l^{-1}) + 30 wt% H_2O_2 + 500 μM (0.16 g l^{-1}) MB	68.4	298.2	---	0.06	96.5
Pd-flyash (100 g l^{-1}) + 50 wt% H_2O_2 + Corafix Red ME4B (0.003 g l^{-1})	46.6	247	0.36	0.1	91.3

In Fig. 6.7, for both the initial MB concentrations, an increase in the COD levels by 61% is observed after the catalyst treatment. It is, however, demonstrated that the increased COD levels can be reduced to significantly lower levels by the adsorption treatment with the AC.[27-28] As shown in Fig. 6.7, an average decrease in the COD level of 89 and 93% is achieved relative to the initial and catalyst-treated dye solutions through the AC treatment of the catalyst-treated decolorized aqueous dye

solutions. It appears that due to its very high specific surface-area and mesoporosity, and the presence of oxygen containing groups on its surface, the AC strongly adsorbs large amount of carbon present in the decolorized aqueous solution, thus drastically reducing the COD levels.
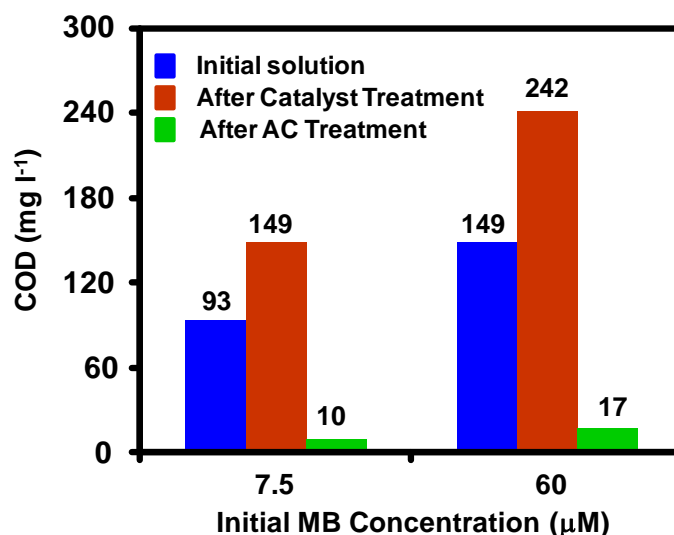
Fig. 6.7. Variation in the COD levels as measured using the aliquots obtained under the different test-conditions. The dye-decomposition experiments were conducted using the non-magnetic Pd-flyash composite particles (50 g l^{-1}) and 30 wt% H_2O_2 solution.

The $^{\bullet}OH$ trapping experiments are conducted in order to confirm the generation of $^{\bullet}OH$, via the chemical reactions presented in Eqs. 6.2 and 6.3, responsible for the decoloration of MB dye solution via the chemical reactions presented in Eq. 6.4. The dynamics of the generation of $^{\bullet}OH$ in the first 60 min, Fig. 6.8a, confirms both the generation of $^{\bullet}OH$ after the addition of catalyst particles to the dye solution containing H_2O_2 and its subsequent decoloration. Following the sudden rise in the $^{\bullet}OH$ concentration during the initial period as observed in Fig. 6.8b, a gradual decrease in the latter is observed with the increasing contact time superimposed with an

intermittent rise and fall in the concentration of $^{\bullet}OH$. It is to be noted that the $^{\bullet}OH$ are not only produced via the chemical reactions presented in Eqs. 6.2 and 6.3 but also consumed by H_2O_2 via the following chemical reaction, Eq. 6.5 [29-30]

$$^{\bullet}OH + H_2O_2 \rightarrow {}^{\bullet}OOH + H_2 \tag{6.5}$$
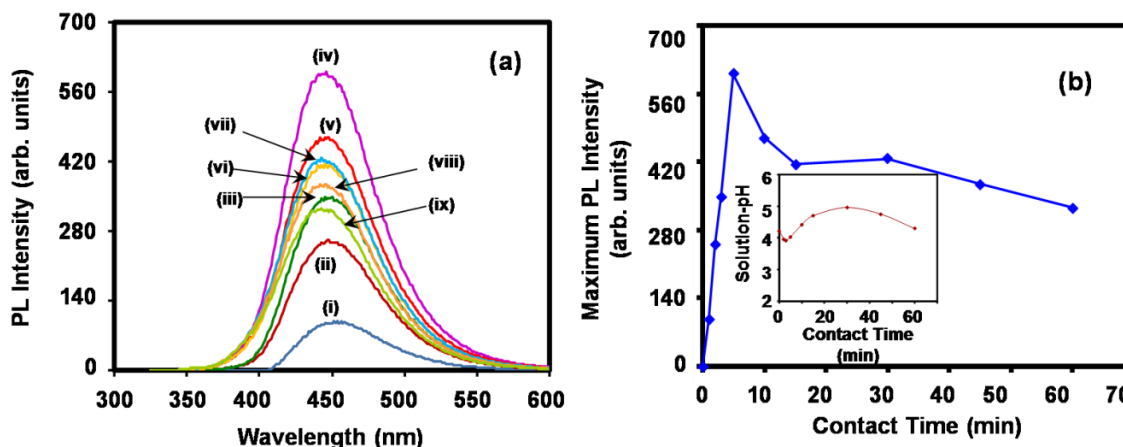
Fig. 6.8. (a) Variation in the PL intensity associated with the formation of 2-hydroxyterpthalic acid for varying contact time as obtained for the non-magnetic Pd-flyash composite particles (40 g l^{-1}) in 3 wt% H_2O_2 solution. The contact time varies as 1 (i), 2 (ii), 3 (iii), 5 (iv), 10 (v), 15 (vi), 30 (vii), 45 (viii), and 60 min (ix). (b) Variation in the maximum PL intensity as a function of contact time. The inset shows variation in the solution-pH as a function of contact time in the absence of TA and MB dye.

The obtained variation in the solution-pH as a function of contact time, conducted in the absence of TA and MB dye, is shown as an inset in Fig. 6.8b. The graph shows fluctuations in the solution-pH which appears to be governed by the competition between the kinetics of the chemical reactions presented in the Eqs. 6.2 and 6.6.[8]

$$Pd^{2+} + 2H_2O_2 \rightarrow Pd^o + 2{}^{\bullet}OOH + 2H^+ \tag{6.6}$$
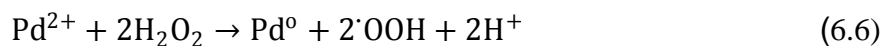
Thus, the variation in the solution-pH also supports the activation and deactivation of the Pd nanoparticles in the presence of H_2O_2.

The catalytic nature of the non-magnetic Pd-flyash composite particles in the decoloration of aqueous solution containing MB dye via the Fenton-like reactions is also confirmed. The variation in the normalized MB dye concentration decomposed as a function of contact time as obtained for the consecutive dye-decomposition cycles (total 30) conducted in the dark-condition, is presented Fig. 6.9a. The corresponding variation in the maximum normalized MB dye concentration decomposed as a function of number of cycles of MB decomposition conducted in the dark-condition, for the constant contact time of 1 h, is presented in Fig. 6.9b. It is noted that the maximum amount of MB dye decomposed in 1 h is ~100% for the first seven-cycles and it decreases to ~87 % after the cycle-30. Hence, considerable catalytic activity is maintained by the non-magnetic Pd-flyash composite particles for the MB decomposition in the dark-condition. It is to be noted that the Pd^o catalyst gets deactivated via the chemical reaction presented in Eq. 6.2; however, it simultaneously gets activated via the chemical reaction presented in Eq. 6.6 similar to the regeneration of Fe^{2+}/Fe^{3+} catalyst-system in the Fenton-reaction.[8]

Due to the consumption of H_2O_2 as a reactant in the chemical reactions (Eqs. 6.5 and 6.6 which are different than those responsible for the generation of $^{\bullet}OH$ (Eqs. 6.2 and 6.3), the large initial concentrations of H_2O_2 (30 and 50 wt%) required for the complete decoloration of highly concentrated MB dye solution, Fig. 6.5b, is justified.
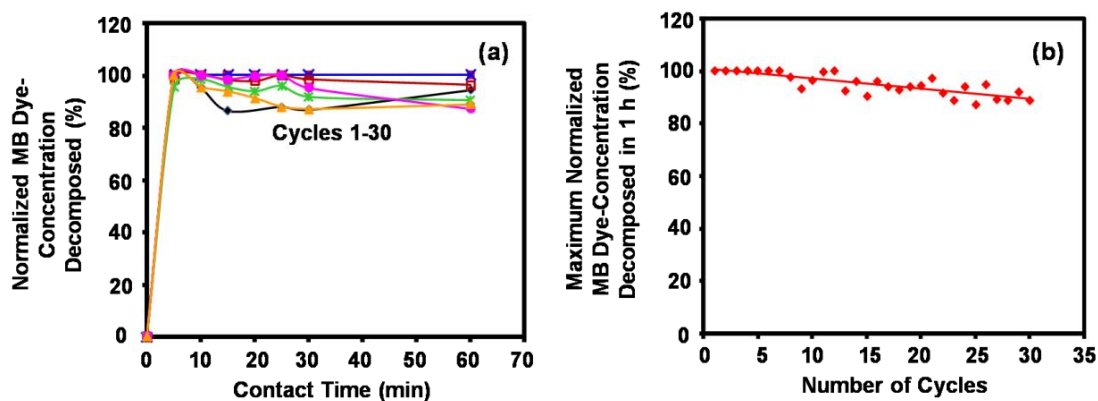
Fig. 6.9. Typical variation in the normalized MB dye-concentration decomposed as a function of contact time as obtained in the dark-condition, using the non-magnetic Pd-flyash composite particles (40 g l^{-1}), in an aqueous solution containing MB with the initial concentration of 7.5 μM (0.0024 g l^{-1}) and 3 wt% H_2O_2 as a strong-oxidizer (a). Total 30 dye-decomposition cycles were conducted out of which only selected cycles (cycles-1, 5, 10, 15, 20, 25 and 30) are shown here for clarity. (b) represents the variation in the maximum normalized MB concentration decomposed after 1 h of contact time as a function of number of cycles conducted in the dark-condition.

Considering the fast decoloration of aqueous solution containing MB dye using the non-magnetic Pd-flyash composite particles, Figs. 6.5 and 6.6, and their catalytic nature, Fig. 6.9, the present composite particles are utilized for the decoloration of aqueous solutions containing the industrial azo reactive dye Corafix Red ME4B which is more stable than the MB dye in an aqueous solution. The variation in the color of dye-solutions as a function of contact time, as obtained for the varying initial Corafix Red ME4B dye concentration, is presented in Fig. 6.10. Very fast decoloration of the initial dye solution within the first 15-30 min of contact time is clearly visible for the initial dye concentrations within the range of 0.003-0.3 g l^{-1}. The variation in the maximum intensity of absorbance-peak located at ~543 nm

related to Corafix Red ME4B dye as observed with the increasing contact time, for the initial dye-concentrations of 0.003 and 0.3 g l^{-1}, is presented in Fig. 6.10a and b respectively. The sharp decrease in the absorbance peak after 15 min of contact time suggests the successful decoloration of initial dye solutions as noted in Fig. 10d and e. Thus, the decoloration of aqueous solution containing the industrial azo reactive dyes using the non-magnetic Pd-flyash composite particles is successfully demonstrated here.
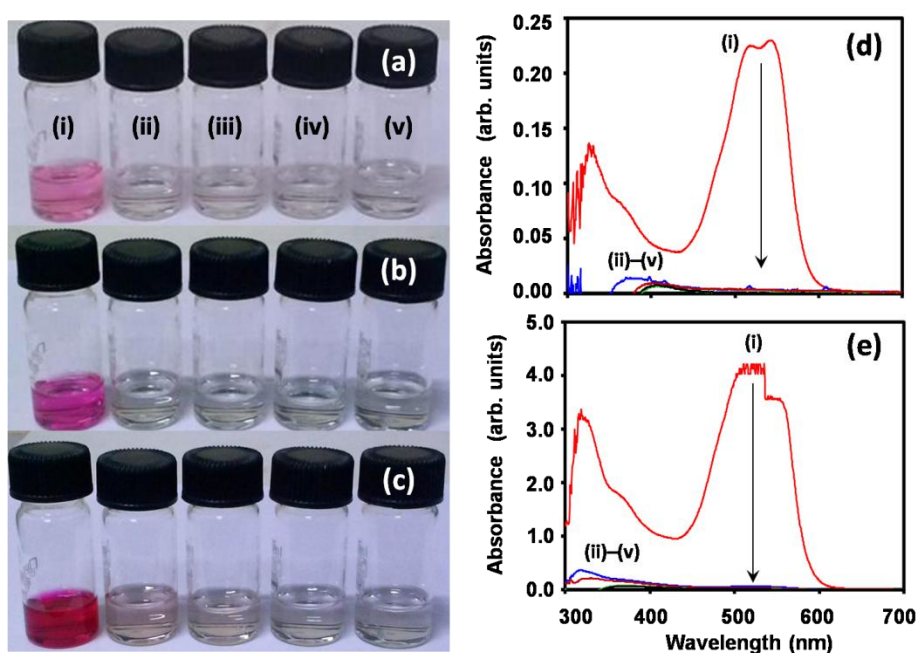
Fig. 6.10. Variation in the color of initial dye-solutions (0.003 (a), 0.03 (b), and 0.3 g l^{-1} (c)) as a function of contact time (0 (i), 15 (ii), 30 (iii), 45 (iv), and 60 min (v)) as obtained for the Corafix Red ME4B dye using the non-magnetic Pd-flyash composite particles (100 g l^{-1}). The initial H$_2$O$_2$ concentration is 50 wt%. Corresponding variation in the intensity of absorbance-peak located at ~543 nm for the initial dye-concentration of 0.003 (d) and 0.3 g l^{-1} (e).

6.3.3. Dye-decoloration via Fenton-like reactions using magnetic Pd-Fe₃O₄-flyash composite particles

Being non-magnetic in nature, the Pd-flyash composite particles utilized in the dye-removal application can only be separated from the treated aqueous solution via the gravity settling, centrifuging, or filtration methods which are time consuming and tedious on the industrial scale. To ease the separation of the catalyst in the dye-removal application using an external magnetic field, the development and use of a magnetic catalyst has been suggested.[31-32] When Fe_3O_4 is deposited on the surface of flyash, the resulting composite contains both the magnetic as well as the non-magnetic flyash particles depending on the amount of Fe_3O_4 deposited. The obtained variation in the weight-fraction of magnetic Fe_3O_4-flyash composite particles as a function of the weight-fraction of Fe_3O_4 deposited is presented in Fig. 6.11. It is noted that the weight-fraction of magnetic part of flyash particles (the balance being the weight of non-magnetic flyash particles) increases with the weight-fraction of Fe_3O_4. When the latter reaches a critical value (40 w%), as pointed by an arrow, the amount of magnetic part of the flyash particles reaches almost 100%. The separation of Fe_3O_4-flyash composite particles containing 40 wt% Fe_3O_4 from an aqueous solution using an external magnetic field provided by a bar magnet is demonstrated as an inset in Fig. 6.11. In view of this, as demonstrated in Fig. 6.3a, the Fe_3O_4 is deposited on the surface of as-received flyash particles to obtain the magnetic Fe_3O_4-flyash composite particles with 40 wt% Fe_3O_4 which are further utilized for the deposition of Pd nanoparticles via the electroless process.
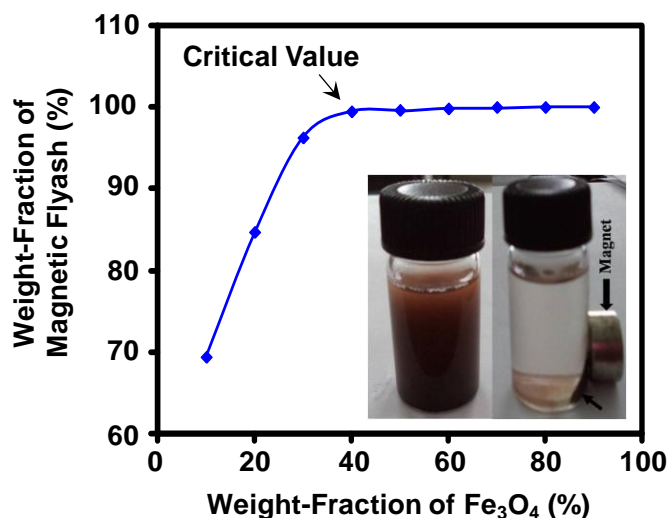
Fig. 6.11. Variation in the weight-fraction of the magnetic part of Fe_3O_4-deposited flyash as a function of weight-fraction of Fe_3O_4. The inset shows the successful magnetic separation of Fe_3O_4-flyash composite containing 40 wt% Fe_3O_4 from an aqueous solution.

Hence, the magnetic Pd-Fe_3O_4-flyash composite particles are utilized for the degradation of a basic dye such as the MB and their performance is compared with that of the non-magnetic Pd-flyash composite particles. In the present investigation, the magnetic Fe_3O_4-flyash composite particles are observed to be ineffective in the decomposition of MB dye via the Fenton-like pathways. The variation in the normalized MB dye concentration decomposed as a function of contact time as obtained for the different initial MB concentrations varying in the range of 60-500 μM (0.0192-0.16 g l^{-1}) at the constant initial H_2O_2 concentration of 3 wt%, is presented in Fig. 6.12a. It is noted that the dye-degradation rate is maximum for the initial MB concentration of 60 μM (0.0192 g l^{-1}); however, the former decreases with the increase in the latter. Moreover, the amount of MB dye decomposed after 1 h of contact time is observed to decrease from 100% to 4% with the increasing initial MB

concentration. Hence, in order to enhance the MB degradation rate and the amount of MB dye decomposed after 1 h of contact time, typically at the highest initial MB concentration (500 μM (0.16 g l^{-1})), the initial H_2O_2 concentration is increased in between the range of 3-50 wt%. The obtained variation in the normalized MB concentration decomposed as a function of contact time as obtained for the different initial H_2O_2 concentration, at a constant initial MB concentration of 500 μM (0.16 g l^{-1}), is presented in Fig. 6.12b.
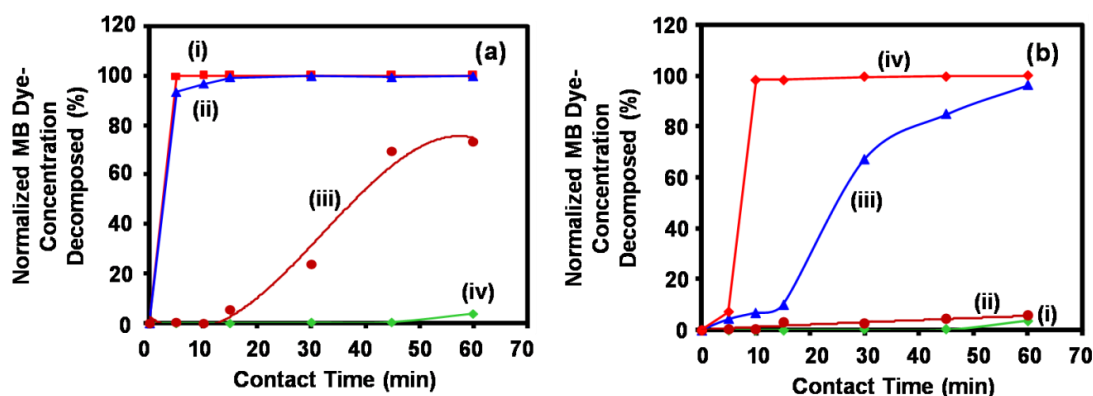
Fig. 6.12. Variation in the normalized MB dye-concentration decomposed in the dark-condition as a function of contact time (a,b) as obtained using the magnetic Pd-Fe$_3$O$_4$-flyash composite particles (40 g l^{-1}). In (a), the initial MB dye-concentration varies as 60 (0.0192) (i), 100 (0.032) (ii), 250 (0.08) (iii), and 500 μM (0.16 g l^{-1}) (iv) at the initial H_2O_2 concentration of 3 wt%. In (b), the initial H_2O_2 concentration is varied as 3 (i), 15 (ii), 30 (iii), and 50 wt% (iv) at the initial MB concentration of 500 μM (0.16 g l^{-1}).

It is noted that the rate of MB decomposition increases with the initial H_2O_2 concentration. Moreover, the amount of MB dye decomposed after 1 h contact time also increases from 4% to 100% with the initial H_2O_2 concentration. The 100% MB decomposition is observed for the initial H_2O_2 concentration of 50 wt%.

Hence, similar to the previous case of non-magnetic Pd-flyash composite particles, it is inferred that for the decoloration of highly concentrated solution of MB dye using the magnetic Pd-Fe_3O_4-flyash composite particles, the initial concentration of H_2O_2 is also required to be very high. The comparison of Fig. 6.12 with Fig. 6.5 suggests that the introduction of magnetic layer of Fe_3O_4 in between the outer catalytic layer of Pd nanoparticles and the base flyash particles has reduced the performance of the catalyst in the dye removal application. There are two possible reasons for this observation. First, the EDX analyses presented earlier clearly show that the amount of Pd deposited on the surface of non-magnetic Pd-flyash composite particles (13 atomic %) is higher (more than the factor of two) than that (5 atomic %) deposited on the surface of magnetic Pd-Fe_3O_4-flyash composite particles. This may reduce the concentration of $^{\bullet}OH$ produced by the latter relative to that produced by the former as a result of the activation of H_2O_2 by the Pd^0 nanoparticles, Eq. 6.2. Secondly, the reduction in the catalytic activity can also be attributed to the possible dissolution of iron in the form of Fe^{2+} ions from the Fe_3O_4 layer in the surrounding aqueous solution containing H_2O_2 which is acidic in nature.[33] (Note: The initial solution-pH of aqueous solutions containing 3-50 wt% of H_2O_2 and typically 150 μM of MB has been reported to be in between ~1-4).[3] The dissolution of Fe^{2+} ions can also reduce the concentration of $^{\bullet}OH$, produced as a result of the activation of H_2O_2 by the Pd^0 nanoparticles, via the following chemical reaction, Eq. 6.7 [18].

$$Fe^{2+} + {}^{\bullet}OH \rightarrow Fe^{3+} + OH^- \qquad\qquad 6.7$$
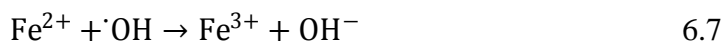
In order to confirm these hypotheses, the $^{\bullet}OH$ trapping experiments are conducted using the magnetic Pd-Fe_3O_4-flyash composite particles as well. The dynamics of the generation of $^{\bullet}OH$, Fig. 6.13, in the first 60 min suggests that the maximum

concentration of $^{\bullet}OH$ produced by the magnetic Pd-Fe$_3$O$_4$-flyash composite particles is less (almost by the factor of half) than that produced by the non-magnetic Pd-flyash composite particles. This strongly supports the lower MB degradation kinetics of the magnetic Pd-Fe$_3$O$_4$-flyash composite particles relative to that of the non-magnetic Pd-flyash composite particles via the two mechanisms as discussed above.
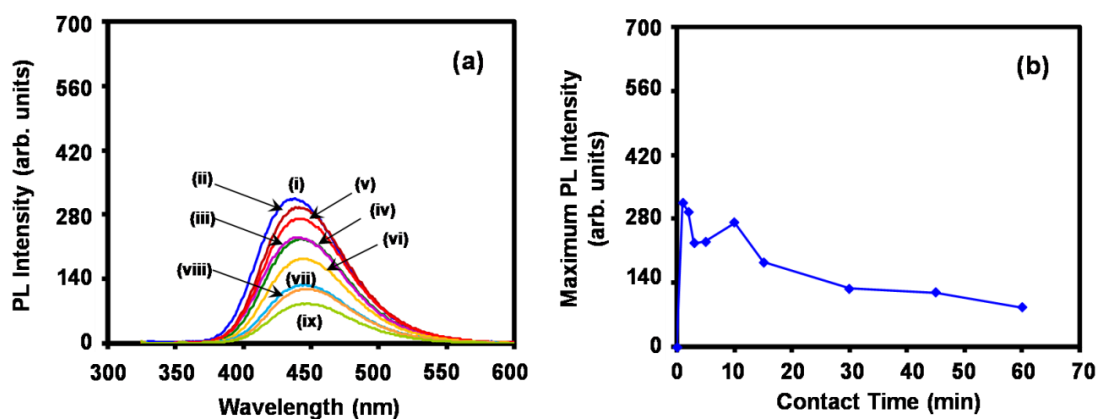
Fig. 6.13. Variation in the PL intensity associated with the formation of 2-hydroxyterpthalic acid for varying contact time as obtained using the magnetic Pd-Fe$_3$O$_4$-flyash composite particles in 3 wt% H$_2$O$_2$ solution (a). The contact time varies as 1 (i), 2 (ii), 3 (iii), 5 (iv), 10 (v), 15 (vi), 30 (vii), 45 (viii), and 60 min (ix). (b) Variation in the maximum PL intensity as a function of contact time.

The catalytic nature of magnetic Pd-Fe$_3$O$_4$-flyash composite particles in the decolorization of aqueous solution containing MB dye via the Fenton-like reactions is confirmed here. The variation in the normalized MB dye concentration decomposed as a function of contact time as obtained for the consecutive dye-decomposition cycles (total # 10) conducted in the dark-condition, is presented Fig. 6.14. It is noted that the maximum amount of MB dye decomposed in 1 h is 100% for the first 10 cycles. Hence, considerable catalytic activity is maintained by the magnetic Pd-Fe$_3$O$_4$-flyash composite particles for the MB decomposition in the dark-condition.
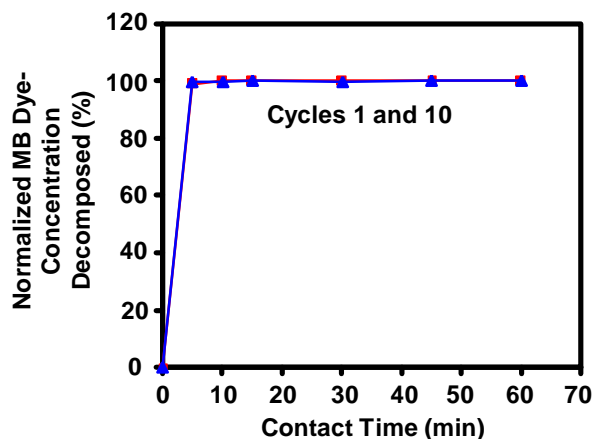
Fig. 6. 14. Typical variation in the normalized MB dye concentration decomposed as a function of contact time as obtained in the dark-condition, using the magnetic Pd-Fe_3O_4-flyash composite particles (40 g l^{-1}), in an aqueous solution containing 7.5 μM (0.0024 g l^{-1}) of MB and 3 wt% H_2O_2 as a strong-oxidizer. Total 10 dye-decomposition cycles were conducted out of which only the selected cycles (cycles-1 and 10) are shown here for clarity.

The magnetic Pd-Fe_3O_4-flyash composite particles are further utilized for the decoloration of aqueous solutions containing the Corafix Red ME4B dye. The variation in the color of the dye-solutions as a function of contact time, as obtained for the varying initial Corafix Red ME4B dye concentrations, is presented in Fig. 6.15. Although the decoloration of initial dye solutions is clearly visible within the first 15-60 min of contact time for all initial dye concentrations, the comparison with Fig. 6.10 qualitatively suggests that the kinetics of the degradation of industrial azo reactive dye is reduced compared with that obtained with the non-magnetic Pd-flyash composite particles, Fig. 6.10.
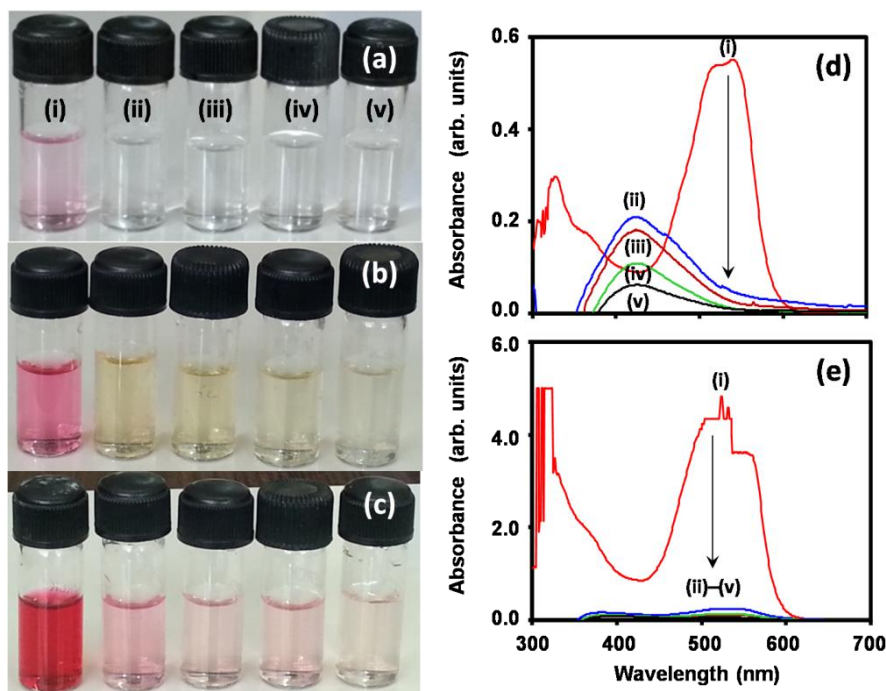
Fig. 6.15. Variation in the color of initial dye-solutions (0.003 (a), 0.03 (b), and 0.3 g l^{-1} (c)) as a function of contact time (0 (i), 15 (ii), 30 (iii), 45 (iv), and 60 min (v)) as obtained for the Corafix Red ME4B dye using the magnetic Pd-Fe$_3$O$_4$-flyash composite particles (100 g l^{-1}). The initial H$_2$O$_2$ concentration is 50 wt%. Corresponding variation in the intensity of absorbance-peak located at ~543 nm for the initial dye-concentration of 0.03 (d) and 0.3 g l^{-1} (e).

The variation in the maximum intensity of absorbance-peak located at ~543 nm related to the Corafix Red ME4B dye as observed with the increasing contact time, for the initial dye-concentrations of 0.03 and 0.3 g l^{-1}, is presented in Fig. 6.15d and e respectively. The comparison with the similar spectra presented in Fig. 6.10 supports the decreased kinetics of the dye degradation as obtained using the magnetic Pd-Fe$_3$O$_4$-flyash composite particles. Nevertheless, the decoloration of the aqueous solution containing the industrial azo reactive dye using the magnetic Pd-Fe$_3$O$_4$-flyash composite particles is successfully demonstrated here. The COD values of the initial

dye solution, catalyst-treated and AC treated solutions are displayed in Fig. 6.16. The trend in the variation in the values of COD levels are observed to be similar in nature to that observed in the case of non-magnetic Pd-flyash composite particles, Fig. 6.7.
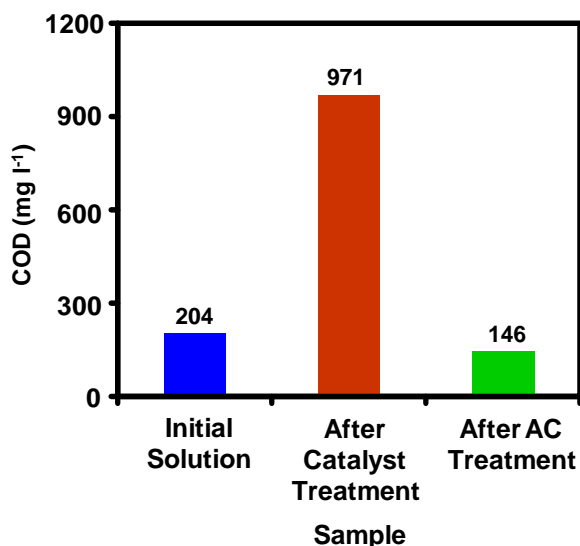
Fig. 6.16. Variation in the COD levels as measured for the aliquots obtained under the different test-conditions. The dye-decomposition experiments were conducted using the Corafix Red ME4B dye in 100 ml of 50 wt% H_2O_2 solution having the initial dye concentration of 0.003 g l^{-1} and catalyst (magnetic Pd-Fe_3O_4-flyash composite particles) concentration of 100 g l^{-1} with the contact time of 1 h. The AC (50 g l^{-1}) treatment was conducted in 100 ml of distilled H_2O for the contact time of 5 h.

An increase in the COD level of 37.6% is observed after the treatment with the magnetic Pd-Fe_3O_4-flyash composite particles which is attributed to the leaching of large amount of carbon already present on the surface of magnetic Pd-Fe_3O_4-flyash composite particles and the possible presence of intermediate products of the degradation of Corafix Red ME4B dye. The COD level is, however, decreased by 28% and 85% relative to the initial and catalyst-treated dye solutions after the

treatment of decolorized solution using the AC. Also, the variations in the composition of the gases emanating from the different initial dye solutions appear to be similar for both the non-magnetic and magnetic composite particles used as the catalyst in this investigation (Table 6.2).

Table 6.3. The contents of gaseous stream emanating from the aqueous solutions containing the magnetic $Pd-Fe_3O_4$-flyash composite particles under the different test-conditions.

Test- Conditions	Gas Concentration (ppm)				Gas Concentration (Vol%)
	CO	CO_2	CH_4	N_2O	O_2
(Blank) $Pd-Fe_3O_4$-flyash (50 g l^{-1}) + 30 wt% H_2O_2	86	273	---	0.05	35
$Pd-Fe_3O_4$-flyash (50 g l^{-1}) + 30 wt% H_2O_2 + 30 μM (0.0096 g l^{-1}) MB	8.5	313	0.68	0.12	78
$Pd-Fe_3O_4$-flyash (50 g l^{-1}) + 30 wt% H_2O_2 + 500 μM (0.16 g l^{-1}) MB	6.0	369	0.77	0.11	65
$Pd-Fe_3O_4$-flyash(100 g l^{-1}) + 50 wt% H_2O_2 + Corafix Red ME4B (0.003 g l^{-1})	8.6	419	0.54	0.06	90

Overall, the current dye-removal technology involving the H_2O_2 activation using the magnetic $Pd-Fe_3O_4$-flyash composite particles, backed-up by the AC-based adsorption process, can be effectively utilized for obtaining the quicker and complete decoloration of aqueous solutions containing the organic synthetic-dyes with considerable reduction in the COD levels of the treated aqueous solutions. Moreover, the magnetic separation of the catalyst is an added advantage in the present

technology for the easy and quick separation of the catalyst without any loss during the solid-liquid separation which is helpful for conducting the number of consecutive dye-removal cycles.

6.4. Conclusions

The non-magnetic Pd-flyash and magnetic Pd-Fe$_3$O$_4$-flyash composite particles have been successfully processed using the combination of electroless and inverse co-precipitation techniques. For the first time, it is demonstrated that these composite particles can be successfully utilized as the catalyst for the decoloration of aqueous solutions containing the basic (such as MB) and industrial azo reactive dye (Corafix Red ME4B) via the Fenton-like reactions. The current dye-removal technology also involves the magnetic separation of the catalyst and the adsorption treatment of high surface-area AC to control the final COD levels of the catalyst-treated aqueous solutions. Overall, the Fenton-like reactions backed up with the AC-based adsorption process is an effective combination for the fast and efficient removal of organic synthetic-dyes from the aqueous solutions. Due to the utilization of flyash as a catalyst-support, the present technology bridges the gap between the thermal power plants and dye-related industries.

References

1. Shukla, S.; Warrier, K. G. K.; Babu, B. K., A process for decomposition of organic synthetic-dyes using semiconductor-oxides nanotubes via dark-catalysis. *World Intellectual Property Organization (WIPO) Publication Number WO/2014/027364*, **20-February-2014**.

2.   Shukla, S.; Oturan, M. A., Dye removal using electrochemistry and semiconductor oxide nanotubes. *Environ. Chem. Lett.* **2015**, *13*, 157-172.

3.   Jose, M.; Haridas, M. P.; Shukla, S., Predicting dye-adsorption capacity of hydrogen titanate nanotubes via one-step dye-removal method of novel chemically-activated catalytic process conducted in dark. *J. Environ. Chem. Eng.* **2014**, *2*(4), 1980-1988.

4.   Babitha, K.; Warrier, K. G.; Shukla, S., Decolorization of aqueous solution containing organic synthetic-dye via dark-catalysis process using hydrothermally synthesized semiconductor-oxides nanotubes. *Adv. Sci., Eng. Med.* **2014**, *6*(2), 173-183.

5.   Lorencon, E.; Brandao, F. D.; Krambrock, K.; Alves, D. C.; Silva, J. C.; Ferlauto, A. S.; Lago, R. M., Generation of reactive oxygen species in titanates nanotubes induced by hydrogen peroxide and their application in catalytic degradation of methylene blue dye. *J. Mol. Catal. A* **2014**, *394*, 316-323.

6.   Zhou, C.; Luo, J.; Chen, Q.; Jiang, Y.; Dong, X.; Cui, F., Titanate nanosheets as highly efficient non-light-driven catalysts for degradation of organic dyes. *Chem. Commun.* **2015**, *51*(54), 10847-10849.

7.   Zazo, J.; Casas, J.; Mohedano, A.; Gilarranz, M.; Rodriguez, J., Chemical Pathway and kinetics of phenol oxidation by Fenton's reagent. *Environ. Sci. Technol.* **2005**, *39*(23), 9295-9302.

8.   Dhakshinamoorthy, A.; Navalon, S.; Alvaro, M.; Garcia, H., Mmetal nanoparticles as heterogeneous Fenton catalysts. *Chem. Sus. Chem.* **2012**, *5*(1), 46-64.

9.   Gil-Lozano, C.; Losa-Adams, E.; Alfonso, F.; Gago-Duport, L., Pyrite nanoparticles as a Fenton-like reagent for in situ remediation of organic pollutants. *Beilstein J. Nanotechnol.* **2014**, *5*(1), 855-864.

10. Yalfani, M. S.; Contreras, S.; Medina, F.; Sueiras, J., Direct generation of hydrogen peroxide from formic acid and O_2 using heterogeneous Pd/γ-Al_2O_3 catalysts. *Chem. Commun.* **2008**, (33)3885-3887.

11. Yalfani, M. S.; Contreras, S.; Medina, F.; Sueiras, J., Phenol degradation by Fenton's process using catalytic in situ generated hydrogen peroxide. *Appl. Catal. B* **2009**, *89*(3), 519-526.

12. Li, X.; Liu, X.; Xu, L.; Wen, Y.; Ma, J.; Wu, Z., Highly dispersed Pd/PdO/Fe_2O_3 nanoparticles in SBA-15 for Fenton-Like processes: confinement and synergistic effects. *Appl. Catal. B* **2015**, *165*, 79-86.

13. Shukla, S.; Seal, S.; Akesson, J.; Oder, R.; Carter, R.; Rahman, Z., Study of mechanism of electroless copper coating of fly-ash cenosphere particles. *Appl. Surf. Sci.* **2001**, *181*(1), 35-50.

14. Muhammad, S.; Saputra, E.; Sun, H.; Izidoro, J. D. C.; Fungaro, D. A.; Ang, H. M.; Tade, M. O.; Wang, S., Coal fly ash supported Co_3O_4 catalysts for phenol degradation using peroxymonosulfate. *RSC Adv.* **2012**, *2*(13), 5645-5650.

15. Shukla, S.; Seal, S., Electroless copper coating of zirconia utilizing palladium catalyst. *J. Am. Ceram. Soc.* **2003**, *86*(2), 279-285.

16. Cheng, J.; Ma, R.; Chen, X.; Shi, D.; Liu, F.; Zhang, X., Effect of ferric ions on the morphology and size of magnetite nanocrystals synthesized by ultrasonic irradiation. *Crys. Res. Technol.* **2011**, *46*(7), 723-730.

17. Rice, E. W.; Baird, R.B.; Eaton, A.D.; Clesceri L.S., (Eds.) Standard methods for the examination of water and wastewater. *American Public Health Association* **2002**, *Washington, 2012, 22*[nd] *Edition*.

18. Narayani, H.; Arayapurath, H.; Shukla, S., Using Fenton-Reaction as a Novel approach to enhance the photocatalytic activity of TiO_2-γ-Fe2O3 magnetic

photocatalyst undergoing photo-dissolution process without silica interlayer. *Catal. Lett.* **2013**, *143*(8), 807-816.

19. Ishibashi, K.i.; Fujishima, A.; Watanabe, T.; Hashimoto, K., Quantum yields of active oxidative species formed on TiO_2 photocatalyst. *J. Photochem. Photobiol.* **2000**, *134*(1), 139-142.

20. Hirakawa, T.; Nosaka, Y., Properties of $O_2^{\bullet-}$ and $^{\bullet}OH$ formed in tio2 aqueous suspensions by photocatalytic reaction and the influence of H_2O_2 and some ions. *Langmuir* **2002**, *18*(8), 3247-3254.

21. Ang, L. M.; Hor, T. A.; Xu, G. Q.; Tung, C. H.; Zhao, S.; Wang, J. L., Electroless plating of metals onto carbon nanotubes activated by a single-step activation method. *Chem. Mater.* **1999**, *11*(8), 2115-2118.

22. Bokare, A. D.; Choi, W., Review of iron-free Fenton-Like systems for activating H_2O_2 in advanced oxidation processes. *J. Hazard. Mater.* **2014**, *275*, 121-135.

23. Choudhary, V. R.; Samanta, C.; Jana, P., Decomposition and/or hydrogenation of hydrogen peroxide over Pd/Al_2O_3 catalyst in aqueous medium: factors affecting the rate of H_2O_2 destruction in presence of hydrogen. *Appl Catal A* **2007**, *332*(1), 70-78.

24. Yuan, S.; Fan, Y.; Zhang, Y.; Tong, M.; Liao, P., Pd-catalytic in situ generation of H_2O_2 from H_2 and O_2 produced by water electrolysis for the efficient electro-fenton degradation of Rhodamine B. *Environ. Sci. Technol.* **2011**, *45*(19), 8514-8520.

25. Baiju, K.; Shukla, S.; Sandhya, K.; James, J.; Warrier, K., Photocatalytic activity of sol-gel-derived nanocrystalline titania. *J. Phys. Chem. C* **2007**, *111*(21), 7612-7622.

26. Lachheb, H.; Puzenat, E.; Houas, A.; Ksibi, M.; Elaloui, E.; Guillard, C.; Herrmann, J.-M., Photocatalytic degradation of various types of dyes (Alizarin S, Crocein orange G, Methyl red, Congo red, Methylene blue) in water by UV-irradiated titania. *Appl. Catal. B* **2002**, *39*(1), 75-90.

27. Aber, S.; Sheydaei, M., Removal of COD from industrial effluent containing indigo dye using adsorption method by activated carbon cloth: optimization, kinetic, and isotherm studies. *Clean - Soil Air Water* **2012**, *40*(1), 87-94.

28. Bansode, R.; Losso, J.; Marshall, W.; Rao, R.; Portier, R., Pecan shell-based granular activated carbon for treatment of chemical oxygen demand (COD) in municipal wastewater. *Bioresource technology* **2004**, *94*(2), 129-135.

29. Jeong, J.; Yoon, J., pH Effect on OH Radical production in photo/ferrioxalate system. *Water Research* **2005**, *39*(13), 2893-2900.

30. Cruz-Gonzalez, K.; Torres-Lopez, O.; Garcia-Leon, A.; Guzman-Mar, J.; Reyes, L.; Hernandez-Ramírez, A.; Peralta-Hernandez, J., Determination of optimum operating parameters for Acid Yellow 36 decolorization by electro-fenton process using bdd cathode. *Chem. Eng. J.* **2010**, *160*(1), 199-206.

31. Harsha, N.; Krishna, K. S.; Renuka, N. K.; Shukla, S., Facile synthesis of γ-Fe_2O_3 nanoparticles integrated $H_2Ti_3O_7$ nanotubes structure as a magnetically recyclable dye-removal catalyst. *RSC Adv.* **2015**, *5*(38), 30354-30362.

32. Thazhe, L.; Shereef, A.; Shukla, S.; Pattelath Reshmi, C.; Varma, M. R.; Suresh, K. G.; Patil, K.; Warrier, K. G., Magnetic dye-adsorbent catalyst: processing, characterization, and application. *J. Am. Ceram. Soc.* **2010**, *93*(11), 3642-3650.

33. Panias, D.; Taxiarchou, M.; Paspaliaris, I.; Kontopoulos, A., Mechanisms of dissolution of iron oxides in aqueous oxalic acid solutions. *Hydrometallurgy* **1996**, *42*(2), 257-265.

Chapter 7

Summary and Suggestions for the Future Work

7.1. Summary

In the present investigation, the dye-removal from the aqueous solutions is studied using three different technologies – photocatalysis, adsorption, and AOPs. The basic and three different industrial azo reactive dyes are considered for this purpose. Different magnetic nanocomposites are developed and their characteristics in the respective dye-removal application are examined relative to those of the non-magnetic counter parts. Attention is paid to resolve some of the pending issues associated with the above dye-removal processes to make them suitable for the commercialization in the near-future.

1. The photocatalysis mechanism is investigated by synthesizing the γ-Fe_2O_3/SiO_2/TiO_2 magnetic nanocomposite with the varying amount of TiO_2 content in the shell via the combination of modified Stober and sol-gel processes. The maximum photocatalytic activity is exhibited by the anatase-TiO_2-coated (cycle-5) SiO_2/γ-Fe_2O_3 magnetic nanocomposite particles, which exhibits the photocatalytic activity which is comparable with that of the commercial (CDH) nanocrystalline anatase-TiO_2. It shows the effective magnetic separation from the treated aqueous solution in the presence of an external magnetic field. The regeneration and reuse of the magnetic nanocomposite is demonstrated for three consecutive cycles of MB degradation. Moreover, it is observed that the photocatalytic activity of anatase-TiO_2 coated (cycles-1 and 5) $(\gamma+\alpha)$/α-Fe_2O_3 core-shell magnetic nanocomposite particles, without the SiO_2 interlayer, is severely affected by the photo-dissolution phenomenon which strongly suggests

the instability in the core (γ-Fe$_2$O$_3$) of the magnetic photocatalyst particles. *For the first time*, it is successfully demonstrated that the involvement of AOPs, such as the Fenton-reaction, makes the same photo-dissolution process responsible for an enhanced photocatalytic activity which is comparable with that of the magnetic nanocomposite particles having SiO$_2$ as an interlayer. However, it appears that, maintaining high catalytic activity for large number of successive dye-degradation cycles, typically with large initial dye-concentrations, is possibly a major issue with the magnetic nanocomposite developed for the photocatalysis mechanism.

2. The adsorption mechanism is, hence, investigated by synthesizing the non-magnetic HTN (as a reference material) having high specific surface-area via hydrothermal method using the pure nanocrystalline anatase-TiO$_2$ as a precursor. The HTN exhibit the maximum MB adsorption capacity of 105 mg g^{-1} involving the electrostatic attraction mechanism. The adsorption of MB on the surface of HTN follows the pseudo-second-order kinetics and the equilibrium isotherm follows the Langmuir model in a highly acidic solution (initial solution-pH~2.5) and DKR model in a highly basic solution (initial solution-pH~11). Within the intermediate range of initial solution-pH (~7.5 and 10), it exhibits a transition from the Langmuir to DKR model. However, being non-magnetic in nature, the HTN could not be separated from the treated aqueous solution using an external magnetic field. Moreover, decomposing the previously adsorbed MB dye on the surface of HTN for its effective regeneration and reuse for the multiple cycles of adsorption is a challenge.

3. The adsorption mechanism is further investigated by converting the non-magnetic HTN to the magnetic HTN. The magnetic HTNF nanocomposite composed of

H$_2$Ti$_3$O$_7$ nanotubes/nanosheets and γ-Fe$_2$O$_3$ nanoparticles are processed by subjecting the sol-gel derived core-shell γ-Fe$_2$O$_3$/SiO$_2$/TiO$_2$ magnetic photocatalyst, having the varying amount of TiO$_2$ in the shell, to the hydrothermal conditions. By this method, the HTNF magnetic nanocomposite with the amount of γ-Fe$_2$O$_3$ varying in the higher range of 61-92 wt% could be synthesized. The HTNF magnetic nanocomposite having 31 wt% H$_2$Ti$_3$O$_7$ exhibits the highest MB adsorption capacity (74 mg g^{-1}). The value of maximum MB adsorption capacity obtained is, however, less than that obtained for the pure HTN. However, the HTNF magnetic nanocomposite could be separated from the treated aqueous solution (in less than a minute) using an external magnetic field which is not possible for the pure HTN. Moreover, the HTNF magnetic nanocomposite could be regenerated and reused using the non-light driven activation of H$_2$O$_2$. *For the first time,* the synergy effect between the constituents of HTNF magnetic nanocomposite in the generation and attack of ROS, such as the O$_2$$^{•-}$ and $^{•}$OH radicals, is demonstrated. Nevertheless, in order to synthesize the HTNF magnetic nanocomposite with the amount of γ-Fe$_2$O$_3$ varying in the lower range, and hence, to increase the MB adsorption capacity, an alternative method of synthesizing the HTNF magnetic nanocomposite is required to be developed.

4. The adsorption mechanism is then investigated by processing the magnetic HTNF nanocomposite using the simple mechanical mixing of the HTN and γ-Fe$_2$O$_3$ nanoparticles in the neutral aqueous solution. *For the first time*, it is demonstrated that the formation of HTNF magnetic nanocomposite via this process involves an ion-exchange bond formation at the interface between the γ-Fe$_2$O$_3$ nanoparticles and short-edges of HTN. By this method, the HTNF magnetic nanocomposite with the amount of γ-Fe$_2$O$_3$ varying in the lower range of 5-25

wt% could be synthesized. The HTNF magnetic nanocomposite having 95 wt% $H_2Ti_3O_7$, exhibits the highest MB adsorption capacity (99 mg g^{-1}) which is marginally lower than that of the pure HTN. The HTNF magnetic nanocomposite could be separated from the treated aqueous solution (in less than two minute) using an external magnetic field which is not possible in the case of pure HTN. Moreover, the HTNF magnetic nanocomposite could be regenerated and reused using the non-light driven activation of H_2O_2 similar to the previous case. It appears that the HTNF magnetic nanocomposites processed with the ion-exchange mechanism has an edge over the samples processed using the combination of sol-gel and hydrothermal methods due to their lower content of γ-Fe_2O_3 and higher MB adsorption capacity. However, as a result of their limited adsorption capacity and the requirement of decomposition of the previously adsorbed dye on the surface required for the recycling, the HTNF magnetic nanocomposite pose a major restriction in the fast and efficient removal of organic synthetic-dyes via the combination of adsorption and H_2O_2 activation (AOPs).

5. On the other hand, the mechanisms merely based on the AOPs appear to be suitable for the fast and efficient removal of organic synthetic-dyes from the aqueous solutions. The non-magnetic Pd-flyash and magnetic Pd-Fe_3O_4-flyash composite particles are, hence, successfully processed using the combination of electroless and inverse co-precipitation techniques and utilized for the dye-removal from the aqueous solutions via the AOPs. The removal of basic as well as highly stable industrial azo reactive dyes is demonstrated using these two types of catalysts. Although the dye-removal rates are higher with the non-magnetic Pd-flyash composite particles; the Pd-Fe_3O_4-flyash composite particles are suitable for the magnetic separation using an external magnetic field. Moreover, both the

244

types of composite particles show much higher catalytic activity than the catalysts investigated in the previous two dye-removal mechanisms. In addition to this, the successful dye-decomposition is also achieved here in highly concentrated dye solutions compared with the catalysts utilized in the previous two mechanisms. Although the increased COD levels of the catalyst treated aqueous solutions is a major concern, it is successfully controlled by using the adsorption treatment using the high surface-area AC.

6. Overall, within the limits of the investigated mechanisms of the dye-removal, the synthesized novel catalysts, and the range of values of different test-parameters, it is proposed that the dye-removal mechanism involving the AOPs backed with the AC treatment is suitable for the fast and efficient removal of organic synthetic-dyes from the aqueous solutions.

7.2. Suggestions for the future work

The following are the recommendations proposed for the future work.

1. Since the AOPs backed up with the AC treatment is a two-step process, the latter increases the time required for the complete dye-removal. To enhance the kinetics of the dye-removal, the processing of the magnetic Pd-Fe_3O_4-AC nanocomposite is suggested which may decompose the organic synthetic-dyes and simultaneously take care of the COD levels of the final treated aqueous solutions.

2. The AOPs based on the H_2O_2 are extremely costlier processes. For the possible commercialization of this technology, the cost-reduction is absolutely essential which may be achieved using the cheaper oxidizers than the H_2O_2.

Output

List of Patents

1. S.V. Shukla, H. Padinhattayil, **H. Narayani**, M. Jose, R. Karunakaran, "Semiconductor Oxide Nanotubes Based Composite Particles Useful for Dye Removal and Process Thereof", Taiwan Patent No. I542564 (Granted on 21-July-2016).

List of Publications (Thesis)

1. **Narayani**, H.; Jose, M.; Sriram, K.; Shukla, S., Hydrothermal Synthesized Magnetically Separable Mesostructured $H_2Ti_3O_7$/γ-Fe_2O_3 Nanocomposite for Organic Dye Removal via Adsorption and Its Regeneration / Reuse through Synergistic Non-Radiation Driven H_2O_2 Activation. *Environ. Sci. Pollut. Res.* **2017**, DOI:10.1007/s11356-017-8381-2.

2. **Narayani, H**.; Augustine, R.; Sumi, S.; Jose, M.; Deepa Nair, K.; Samsuddin, M.; Prakash, H.; Shukla, S., Removal of basic and industrial azo reactive dyes from aqueous solutions via Fenton-like reactions using catalytic non-magnetic Pd-flyash and magnetic Pd-Fe_3O_4-flyash composite particles. *Sep. Purif. Technol.* **2017,** 172, 338-349.

3. **Harsha, N**.; Krishna, K. S.; Renuka, N. K.; Shukla, S., Facile synthesis of γ-Fe_2O_3 nanoparticles integrated $H_2Ti_3O_7$ nanotubes structure as a magnetically recyclable dye-removal catalyst. *RSC Adv.* **2015,** *5* (38), 30354-30362.

4. **Narayani, H**.; Arayapurath, H.; Shukla, S., Using Fenton-reaction as a novel approach to enhance the photocatalytic activity of TiO_2-γ-Fe_2O_3 magnetic photocatalyst undergoing photo-dissolution process without silica interlayer. *Catal. Lett.* **2013,** *143* (8), 807-816.

5. **Narayani, H**.; Arayapurath, H.; Shukla, S., Significance of silica interlayer in magnetic photocatalyst having γ-Fe$_2$O$_3$ as a magnetic ceramic core. *Sci. Adv. Mater.* **2013**, *5*, 1060-1073.

6. **Narayani, H**.; Kunniveetil, S. P.; Shukla, S., Effect of solution-ph on methylene blue dye adsorption on hydrogen titanate nanotubes processed via hydrothermal method. *Adv. Sci. Eng. Med.* **2013,** *5* (1), 63-72.

List of Publications (Non-Thesis)

1. Jose, M.; **Narayani, H**.; Kumar, J.; Shukla, S., Photocatalytic activity of acid-catalyst-modified sol-gel processed nanocrystalline titania: on dual-role of active surface-sites. *Sci. Adv. Mater.* **2015,** *7* (4), 729-745.

2. Jose, M.; **Harsha, N**.; Suhailath, K.; Mohamed, A. P.; Shukla, S., Hydrogen phosphate anions modified hydrogen titanate nanotubes for methylene blue adsorption from aqueous solution: Validating novel method of predicting adsorption capacity. *JECE* **2016,** *4* (1), 1295-1307.

List of Conference Presentations

1. **Harsha, N**.; Shukla, S., "Hydrothermal processing of hydrogen titanate nanosheets /nanotubes-γ-Fe$_2$O$_3$core-shell structures and their dye-adsorption characteristics", (**Poster Presentation**) In: International Conference on Advanced Functional Materials (ICAFM) Organized by the National Institute for Interdisciplinary Science and Technology (CSIR-NIIST), Materials Research Society of India (MRSI), Indian Ceramic Society (InCerS), Indian Institute of Metals (IIM), and Society for Polymer Science (SPS, India), Thiruvananthapuram, Kerala, 19-21 February 2014.

2. **Harsha, N**.; Manu, J.; Rimesh, A.; Manoj, P. H.; Hareesh, P.; Shukla, S., "Hydrogen titanate nanotubes and nanosheets for dye-removal via novel dark-catalysis", (**Poster Presentation**) In: Nano India 2013, Organized by Department

of Science and Technology (DST) and National Institute for Interdisciplinary Science and Technology (CSIR-NIIST), Thiruananthapuram, Kerala, India, 19-20 Februrary 2013.

3. **Harsha, N**.; Manu, J.; Shukla, S., "Semiconductor oxides nanotubes/nanosheets-based magnetic / non-magnetic dye-adsorbent catalysts" (**Oral Presentation**) In: National Conference on Green Manufacturing Technologies in Glass and Ceramics (GTGC-2013), 76th Annual Session of the Indian Ceramic Society (InCerS), Ahmedabad, Gujarat, 18-19 January 2013.

4. **Harsha, N**.; Lajina, M. T.; Babitha, K. B.; Remya, R.; Shukla, S., "Industrial dye-removal using hydrogen titanate nanotubes", (**Poster Presentation**) In: International Conference and Workshop on Nanostructured Ceramics and Other Nanomaterials (ICWNCN-2012)", Organized by the Department of Physics and Astrophysics, University of Delhi, New Delhi, India, 12-16 March 2012.

5. **Harsha, N**.; Hareesh, P.; Manu, J.; Babitha, K. B.; Remya, K.; Shukla, S., "Novel dye-removal technology based on nanotubes of semiconductor oxides", (**Poster Presentation**) In: 14th CRSI National Symposium in Chemistry (NSI), Thiruvananthapuram, Kerala, 3-5 February 2012.

6. **Harsha, N**.; Shyama, P. K.; Shukla, S., "Hydrothermally processed hydrogen titanate nano-tubes and their dye-adsorption capacity", (**Poster Presentation**) In: National Seminar on Current Trends in Chemistry (CTriC-2012), Department of Applied Chemistry, Cochin University of Science and Technology (CUSAT), Cochin, Kerala, India, 20-21 January 2012.

7. **Harsha, N**.; Shukla, S., "Pure and surface-functionalized hydrothermally processed nanotubes of anatase-titania as dye-adsorbent" (**Oral Presentation**) In: National Seminar on Current Trends in Chemistry (CTriC-2011), Department of Applied Chemistry, Cochin University of Science and Technology (CUSAT), Cochin, Kerala, India, 04-05 March 2011.

8. **Harsha, N**.; Shyama, P. K.; Babitha, K. B.; Shukla, S., "Dye-adsorption characteristics of hydrogen titanate and anatase-titania nanotubes", (**Poster Presentation**) In: Platinum Jubilee Session of Indian Ceramic Society (InCerS), Agra, Uttar Pradesh, India 20-22 December 2011 (**BEST POSTER AWARD**).